AN ABSTRACT OF THE THESIS OF

Patrick M. Woodward for the degree of Doctor of Philosophy in Chemistry presented on November 22, 1996. Title: Structural Distortions, Phase Transitions, and Cation Ordering in the Perovskite and Tungsten Trioxide Structures.

Abstract Approved: Redacted for privacy
Arthur W. Sleight

The 23 Glazer tilt systems describing octahedral tilting in perovskites have been investigated. It is shown that in tilt systems $a^+a^+a^-$, $a^+b^+b^-$, $a^+a^+c^-$, $a^+b^+c^-$, $a^0b^+b^-$, and $a^0b^+c^-$ it is not possible to link together a three dimensional network of perfectly rigid octahedra. A table of predicted space groups for ordered perovskites, $A_2MM'O_6$, in all 23 tilt systems is given. The various tilt systems have been compared in terms of their A cation coordination and it is shown that for AMX_3 compounds those tilt systems in which all of the A cation sites remain crystallographically equivalent are strongly favored. Tilt systems with nonequivalent A site environments are observed when at least two A cations with different sizes and/or bonding preferences are present. In these compounds the ratio of large to small cations dictates the most stable tilt system.

Over thirty double perovskite, $A_2MM'O_6$, compounds have been synthesized and structurally characterized using X-ray and neutron powder diffraction and the Rietveld method. Sr_2CrTaO_6 is shown to be tetragonal rather than cubic as originally thought. Sr_2YTaO_6 is shown to be the only structurally characterized member of tilt system $a^+b^-c^-$. A formula is derived which is capable of accurately predicting the unit cell volume and tilt system for double perovskite compounds with A=Ca, Sr, or Ba from the ionic radii of the octahedral cations. The differences in charge and size, bonding preferences, and oxidation state stability of the octahedral site cations are shown to be the primary factors in determining the degree of long range order in $A_2MM'O_6$ compounds. The A cation does not appear to play a significant role in the ordering behavior.

The structure of triclinic δ-WO_3 is determined from neutron powder diffraction for the first time. This phase is the thermodynamically stable form of WO_3 at room temperature. The structure of the low temperature ε-WO_3 has been determined for the first time. Earlier inconclusive evidence for ferroelectricity in this phase is confirmed. The ε to δ phase transition is shown to be driven by shifts in the tungsten positions, while the δ to γ phase transition is driven by a change in the octahedral tilt system.

Structural Distortions, Phase Transitions, and Cation Ordering in the Perovskite and Tungsten Trioxide Structures

by

Patrick M. Woodward

A THESIS

submitted to

Oregon State University

in partial fulfillment of
the requirements for the degree of

Doctor of Philosophy

Completed November 22, 1996
Commencement June 1997

Doctor of Philosophy thesis of Patrick M. Woodward presented on November 22, 1996.

APPROVED :

Redacted for privacy

Major Professor, representing Chemistry

Redacted for privacy

Head of Department of Chemistry

Redacted for privacy

Dean of the Graduate School

I understand that my thesis will become part of the permanent collection of Oregon State University libraries. My signature below authorizes release of my thesis to any reader upon request.

Redacted for privacy

Patrick M. Woodward, Author

Acknowledgment

My tenure at Oregon State University has been an extremely enjoyable and rewarding experience, for this I owe a debt of thanks to several people. First of all I would like to acknowledge my advisor, Professor Arthur Sleight. He has allowed me to work independently, letting primarily my curiosity dictate the course of my research. Yet whenever I needed guidance or advice he was always easily accessible, and a great source of knowledge. On top of that he supported me as a research assistant almost continuously, and provided any equipment or supplies I needed. Upon choosing a graduate school it seemed as though there were many interesting options, but I can say now that I could have found no better place to study solid state chemistry. The work contained in this thesis is to some extent a continuation of ideas explored in his own Ph.D. thesis. I hope that he finds this work interesting and a worthy extension of the ideas first presented in that thesis.

I learned a great deal from all of the people with whom I shared the lab with over the past five years: Vince, Phong, Sasi, Nazy, Matt, Paul, Maddy, Tao, Ivana, Amar, Jinfan, Laura, Ruiping, Mark, Richard, Mary, Seung-Tae, Martin, Corrine, Claire, Xinhau, Nobu, Ryogi, Svetlana, Marina, Duk-Soo, and Ho-Kun. I would also like to acknowledge the friendship and advice obtained from Chris and Steve in Dr. Lerner's group, as well as Chris Pyle and Cheryl Hills. There are two people however, who deserve special mention. Rolf-Dieter Hoffmann introduced me to X-ray diffraction, the Rietveld method, and size-strain analysis. Practically all I know about crystallography I learned from Rolf. He was also a gracious host to me last year when I visited Germany. Most of what I didn't learn from Dr. Sleight and Rolf, I learned from John Evans. John continuously answered questions about computing and crystallography, proofread chapters two and three in their entirety, introduced me to the pleasure of stouts, porters, and bitters, and still had time to beat me soundly at squash. His friendship I will always remember as being one of the best things I got out of graduate school. Thanks to my brothers at Phi Sigma Kappa fraternity for providing me a place to live, and significantly easing my adjustment to Corvallis. I particularly want to thank Sam, Brian, Brent, Brian, Tony, and Loyan for their continual friendship over the years. All of these people made my stay in Corvallis a wonderful period in my life.

Tom Vogt collected all of the neutron diffraction patterns, which are an integral part of chapters four, seven, and eight. I thank him for that, and look forward to continued

collaboration once I arrive at Brookhaven. Discussions and e-mail correspondence with Dong-Kyun Seo, of North Carolina State University, were instrumental in helping a novice properly interpret the results of the extended Hückel calculations.

Finally, I want to thank my family. My wife Laurinda has been supportive of me throughout the past 62 months of late nights and small paychecks. Without her emotional (and financial) support I could not have completed this degree. My son Denver has been a great inspiration to me. He is always able to get my mind off chemistry, which is essential to maintain both my sanity and creativity. I anxiously look forward to being reunited with them upon completion of my dissertation. My parents and grandparents: Lynn and James, Woody, Carolyn and Denver, Carl and Barbara have all given a great deal to me over the years, it is their guidance through the years that has made me who I am today.

Table of Contents

Table of Contents (Continued)

Table of Contents (Continued)

Table of Contents (Continued)

Table of Contents (Continued)

List of Figures

List of Figures (Continued)

List of Figures (Continued)

List of Tables

List of Tables (continued)

List of Tables (continued)

List of Tables (continued)

List of Appendices

List of Appendix Tables

Structural Distortions, Phase Transitions, and Cation Ordering in the Perovskite and Tungsten Trioxide Structures

Chapter 1

Introduction

1.1 History of Perovskites

The term "perovskite" was originated as the name of the mineral whose empirical formula is $CaTiO_3$. The mineral perovskite was discovered in 1839 by the German chemist and mineralogist Gustav Rose, presumably discovered on an expedition to a remote region of the Russian empire (Ural). It was named after Lev Alexeievitch Perovsky (1792-1856) a Russian dignitary who held the posts of Secretary of the Interior and Director of the Imperial Cabinet (Navrotsky & Weidner, 1989). As time went by many compounds were found to possess a crystal structure very similar to $CaTiO_3$, and today the term "perovskite" is used to describe the large class of compounds that adopt crystal structures similar to $CaTiO_3$. In this way it has come to pass that a relatively unimportant mineral, named after a minor Russian dignitary, has lent its name to one of the most important structure classes in all of chemistry, materials science, and mineralogy.

1.2 Crystal Structure of Perovskites

The ideal perovskite structure has an AMX_3 stoichiometry and belongs to the cubic space group $Pm\bar{3}m$. The A cation is surrounded by 12 X anions in a dodecahedral environment, the M cation is octahedrally coordinated by 6 X ions, and the X anions are coordinated by 2 M cations and 4 A cations. There are at least two ways of visualizing the structure. The most common description of the perovskite structure is a three dimensional cubic network of corner sharing MX_6 octahedra. In this description the A cation sits in the center of a cube defined by eight corner sharing octahedral units. An alternative way of visualizing the perovskite structure is to begin with a cubic close packed array of X anions, then replace one out of every four X ions with an A cation in an ordered way to obtain a cubic close

a)

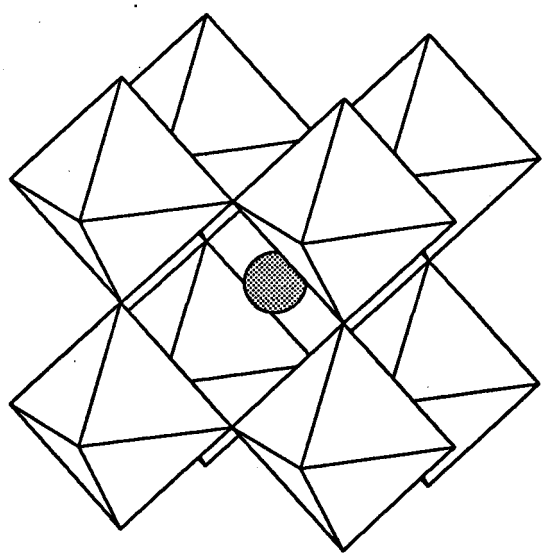

b)

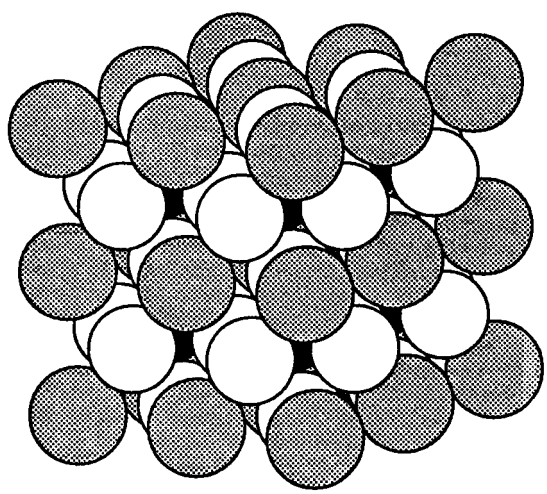

Figure 1.1 : Two views of the perovskite structure, a) the MX_6 octahedra are stressed with the A cation represented as a shaded sphere, b) the cations are plotted with their true radii to illustrate the close packing present in the structure, A cations are represented as shaded spheres, M cations as black spheres, and X anions as open spheres.

packed AX_3 array. Finally, all of the octahedral holes in the AX_3 lattice that do not border an A cation are filled with M cations (25% of the octahedral holes). Two alternate ways of depicting the ideal perovskite structure are shown in figure 1.1.

Even though there are a large number of simple perovskites, AMX_3, the number of possible compounds is greatly expanded when multiple ions are substituted for one or more of the original ions. In most cases this substitution occurs on the cation sites and leads to a large class of compounds known either as double or complex perovskites, $AA'MM'X_6$. When such substitutions are made the ions can occupy the original cation site of the simple structure in either a random or an ordered fashion. If an ordered arrangement is adopted the symmetry and, in many cases, the size of the unit cell are changed.

Although the ideal perovskite structure is cubic there are several structural deviations from the ideal cubic structure, both for simple and ordered perovskites. Distortions from the ideal cubic structure can be attributed to one of three mechanisms: tilting of the octahedra, distortions of the octahedra, and displacement of the cations. Tilting of the octahedra is by far the most common of these three and is discussed in greater detail in chapters 2-5.

1.3 Applications of Perovskites

The perovskite structure class encompasses a huge variety of compounds. Most of the metallic ions in the periodic table can be incorporated into the perovskite structure. Oxides and fluorides comprise the vast majority of perovskite compounds (Goodenough & Longo, 1970), but the perovskite structure is found for many combinations of cations and anions. Chlorides (Brynestad, Yakel & Smith, 1966; Horowitz *et al.* 1982), bromides (Knochenmuss, Reber, Rajasekharan & Güdel, 1986), hydrides (Messer, Eastman, Mers & Maeland, 1964), oxynitrides (Bacher *et al.*, 1988), and sulfides (Clearfield, 1963; Rodier & Laruelle, 1970; Noël, Padiou & Prigent, 1975) are all known with the perovskite structure. Metal rich phases are also known which adopt the perovskite structure, such as the carbides ACM_3 and nitrides ANM_3, where A is a main group metal and M is a transition metal (Nowotny & Ettmayer, 1969; Galasso, 1969). In these compounds the anion (C or N) actually occupies the octahedral sites normally filled by cations, and the transition metal occupies the X sites normally filled by oxygen. The number of perovskites is further expanded by the ability of this structure to support defects, particularly cation and anion vacancies. Not only does this lead to structures such as the tungsten bronzes Na_xWO_3, and $Sr_2SrTaO_{5.5}$, but also perovskite

related structures such as the high T_c cuprate superconductors, Aurivillius phases, and the brownmillerite structure ($Sr_2Fe_2O_5$).

Because the perovskite structure can accommodate such a wide variety of ions, the physical properties of perovskite compounds are wonderfully diverse. Perovskite compounds with interesting dielectric, magnetic, electrical, optical, and catalytic properties are all known and have been widely studied. Technological applications vary from the dielectric properties of $BaTiO_3$ (Shirane, Danner & Pepinski, 1957; Galasso, 1969), which make it an important material in the capacitor industry, to the superconductivity displayed by $Ba(Bi_{1-x}Pb_x)O_3$ (Sleight, Gillson & Bierstedt, 1975) and the perovskite-related high temperature cuprate superconductors, to the fascinating magnetoresistive and magnetostrictive properties of $(La_{1-x}Ca_x)MnO_3$ (Hwang *et al.*, 1995; Fontcuberta *et al.*, 1996). The technological importance of these compounds and many others make the perovskite structure one of the most important structures in all of materials science.

Application	Compound
Multilayer Capacitor	$BaTiO_3$
Piezoelectric Transducer	$Pb(Zr,Ti)O_3$
P.T.C. Thermistor	$BaTiO_3$
Electrooptic Modulator	$(Pb,La)(Zr,Ti)O_3$
Dielectric Resonator	$BaZrO_3$
Thick Film Resistor	$BaRuO_3$
Electrostrictive Actuator	$Pb(Mg,Nb)O_3$
Superconductor	$Ba(Pb,Bi)O_3$
Magnetic Bubble Memory	$GdFeO_3$
Laser Host	$YAlO_3$
Ferromagnet	$(Ca,La)MnO_3$
Refractory Electrode	$LaCoO_3$
Second Harmonic Generator	$KNbO_3$

Table 1.1 : Electrical and optical applications of various perovskite compounds, based on information given in the literature (Newnham, 1989).

From a technological point of view perovskites with interesting dielectric properties may make the largest impact on our society today. Of the applications listed in table 1.1 the first three are the most commercially important applications. Capacitors are essential components in almost all electronic circuitry, and such circuitry is so widespread as to be found in almost all walks of life. Piezoelectric transducers convert mechanical energy to electrical energy. Their most common uses are as pressure transducers, ultrasonic

vibrators and imagers, as well as microphones and speakers used to convert audio signals into electrical signals and vice versa. P.T.C. Thermistors are resistors whose resistance changes dramatically with temperature. They are used in many control system applications such as the electric choke in the automobile. They also are the active component of many surge protectors and electrical protection devices. The perovskite materials used in all three of these applications are ferroelectric ceramics. The world markets for ceramic capacitors, piezoelectric transducers, and thermistors were estimated in 1989 to be approximately two billion, one billion, and 200 million dollars per year respectively (Newnham, 1989).

Some of the other applications listed in table 1.1 for high dielectric perovskites are worth mentioning. Dielectric resonators with high dielectric constants, low dielectric loss, and a small temperature dependence are increasingly required for use in microwave integrated circuits (ultrafast computers) (Kawashima, Nishida, Ueda & Ouchi, 1983). Thin film electrooptic modulators are important components of ac TFEL (transient field electroluminescent) panels (Kuwata, *et al.*, 1984). If perfected these display panels would take a large share of the computer and video display panel market. This is particularly true in the areas of large screen displays and portable computers, where liquid crystal displays now are prevalent. Ideally these materials need to combine a high dielectric constant or permitivity with a large breakdown voltage.

Electrostrictive actuators (components which modify an electrical signal depending upon its frequency, such as a band pass filter) are based on a class of materials known as "relaxor ferroelectrics". These materials are similar to normal ferroelectric materials in that the application of an electric field can cause some of the atoms to shift their positions in the unit cell. This causes a net polarization of the material which remains even after the external field has been removed. Relaxor ferroelectric materials differ from normal ferroelectric materials in several ways (Randall, Bhalla, Shrout & Cross, 1990). First of all the dielectric constant changes dramatically near the Curie temperature in normal ferroelectrics as they undergo sharp 1st or 2nd order transitions. However, in relaxor ferroelectrics the broad-diffuse phase transition removes the sharp temperature dependent changes of the dielectric constant. This property is of great importance in applications where the temperature may approach the Curie temperature of normal ferroelectric materials ($BaTiO_3$ has a sharp spike in the dielectric constant vs. temperature curve near 120°C (Galasso, 1969)). Another important difference is that the dielectric constant is only weakly frequency dependent in normal ferroelectrics, but is strongly frequency dependent in relaxor ferroelectrics. This is the basis for an electrostrictive actuator. Another difference is that normal ferroelectrics have a strong remnant polarization while relaxor ferroelectrics do not.

The understanding and behavior of relaxor ferroelectrics is strongly tied to the research outlined in this thesis. All relaxor ferroelectric materials (perovskite) have more than one ion on the M site of the perovskite lattice, such as $Pb(Zn_{.33}Nb_{.67})O_3$, Pb_2InNbO_6, and Pb_2ScTaO_6 (Randall, Bhalla, Shrout & Cross, 1990). There are two theories which attempt to explain why relaxor materials behave as they do. The inhomogeneous chemical microregion model postulated by Smolenski (1970) attributes the unusual behavior to an inhomogeneous distribution of ions throughout the crystal. The second model proposed by Randall and Bhalla states that regions of nanoscale order among disordered regions are responsible for the relaxor behavior (Randall, Bhalla, Shrout & Cross, 1990). The second model if correct directly relates the ordering behavior, studied in chapter five, to the ferroelectric properties of these materials.

Another application of perovskite compounds is that of giant magnetoresistance (GMR). In such compounds the resistance is very sensitive to the presence of magnetic fields. The effect is largest near the magnetic ordering temperature, or Curie point, of the material. For example, in $(La_{1-x}Ca_x)MnO_3$ films the resistance decreased by three orders of magnitude (1.35MΩ to 1.06kΩ) upon application of a 6 Tesla field at 77K (Jin, McCormack, Tiefel & Ramesh, 1994). At room temperature the resistivity change was decreased, but the $\Delta R/R_H$ value was still ≅1300%. The primary application for such materials is the realm of magnetic data storage and retrieval (Hwang, Palstra, Cheong & Batlogg, 1995). Although the magnetoresistive effect has been observed in the pyrochlore structure (Subramanian, *et al.*, 1996) the vast majority of oxide based GMR materials are manganese containing perovskites. Interestingly, the magnetoresistive effect is very sensitive to the exact structure of the compound. In particular, octahedral tilting distortions have been shown to play a critical role in determining the size of the magnetoresistive effect and the Curie temperature (Hwang *et al.*, 1995; Hwang, Palstra, Cheong & Batlogg, 1995; Fontcuberta, *et al.*, 1996). Understanding and characterizing such distortions are discussed extensively in chapters 2-5.

Perhaps the most promising application of perovskites (though certainly not as yet the most commercially important) is high temperature superconductivity. Reduced $SrTiO_3$ has long been known to be superconducting, but with a critical temperature less than 1K. The discovery of superconductivity in the $Ba(Bi_{1-x}Pbx)O_3$ perovskite system by Sleight, Gillson, and Bierstedt (1975) generated much excitement about the prospects of high temperature superconductivity in oxides. This was followed by the discovery of superconductivity above liquid nitrogen temperatures in the high temperature cuprate superconductors such as $YBa_2Cu_3O_{7-x}$, which led to an extensive search for new superconducting compounds. Not

only were the bismuth superconductors perovskites, but all of the cuprate superconductors have structures which are very closely related to the perovskite structure. The ordering behavior of cations and defects play an important role in the superconducting behavior in at least some of these compounds. For example the perovskite $BaBiO_3$ contains an ordered distribution of Bi^{3+} and Bi^{5+} ions on the octahedral site and is not superconducting (Cox & Sleight, 1979). However, when enough lead or potassium is introduced onto the bismuth site it destroys the long range order between trivalent and pentavalent bismuth and the compound becomes superconducting. A better understanding of the factors influencing long range order in perovskite and perovskite related structures may give additional insight into the mechanism of high temperature superconductivity in oxides. Even if it is not useful in better understanding superconductivity, hopefully such knowledge might at least guide searches for new superconducting oxide materials.

Interestingly enough the discovery and possible applications of high temperature cuprate superconductors have created a technological need for another class of materials, substrates for thin film growth of high Tc superconducting (HTS) materials. These materials should be able to serve as substrates and/or buffer layers in the fabrication of HTS thin film devices. The desired properties of such materials are a good lattice match to $YBa_2Cu_3O_{7-x}$ films, a low dielectric constant and dielectric loss, and a cubic structure with no phase transitions between film growth temperatures and superconducting temperatures (77K-873K) (Brandle & Fratello, 1990). Perhaps not coincidentally the compounds which best meet these materials limitations are also perovskites. However, the presence of phase transition between the synthesis temperature (either single crystal growth or epitaxial thin film deposition) and room temperature typically leads to twinning, which is deleterious to the properties of subsequently deposited superconducting films. Therefore, as with the GMR perovskites characterizing, understanding, and controlling the phase transitions in perovskite compounds is critical.

The above discussion only touches on some of the important properties and applications of perovskites. Catalytic, optical, magnetic, conducting and thermoelectric materials have not been discussed. Hopefully, the discussion has been detailed enough to give the reader some idea of the importance of the perovskite structure. Furthermore, there has been some mention of the often times significant role symmetry and long range order play in determining many of the physical properties of complex perovskites. The work that is described in this thesis has been done with the goal of understanding the factors which influence the symmetry and long range order in the perovskite structure. Although relatively few property measurements were taken in this work, it is hoped that the structural understanding gained during this research will help further a structure-property

understanding of perovskite materials. If this goal is even partially attained then this work will be a significant contribution to the solid state and materials science literature.

1.4 Tungsten Trioxide

The ideal structure of tungsten trioxide is identical to the perovskite structure, with one exception, the A cation is missing. The many different polymorphs of tungsten trioxide are distorted from the ideal structure by octahedral tilting and displacements of tungsten from the centers of the octahedra. Therefore, even though WO_3 is very simple compositionally the structural distortions are quite complex. Furthermore, the high pseudosymmetry of WO_3 has made structural studies on WO_3 very difficult. In particular there is a lack of knowledge about the structure of tungsten trioxide below room temperature. The material in chapters seven and eight detail a comprehensive structural study of WO_3 at room temperature and below, using high resolution neutron powder diffraction. The similarities and added complexities, with respect to perovskites, of the phase transitions in tungsten trioxide are examined in these two chapters.

1.5 References

Bacher, P., Antoine, P., Marchand, R., L'Haridon, P., Laurent, Y. & Roult, G. (1988). *J. Solid State Chem.* **77**, 67.

Brandle, C.D. & Fratello, V.J. (1990). *J. Mater. Res.*, **5**, 2160.

Brynestad, J., Yakel, H.L. & Smith, G.P. (1966). *J. Chem. Phys.* **45**, 4652.

Clearfield, A. (1963). *Acta Cryst.* **16**, 135.

Cox, D.E. & Sleight, A.W. (1979). *Acta Cryst.*, **B35**, 1.

Fontcuberta, J., Martinez, B, Seffar, A., Piñol, S., Garcia-Muñoz, J.L. & Obradors, X. (1996a). *Phys. Rev. Lett.* **76**, 1122.

Galasso, F.S. (1969). *"Structure, Properties, and Preparation of Perovskite Type Compounds"*, Pergammon Press, Oxford.

Goodenough, J.B. & Longo, J.M. (1970). *Landolt-Börnstein* **4**, 126.

Horowitz, A., Amit, M., Makovsky, Ben Dor, L. & Kalman, Z.H. (1982). *J. Solid State Chem.* **43**, 107.

Hwang, H.Y., Cheong, S.-W., Radaelli, P.G., Marezio, M. & Batlogg, B. (1995a). *Phys. Rev. Lett.* **75**, 914.

Hwang, H.Y., Palstra, T.T.M., Cheong, S.-W. & Batlogg, B. (1995b). *Phys. Rev.* **52**, 15046.

Jin, S., McCormack, M., Tiefel, T.H. & Ramesh, R. (1994). *J. Appl. Phys.* **76**, 6929.

Kawashima, S., Nishida, M., Ueda, I. & Ouchi, H. (1983). *J. Am. Ceram. Soc.*, **66**(6), 421.

Knochenmuss, F., Reber, C., Rajasekharan, M.V. & Güdel, H.U. (1986). *J. Chem. Phys.* **85**, 4280.

Kuwata, J., Fujita, Y., Matsuoka, T., Tohda, T., Nishikawa, M. & Abe, A. (1984). *Proc. of the SID*, **25**(3), 177.

Messer, C.E., Eastman, J.C., Mers, R.G. & Maeland, J.A. (1964) *Inorg. Chem.* **3**, 776.

Navrotsky, A. & Weidner, D.J. (1989). *"Perovskite: A Structure of Great Interest to Geophysics and Materials Science"*, Am. Geopysical Union (Geopysical Monograph #45), Wahington D.C., pp. xi.

Newnham, R.E. (1989). *"Perovskite: A Structure of Great Interest to Geophysics and Materials Science"*, Am. Geopysical Union (Geopysical Monograph #45), Wahington D.C., pp. 91.

Noel, H., Padiou, J. & Prigent (1975). *C.R. Acad.Sci. Ser.* C **280**, 123.

Nowotny, H. & Ettmayer, P. (1969). *J. Inst. Met.* **97**, 180.

Randall, C.A., Bhalla, A.S., Shrout, T.R. & Cross, L.E. (1990). *J. Mater. Res.*, **5**(4), 829.

Rodier, N. & Laruelle, P. (1970). *C.R. Acad. Sci.* **270**, 2127.

Shirane, G., Danner, H. & Pepinski, R. (1957). *Phys. Rev.*, **105**(3), 856.

Sleight, A.W. Gillson, J.L. & Bierstedt, P.E. (1975). *Solid State Commun.*, **17**, 27.

Sleight, A.W., Gillson, J.L. & Bierstedt, P.E. (1975). *Solid State Commun.* **17**, 27.

Smolenski, G.A. (1970). *J. Phys. Soc. Jpn. (Suppl.)*, **28**, 26.

Subramanian, M.A., Toby, B.H., Ramirez, A.P., Marshall, W.J., Sleight, A.W. & Kwei, G.H. (1996). *Science* **273**, 81.

Chapter 2

Octahedral Tilting in Perovskites I : Geometrical Considerations

2.1 Introduction

Although the ideal perovskite structure is cubic (see chapter one), there are several structural deviations from the ideal structure, both for simple and ordered perovskites. In fact there are many more distorted perovskites than there are cubic perovskites. Even the mineral perovskite itself, $CaTiO_3$, is orthorhombic rather than cubic (Sasaki, Prewitt, Bass & Schulze, 1987). Cubic, tetragonal, orthorhombic, rhombohedral, monoclinic, and triclinic perovskites are all known. These structural distortions are of interest not only from a crystallography point of view, but also because they can have important effects on the physical properties of perovskite compounds, particularly the electrical and magnetic properties. The influence small structural changes have on the magnetoresistance properties of manganese and cobalt based perovskites is an important example this phenomenon (Hwang *et al.*, 1995; Fontcuberta *et al.*, 1996; Briceño *et al.*, 1995).

Distortions from the ideal perovskite structure can be attributed to one of three mechanisms: distortions of the octahedra, cation displacements within the octahedra, and tilting of the octahedra. The first two distortion mechanisms are driven by electronic instabilities of the octahedral metal ion. The Jahn-Teller distortion in $KCuF_3$ (Okazaki & Suemune, 1961) is an example of an electronic instability that leads to octahedral distortions. The ferroelectric displacement of titanium in $BaTiO_3$ (Shirane, Danner & Pepinski, 1957) is an example of an electronic instability that leads to cation displacements. Although these distortion mechanisms are important in many compounds, they are not discussed further in this paper. The third and most common distortion mechanism, octahedral tilting, can be realized by tilting essentially rigid MO_6 octahedra while maintaining their corner sharing connectivity. This type of distortion is typically observed when the A cation is too small for the cubic MO_3 corner sharing octahedral network. In such cases it is the lowest energy distortion mode, because the A-O distances can be shortened while the first coordination sphere about the M cation remains unchanged. (In terms of the MO_3 lattice, only the soft M-O-M bond angle is disturbed.) Geometrical considerations associated with this distortion are the subject of this chapter, while the interatomic forces that drive octahedral tilting distortions are the subject of the following chapter.

2.2 Previous Octahedral Tilting Studies

Over the years many investigators have studied distortions in the perovskite structure. Thomas has devised a system for classifying perovskites based on the polyhedral volumes of the A and M cations, which is particularly useful when both cation displacements and octahedral tilting occur (Thomas, 1989; Thomas & Beitollahi, 1994; Thomas, 1996). O'Keeffe and Hyde structurally described the three most common octahedral tilt systems; $a^+b^-b^-$, $a^-a^-a^-$, and $a^+a^+a^+$ (O'Keeffe & Hyde, 1977). Megaw and Darlington studied, in great detail, the effect of octahedral tilting and octahedral deformation in rhombohedral perovskites (Megaw & Darlington, 1975), and Deblieck and coworkers classified possible tilting combinations in perovskite-like ABX_4 compounds (Deblieck, 1986; Deblieck, Van Tendeloo, Van Landuyt, & Amelinckx, 1985). But almost certainly the most influential work was published in 1972 by Glazer. This work contained an eloquent description of all possible simple octahedral tilting combinations (Glazer, 1972). An updated description, including a few minor corrections, can be found in the book *"Space Groups for Solid State Scientists"*, by Burns and Glazer (Burns & Glazer, 1990). A similar but much less known approach was developed in Russia around the same time by Aleksandrov (Aleksandrov, 1975). However, it is the notation developed by Glazer, to describe octahedral tilting distortions, that has become standard notation in the perovskite literature.

Somewhat surprisingly, a paper by Leinenweber and Parise claimed that tilt systems $a^+a^+c^-$ (#5) and $a^+a^+a^-$ (#7) do not produce structures belonging to space group Pmmn as predicted by Glazer. They contended that these two tilt systems actually result in structures belonging to space group $P4_2/nmc$ (Leinenweber & Parise, 1995). In addition to this discrepancy, the complications that arise when cation ordering and octahedral tilting occur simultaneously have not been addressed in a comprehensive manner. Both of these issues are discussed in detail in the sections that follow.

2.3 A Brief Review of Glazer Notation

The notation developed by Glazer over 20 years ago to describe octahedral tilting distortions in perovskites has become the standard by which such distortions are described (Glazer, 1972). A familiarity with this notation is necessary to follow the discussion throughout this paper. As an aid to those unfamiliar with Glazer notation a brief review is presented below. Further explanation can be found in the original reference (Glazer, 1972).

Using Glazer notation a tilt system is described by specifying the rotations of the octahedra about each of the three Cartesian axes. The rotations about each axis are described by two parameters. The first of these parameters is a letter specifying the magnitude of the rotation about that axis, relative to the magnitude of the rotations about the other Cartesian axes. For example, in the system $a^+a^+a^+$ the rotation angle is the same about each of the three axes; whereas, in the $a^+a^+c^+$ tilt system the rotation angle about the z axis is different from the rotation angle about the x and y axes. The second parameter is a superscript indicating whether the rotations in adjacent layers are in the same or opposite directions. A negative superscript indicates that the rotations of two neighboring octahedra, along the tilt axis, are in the opposite directions. While a positive superscript is used to indicate they tilt in the same direction. A zero superscript is used when no rotations occur about an axis.

The clearest example of how Glazer notation describes tilted perovskite structures is a comparison of the two one tilt systems, $a^0a^0c^+$ and $a^0a^0c^-$. The octahedra in both of these tilt systems are rotated only about four fold axes parallel to the z axis. Figure 2.1 shows a view looking down the z axis at eight octahedra in both tilt systems. It is clear in this figure that rotation of one octahedron forces four of the neighboring six octahedra to rotate in the opposite sense. This in turn causes all of the octahedra in the (001) plane to be rotated with the same magnitude as the first octahedron. The final two neighboring octahedra, connected along the z axis, are not coupled in the same way and can rotate independently. If these final two neighboring octahedra rotate in the same direction, as in figure 2.1b, the $a^0a^0c^+$ tilt system results. If they rotate in the opposite direction, as in figure 2.1a, the $a^0a^0c^-$ tilt system results. More complicated structures where tilting has to be considered in more than two layers is not described by Glazer notation.

2.4 Space Group Descriptions of all 23 Tilt Systems

2.4.1 Simulated Structures and their Comparison with Glazer's Space Group Assignments

Although Glazer completely described the space group and symmetry associated with each tilting system it is far from trivial in many cases to turn that information into a model structure, complete with atomic positions. A complete description of the unit cell, where all of the atomic positions are given, would be very useful in several situations. Such a model is

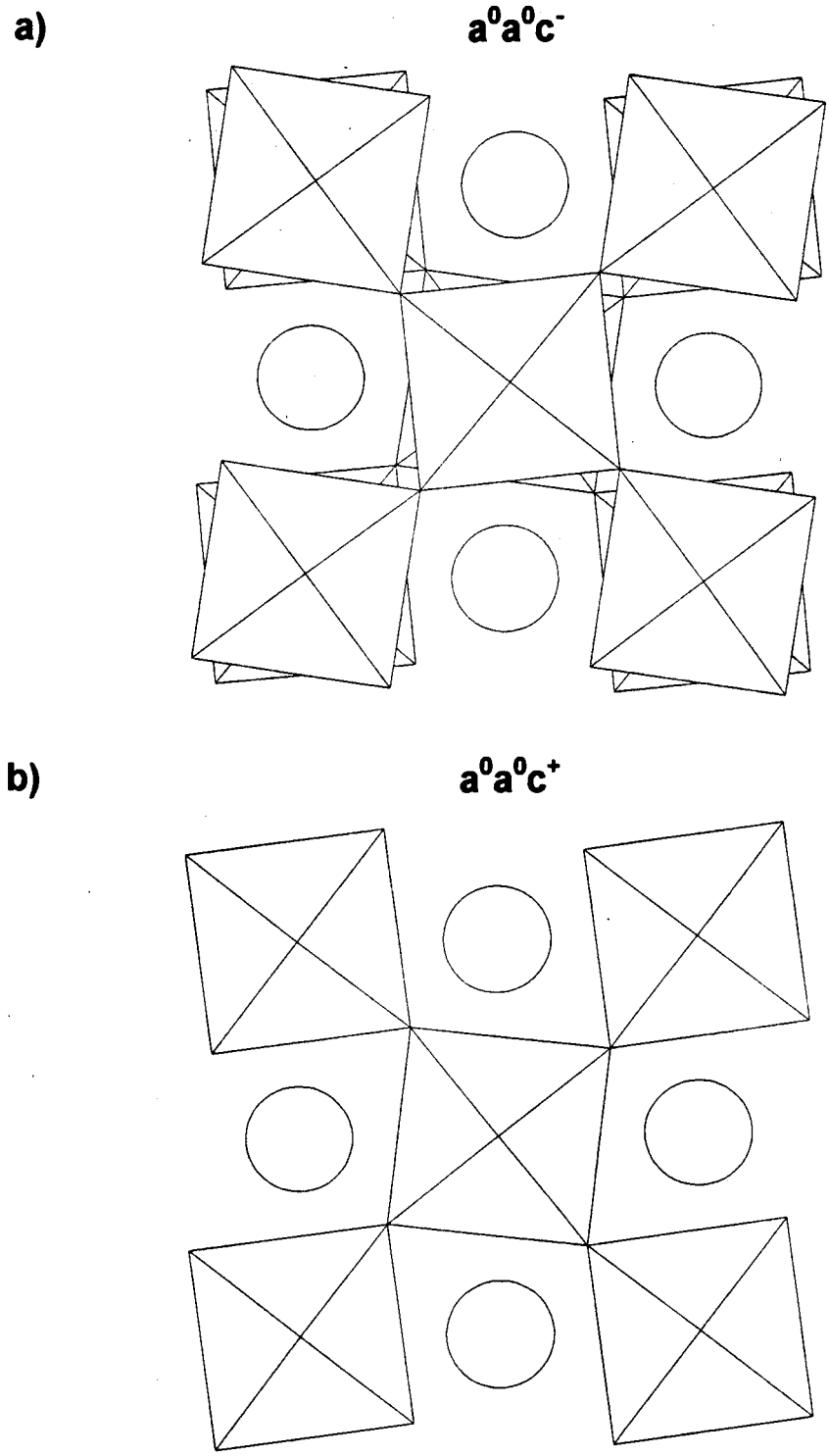

Figure 2.1: A view looking down the z-axis of two adjacent layers of octahedra for a) the $a^0a^0c^-$ tilt system, and b) the $a^0a^0c^+$ tilt system. In this polyhedral representation of the structure each octahedron symbolizes a metal atom M surrounded by 6 oxygen atoms. The round circles represent the A ions.

needed to compare experimentally determined structures with ideal structures, as a starting point for Rietveld refinements, or to systematically study the differences in the ideal structures associated with each tilt system. With these applications in mind the FORTRAN program POTATO (Program Originated To Analyze Tilted Octahedra) was developed (see appendix 4). Given the Glazer symbol, the rotation angle about each of the Cartesian axes, and the M-O bond distances as input, POTATO outputs a unit cell description of the compound complete with atomic positions. The unit cell calculated by POTATO is always described as centrosymmetric triclinic ($P\bar{1}$) and doubled along all three axes. The true asymmetric unit is then found by examination of relationships between atomic positions, or more conveniently with one of the automated routines now available (e.g. "find symmetry" within the Biosym Insight II package (Insight II, 1993))*. Using this approach the space group and asymmetric unit were calculated for each of the 23 Glazer tilt systems. The results of these calculations are compared to Glazer's findings in table 2.1. The complete unit cell descriptions for each tilt system are given in appendix 1.

One curiosity of this analysis was that for tilt systems $a^+b^+c^-$ (#4), $a^+a^+c^-$ (#5), $a^+b^+b^-$ (#6), $a^+a^+a^-$ (#7), $a^0b^+c^-$ (#17), and $a^0b^+b^-$ (#18) slight distortions of the octahedra were found to be necessary in order to retain the connectivity of the octahedra†. Interestingly the two tilt systems, $a^+a^+c^-$ (#5) and $a^+a^+a^-$ (#7), that Leinenweber and Parise claimed were incorrectly assigned by Glazer are among this group. At first this seemed to be a shortcoming of the algorithms used in POTATO. However, despite several modifications to POTATO this anomaly persisted. This led to the realization that the octahedral distortions were not caused by an error in POTATO, but rather are an inherent geometric property of these six tilt systems. Proof of this claim is given in appendix 2, and demonstrated in appendix 3 by calculating the metal-oxygen vectors that define octahedra in the $a^+a^+a^-$ tilt system.

2.4.2 Space Group Assignments for Tilt Systems 4, 5, 6, 7, 17, & 18

With the exception of the above mentioned tilt systems POTATO was able to generate perfectly linked networks of rigid octahedra for all tilt systems. Furthermore, for these tilt

*Based on the results contained in this paper the current version of POTATO also gives the true space group and asymmetric unit for each tilt system.

systems the space groups and lattice constants predicted by Glazer were found to agree exactly with the unit cell descriptions generated by POTATO. In regard to those tilt systems where distortions of the octahedra must occur it becomes impossible to uniquely define a space group. The problem arises because the symmetry of the unit cell depends on the way in which the octahedra are distorted. Table 2.2 compares the atomic positions, bond distances, and bond angles for a hypothetical compound belonging to the $a^+a^+a^-$ tilt system. The first two structures have symmetry described by space group Pmmn as suggested by Glazer (Glazer, 1972; Burns & Glazer 1990). The difference between the two structures is that in the first structure all of the bond distances have remained rigid while in the second structure all of the bond angles have been constrained to be 90°. The third structure has symmetry corresponding to space group $P4_2/nmc$ as suggested by Leinenweber and Parise (Leinenweber & Parise, 1995). It is evident from this table that the atomic positions are quite similar in all three structures. In table 2.3 the results of a similar calculation for the $a^0b^+b^-$ tilt system are shown. Here the description in Pmmn as output from POTATO is very close to a unit cell having Bmmb symmetry as predicted by Glazer. In this tilt system the octahedral distortions are very small. Although it is not possible to rigorously assign a space group for these tilt systems it seems reasonable to assume that actual compounds will crystallize in the more symmetric of the two available space groups. Based on that assumption the $a^+a^+b^-$ and $a^+a^+a^-$ tilt systems are assigned to $P4_2/nmc$, and the $a^0b^+c^-$ and $a^0b^+b^-$ tilt systems assigned to Bmmb (standard setting Cmcm). The $a^+b^+c^-$ and $a^+b^+b^-$ tilt systems can not be tetragonal because the a and b lattice constants are different and so they remain orthorhombic, Pmmn, as originally suggested by Glazer (Glazer, 1972). Therefore, in essence none of the assignments in Glazer's work (Burns & Glazer, 1990) are incorrect. However, for tilt systems $a^+a^+b^-$ (#5) and $a^+a^+a^-$ (#7) the space group $P4_2/nmc$ suggested by Leinenweber and Parise is equally justified and may be favored due to its higher symmetry.

2.5 Combined Effect of Cation Ordering and Octahedral Tilting

In the cubic perovskite structure 1:1 ordering of the M site cations requires the unit cell be doubled along all three crystallographic directions, in order to maintain translational symmetry. The lattice also changes from simple cubic (space group $Pm\bar{3}m$) to face

---

† O'Keeffe and Hyde (1977) comment that regular octahedra cannot be maintained in all 23 Glazer tilt systems, but do not comment as to which tilt systems cannot accommodate regular octahedra.

Tilt System Number	Tilt System Symbol	Space Group (Glazer)	Space Group (Potato)
3-Tilt Systems			
1	$a^+b^+c^+$	Immm (#71)	Immm (#71)
2	$a^+b^+b^+$	Immm (#71)	Immm (#71)
3	$a^+a^+a^+$	$Im\bar{3}$ (#204)	$Im\bar{3}$ (#204)
4	$a^+b^+c^-$	Pmmn (#59)	Pmmn (#59-2)
5	$a^+a^+c^-$	Pmmn (#59)	Pmmn (#59-2)
6	$a^+b^+b^-$	Pmmn (#59)	Pmmn (#59-2)
7	$a^+a^+a^-$	Pmmn (#59)	Pmmn (#59-2)
8	$a^+b^-c^-$	$A2_1/m11$ (#11)	$P2_1/m$ (#11-1)
9	$a^+a^-c^-$	$A2_1/m11$ (#11)	$P2_1/m$ (#11-1)
10	$a^+b^-b^-$	Pmnb (#62)	Pnma (#62)
11	$a^+a^-a^-$	Pmnb (#62)	Pnma (#62)
12	$a^-b^-c^-$	$F\bar{1}$ (#2)	$F\bar{1}$ (#2)
13	$a^-b^-b^-$	I2/a (#15)	I2/a (#15-3)
14	$a^-a^-a^-$	$R\bar{3}c$ (#167)	$R\bar{3}c$(#167-2)
2 Tilt Systems			
15	$a^0b^+c^+$	Immm (#71)	Immm (#71)
16	$a^0b^+b^+$	I4/mmm (#139)	I4/mmm (#139)
17	$a^0b^+c^-$	Bmmb (#63)	Pmmn (#59-2)
18	$a^0b^+b^-$	Bmmb (#63)	Pmmn (#59-2)
19	$a^0b^-c^-$	F2/m11 (#12)	I2/m (#12-3)
20	$a^0b^-b^-$	Imcm (#74)	Imma (#74)
1-Tilt Systems			
21	$a^0a^0c^+$	C4/mmb (#127)	P4/mbm (#127)
22	$a^0a^0c^-$	F4/mmc (#140)	I4/mcm (#140)
0-Tilt Systems			
23	$a^0a^0a^0$	$Pm\bar{3}m$ (#221)	$Pm\bar{3}m$ (#221)

Table 2.1 : A comparison of the space groups predicted for each of the 23 simple tilt systems by Glazer (Glazer, 1972) with those generated by POTATO. For tilt systems 4, 5, 6, 7, 17, and 18 the atomic positions calculated by POTATO always indicated slight distortions of the octahedra and therefore, no space group could be assigned as rigorously correct. This is result discussed in more detail in the text.

centered cubic (space group $Fm\bar{3}m$). Octahedral tilting can also cause a doubling of the unit cell, and often accompanies cation ordering. Therefore, it is instructive to consider the combined effects of cation ordering and octahedral tilting.

	Pmmn (Potato, Const. Dist.)			Pmmn (Potato, 90° Angles)			$P4_2/nmc$		
Atom	**x**	**y**	**z**	**x**	**y**	**z**	**x**	**y**	**z**
O1	¼	-0.0404	0.0482	¼	-0.0404	0.0482	¼	-0.0404	0.0482
O2	0.0482	¼	-0.0404	0.0482	¼	-0.0404	0.0482	¼	-0.0404
O3	0.4518	¼	-0.0404	0.4518	¼	-0.0404	0.4518	¼	-0.0404
O4	¼	0.5404	0.0482	¼	0.5404	0.0482	¼	0.5404	0.0482
O5	-0.0404	0.0482	¼	-0.0404	0.0482	**0.2513**	-0.0404	**0.0404**	¼
O6	0.5404	0.0482	¼	0.5404	0.0482	**0.2513**	0.5404	**0.0404**	¼
O7	-0.0404	0.4518	¼	-0.0404	0.4518	**0.2513**	-0.0404	**0.4596**	¼
O8	0.5404	0.4518	¼	0.5404	0.4518	**0.2513**	0.5404	**0.4596**	¼
O9	¼	0.0553	0.4703	¼	**0.0394**	**0.4667**	¼	**0.0482**	**0.4596**
O10	-0.0329	¼	0.5535	**-0.0322**	¼	**0.5542**	**-0.0404**	¼	**0.5482**
O11	0.5329	¼	0.5535	**0.5322**	¼	**0.5542**	**0.5404**	¼	**0.5482**
O12	¼	0.4447	0.4703	¼	**0.4606**	**0.4667**	¼	**0.4518**	**0.4596**
	All Distances 2.00 Å			1/3 of the Distances 1.98 Å			1/3 of the Distances 1.98 Å		
	1/3 of the Angles 86.5°			All Angles 90°			1/3 of the Angles 88.4°		

Table 2.2 : Three different descriptions of the atomic positions of an $a^+a^+a^-$ tilted perovskite (a=10°). The first two descriptions were generated in POTATO. In the first structure the distances were constrained to be constant (2.00Å), while in the second structure the angles were constrained to remain 90°. The third description was generated using the O1, O2, and O3 positions common to all three descriptions and the symmetry generators associated with $P4_2/nmc$. All other oxygens in the unit cells can be generated from these 12 using the inversion centers on the M ions. The coordinates shown in bold face type are those where the second and third description differ from the first description.

To illustrate the combined effect of cation ordering and octahedral tilting consider the tetragonally distorted $a^0a^0c^-$ tilt system. Upon tilting the structure distorts from cubic to face centered tetragonal, space group F4/mmc. This is a nonstandard setting and the unit cell must be redefined in order describe the structure in terms of the standard space group setting, I4/mcm. The new unit cell is body centered and the relationship between the lattice constants in the face centered cell and the new cell is $a_I=a_F/\sqrt{2}$ and $c_I=c_F$. Introducing cation order lowers the symmetry once again to I4/m. The relationship between the a and b axes in the simple cubic cell, the face centered tetragonal cell, and the body centered tetragonal cell is illustrated in figure 2.2. The introduction of cation ordering will always result in a loss of symmetry, either space group symmetry elements or translational symmetry. The symmetry

	Pmmn (Potato, Const. Dist.)			Pmmn (Potato, 90° Angles)			Bmmb		
Atom	x	y	z	x	y	z	x	y	z
O1	¼	-0.0438	0.0438	¼	-0.0438	0.0438	¼	-0.0438	0.0438
O2	0.0445	¼	0.0038	0.0445	¼	0.0038	0.0445	¼	0.0038
O3	0.4555	¼	0.0038	0.4555	¼	0.0038	0.4555	¼	0.0038
O4	¼	0.5438	0.0438	¼	0.5438	0.0438	¼	0.5438	0.0438
O5	-0.0445	0.0038	¼	-0.0445	0.0038	¼	-0.0445	0.0038	¼
O6	0.5445	0.0038	¼	0.5445	0.0038	¼	0.5445	0.0038	¼
O7	-0.0445	0.4962	¼	-0.0445	0.4962	¼	-0.0445	0.4962	¼
O8	0.5445	0.4962	¼	0.5445	0.4962	¼	0.5445	0.4962	¼
O9	¼	0.0451	0.4576	¼	**0.0438**	0.4576	¼	**0.0438**	**0.4562**
O10	-0.0431	¼	0.5113	-0.0431	¼	0.5113	**-0.0445**	¼	**0.5038**
O11	0.5431	¼	0.5113	0.5431	¼	0.5113	**0.5445**	¼	**0.5038**
O12	¼	0.4549	0.4576	¼	**0.4562**	0.4576	¼	**0.4562**	**0.4562**
	All Distances 2.000 Å			1/3 of the Distances 1.998 Å			All Distances 2.000 Å		
	1/6 of the Angles 90.3°			All Angles 90°			1/3 of the Angles 90.9°		

Table 2.3 : Three different descriptions of the atomic positions of an $a^0b^+b^-$ tilted perovskite (a=10°). The first two descriptions were generated in POTATO. In the first structure the distances were constrained to be constant (2.00Å), while in the second structure the angles were constrained to remain 90°. The third description was generated using the O1, O2, and O3 positions common to all three descriptions and the symmetry generators associated with Bmmb (non-standard setting of space group #63, Cmcm). All other oxygens in the unit cells can be generated from these 12 using the inversion centers on the M ions. The coordinates shown in bold face type are those where the second and third description differ from the first description. The Bmmb coordinates have been shifted by (-¼,-¼,0) for comparison with the Pmmn coordinates.

of the ordered unit cell must be lower than the disordered or simple unit cell because the octahedral cation sites are no longer equivalent. This destroys any symmetry operations that relate neighboring octahedral sites. In this example half of the symmetry elements are destroyed including the mirror plane perpendicular to the 4-fold axis and c glide planes parallel to the 4-fold axis, lowering the symmetry of the ordered $a^0a^0c^-$ structure from I4/mcm to I4/m. In a similar manner the space groups for ordered perovskites in all 23 of the simple tilt systems can be determined. This analysis was performed using the *International Tables for Crystallography* (Hahn, 1983) and double checked using POTATO with an ordered arrangement of cations. The results are given in table 2.4 along with the final space group assignments for simple tilt systems. For each tilt system the space group describing the ordered perovskite is a maximal non-isomorphic subgroup of the space group describing the simple perovskite, and of course, all of the ordered perovskite space groups are subgroups of $Fm\bar{3}m$. Unlike Glazer's work with the tilt systems of simple perovskites there is no

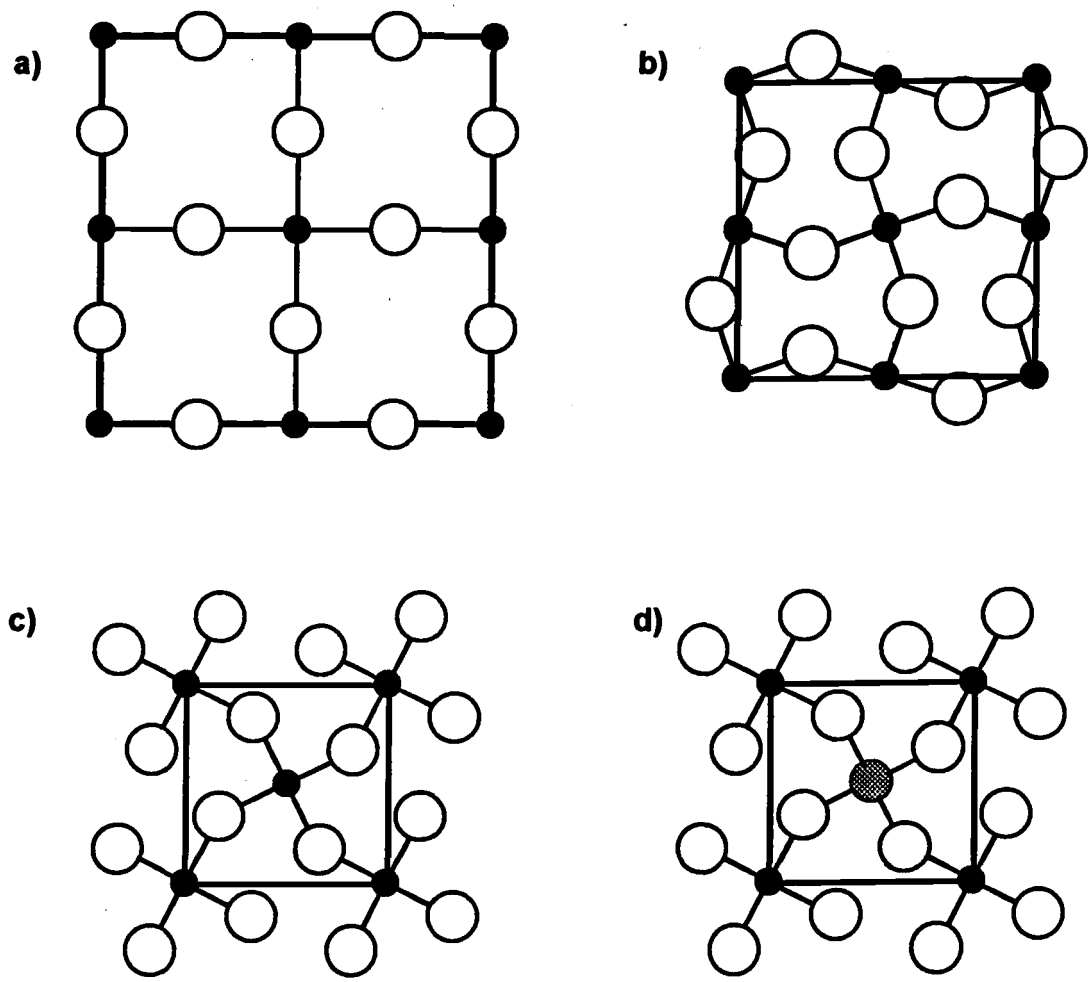

Figure 2.2 : The relationship between the a and b axes in a) the simple cubic perovskite cell before an octahedral tilting distortion, b) the face centered tetragonal cell after an octahedral tilting distortion, c) the body centered tetragonal cell, and d) the ordered body centered tetragonal cell. Mirror planes parallel to the c axis cut through the oxygen atoms and relate the corner M ions (0,0,0) with the M ion at the center of the ab face (½,½,0) in the unit cell shown in c). Ordering of different cations on the M site destroys those mirror planes (as well as all of the glide planes) as shown in d).

Tilt System Number	Tilt System Symbol	Space Group (No Ordering)	Space Group (1:1 Ordering)
3-Tilt Systems			
1	$a^+b^+c^+$	Immm (#71)	Pnnn (#48)
2	$a^+b^+b^+$	Immm (#71)	Pnnn (#48)
3	$a^+a^+a^+$	$Im\bar{3}$ (#204)	$Pn\bar{3}$ (#201)
4	$a^+b^+c^-$	Pmmn (#59-2)	P2/c (#13)
5	$a^+a^+c^-$	$P4_2/nmc$ (#137-2)	$P4_2/n$ (#86)
6	$a^+b^+b^-$	Pmmn (#59-2)	P2/c (#13)
7	$a^+a^+a^-$	$P4_2/nmc$ (#137-2)	$P4_2/n$ (#86)
8	$a^+b^-c^-$	$P2_1/m$ (#11-1)	$P\bar{1}$ (#2)
9	$a^+a^-c^-$	$P2_1/m$ (#11-1)	$P\bar{1}$ (#2)
10	$a^+b^-b^-$	Pnma (#62)	$P2_1/n$ (#14-2)
11	$a^+a^-a^-$	Pnma (#62)	$P2_1/n$ (#14-2)
12	$a^-b^-c^-$	$F\bar{1}$ (#2)	$F\bar{1}$ (#2)
13	$a^-b^-b^-$	I2/a (#15-3)	$F\bar{1}$ (#2)
14	$a^-a^-a^-$	$R\bar{3}c$ (#167-2)	$R\bar{3}$ (#148-2)
2 Tilt Systems			
15	$a^0b^+c^+$	Immm (#71)	Pnnn (#48)
16	$a^0b^+b^+$	I4/mmm (#139)	$P4_2/nnm$ (#134)
17	$a^0b^+c^-$	Cmcm (#63)	C2/c (#15-1)
18	$a^0b^+b^-$	Cmcm (#63)	C2/c (#15-1)
19	$a^0b^-c^-$	I2/m (#12-3)	$I\bar{1}$ (#2)
20	$a^0b^-b^-$	Imma (#74)	I2/m (#12-3)
1-Tilt Systems			
21	$a^0a^0c^+$	P4/mbm (#127)	P4/mnc (#128)
22	$a^0a^0c^-$	I4/mcm (#140)	I4/m (#87)
0-Tilt Systems			
23	$a^0a^0a^0$	$Pm\bar{3}m$ (#221)	$Fm\bar{3}m$ (#225)

Table 2.4 : Space groups for all possible simple tilt systems both with and without 1:1 cation ordering.

precedent in the literature with which to compare the results of table 2.4. However, Leinenweber has derived a similar table of predicted space groups for ordered perovskites, using a completely different approach similar to the method used originally by Glazer, and his results are in complete agreement with the results of table 2.4 (Leinenweber, 1996).

POTATO is also able to generate unit cell descriptions for ordered perovskites $A_2MM'O_6$ where the M'-O distance differs from the M-O distance. When the two bond distances are non-equivalent and structures are generated for each of the 23 tilt systems, distorted octahedra result for several of the tilt systems, including tilt systems 4-7 and 17-18. This is

not unexpected because these are the same tilt systems where, as shown by geometrical arguments made earlier, the octahedra are forced to distort, for simple perovskites. In addition, tilt systems 8-11 now also show slight distortions in their octahedra as the M-O and M'-O bond distances become increasingly different. It is uncertain at this time whether this is a geometrical limitation of these tilt systems when the M-O and M'-O bond distances differ. More work is necessary to conclusively prove this point.

2.6 Conclusions

With the aid of POTATO the 23 tilt systems originally described by Glazer have been investigated. It has been shown that in the tilt systems $a^+a^+a^-$, $a^+b^+b^-$, $a^+a^+c^-$, $a^+b^+c^-$, $a^0b^+b^-$, and $a^0b^+c^-$ it is not possible to link together a three dimensional network of perfectly rigid octahedra. In these tilt systems small distortions of the octahedra must occur to preserve connectivity of the octahedra. The distortions are smaller in the $a^0b^+c^-$ and $a^0b^+b^-$ tilt systems, than they are in the other four tilt systems. These distortions can have important consequences, particularly on the crystallography. For example, in tilt systems $a^+a^+c^-$ (#5) and $a^+a^+a^-$ (#7) it appears as though $P4_2/nmc$ is a more reasonable space group assignment than Pmmn, based on its higher symmetry. Finally, a table of predicted space groups for compounds that display both cation ordering and octahedral tilting has been derived.

2.7 References

Aleksandrov, K.S. (1976). *Kristallografiya* **21**, 249.

Biosym (1993). Insight II, ver. 2.3.5. Crystal structure analysis software. San Diego: Biosym Technologies.

Briceñ, G., Chang, H., Sun, X., Schultz, P.G. & Xiang, X.-D. (1995). *Science* **270**, 273.

Burns, G. & Glazer, A.M. (1990). *Space Groups for Solid State Scientists*, 2nd ed., Appendix A9-6 Boston: Academic Press.

Deblieck, R. (1986). *Acta Cryst.* A**42**, 318.

Deblieck, R., Van Tendeloo, G., Van Landyt, J. & Amelinckx, S. (1985). *Acta Cryst.* B**41**, 319.

Fontcuberta, J., Martinez, B., Seffar, A., Piñol, S., Garcia-Munoz, J.L. & Obradors, X. (1996). *Phys. Rev. Lett.* **76**, 1122.

Galasso, F.S. (1969). *Structure, Properties, and Preparation of Perovskite Type Compounds* Oxford: Pergammon Press.

Glazer, A.M. (1972). *Acta Cryst.* B**28**, 3384.

Hwang, H.Y., Cheong, S-W., Radaelli, P.G., Marezio, M. & Batlogg, B. (1995). *Phys. Rev. Lett.* **75**, 914.

Leinenweber, K. (1996). *Personal Communication, July 21st, 1996.*

Leinenweber, K. & Parise, J. (1995). *J. Solid State Chem.* **114**, 277.

Megaw, H.D. & Darlington, C.N.W. (1975). *Acta Cryst.* A**31**, 161.

Okazaki, A. & Suemune, Y. (1961). *J. Phys. Soc. Japan*, **28,** 443.

O'Keeffe, M. & Hyde, B.G. (1977). *Acta Cryst.* B**33**, 3802.

Sasaki, S., Prewitt, C.T., Bass, J.D. & Schulze, W.A. (1987). *Acta Cryst.* C**43**, 1668.

Shirane, G., Danner, H., Pepinski, R. (1957). *Phys. Rev.* **105**, 856.

Thomas, N.W. & Beitollahi, A. (1994). *Acta Cryst.* B**50**, 549.

Thomas, N.W. (1989). *Acta Cryst.* B**45**, 337.

Thomas, N.W. (1996). *Acta Cryst.* B**52**, 16.

Chapter 3

Octahedral Tilting in Perovskites II: Structure Stabilizing Forces

3.1 Introduction

The preceding chapter describes octahedral tilting distortions in the perovskite structure. In particular the symmetry and crystallographic description of the 23 Glazer tilt systems are presented in detail. However, no suggestions are made as to the cause of these distortions. In this article the physical forces responsible for these tilts are discussed.

The fact that the vast majority of metallic ions in the periodic table can be incorporated into the perovskite structure makes it ideal for studying the role atomic properties (ionic radius, electronegativity, bonding preferences, etc.) play in determining the structure and physical properties of crystalline materials. This fact has long been realized by Goodenough who has written extensively about the magnetic (Goodenough, 1963), and electrical (Goodenough, 1971; Takano, *et al.* 1988) properties of perovskites. Goodenough, and others, have also compared different perovskite compounds in an attempt to understand the effects of bonding on the crystal structure and properties of solid state materials (Goodenough, 1967; Choy, Park, Hong & Kim, 1994). Such work not only advances the scientific understanding of solid state materials, but can also be a powerful tool for enhancing physical properties of materials through structural modifications and atomic substitutions; one need only consider the vast body of synthetic research performed on the perovskite related cuprates over the past decade to appreciate the importance of such understanding.

Although geometrical descriptions of the crystal systems describing octahedral tilting in perovskites and perovskite-like compounds have been treated comprehensively on several occasions (Glazer, 1972; Aleksandrov, 1975; Deblieck, Van Tendeloo, Van Landuyt & Amelinckx, 1985), a thorough and comprehensive treatment of the physical forces behind these distortions has never appeared in the literature. Despite the lack of a comprehensive treatment, several researchers have considered the structure stabilizing forces associated with some of the more common tilt systems. Megaw and Darlington (1975) examined distortions in rhombohedral perovskites in detail as did Thomas and

Beitollahi (1994). The former study concluded that there were a variety of causes which lead to distortion from ideal cubic symmetry, while the latter study showed that the tilt angle is strongly correlated with the polyhedral volume ratio of the A and M cations. Both studies also investigated octahedral distortions and M cation shifts, which are not examined in this chapter. In a later study, based once again on polyhedral volume ratio, Thomas compared the relative stabilities of cubic ($a^0a^0a^0$), rhombohedral ($a^-a^-a^-$), and orthorhombic ($a^+b^-b^-$) perovskites. He concluded that the polyhedral volume of the A cation could be maximized, thereby reducing anion-anion repulsion, in the orthorhombic structure explaining why this tilt system is so frequently observed when the A cation becomes small. Computational approaches using the concept of static energy surfaces have also been used to predict temperatures of phase transitions between different tilt systems in halide-based perovskites (Flocken, Guenther, Hardy & Boyer 1985; 1986). This approach, though capable of giving accurate and detailed results for individual compounds, does not provide insight on the underlying cause of the distortion. Furthermore, the time and computational requirements associated with this method are prohibitive for everyday use by experimentalists. The research contained in this article seeks to go beyond earlier works in this field by considering all 23 Glazer tilt systems simultaneously, with the goal of understanding the factors stabilizing individual tilt systems.

3.2 A Cation Coordination

Octahedral tilting causes the first coordination sphere about the A cation to change, in many cases quite dramatically. At the same time, the first coordination sphere about the M cation is left virtually unchanged. Therefore, it is logical to assume that to a first approximation octahedral tilting is driven by the need to optimize the anion coordination about the A cation. This fact is widely accepted and was first pointed out almost 70 years ago by Goldschmidt. He calculated the optimal size of the A cation from ionic radii, by treating the lattice as a close packed array of hard spheres. If the combination of ions is the right size to close pack perfectly, twice the M-O bond distance is equal to the cell edge and twice the A-O distance is equal to the length of a face diagonal. Goldschmidt (1926) first recognized this geometric relationship and quantified the quality of fit of the A cation with a factor known as the Goldschmidt tolerance factor, t:

$$t = (R_A+R_O)/[\sqrt{2}\times(R_M+R_O)].$$

In the case of complex perovskites where more than one ion occupies the M and/or A sites the average radius of the ions on each site is used for R_M and R_A respectively. Compounds in the perovskite family are found to exist over the range 1.05>t>0.78 (Randall, Bhalla, Shrout & Cross, 1990).

Although the Goldschmidt tolerance factor can be useful for predicting whether a tilting distortion is expected, it does not directly give any information about which of the 23 tilt systems will be observed for a given combination of ions. To understand octahedral tilting on that level one must look carefully at the A cation coordination from one tilt system to the next. The first step in understanding the effect of A cation coordination is to systematically describe the A cation coordination associated with each tilt system. In order to do this structures were generated by POTATO (see appendix 4) for 10 different tilt systems and the A cation coordination in each of these structures was examined. The tilt systems that were studied were the most symmetric representatives of each of the 10 classes of tilt systems: 000, 00-, 00+, 0++, 0+-, 0--, ---, +--, ++-, and +++. The most symmetric tilt systems were chosen so that the tilt angles could remain constant from one system to the next. Analysis of less symmetric tilt systems would be difficult to carry out in a systematic way. For example in the tilt system $a^0b^-c^-$ if the tilt angle about the z axis is taken to be 10° what should the tilt angle about the y axis be? If that value is very small the A cation coordination will be similar to that found in $a^0a^0c^-$, while if the tilting about y is near 10° the A cation coordination will be similar to that found in $a^0b^-b^-$, and if the tilt angle is intermediate the coordination will be different still. Therefore, only the symmetric tilt systems are analyzed and the A cation coordination spheres in the less symmetric tilt systems are assumed to be a modification of the coordination spheres found in the more symmetric tilt systems.

Table 3.1 summarizes the results of this study. This table was generated by starting with an M-O bond distance of 2.00Å and setting all tilt angles to 10°. Some space groups allow the A cation to move off of its ideal site, in those cases the A cation has been shifted in an attempt to give the most symmetric coordination geometry. The reduced coordination numbers of the A cation are a result of some of the anions moving too far away to be considered a significant part of the coordination sphere. Specifically, any anions more than 3.00Å away from the A cation were considered to be outside the coordination sphere. The bond valence calculations were performed by assuming the composition was $SrTiO_3$. These numbers are only meaningful when compared relative to the other values found in table 3.1.

Tilt System	A Cation Site(s)	Coord. #	Bond Distances (Å)	Geometry of 1st Coordination Sphere	Bond Valence	Cell Vol. (Å^3)	Fig.
$a^0a^0a^0$ ($Pm\bar{3}m$)	1b	12	12 x 2.83	Cubo-Octahedral	1.76	64.00	1a
$a^0a^0c^-$ (I4/mcm)	4b	4 + 4	4 x 2.58 4 x 2.79	Distorted Tetrahedral (Angles = 78° & 127°)	2.13	62.13	1b
$a^0a^0c^+$ (P4/mbm)	2c	4 + 4	4 x 2.58 4 x 2.79	Rectangular Planar (Angles = 78° & 102°)	2.13	62.13	1c
$a^0b^-b^-$ (Imma)	4e	5 + 2	5 x 2.42-2.45 2 x 2.90	Square Pyramidal	2.68	60.19	1d
$a^0b^+b^-$ (Cmcm)	4c	4 + 2	4 x 2.39-2.41 2 x 2.74	Distorted Tetrahedral (Angles = 84° & 123°)	2.71	60.20	None
	4c	6 + 2	6 x 2.53-2.56 2 x 2.83	Face Centered Trigonal Prismatic	2.48		
$a^0b^+b^+$ (I4/mmm)	2a	4	4 x 2.30	Square Planar	3.13	60.20	None
	2b	8	8 x 2.56	Square Prismatic	2.61		
	4c	4 + 4	4 x 2.51 4 x 2.82	Rectangular Planar (Angles = 79° & 101°)	2.34		
$a^-a^-a^-$ ($R\bar{3}c$)	2a	3 + 6	3 x 2.25 6 x 2.83	Trigonal Planar	3.36	58.34	1e
$a^+a^-a^-$ (Pnma)	4c	4 + 4	4 x 2.31-2.45 4 x 2.58-2.70	Distorted Tetrahedral (Angles 85° & 109°)	3.02	58.38	1f
$a^+a^+a^-$ ($P4_2/nmc$)	2a	4 + 4	4 x 2.26 4 x 2.83	Distorted Tetrahedral (Angles 92° & 119°)	3.60	58.38	None
	2b	4 + 4	4 x 2.30 4 x 2.83	Square Planar	3.25		
	4d	6 + 4	6 x 2.43-2.55 4 x 2.81	Face Centered Trigonal Prismatic	2.76		
$a^+a^+a^+$ ($Im\bar{3}$)	2a	12	12 x 2.74	Dist. Cubo-octahedral (Angles = 62°)	2.21	58.38	None
	6b	4 + 4	4 x 2.25 4 x 2.82	Square Planar	3.53		

Table 3.1: The A cation coordination in each of the 10 tilt system classifications. This table was generated using POTATO with all tilt angles either 10° or 0°, and a metal oxygen distance of 2.00Å. Bond valence calculations were performed with the program Eutax, by assuming the compound was $SrTiO_3$. The cell volumes have been normalized to the small perovskite cell containing 1 formula unit.

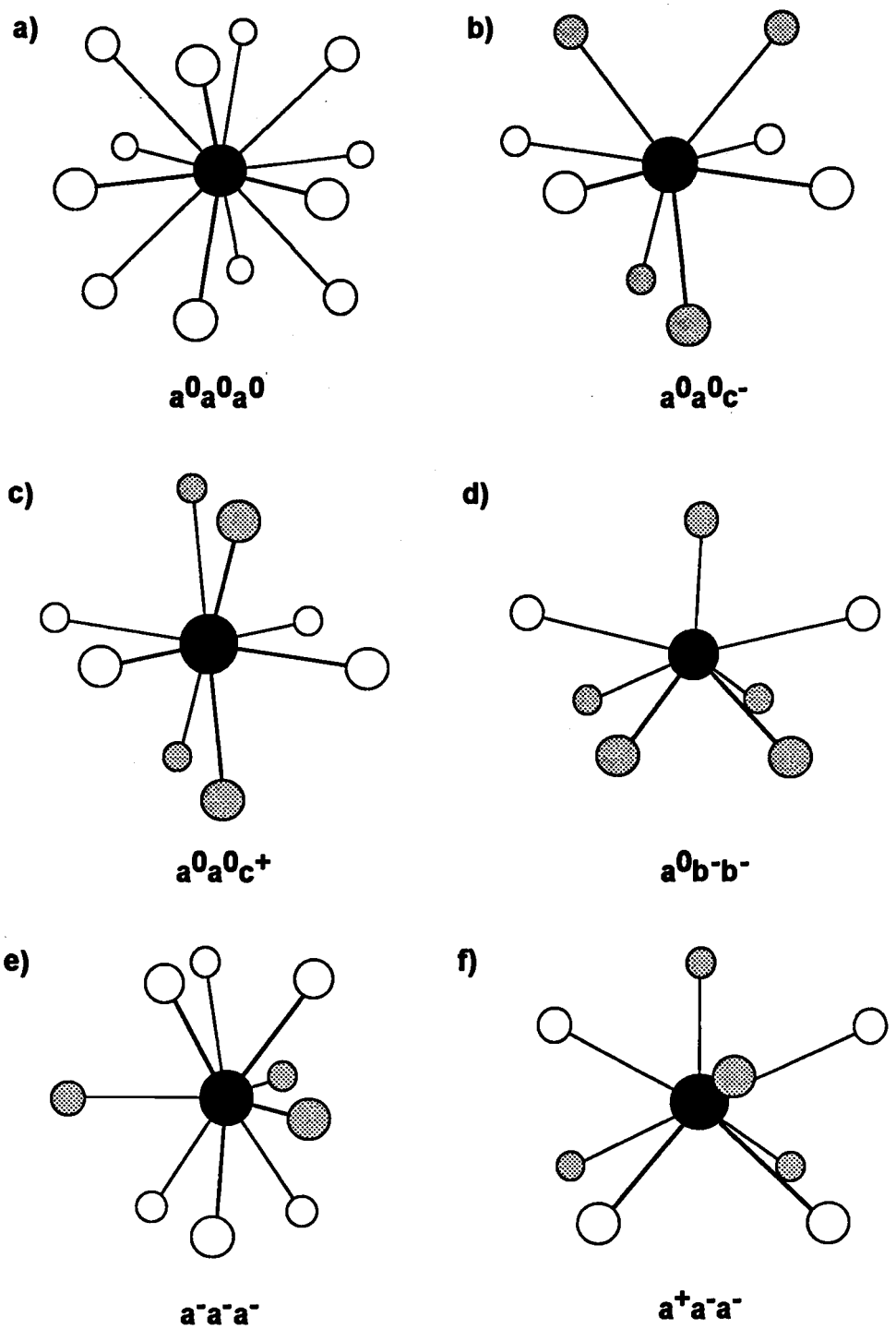

Figure 3.1: The A cation coordination for several of the tilt systems listed in table 3.1. The different figures correspond to the A cation coordination in a) $a^0a^0a^0$ (#23), b) $a^0a^0c^-$ (#22) , c) $a^0a^0c^+$ (#21), d) $a^0b^-b^-$ (#20), e) $a^-a^-a^-$ (#14), and f) $a^+a^-a^-$ (#11). The filled circles represent the A cation, the lightly shaded circles the 1st anion coordination sphere, and the open circles the 2nd anion coordination sphere. The bond distances are as listed in table 3.1.

The bond valence method, based on ideas originally put forward by Pauling (1929), and developed primarily by Brown (1981) and O'Keeffe (1989), is a simple yet powerful method of evaluating the coordination sphere about an ion. This method assigns a valence to each bond in a crystal, based on the distance between ions. The calculations are empirical and make no assumption about the degree of ionicity/covalency in each bond. In a well behaved compound the bond valence of each ion will be close to its oxidation state (i.e. in $SrTiO_3$ the bond valences are expected to be Sr=+2, Ti=+4, and O=-2). The bond valence calculations were performed with the program Eutax (O'Keeffe, 1992). The calculational details are described in more detail by Brese and O'Keeffe (1991).

One principle clearly illustrated in table 3.1 is the fact that in some tilt systems all of the A cation sites remain crystallographically equivalent, while in other tilt systems the A cation sites become nonequivalent. The A cation coordination geometries in each of the six tilt systems with equivalent A site positions are shown in figure 3.1. Figure 3.1a shows the A cation coordination for the ideal undistorted structure (tilt system #23). The A cation is coordinated by 12 equidistant anions in a cubo-octahedral geometry. This coordination can best be described by placing the A cation at the center of a cube and the anions at the middle of each of the 12 edges of the cube.

Figure 3.1b shows the A cation coordination in the $a^0a^0c^-$ tilt system. Here the octahedra have tilted about the [001] axis in opposite senses (clockwise and counterclockwise) in adjacent layers. This results in four short, four medium, and four long A-O distances. Neglecting the four most distant anions gives the coordination description in table 3.1 and shown in figure 3.1b. The four closest anions surround the A cation in a very distorted tetrahedron and the four anions in the second coordination sphere surround the A cation in a square planar geometry. The bond distance between the four closest anions and the A cation is dependent upon tilt angle, becoming smaller as the tilt angle increases. However, regardless of the tilt angle the first coordination sphere is always severely distorted from tetrahedral. In the cubic structure there are four 120° and two 90° bond angles making up the tetrahedron, while after a 10° tilt operation the bond angles become 127° and 78°.

Figure 3.1c shows the A cation coordination for tilt system $a^0a^0c^+$ (#21). The octahedra tilt about the [001] axes here as they did for $a^0a^0c^-$ but now they tilt in the same sense in adjacent layers. The bond distances and bond valence given in table 3.1 are the same for this system as they were for the $a^0a^0c^-$ system, but the A cation coordination is somewhat different. Now the first coordination sphere is rectangular planar instead of distorted tetrahedral. As the tilt angle increases, the four closest anions move closer to the A cation (and to each other) and the bond angles continue to distort away from 90°.

Figure 3.1d shows the coordination about the A cation for tilt system $a^0b^-b^-$ (#20). This is the most symmetric of the 2-tilt systems where now the octahedra have tilted about both the [010] and [001] axes. The coordination is seven coordinate with the nearest five cations arranged in a square pyramidal geometry. Unlike earlier tilt systems, in space group Imma, the A cation has one free parameter. This gives the A cation some freedom to adjust its position to obtain the optimal coordination. For the 10° tilts used in table 3.1, the distance to the apex ion of the square pyramid, before shifting the A cation, was a very short 2.25Å. To obtain a more symmetrical environment the A cation was shifted toward the base of the square pyramid.

The fifth tilt system, $a^-a^-a^-$, represented in figure 3.1e, gives rise to a rhombohedrally distorted unit cell. This tilt system can also be described by a single tilt angle about one body diagonal (3-fold axis) of the cubic cell (Megaw & Darlington, 1975; O'Keeffe & Hyde, 1977; Hyde & Andersson, 1988; Thomas & Beitollahi, 1994). Here the A cations are nine coordinate as indicated in table 3.1, and shown in figure 3.1e. The three closest anions form a perfect trigonal planar coordination in a plane perpendicular to the 3-fold axis, while the other six anions are arranged in a twisted trigonal prism about the A cation. The 10° tilts used to generate the numbers in table 3.1 are larger than the tilt angles observed in actual compounds adopting this tilt system. For example the structure of $LaAlO_3$ can be generated using approximately 3° tilts about each axis, and in $NdAlO_3$ there are 3 short Nd-O distances of 2.39Å and 6 longer Nd-O distances of 2.66Å (Marezio, Dernier & Remeika, 1972). So the numbers in table 3.1 suggesting three very short distances are somewhat exaggerated.

Figure 3.1f shows the A cation coordination for the tilt system $a^+a^-a^-$ (#11). Both this tilt system, and the less symmetric $a^+b^-b^-$ (#10) tilt system, result in an orthorhombic unit cell (the commonly observed $GdFeO_3$ structure) for simple perovskites, and a monoclinic unit cell when cation ordering is present. Table 3.1 shows that the A cation is eight coordinate with four shorter and four longer bonds all of them spread over a range of distances. As was the case for $a^-a^-a^-$ there is only one crystallographic site for the A cation. In contrast to $a^-a^-a^-$, the A cation position now has two free parameters (x and z in Pnma). This is very important as it allows the A cation to shift to a more favorable coordination as the short A-O distances become too small. The coordination sphere of the four closest oxygens is a distorted tetrahedral geometry similar to that found in the $a^0a^0c^-$ tilt system. However, here the tetrahedron is less distorted. For example in $YAlO_3$ the six O-Y-O angles defining the tetrahedron are 83.4°, 88.2°, 108.5°, 108.5°, 127.3° and 127.3° (Diehl & Brandt, 1975). This compares to six 90° angles in the cubic structure or two 88° and four 128° angles in the $a^0a^0c^-$ tilt system. The overall coordination geometry about the A cation is a distorted

archimedian antiprism (square antiprism) in the $a^+a^-a^-$ tilt system. As with tilt system $a^0b^-b^-$ (#20) the geometry is dependent upon the exact shift of the A cation.

3.3 Known Tilt Systems

In his original work Glazer (1972) gives known examples of tilt systems, and he notes that only 9 of the 23 tilt systems were found to exist among well characterized compounds at that time. Much work on both the synthesis and structural characterization of perovskites has been done since then, necessitating a search of the literature in order to update Glazer's list. The results of this search are given in table 3.2, except for tilt systems $a^+b^-b^-$ (#10) and $a^+a^-a^-$ (#11), which are listed separately in table 3.3. It is worth noting that since 1972 the scope of known compounds has expanded such that representatives of 15 of the 23 tilt systems are now known to exist. The total number of perovskite compounds is quite large so despite the fact that the search was intended to be comprehensive some omissions are inevitable. However, the focus of the search was to find compounds belonging to uncommon tilt systems, so that it is not likely that well characterized examples of the other 8 tilt systems exist.

The $a^+a^-a^-$ (#11)/$a^+b^-b^-$ (#10) tilt systems are combined because they both lead to structures with the same space group, Pnma (#62). Because there is no additional symmetry gained by keeping all three rotation angles equal, one might expect the $a^+b^-b^-$ (#10) tilt system to be more commonly observed because it has an additional degree of freedom. In an attempt to test this assertion, POTATO was used to simulate atomic positions of a handful of known structures. As expected, the $a^+b^-b^-$ tilt system was found to be the correct tilt system in all cases. A somewhat unexpected result of these calculations was the observation that the two rotation angles tended be very similar in magnitude, but in opposite directions (i.e. a clockwise rotation about the [100] axis and a counterclockwise rotation about the [010] and [001] axes)*. Why the rotations occur in opposite directions and how widely this generalization can be extended remain unclear. All of the calculational methods employed in this chapter indicate no energetic difference between the two tilt systems (if the rotation magnitudes a and b are equal). Therefore, for the remainder of this chapter the two tilt systems will be regarded as equivalent and will be referred to as the $a^+b^-b^-$ (#10) tilt system. A partial but extensive list of these compounds is given in table 3.3.

Table 3.2 : Examples of known tilt systems. Tolerance factors have been calculated for the oxides and fluorides stable at room temperature and below, with unique or at least similar A cations. If no temperature is listed room temperature is implied. Crystal radii of Shannon have been used (Shannon, 1976). For the A cation, 12 coordinate radii have been used, if necessary these radii have been extrapolated, 2 coordinate anion radii have been used

Table 3.3 : Examples of known $a^+a^-a^-/a^+b^-b^-$ simple perovskites. Tolerance factors have been calculated for those structures stable at room temperature and below. Covalent radii of Shannon have been used (Shannon, 1976). Tolerance factors have not been calculated for compounds with lone pair A cations. If no temperature is listed it is implied that the structural analysis was performed at room temperature.

---

*The direction of the tilts should not be confused with the phase of the tilts. Both $a^+a^-a^-$ and $a^+b^-b^-$ have in phase tilting about the [100] axis, and out of phase tilting about the [010] and [001] axes (see figure 2.1).

Tilt System	Tol. Factor	Compound	Reference
3-Tilt Systems			
$a^+b^+c^+$/ $a^+b^+b^+$		No known examples	
$a^+a^+a^+$		$(Na_{.25}Mn_{.75})MnO_3$	Marezio, *et al.* (1973)
		$(Ca_{.25}Cu_{.75})MnO_3$	Chenevas, *et al.* (1975)
		$(Ca_{.25}Cu_{.75})TiO_3$	Bochu, *et al.* (1979)
		$(Tb_{.17}Cu_{.75})TiO_3$	Bochu, *et al.* (1979)
		$(Na_{.25}Cu_{.75})(Ta_{.25}Ti_{.75})O_3$	Bochu, *et al.* (1979)
		$(Na_{.25}Cu_{.75})(Nb_{.25}Ti_{.75})O_3$	Bochu, *et al.* (1979)
		$(Na_{.25}Cu_{.75})(Sb_{.25}Ti_{.75})O_3$	Bochu, *et al.* (1979)
		$(Ca_{.25}Cu_{.75})GeO_3$	Ozaki *et al.* (1977)
		$(Na_{.25}Cu_{.75})RuO_3$	Labeau, *et al* (1980)
		$(Ca_{.25}Cu_{.75})RuO_3$	Labeau, *et al* (1980)
		$(La_{.25}Cu_{.75})RuO_3$	Labeau, *et al* (1980)
		$(Ca_{.25}Fe_{.75})TiO_3$	Leinenweber & Parise (1995)
		$(Th_{.25}Cu_{.75})MnO_3$	Deschizeaux, *et al.* (1976)
		$(Y_{.25}Cu_{.75})MnO_3$	Collomb, *et al.* (1983)
		$(Nd_{.25}Cu_{.75})RuO_3$	Müller, *et al.* (1986)
		$(Th_{.25}Cu_{.75})MnO_3$	Fesenko, *et al.* (1991)
		$Li_{.36}WO_3$	Wiseman & Dickens (1976)
		$Na_{.73}WO_3$	Wiseman & Dickens (1976)
		$Na_{.54}WO_3$	Wiseman & Dickens (1976)
		$D_{.53}WO_3$	Wiseman & Dickens (1973)
		$D_{.99}MoO_3$	Parise, McCarron & Sleight (1987)
		$HNbO_3$	Forquet *et al.* (1983)
$a^+b^+c^-$		$NaNbO_3$ (480-520°C)	Ahtee, Glazer & Megaw (1972)
$a^+a^+c^-$		$CaFeTi_2O_6$	Leinenweber & Parise (1995)
$a^+b^+b^-$/ $a^+a^+a^-$		No known examples	
$a^+b^-c^-$/ $a^+a^-c^-$		WO_3 (~300-600K)	Loopstra & Rietveld (1969)
		$GaLiBr_3$	Hönle & Simon (1986)
		$GaLiI_3$	Hönle, Miller & Simon (1988)
$a^-b^-c^-$		WO_3 (~230-300K)	Diehl, Brandt, & Salje (1978) Woodward, Sleight, & Vogt (1995)
$a^-b^-b^-$		No known examples	

Table 3.2

$a^-a^-a^-$	1.017	$LaAlO_3$	Derighetti *et al.* (1965)
	1.014	$LaCuO_3$	Demazeau *et al.* (1972)
	1.011	$LaCoO_3$	Menyuk, Dwight, & Raccah (1967)
	1.003	$LaNiO_3$	Thornton, Tofield, Hewat (1986)
	0.998	$(Sr_{.66}La_{.33})FeO_{3-x}$	Battle, Gibb & Lightfoot (1990)
	0.994	$PrAlO_3$ (298-205K)	Burbank (1970)
	0.992	$BaTbO_3$	Jacobson, Tofield & Fender (1972)
	0.991	$(La_{.75}Sr_{.25})CrO_3$	Khattak & Cox (1977)
	0.983	$NdAlO_3$	Marezio, Dernier, & Remeika (1972)
	0.974	$NaNbO_3$ (< 173°C)	Darlington (1971)
	0.960	$BiFeO_3$	Michel *et al.* (1969)
		$HgTiO_3$	Sleight & Prewitt (1973)
		$(Li_{.66}Cu_{.33})TaO_3$	Sato, Jin, Hama & Uematsu (1993)
		$(Sr_xLa_{1-x})FeO_3$ $(0.7\geq x\geq 0.4)$	Dann *et al.* (1994)
		$PrNiO_3$ (> 400°C)	Huang *et al.* (1990)
		$LiNbO_3$	Megaw (1968)
		$LiTaO_3$	Abrahams & Bernstein (1967)
		MF_3 M=Fe,Co,Ru,Rh,Pd,Ir	Hepworth, *et al* (1957)
2-Tilt Systems			
$a^0b^+c^+$/ $a^0b^+b^+$		No known examples	
a^0b^+c/ $a^0b^+b^-$		$SrZrO_3$ (700-830°C)	Ahtee, Glazer & Hewat (1978)
		$NaNbO_3$ (520-575°C)	Ahtee, Glazer & Megaw (1972)
		$NaTaO_3$ (530,600°C)	Ahtee & Darlington (1980)
		NH_4MnCl_3 (128 K)	Tornero, *et al* (1978)
$a^0b^-c^-$	0.994	$PrAlO_3$ (<135 K)	Burbank (1970)
	0.985	$BaPbO_3$	Marx *et al.* (1992)
			Ritter *et al.* (1989)
		$Ba(Pb_{1-x}Bi_x)O_3$ $(0.2\geq x\geq 0)$	Marx *et al.* (1992)
$a^0b^-b^-$	0.997	$(Pr_{.65}Ba_{.35})MnO_3$ (298 K)	Jirak *et al.* (1990)
	0.985	$BaPbO_3$ (4 K)	Thornton & Jacobson (1976)
	0.994	$PrAlO_3$ (151-205 K)	Burbank (1970)
		$Ba(Pb_{1-x}Bi_x)O_3$ $(0.75\geq x\geq 0.35)$	Marx *et al.* (1992)
		$Ba(Pb_{.8}Tl_{.2})O_{2.8}$	Greedan, Willmer & Gibbs (1992)

Table 3.2 (Continued)

1-Tilt Systems			
$a^0a^0c^+$		$NaTaO_3$ (620°C)	Ahtee & Darlington (1980)
		$NaNbO_3$ (575-641°C)	Glazer & Megaw (1972)
		$CsSnI_3$ (78-153°C)	Yamada *et al.* (1991)
		$CsDyBr_3$	Hohnstedt & Meyer (1993)
$a^0a^0c^-$	1.009	$SrTiO_3$ (<110 K)	Unoki, Sakudo (1967)
	1.006	$CsAgF_3$	Odenthal & Hoppe (1971)
	0.997	$(Pr_{.65}Ba_{.35})MnO_3$ (210 K)	Jirak *et al.* (1990)
	0.978	$KMnF_3$ (88-184 K)	Minkiewwicz, Fujii & Yamada (1970)
	0.955	$RbAgF_3$	Odenthal & Hoppe (1971)
		$SrZrO_3$ (830-1170°C)	Ahtee, Glazer & Hewat (1978)
		WO_3 (467-680°C)	Salje (1977)
		$Ba(Pb_{.8}Bi_{.2})O_3$ (180°C)	Marx *et al.* (1992)
0-Tilt Systems			
$a^0a^0a^0$	1.049	$SrGeO_3$	Shimizu, Syono & Akimoto (1970)
	1.047	$BaMoO_3$	Brixner (1960)
	1.032	$KMgF_3$	Zhao *et al.* (1996)
	1.031	$BaNbO_3$	Svenson & Werner (1990)
	1.026	$BaSnO_3$	Smith & Welch (1960)
	1.022	$SrVO_3$	Rey *et al.* (1990)
	1.021	$KZnF_3$	Buttner & Maslen (1988)
	1.020	$SrFeO_3$	Takano *et al.* (1988)
	1.019	$KCoF_3$	Kijima, Tanaka & Marumo (1981)
	1.014	$KNiF_3$	Kijima, Tanaka & Marumo (1983)
	1.011	$BaZrO_3$	Roth (1957)
	1.009	$SrTiO_3$	Unoki & Sakudo (1967)
	1.002	$KFeF_3$	Miyata, Tanaka & Marumo (1983)
	1.001	$BaLiF_3$	Zhao *et al.* (1996)
	0.998	KUO_3	Dickens & Powell (1991)
	0.986	$SrMoO_3$	Liu, Zhao & Eick (1992)
		$NaNbO_3$ (>641°C)	Glazer & Megaw (1972)
		$CsSnI_3$ (>153°C)	Yamada *et al.* (1991)
		$La_{.14}WO_3$	Wiseman & Dickens (1976)
		ReO_3	Ferretti, *et al.* (1965)

Table 3.2 (Continued)

Tilt System	Tol. Factor	Compound	Reference
$a^+b^-b^-$	1.012	$CaMnO_3$	Poeppelmeier *et al.* (1982)
$a^+a^-a^-$	1.012	$CaGeO_3$	Sasaki, Prewitt & Liebermann (1983)
	1.001	$SrRuO_3$	Jones, Battle, Lightfoot & Harrison (1989)
	0.986	$CaVO_3$	Bouloux & Galy (1976)
	0.981	$PrNiO_3$ (298-400°C)	Lacorre *et al.* (1991); Huang *et al.* (1990)
	0.975	$LaCrO_3$	Khattak & Cox (1977)
	0.974	$NaTaO_3$ (25-530°C)	Ahtee & Darlington (1980)
	0.973	$LaGaO_3$	Wang *et al.* (1991)
	0.973	$CaTiO_3$	Sasaki, Prewitt, Bass & Schulze (1987)
	0.972	$SmAlO_3$	Marezio, Dernier & Remeika (1972)
	0.967	$SrSnO_3$	Vegas, *et al.* (1986)
	0.965	$CaRuO_3$	Bensch, Schmalle & Reller (1990)
	0.964	$KPdF_3$	Alter (1974)
	0.962	$CdTiO_3$	Sasaki, Prewitt, Bass & Schulze (1987)
	0.961	$LaMnO_3$	Elemans, *et al.* (1971)
	0.961	$LaFeO_3$	Geller & Wood (1956)
	0.953	$SrZrO_3$ (<700°C)	Ahtee, Glazer & Hewat (1978)
	0.951	$DyAlO_3$	Bidaux & Mériel (1968)
	0.951	$CaMoO_3$	Kamata, Nakamura & Sata (1975)
	0.951	$BaPrO_3$	Jacobson, Tofield & Fender (1972)
	0.950	$NdNiO_3$	Lacorre *et al.* (1991)
	0.947	$BaPuO_3$	Christoph *et al.* (1988)
	0.945	$YAlO_3$	Diehl & Brandt (1975)
	0.943	$BaCeO_3$	Jacobson, Tofield & Fender (1972)
	0.940	$SmNiO_3$	Lacorre *et al.* (1991)
	0.941	$PrMnO_3$	Quezel-Ambrunaz (1968)
	0.932	$CaSnO_3$	Vegas, *et al.* (1986)
	0.930	$KAgF_3$	Odenthal & Hoppe (1971)
	0.928	$SrPbO_3$	Keller, Meier & Müller-Buschbaum (1975)
	0.919	$CaZrO_3$	Koopmanns, *et al.* (1983)
	0.918	$NaUO_3$	Bartram & Fryxell (1970)
	0.907	$YCrO_3$	Geller & Wood (1956)
	0.893	$YFeO_3$	Geller & Wood (1956)
	0.889	$SrCeO_3$	Saiki *et al.* (1991)
	0.842	$NaIO_3$	Svensson & Stahl (1988)
	0.96-0.87	$REVO_3$ RE=La,Ce,Nd,Tb,Er,Tm,Yb	Zubkov *et al.* (1986)
	0.95-0.88	$RETiO_3$ RE=La,Nd,Sm,Gd,Y	MacLean, Ng & Greedan (1979)
	.94-.88	$REFeO_3$ RE=Pr-Lu	Marezio, Remeika & Dernier (1970)
	0.912	$NaFeF_3$	Benner & Hoppe (1990)
	0.95-0.93	$NaMF_3$ M=Ni,Mg,Cu,Zn,Co	Luetgert & Babel (1992)
		$MgSiO_3$	Hemley *et al.* (1989)
		$SeMO_3$ M=Mg,Mn,Co,Ni,Cu	Kohn, Inoue, Horie & Akimoto (1976)
		$TeMO_3$ M=Mn,Co,Ni	Kohn, Inoue, Horie & Akimoto (1976)
		$BaUS_3$	Brochu, Padiou & Grandjean (1970)
		$UCrS_3$	Noël, Padiou & Prigent (1975)
		$YScS_3$	Rodier & Laruelle (1970)
		$LaYbS_3$	Rodier, Julien & Tien (1983)
		$KMgCl_3$	Brynestad, Yakel & Smith (1966)
		$KMnCl_3$	Horowitz *et al.* (1982)
		$CsSnI_3$	Yamada *et al.* (1991)

Table 3.3

Inspection of tables 2 and 3 show that when the A site is occupied by a single type of cation the most commonly observed tilt systems are $a^0a^0a^0$ (#23), $a^-a^-a^-$ (#14), and $a^+b^-b^-$ (#10). From table 3.1 one sees that all of these tilt systems have crystallographically equivalent A cation sites. In fact, at room temperature, all of the compounds belonging to tilt systems with nonequivalent A sites have two different cations on the A site. This result is not surprising assuming the octahedra tilt in such a way as to optimize the coordination about the A cations. Assuming this is true, in cases where a single species occupies all of the A cation sites, one would expect the structure to distort in a manner that achieves the same optimal coordination about each A site. This principle was stated most eloquently almost 70 years ago by Linus Pauling as his fifth rule, the rule of parsimony (Pauling, 1929). The information in tables 2 and 3 shows convincingly that for simple AMO_3 compounds the rule of parsimony dictates that only tilt systems with equivalent A sites need be considered.

3.4 Equivalent A Site Tilt Systems

It has been shown that there are seven tilt systems that lead to equivalent A sites; $a^0a^0a^0$ (#23), $a^0a^0c^-$ (#22), $a^0a^0c^+$ (#21), $a^0b^-b^-$ (#20), $a^-a^-a^-$ (#14), and $a^+a^-a^-$ (#11)/$a^+b^-b^-$ (#10). However, tables 2 and 3 show that there is not an even distribution of compounds among these tilt systems. By far the most commonly observed tilt system is $a^+b^-b^-$ (#10) followed by $a^-a^-a^-$ (#14) and $a^0a^0a^0$ (#23). This distribution of compounds raises some interesting questions. For example, what factors favor these three tilt systems over the others? For a given composition can we predict which tilt system will result? To answer these questions we need to understand what factors energetically favor the structure of one tilt system over the structures of competing tilt systems. To provide such an understanding both ionic and covalent bonding interactions must be considered. Both types of interactions must be examined because the bonding in perovskites is well known to be intermediate between the extremes of ionic and covalent bonding. Unfortunately, most comparative models are based primarily on either the ionic or the covalent model. Therefore, the seven equivalent A site tilt systems have been analyzed using first an ionic model and then a covalent model. Hopefully, approaching the problem from both extremes will lead to an improved understanding of the intermediate regime.

3.4.1 Ionic Bonding

Ionic interactions in solids include both coulombic interactions and short-range non-coulombic interactions, such as Pauli repulsion and dispersion forces. Total lattice energy calculations using empirically derived atomic parameters provide one way of modeling these interactions (Bush, *et al.*, 1992; Mackrodt, 1984). In these calculations each ion is typically modeled as a core and a shell. The ionic charge is empirically divided between the core and the shell and the force that holds the two together is approximated by a harmonic spring constant. Both the coulombic and non-coulombic interactions between the various cores and shells are then calculated, based on empirically derived potentials for each ion. The core/shell approach allows the calculations to approximate the effect of polarization, particularly polarization of the oxygen electron cloud by highly charged cations. The key to performing meaningful calculations is to obtain a good set of empirical potentials for each ion in the structure. The empirical potentials for a given system are usually derived by fitting experimental data on the compound or compounds of interest. This approach, however, is of limited usefulness in comparing known structures with hypothetical structures, because the empirical potentials cannot help but show a bias in favor of the known structure from which they were derived. Fortunately, a self consistent set of potentials was recently derived for oxides (Bush, Gale, Catlow & Battle, 1994). This set of transferable potentials was derived from binary oxides, and allow this powerful calculational approach to be used as a predictive and a comparative tool for more complex oxide structures. All of the calculations in this chapter were performed with the General Utility Lattice Program (GULP), written by Julian Gale of Imperial College, London (Gale, 1992-1994).

The most significant structural change caused by octahedral tilting is the distortion of the A cation coordination sphere. Given the large difference in electronegativity between typical A cations and oxygen, the bonding between the two species is expected to be largely ionic. Therefore, it seems reasonable to expect that calculations based on ionic energies may explain the observed distribution of structures. Using POTATO idealized structures can be easily generated in any of the 23 tilt systems. The lattice energies of these structures can then be compared using GULP. The difficulty lies in determining when structures from different tilt systems and space groups are equivalent. Obviously, by keeping the M-O bond distance constant the first coordination sphere about the M cation can remain unchanged from one tilt system to the next. Beyond that it becomes somewhat subjective as to what additional constraints to impose on each structure in order to define equivalency from one tilt system to the next. This problem is particularly apparent when attempting to compare structures from tilt systems with differing numbers of tilts (i.e. the three tilt systems $a^+b^-b^-$ and

$a^-a^-a^-$ with the two tilt system $a^0b^-b^-$). Because this comparison is based primarily on an ionic model the approach adopted in this analysis was to keep the unit cell volume constant. In this way the calculations reveal the tilt system that can maximize ionic interactions within the same volume of free space.

$YAlO_3$ was chosen as the model compound for these calculations for a variety of reasons. First of all, to detect subtle differences in the A-O interactions it is best to use a compound that has a reasonably strong A-O interaction. $YAlO_3$ is such a compound because of the relatively high oxidation state and electronegativity of yttrium (compared to other A cations such as Ba^{2+}, Sr^{2+}, and La^{3+}). Secondly, the experimental octahedral rotation angles are significant in this compound which should also help to magnify the energetic differences between tilt systems. Finally, the AlO_6 octahedra in this compound are very regular so that the assumption of perfect octahedra is a reasonably good one.

POTATO was used to generate the idealized structures that serve as the starting point for these calculations. The Al-O distance was taken to be 1.911Å and the unit cell volume of the $2a_p x 2a_p x 2a_p$ unit cell was set equal to 407.2Å^3. Both of these values were matched as closely as possible with the experimentally determined values from single crystal structure solution (Diehl & Brandt, 1975). The rotation angles were as follows for each tilt system:

$a^+b^-b^-$ (#10)	-10.02°,10.02°,10.02°,
$a^-a^-a^-$ (#14)	10.00°,10.00°,10.00°,
$a^0b^-b^-$ (#20)	0°,12.23°,12.23°,
$a^0a^0c^+$ (#21)	0°,0°,17.29°,
$a^0a^0c^-$ (#22)	0°,0°,17.29°.

For the cubic system $a^0a^0a^0$ (#23) in order to keep the volume at 407.2Å^3 the Al-O distance had to be shortened to 1.853Å. Each structure was described as centrosymmetric triclinic, space group $P\bar{1}$, even though the true symmetry was always higher.

Using GULP, lattice energy calculations were performed on the starting structure associated with each tilt system. The ionic potentials used were taken directly from the set of transferable potentials mentioned earlier (Bush, Gale, Catlow & Battle, 1994). A Newton/Raphson minimization algorithm was employed. This allowed the program to stay in the local energy minimum associated with each tilt system. GULP is able to not only calculate the total lattice energy, but it also has the capability to vary certain structural parameters, under a variety of constraints, to minimize the energy. Using the minimization

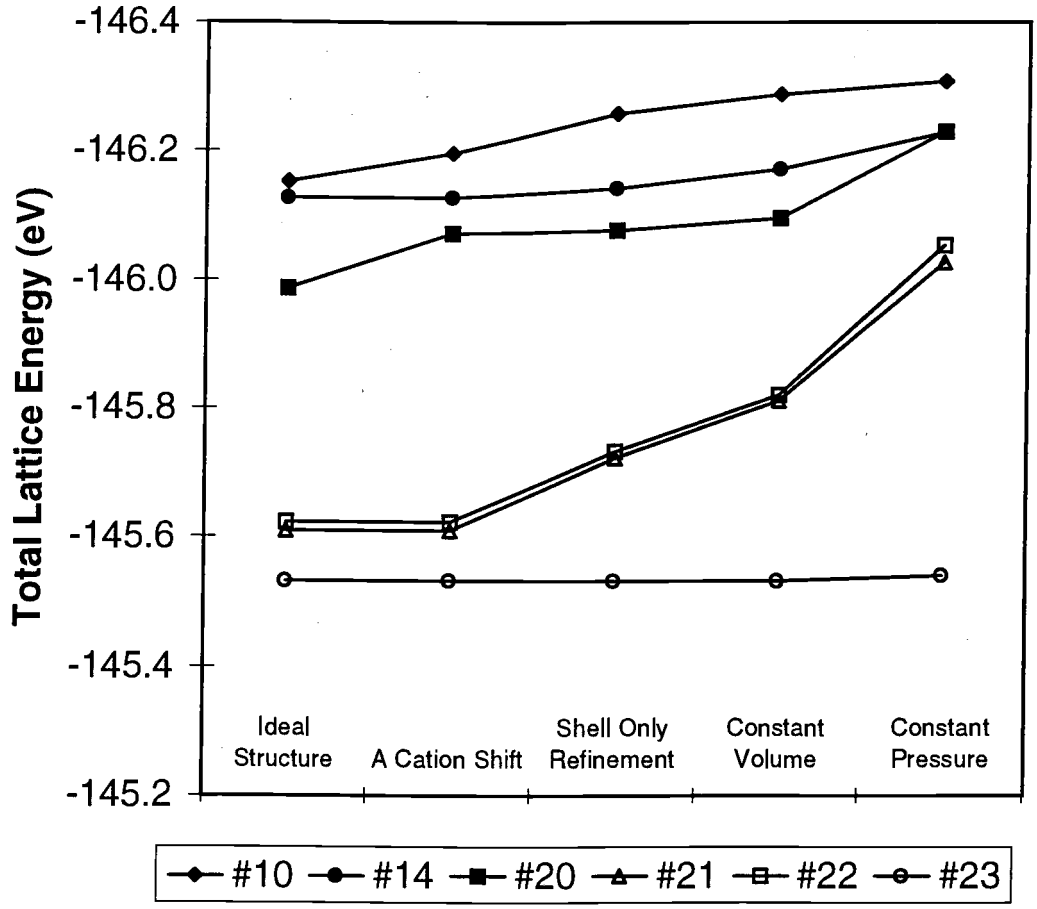

Figure 3.2 : Total lattice energy after each stage of the GULP refinements of the $YAlO_3$ structure. Filled diamonds represent the $a^+b^-b^-$ (#10) tilt system, filled circles represent the $a^-a^-a^-$ (#14) tilt system, filled squares represent the $a^0b^-b^-$ (#20) tilt system, open triangles represent the $a^0a^0c^+$ (#21) tilt system, open squares represent the $a^0a^0c^-$ (#22) tilt system, and open circles represent the $a^0a^0a^0$ (#23) tilt system.

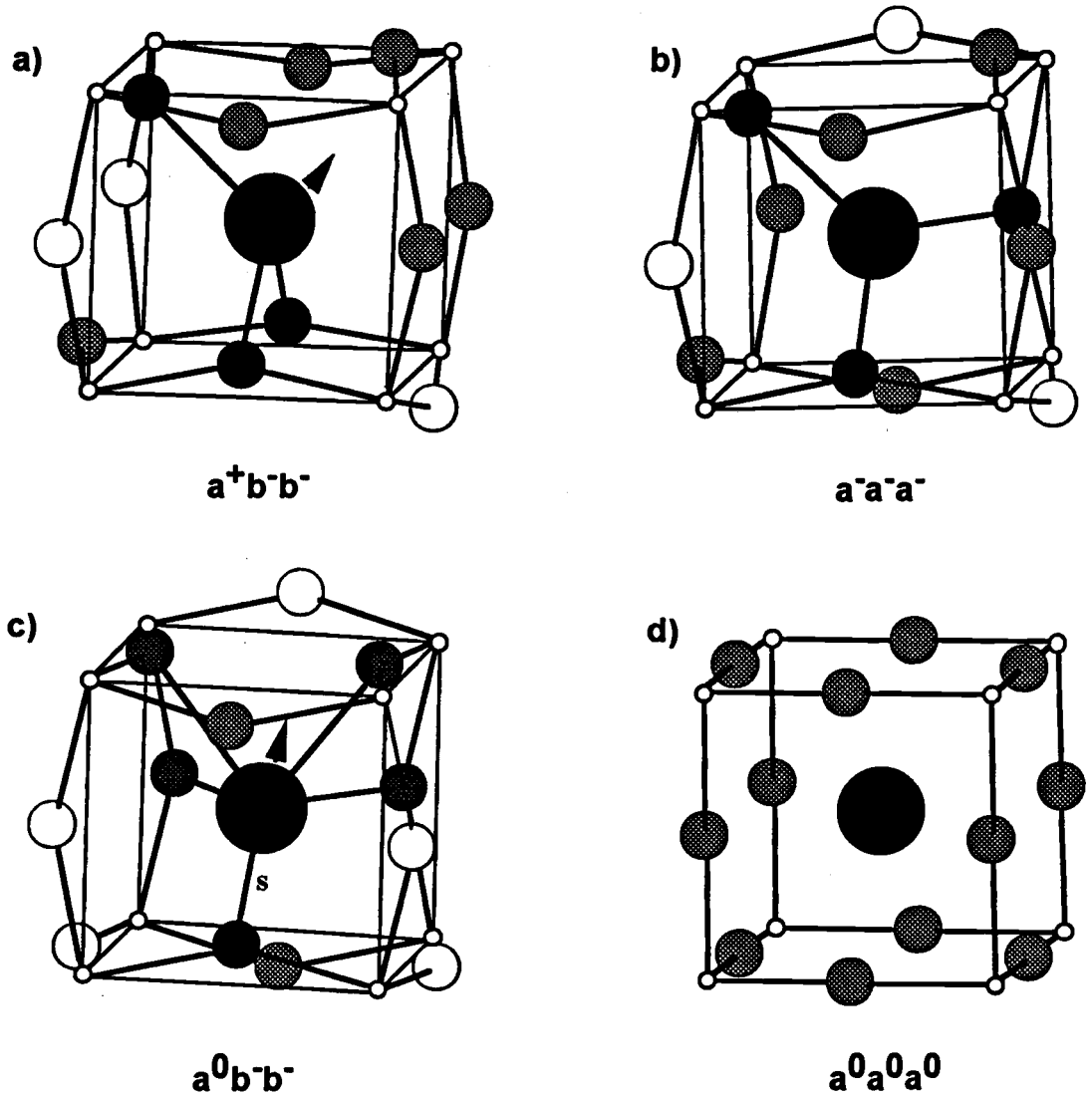

Figure 3.3: The arrangement of oxygen ions about the A cation after octahedral tilting in $YAlO_3$ in the a) $a^+b^-b^-$ tilt system, b) $a^-a^-a^-$ tilt system, c) $a^0b^-b^-$ tilt system, and d) $a^0a^0a^0$ tilt system. The large dark circles represent Y, the small open circles represent Al, and the intermediate sized circles represent oxygen. The dark oxygens have the shortest Y-O distances, the shaded oxygens have intermediate Y-O distances, and the open oxygens have the longest Y-O distances. In figure c) the Y-O bond marked with an S is shorter than the other four short Y-O distances. The arrows in parts a) and c) indicate the direction in which the Y ion can shift in order to achieve a more even distribution of bond distances.

capabilities of GULP varying degrees of structural freedom were introduced in a stepwise fashion: first the A site position was refined, then the ion shells were refined, then all of the ion positions were allowed to refine, and finally the unit cell constants were allowed to refine. The changes in energy were recorded after each step. The results of these calculations are plotted in figure 3.2. The lattice energy calculations on the initial structures show that the $a^+b^-b^-$ tilt system (#10) and the $a^-a^-a^-$ tilt system (#14) have the most favorable lattice energies, while the one and zero tilt system structures are less stable. The energies of the $a^+b^-b^-$ and $a^-a^-a^-$ systems are quite similar, but when the Y is allowed to shift off of its ideal position, the energy of the $a^+b^-b^-$ tilt system lowers by 0.056 eV, while the energy of the $a^-a^-a^-$ tilt system remains unchanged. To illustrate why this should be, the A cation environments in the $a^+b^-b^-$, $a^-a^-a^-$, $a^0b^-b^-$, and $a^0a^0a^0$ tilt systems are shown in figure 3.3. Notice that in the $a^-a^-a^-$ system the A cation sits on a three fold axis running along the [111] direction and a two fold axis running along the $[1\bar{1}0]$ direction. The electric field gradient set up by the surrounding oxygen ions in this highly symmetrical environment make the ideal site for the Y ion a minimum on the potential energy surface. This keeps the Y ion from moving, despite the fact that the lattice energy minimizations were all done in space group $P\bar{1}$, so that no explicit symmetry constraints fix the Y ion to its ideal site. Turning now to tilt system $a^+b^-b^-$, figure 3.3a shows that the Y ion sits on a mirror plane running perpendicular to the x axis. This restricts its movement in the x direction, but not in the y and z directions. The Y ion can then shift away from the three closest oxygens, shaded in black, and toward five of the six next-nearest oxygen ions, as indicated by the arrow in figure 3.3a. This shifting of the Y reduces the repulsion between yttrium and oxygen that arises when the octahedral tilting distortion becomes fairly large. Figures 3.2 and 3.3c both show that the Y can also shift in tilt system $a^0b^-b^-$ (#20), but the total energy of this tilt system is still higher than the $a^+b^-b^-$ and $a^-a^-a^-$ systems. This difference between the $a^+b^-b^-$ and $a^-a^-a^-$ tilt systems is crucial in stabilizing the $a^+b^-b^-$ tilt system over the $a^-a^-a^-$ tilt system as the tolerance factor decreases.

The next stage in energy minimization was to let the ion shell positions refine, while keeping the ion cores stationary. Once again the energy of the $a^+b^-b^-$ (#10) structure decreases (becomes more stable), this time by 0.041 eV, while the energies of the $a^-a^-a^-$ (#14) and $a^0b^-b^-$ (#20) structures only increase by 0.015 eV and 0.005 eV respectively. The decrease in energy during this stage of the refinement gives an estimate of how effectively the cation arrangement can polarize the electron clouds around the oxygen ions. One interesting observation was that if the shell refinement was performed before the Y ion was allowed to shift off of its ideal site the decrease in energy in the $a^+b^-b^-$ tilt system was only 0.011 eV. This is much lower than the 0.041 eV decrease observed if the shell refinement

was done after shifting the Y ion, once again emphasizing the importance of the A cation shift in the $a^+b^-b^-$ tilt system.

The last two minimization steps in figure 3.2 are labeled constant volume and constant pressure. The former allows all of the atom positions to refine while the unit cell constants remain fixed. The latter allows both the positional parameters and the unit cell constants to refine simultaneously. The constant volume refinement removes the constraint that the octahedra must remain perfect. During this stage of the minimization the energy of the $a^+b^-b^-$ tilt system decreases by 0.028 eV and the energy of the $a^-a^-a^-$ tilt system decreases by 0.031 eV. The fact that both tilt systems show essentially the same decrease in energy implies that small distortions of the octahedra do not play a deciding role in determining the lowest energy structure. The constant pressure refinement removes the constraint that the unit cell volumes remain equal. When this constraint is removed the unit cell volumes increase for all of the structures (except the cubic $a^0a^0a^0$ structure which shows a slight decrease) this reduces both the coulombic attractions and the repulsive ion-ion interactions. Because the program minimizes the total energy, the benefit of reducing the repulsive terms will always outweigh the decrease in the magnitude of the coulomb term. However, the final structure will be very dependent upon the empirical potentials used. For example, in the $a^+b^-b^-$ tilt system the Y-O bond distances undergo relatively little change but two of the six Al-O distances expand from 1.92Å to 1.95Å. This moves the structure away from the experimentally determined structure, yet only decreases the energy by a modest 0.019 eV. For this reason the constant volume minimization step seems to provide a more accurate comparison of the lattice energies of the different structures. The constant pressure minimization is included primarily to show that removing the constraint of constant volume does not change the overall conclusions reached earlier in the minimization process. Taking the refinement one step further the minimization algorithm can be changed from a Newton/Raphson to rational function optimizer (rfo) to avoid local minima. When this is done the final structure is always the orthorhombic $a^+b^-b^-$ tilt system regardless of the starting point, indicating that it is truly the global minimum in energy.

In order to quantitatively compare the results from the GULP calculations table 3.4 contains the results obtained after the constant volume minimization stage. The trends in these results are representative of other points in the minimization process. The critical piece of information in this table is the fact that the rhombohedral $a^-a^-a^-$ (#14) tilt system maximizes the coulomb attraction between ions, but at the same time it also maximizes the repulsive energy term. In the case of $YAlO_3$ the repulsive term outweighs the attractive term and the $a^+b^-b^-$ (#10) tilt system gives the lowest energy structure. This trend held throughout the minimization process, and was also evident in calculations on other model compounds

such as $CaTiO_3$ and $NdAlO_3$. The tilt system predicted by the calculations to have the lowest overall energy will be sensitive to the exact values of the empirical potentials employed. But regardless of the empirical potentials employed, the conclusion that the $a^-a^-a^-$ tilt system maximizes both the coulomb (Madelung) energy and the repulsive energy, seems to be widely applicable. Both of these properties are apparently a consequence of the high degree of symmetry found in this tilt system. Additional calculations show that the energy stabilization attributable to the coulomb term in the $a^-a^-a^-$ system, with respect to the other tilt systems, decreases as the charge on the A cation decreases. This helps to explain why the rhombohedral distortion of the perovskite structure is commonly observed for $A^{3+}M^{3+}O_3$ compounds, but rarely observed for $A^{2+}M^{4+}O_3$ compounds.

	Total Lattice Energy (eV)	Repul-sive Energy (eV)	Attrac-tive Energy (eV)	Al-O-Al Bond Angles	Y	Al	O
Actual Struct.	-146.25	27.92	-174.17	151.7° 151.9°	3.16	2.97	2.14 2.00
$a^+b^-b^-$ (#10)	-146.25	27.99	-174.24	151.7° 151.8°	3.19	2.97	2.10 2.03
$a^-a^-a^-$ (#14)	-146.14	28.89	-175.03	151.9°	3.39	2.97	2.12
$a^0b^-b^-$ (#20)	-146.08	28.22	-174.29	145.4° 155.8°	3.26	2.97	2.12 2.06
$a^0a^0c^+$ (#21)	-145.72	27.34	-173.06	145.4° 180°	3.01	2.97	2.06 1.86
$a^0a^0c^-$ (#22)	-145.73	27.34	-173.07	145.4° 180°	3.01	2.97	2.06 1.86
$a^0a^0a^0$ (#23)	-145.53	27.59	-173.12	180°	1.87	2.97	1.61

Table 3.4 : The results of total lattice energy (GULP), and bond valence calculations on $YAlO_3$ and idealized (constant volume) $YAlO_3$ structures. The cell volume was 407.2 $Å^3$ for each tilt system. Details of the calculation are given in the text.

Considering, once again the tolerance factors of compounds in the various tilt systems the overall trends can now be understood. Coulombic interactions favor the $a^-a^-a^-$ (#14) tilt system, when the repulsive interactions are relatively small. This is particularly true when the charge on the A cation is high and the tolerance factor is roughly in the range $0.975<t<1.01$. Repulsive interactions become important when the tolerance factor exceeds

unity, because the oversized A cation is too large for the MO_3 lattice. At this extreme the cubic $a^0a^0a^0$ (#23) tilt system is favored because it minimizes ion-ion repulsion. Repulsive interactions also become important when the tolerance factor becomes small (t<0.975), as shown above. In this situation the large rotation angles necessary to accommodate the undersized A cation lead to some rather short A-O distances, as well as increased anion-anion repulsions. In such cases the orthorhombic $a^+b^-b^-$ (#10) tilt system is favored because it achieves the best balance between maximizing coulombic attractions and minimizing repulsive ion-ion interactions. This is due to the local symmetry about the A cation site, which allows an A cation shift and results in a better distribution of A-O distances. Thomas (1996) reached a similar conclusion when comparing orthorhombic and rhombohedral distortions of the perovskite structure.

3.4.2 Covalent A-O Bonding

The covalent bonding interactions of importance in perovskites are A-O σ bonding, M-O σ bonding, and, when M is a transition metal, M-O π bonding (Goodenough, 1971; Choy, Park, Hong & Kim, 1994; Takano *et al.*, 1991). Extended Hückel band structure calculations using the tight binding approximation (EHTB) are one insightful way to evaluate bonding interactions in solids. These calculations have been used extensively to interpret and predict band structures of complex inorganic compounds (Hoffmann, 1988; Whangbo, Evain, Canadell & Ganne, 1989; Burdett & Mitchell, 1993). The extended Hückel method was developed initially by Hoffmann (1963), and later implemented on an extended solid by Whangbo and Hoffmann (1978). Hoffmann gives an excellent description of the interpretation and use of EHTB calculations in his book *Solids and Surfaces* (Hoffmann, 1988). All extended Hückel tight binding (EHTB) calculations performed in this chapter were carried out using the program NEW5, written by Dr. Gordon Miller of Iowa State University (Miller, 1990). Default atomic parameters were used for all EHTB calculations in this work, and are given in appendix 5. In the sections that follow EHTB calculations are used to examine more closely both A-O and M-O covalent bonding interactions.

The same factors that made $YAlO_3$ a good model compound for the ionic model lattice energy calculations make it a good model compound for examining A-O covalent bonding interactions. However, because of the strong dependence of covalent bond strength on exact bond distances, the constant volume approach for defining equivalent structures is not appropriate for a covalent model analysis. The problem once again is to define equivalent A

site environments from one tilt system to the next. One widely accepted and successful method of comparing ion site environments across a variety of structures is the bond valence concept (Brown, 1981; O'Keeffe, 1989). The bond valence and covalent bond strength of an ion are related in that they both are dependent upon the bond distances of the surrounding ions. The two concepts differ because the covalent bond interactions are also dependent upon the energetic and spatial overlap of atomic orbitals. Therefore, by keeping the ionic bond valences constant from one structure to the next the "average bonding capacity" of each ion remains unchanged between structures. More sophisticated calculations, such as the extended Hückel method, can then differentiate the structures based on subtle geometrical differences in the ion coordination spheres of each structure. In other words, even though the "average ion site environment" is the same in all structures, small changes in the structure will modify orbital overlap and lead to varying degrees of covalent interactions. Using the bond valence concept the following set of rules were used to generate equivalent structures:

1) The M-O bond distance is set to a constant value, resulting in a constant bond valence for the M ion.

2) For the $a^+b^-b^-$ (#10) tilt system the two rotation angles are constrained to be the same magnitude but in opposite directions. For the other tilt systems studied, such as $a^-a^-a^-$ (#14) and $a^0b^-b^-$ (#20), there are no ambiguities in the tilt angle relationships.

3) The tilt angles are adjusted to give the same bond valence for the A cation regardless of the structure (with the exception of the cubic structure where rule 1 completely determines the structure).

4) If the A cation has free positional parameters they are adjusted to give bond valence values for the oxygen ions that most closely match the bond valence values found for the oxygen ions in the actual structure.

Using the above set of rules, equivalent structures were generated in tilt systems $a^0a^0a^0$ (#23), $a^0a^0c^-$ (#22), $a^0a^0c^+$ (#21), $a^0b^-b^-$ (#20), $a^-a^-a^-$ (#14), and $a^+b^-b^-$ (#10) for a hypothetical series of $YAlO_3$ compounds. The bond valences of the ions were matched as closely as possible to the values found in the actual structure of $YAlO_3$: 3.16, 2.97, 2.14, and 2.00 for Y, Al, O1, and O2 respectively.

Extended Hückel calculations were carried out on the model $YAlO_3$ structures. Table 3.5 shows the results of these calculations. The total energy of the valence electrons has been calculated for both $YAlO_3$ and AlO_3^{3-} lattices in an attempt to separate effects due to Y-O bonding from those due to Al-O bonding. The total energy of the observed, and idealized

	Extended Hückel			GULP			
	Total Energy $YAlO_3$ (eV)	**Total Energy AlO_3^{3-} (eV)**	**Mulliken Y Electron Pop.**	**Total Lattice Energy (eV)**	**Unit Cell Volume ($Å^3$)**	**Oxygen Bond Valence**	**Al-O-Al Bond Angles**
Actual Struct.	-471.31	-466.49	1.10	-146.23	203.6	2.136 2.001	151.7°
$a^+b^-b^-$ (#10)	-471.30	-466.50	1.10	-146.23	203.6	2.139 1.997	151.2° 152.0°
$a^-a^-a^-$ (#14)	-471.14	-466.50	1.05	-146.20	205.8	2.045	153.5°
$a^0b^-b^-$ (#20)	-471.16	-466.52	1.06	-146.09	204.7	2.136 2.000	146.4° 156.4°
$a^0a^0c^+$ (#21)	-470.98	-466.38	1.05	-145.62	201.2	1.892 2.122	180° 143.3°
$a^0a^0c^-$ (#22)	-471.03	-466.38	1.07	-145.63	201.2	1.892 2.122	180° 143.3°
$a^0a^0a^0$ (#23)	-469.54	-466.57	0.75	-145.27	223.3	1.613	180°

Table 3.5 : The results of extended Hückel, total lattice energy (GULP), and bond valence calculations on $YAlO_3$, and idealized $YAlO_3$ structures. The only the ion shells were allowed to move in the GULP calculations. The bond valences of Y and Al were 3.164 and 2.971 respectively for all systems, with the exception of $a^0a^0a^0$ where the Y bond valence was 1.866. The details of the calculation are given in the text. Keep in mind that the energy differences are more important than the absolute energy values, especially for the extended Hückel calculations.

$a^+b^-b^-$ structures are approximately the same, 0.15 eV lower than the $a^0b^-b^-$ and $a^-a^-a^-$ tilt systems, 0.30 eV lower than the one tilt systems, and 1.25 eV lower than the cubic structure. Table 3.5 also shows that if only Al-O bonding is considered the lowest energy structure is the undistorted cubic structure. Its energy is slightly lower than the $a^0b^-b^-$, $a^-a^-a^-$, and $a^+b^-b^-$ structures, which all have essentially the same energy. Lattice energy calculations, using GULP, were also performed on these structures in order to compare ionic energies. The lattice energies become increasingly more favorable as the order of the tilt system increases. That is the three tilt systems, $a^+b^-b^-$ and $a^-a^-a^-$, have the lowest lattice energies, and the zero tilt system $a^0a^0a^0$ has the highest lattice energy. The fact that the energy stabilization of the $a^+b^-b^-$ tilt system disappears, when either the Y atom is removed from the calculation or when ionic lattice energy calculations are performed, implies that the energy

stabilization of the $a^+b^-b^-$ structure is directly attributable to covalent bonding interactions between yttrium and oxygen.

The calculation results in table 3.5 indicate that the $a^+b^-b^-$ tilt system leads to a structure that optimizes the bonding overlap between the A cation and oxygen. But can an energy difference of 0.15 eV, or 0.03% of the total energy, be considered significant? Both experimental and theoretical calculations indicate that the magnitude of the energy difference between two competing structures can be as small as 10^{-3} to 10^{-4} of the total lattice energy (Zunger, 1980). For example $BaTiO_3$ has a heat of formation of 152 kJ/mol (Navrotsky, 1989). The lowest temperature phase transition in this material has a transformation heat of only 33 J/mol (Galasso, 1969), or 0.02% of the heat of formation. The energy differences suggested by the EHTB calculations are of this order of magnitude. Nonetheless, one may still question if the way in which the idealized structures were generated was exact enough to warrant placing significance on such a small difference in energy. In order to check the sensitivity of the total EHTB energy to small changes in the bond valence values the tilt angle of the $a^-a^-a^-$ structure was changed so that the three closest A-O bond distances decreased by 0.01 Å each. Changing the structure in this way caused the bond valence of Y to increase by 0.06, but the total EHTB energy changed only by 0.05 eV. If the Al-O distance was either shortened or lengthened by 0.01 Å (this also led to a changing of the nearest neighbor Y-O distance of 0.01 Å), it caused the bond valence of Al to change by 0.08, and the bond valence of Y to change by 0.11. Despite the significant changes in both bond valences, the total EHTB energy change was a relatively small, only 0.10 eV. On this scale the energy differences in table 3.5 should be considered significant.

If Y-O bonding has a covalent component then the Y atomic orbitals must make a contribution to the density of states (DOS) below the Fermi level. Figure 3.4 shows the DOS plots for several of the structures from table 3.5. The shaded area is the partial density of states of the Y atom. Figure 3.4 clearly indicates that the Y makes a significant contribution to the DOS below the Fermi level. Furthermore, the DOS curves above the Fermi level change significantly from one tilt system to the next. The sensitivity of these levels to the Y coordination is an indication that they are better described as antibonding rather than nonbonding. This conclusion is verified by the electron population values for Y, tabulated in table 3.5. These values were calculated using the Mulliken population analysis method. This approach assigns all unshared electron density to the atoms from which the respective atomic orbitals originate, and then equally divides the shared electron density between the neighboring atoms involved in bond overlap (Hoffmann, 1988). This approach is one arbitrary method of dividing up the electron density in the unit cell among the constituent atoms. Yttrium is not expected to possess any unshared (nonbonded) electrons so that all

of the electron density associated with yttrium in the Mulliken population analysis comes from Y-O bonding overlap. Table 3.5 shows Y populations values on average of just over 1 electron per yttrium, indicative of Y-O bond formation. In comparison, the Al ions are calculated to have electron population values in the range 1.02-1.06. Also note that tilt system $a^+b^-b^-$ (#10) shows the maximum electron density on the Y ion, suggesting it also has the maximum Y-O bonding overlap. This is consistent with the total energy values.

How can we understand the results of these calculations? What geometrical factor leads to the optimal A-O orbital overlap in the $a^+b^-b^-$ tilt system? Two factors must be considered, the bond distances and symmetry of the anions about the A site. Considering first the symmetry, figure 3.1 clearly shows that in tilt systems $a^-a^-a^-$ (#14) and $a^0a^0c^+$ (#21) the first coordination sphere of oxygens about the A cation are coplanar. If the p_x and p_y orbitals of the A cation are directed in this plane then the p_z and the d_{z2} orbitals will both be orthogonal to this plane and will have zero overlap with the first coordination sphere of oxygens. In the corresponding tilt systems $a^+b^-b^-$ (#10) and $a^0a^0c^-$ (#22) the nearest neighbor oxygen coordination sphere is no longer planar, increasing the number of A cation orbitals that can participate in bonding. The distribution of bond distances also affects the orbital overlap, between yttrium and oxygen. Table 3.6 shows the bond distances, bond valences, and crystal orbital overlap populations (COOP), for all 12 Y-O interactions in each tilt system. The majority of the Y-O bonding is confined to three oxygens in $a^-a^-a^-$, four oxygens in $a^0a^0c^+$ and $a^0a^0c^-$, and five oxygens in the $a^0b^-b^-$ system. In the $a^+b^-b^-$ system bond valence calculations suggest that eight oxygens effectively coordinate yttrium, while a crystal orbital overlap population (COOP) analysis performed in the EHTB calculations (Hoffmann, 1988) indicates a coordination number of six. The yttrium coordination number of six is supported by crystallographic data. In the rare earth orthoferrites, $AFeO_3$, the six closest A-O bond distances linearly decrease as the size of the rare earth ion decreases across the entire lanthanide series. In contrast, the seventh and eighth oxygen neighbors move slightly closer to the rare earth ion with decreasing size only from La to Tb, then as the size of the rare earth ion decreases further these two A-O distances actually begin to increase (Marezio, Remeika & Dernier, 1970). The rare earth titanates, $ATiO_3$, also behave in a similar way (MacLean, Ng & Greedan, 1979). Regardless of whether the A cation coordination is eight or six, the $a^+b^-b^-$ system maximizes the coordination number of yttrium, as well as the number of orbitals on yttrium that can participate in Y-O bonding. Both of these factors should help to make the $a^+b^-b^-$ tilt system the most favorable in terms of A-O covalent bonding overlap.

How applicable are the $YAlO_3$ results to other compounds? Obviously, as the electronegativity of the A cation increases the importance of the covalent A-O bonding

Figure 3.4 : Density of states plots for extended Hückel calculations on $YAlO_3$. The darkened curves on the left hand side of each frame show the partial density of states contribution of Y, the darkened curves on the right hand side of each frame show the partial density of states contribution of Al. DOS plots correspond to the following structures; a) $a^-b^+b^+$ tilt system, b) $a^-a^-a^-$ tilt system, c) $a^0b^-b^-$ tilt system, and d) $a^0a^0a^0$ tilt system.

a)

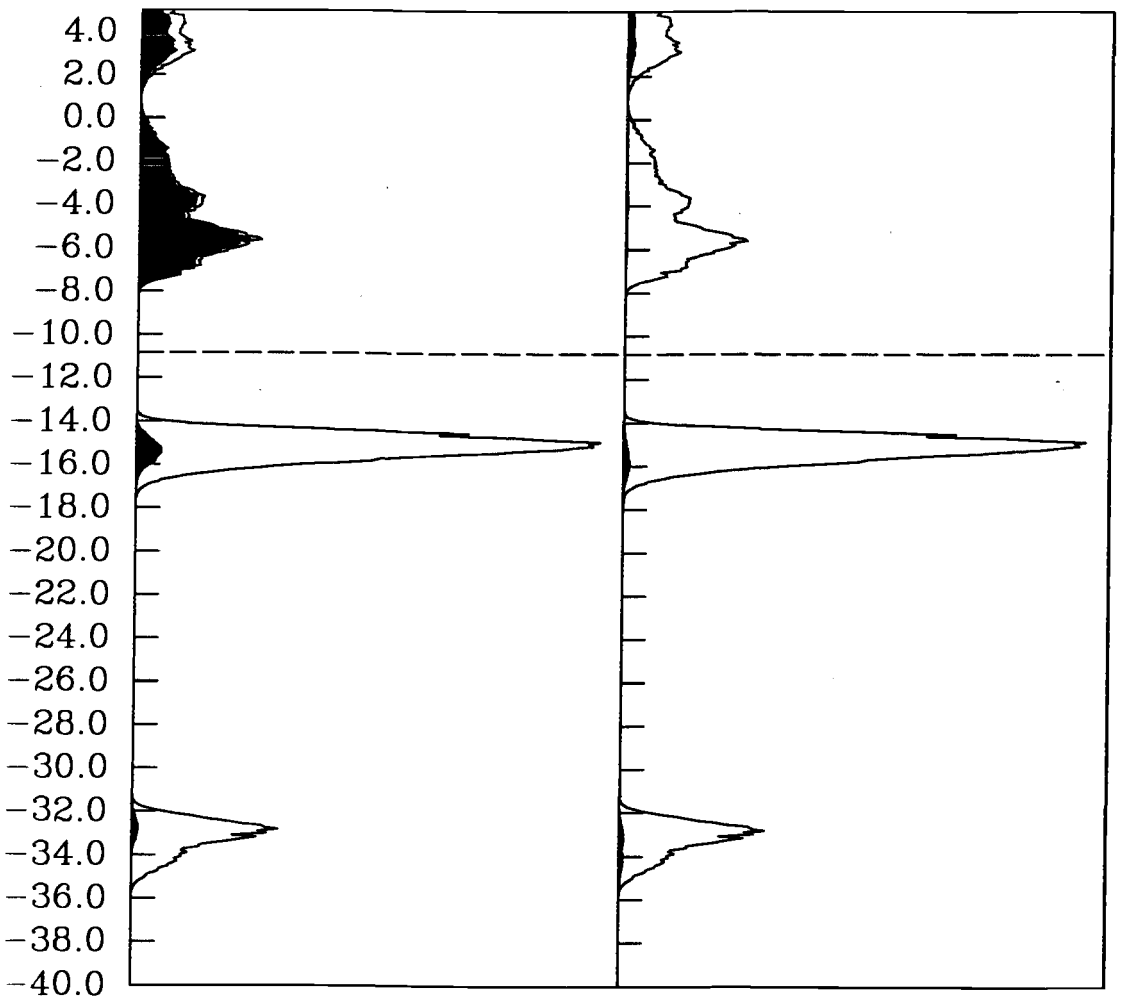
4.0
2.0
0.0
−2.0
−4.0
−6.0
−8.0
−10.0
−12.0
−14.0
−16.0
−18.0
−20.0
−22.0
−24.0
−26.0
−28.0
−30.0
−32.0
−34.0
−36.0
−38.0
−40.0
Y Density of States
Al Density of States
a+b-b- (#10)

Figure 3.4

b)

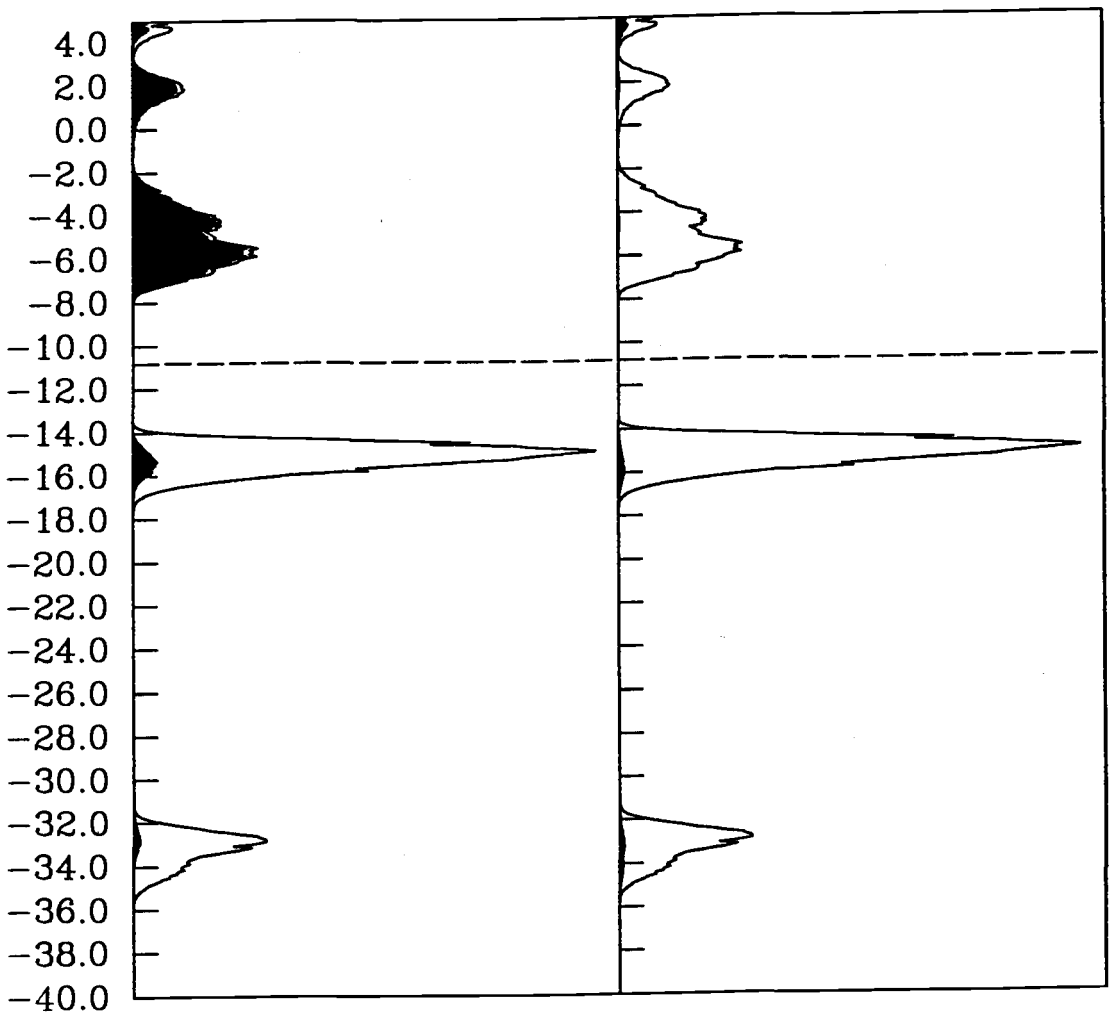

Figure 3.4 (Continued)

c)

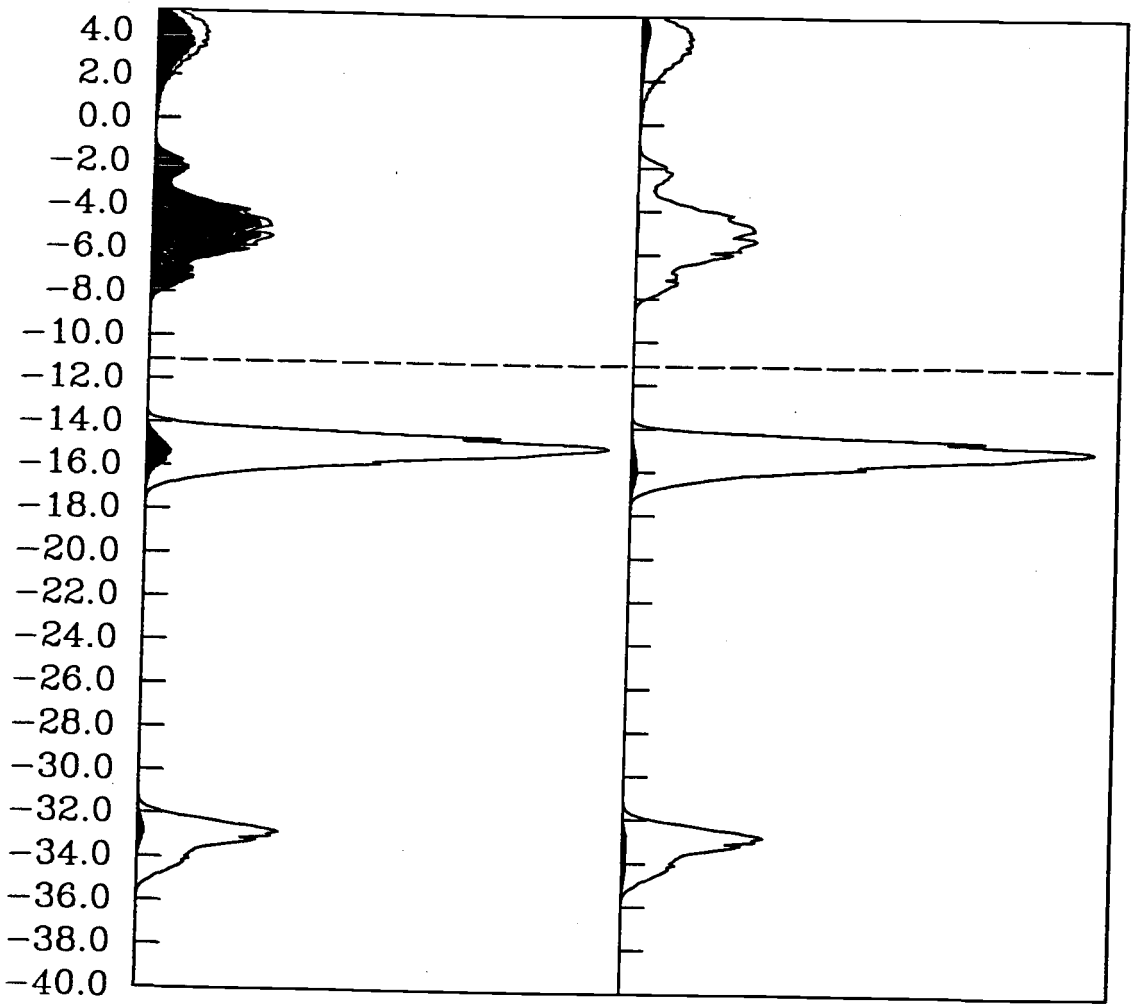

Figure 3.4 (Continued)

d)

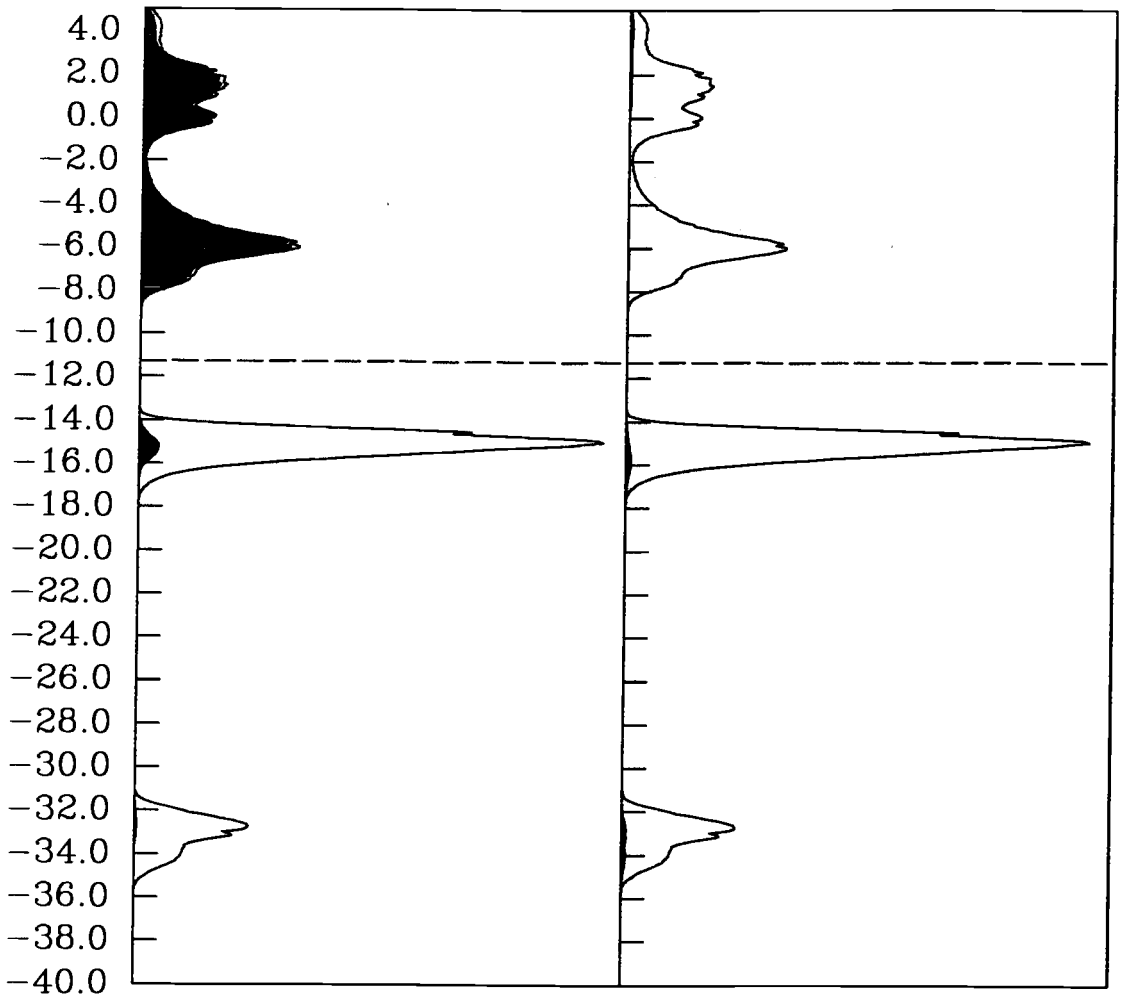

Figure 3.4 (Continued)

interactions will increase, and the $a^+b^-b^-$ tilt system will become increasingly stable. The A-O bonding interactions will also play a more prominent role as the distortion from the cubic structure increases, due to the increased overlap of oxygen orbitals with the A cation orbitals. For many of the basic cations found on the A site, the ionic arguments of Madelung energy and ion repulsion are probably the structure determining forces. One case in which the ionic arguments fail to predict the symmetry correctly is when A=Ca. When the A cation is Ca the orthorhombic $GdFeO_3$ structure is almost always formed even when the tolerance factor is greater than one, as is the case for $CaMnO_3$ (Poeppelmeier, Leonowicz, Scanlon, Longo & Yelon, 1982) and $CaGeO_3$ (Sasaki, Prewitt & Liebermann, 1983). In these compounds presumably the orthorhombic, cubic, and rhombohedral structures are all in competition. If ion core repulsion is the most important factor the cubic structure will be formed. If Madelung energy is the structure determining force the rhombohedral structure should be favored, and if A-O covalent bonding interactions outweigh Madelung energy and ion core repulsion, the orthorhombic ($a^+b^-b^-$) structure will be the most stable. The fact that $CaM^{4+}O_3$ compounds adopt the orthorhombic $GdFeO_3$ structure, rather than the rhombohedral or cubic structures, would seem to indicate that there is a significant amount of covalency in the Ca-O bonds. Goodenough has long supported this point of view based on the physical properties of perovskite compounds (Goodenough, 1971; Takano *et al.*, 1991).

3.4.3 Covalent M-O Bonding

No treatment of structure stabilizing forces in perovskites would be complete without considering covalent M-O interactions. With few exceptions, the M cation is more electronegative than the A cation. Consequently, the M-O interactions are expected to be stronger than the A-O interactions. The dominance of the M-O interactions is clearly demonstrated by the structural changes associated with octahedral tilting distortions. The coordination sphere about the A cation changes considerably, while the coordination sphere about the M cation remains, to a first approximation, unchanged. However, since the first coordination sphere about the M cation is the same in all tilt systems, one could argue that the M-O interactions have little influence in determining the lowest energy tilt system. Nonetheless, because of their strength they must be considered.

From the physical properties of perovskites it is well known that both M-O σ and M-O π bonding can play important roles (Goodenough, 1971). Because the M-O distances and

	Y-O Bond Distances (Å)	Y-O Bond Valences	Y-O Integrated COOP Values
Actual Struct.	2.2370	0.5474	0.2126
	2x2.2843	2x0.4817	2x0.1933
	2.3061	0.4541	0.1512
	2x2.4807	2x0.2833	2x0.1277
	2x2.5691	2x0.2230	2x0.0601
	3.0102	0.0677	0.0021
	3.1188	0.0505	0.000
	2x3.2604	2x0.0344	2x0.000
$a^+b^-b^-$ (#10)	2.1829	0.6335	0.2373
	2x2.2969	2x0.4655	2x0.1880
	2.3597	0.3929	0.1311
	2x2.4682	2x0.2930	2x0.1340
	2x2.5872	2x0.2124	2x0.0562
	3.0290	0.0644	0.0041
	3.0670	0.0581	0.000
	2x3.2513	2x0.0353	2x0.000
$a^+a^-a^-$ (#11)	2.1893	0.6226	0.2341
	2x2.2906	2x0.4735	2x0.1905
	2.3537	0.3993	0.1331
	2x2.4804	2x0.2835	2x0.1285
	2x2.5782	2x0.2176	2x0.0581
	3.0219	0.0656	0.0038
	3.0647	0.0584	0.000
	2x3.2574	2x0.0347	2x0.000
$a^-a^-a^-$ (#14)	3x2.1570	3x0.6794	3x0.3295
	6x2.7026	6x0.1555	6x0.0328
	3x3.0318	3x0.0639	3x0.000
$a^0b^-b^-$ (#20)	2.0825	0.8309	0.1909
	4x2.3354	4x0.4195	4x0.1867
	2x2.7680	2x0.1303	2x0.0351
	4x2.9241	4x0.0854	4x0.0060
	3.0928	0.0542	0.000
$a^0a^0c^+$ (#21)	4x2.2635	4x0.5095	4x0.1512
	4x2.5654	4x0.2253	4x0.0801
	4x3.0796	4x0.5061	4x0.000
$a^0a^0c^-$ (#22)	4x2.2635	4x0.5095	4x0.1559
	4x2.5654	4x0.2253	4x0.0688
	4x3.0796	4x0.5061	4x0.000
$a^0a^0a^0$ (#23)	12x2.7026	12x0.1555	12x0.0505

Table 3.6 : Y-O bond distances, bond valences, and integrated COOP values for $YAlO_3$ and idealized $YAlO_3$ structures used in the EHTB analysis of $YAlO_3$. The bond valences of the ions were matched as closely as possible to the values found in the actual structure of $YAlO_3$: 3.16, 2.97, 2.14, and 2.00 for Y, Al, O1, and O2 respectively.

octahedral coordination sphere are essentially the same in all 23 tilt systems, the major difference between structures will be the M-O-M angles (Marezio, Remeika & Dernier, 1970). As these angles distort from 180° the orbital overlaps that determine the strength of both the σ and π interactions will decrease. In order to investigate the sensitivity of each of these two bonding interactions to changes in the M-O-M angles, extended Hückel calculations were performed on ideal MoO_3^{2-} and SnO_3^{2-} lattices. These two compounds were chosen because both Mo and Sn are tetravalent, belong to the same period of the periodic table, and have similar ionic radii. The major difference between the two metal ions is the presence of partially filled d-orbitals on the Mo^{4+}, which allow the formation of π and π^* bands in MoO_3^{2-}. Therefore, the MoO_3^{2-} energy will be sensitive to changes in both σ and π bonding overlaps, while the SnO_3^{2-} energy will only depend upon the σ orbital overlap. Figure 3.5 shows the results of these calculations. The electronic energy, as calculated by the extended Hückel method, is plotted against the magnitude of the rotation angles. Tilt system $a^+b^-b^-$, with perfect octahedra, was used for the analysis. The Mo-O and Sn-O distances were calculated from the standard ionic radii (Shannon, 1976). The energy of the MoO_3^{2-} lattice drops off twice as fast as the energy of the SnO_3^{2-} lattice. This suggests that both the σ and π covalent M-O interactions decrease at approximately the same rate, as the M-O-M angle decreases.

When considering the effect of M-O bonding in determining the lowest energy tilt system, it is useful to consider AMO_3 compounds where M is a p-block element separately from those compounds where M is a transition metal. When M is a p-block element, π bonding does not contribute to the stability of the structure because the (n-1)d orbitals are completely filled, and the nd orbitals are too high in energy to overlap significantly with the oxygen 2p orbitals. Even in the absence of π bonding, the analysis up to this point still suggests that the cubic structure maximizes orbital overlap, and hence M-O covalent bonding. However, as seen in figure 3.5 the energy destabilization due to decreased M-O σ bond overlap is relatively small for moderate tilt angles. This term may be overcome by gains in either ionic energy, or the A-O covalency, both of which stabilize the distorted structures with respect to the cubic structure. Examining tables 2 and 3 the only cubic perovskites that contain a p-block element as the M cation are $SrGeO_3$ (Shimizu, Syono & Akimoto, 1970) and $BaSnO_3$ (Smith & Welch, 1960). Both of these compounds have tolerance factors (1.049 and 1.026 respectively) in the range where ion-ion repulsion strongly favors the cubic structure. $CaGeO_3$ (Sasaki, Prewitt & Liebermann, 1983) and $LaAlO_3$ (Derighietti, et al., 1965; deRango, Tsoucarus & Zelwer, 1966) both have tolerance factors greater than unity, but both are distorted from cubic. Based on the behavior of these compounds it would appear

as though M-O σ bonding, in the absence of M-O π bonding, does not play a major role in determining the lowest energy tilt system.

Simple geometry and the EHTB calculations on the SnO_3^{2-} lattice show that a 180° M-O-M bond angle leads to the maximum overlap between σ orbitals on the octahedral cation and oxygen. However, the behavior of real compounds suggests that the cubic structure may not always lead to the maximum M-O σ bonding. Two examples which illustrate this point are WO_3 and $NaSbO_3$. The WO_3 structure has the same MO_3 corner sharing octahedral framework as the perovskite structure, but in WO_3 the A cations are absent. From the simple overlap analysis given thus far one would expect WO_3 to have a cubic structure. In fact, even though WO_3 undergoes at least five phase transitions between 0 and 950 K, an octahedral tilting distortion is always present, along with a displacement of the tungstens from the center of the octahedra (Salje, 1977; Diehl, Brandt & Salje, 1978; Woodward, Sleight & Vogt, 1995). In this compound no A-O interactions are present, therefore, M-O bonding forces must be responsible for the observed distortions from cubic symmetry. $NaSbO_3$ adopts the ilmenite structure with 90° M-O-M bond angles rather than the perovskite structure, even though the tolerance factor (t=0.994) is nearly ideal for the perovskite structure, and the Madelung energy of the perovskite structure is more favorable. Since the Na-O bond is expected to be almost completely ionic, the ilmenite structure can only be stabilized by Sb-O covalency. Goodenough and Kafalas explain the behavior of this compound by pointing out that in a 180° Sb-O-Sb bond, only one oxygen p_σ orbital is present and it must simultaneously bond to both neighboring antimony ions. On the other hand, if the Sb-O-Sb bond angle is 90° then two of the p-orbitals on oxygen can participate in σ bonding, each one to a separate antimony ion. For this reason the 90° Sb-O-Sb bond angle is expected to optimize the Sb-O covalent interaction (Goodenough & Kafalas, 1972).

Figure 3.5 shows that the energy stabilization of the cubic structure, due to M-O covalency, is enhanced considerably when M-O π bonding can take place. Experimental evidence also suggests that M-O π bonding can play an important role in stabilizing 180° bond angles. For example, both $NaNbO_3$ and $NaTaO_3$ crystallize in the orthorhombically distorted perovskite structure. This is in contrast to $NaSbO_3$, despite the fact that Nb^{5+} and Ta^{5+} have the same oxidation state and are almost the same size as Sb^{5+}. The structural change is thought to be driven by the overlap of the 4d/5d metal t_{2g} orbitals with the oxygen p_π orbitals (Goodenough & Kafalas, 1972; Blasse, 1965). This overlap presumably drives the M-O-M angles much closer to the 180° value that maximizes π bonding overlap. The importance of π bonding as a structure determining force can also be seen if the tungsten ions in WO_3 are replaced with rhenium ions, to give ReO_3. The extra electron on rhenium

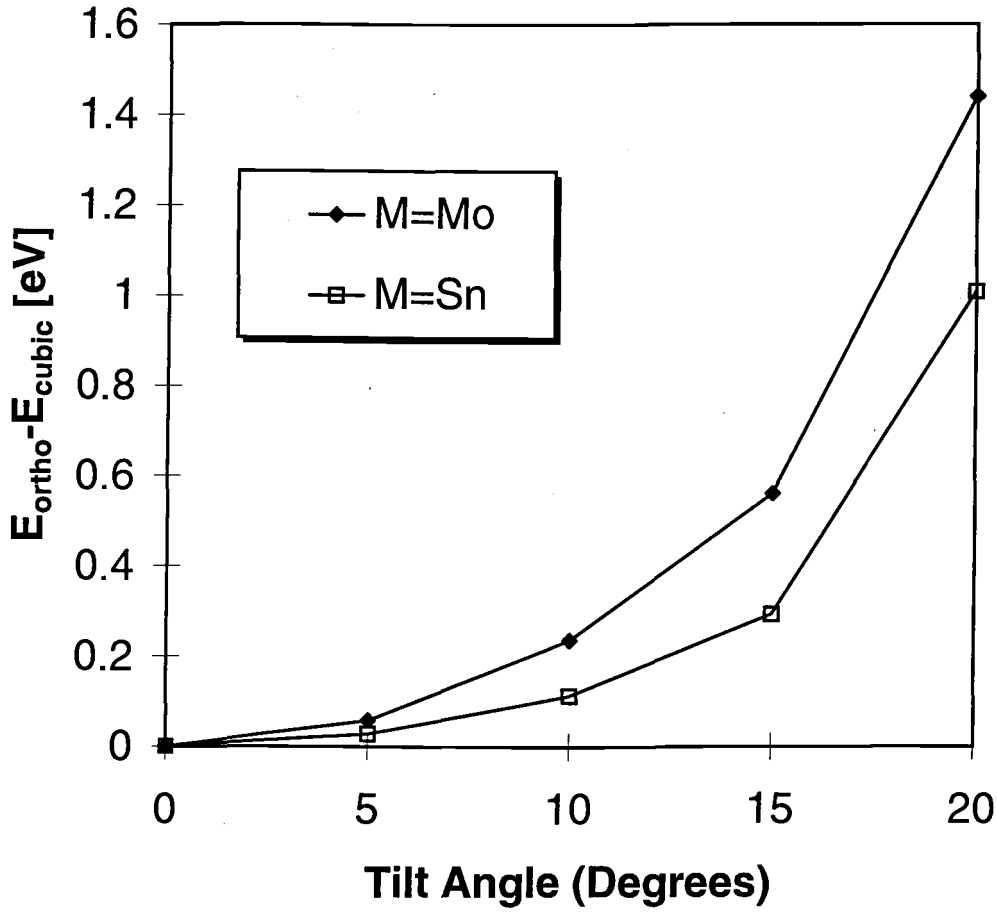

Figure 3.5 : The energy difference as calculated by the EHTB method between the cubic $a^0a^0a^0$ tilt system and the orthorhombic $a^+b^-b^-$ tilt system. The open squares represent calculations done on a SnO_3^{2-} lattice, where only M-O σ interactions are possible, and the filled diamonds represent calculations done on a MoO_3^{2-} lattice where both σ and π interactions can contribute to the bonding.

partially fills the antibonding π^* conduction band, and leads to metallic conduction. At the same time the cubic structure is stabilized (Ferretti, Rogers & Goodenough, 1965; Morin, 1961). The same result can be obtained by introducing sodium ions, which donate their electrons to the π^* band, onto the vacant A cation site. Na_xWO_3 is known to be metallic and cubic for $0.32 \leq x \leq 0.93$ (Hägg, 1935). The fact that ReO_3 is cubic while WO_3, $NaNbO_3$, and $NaTaO_3$ all display octahedral tilting distortions suggests that not only the presence but the filling of the π and π^* bands will play a role in determining the structure.

Table 3.7 shows all of the well characterized AMO_3 perovskites where M is a transition metal ion and the tolerance factor is larger than 0.98. In those compounds with tolerance factors less than 0.98 the increase in ionic energy associated with the orthorhombic distortion ($a^+b^-b^-$) seems to outweigh any M-O π bonding stabilization of the cubic structure. The majority of known cubic AMO_3 perovskites are found in table 3.7. The cubic structure is even found in some compounds, such as $SrMoO_3$, where the tolerance factor is less than one. This relatively high rate of occurrence of the cubic structure can undoubtedly be at least partially attributed to the stabilizing influence of M-O π bonding.

Compound	Tilt System	Tolerance Factor	# of e^- in t_{2g} Orb.	Total # of d e^-	d Orbital Radii*
$BaMoO_3$	$a^0a^0a^0$	1.047	2	2	0.49
$BaNbO_3$	$a^0a^0a^0$	1.031	1	1	0.51
$SrVO_3$	$a^0a^0a^0$	1.022	1	1	0.26
$SrFeO_3$	$a^0a^0a^0$	1.020	3	4	0.22
$BaZrO_3$	$a^0a^0a^0$	1.011	0	0	0.54
$SrTiO_3$	$a^0a^0a^0$	1.009	0	0	0.28
$SrRuO_3$	$a^+b^-b^-$	1.001	4	4	0.45
$SrMoO_3$	$a^0a^0a^0$	0.986	2	2	0.49
$CaMnO_3$	$a^+b^-b^-$	1.012	3	3	0.23
$CaVO_3$	$a^+b^-b^-$	0.986	1	1	0.26
$CaTiO_3$	$a^+b^-b^-$	0.973	0	0	0.28
$LaCuO_3$	$a^-a^-a^-$	1.013	6	8	0.185
$LaCoO_3$	$a^-a^-a^-$	1.011	6**	6	0.21
$LaNiO_3$	$a^-a^-a^-$	1.003	6	7	0.195
$PrCoO_3$	$a^-a^-a^-$	0.989	6	6	0.21
$PrNiO_3$	$a^+b^-b^-$	0.981	6	7	0.195

Table 3.7 : Structurally well characterized AMO_3 perovskites, where M is a transition metal and the tolerance factor is greater than 0.98. * The radii of the d orbitals are theoretical pseudopotential radii and are in atomic units (Zunger, 1980). ** In $LaCoO_3$ the Co^{3+} is intermediate between high and low spin and the number of t_{2g} electrons is not well defined.

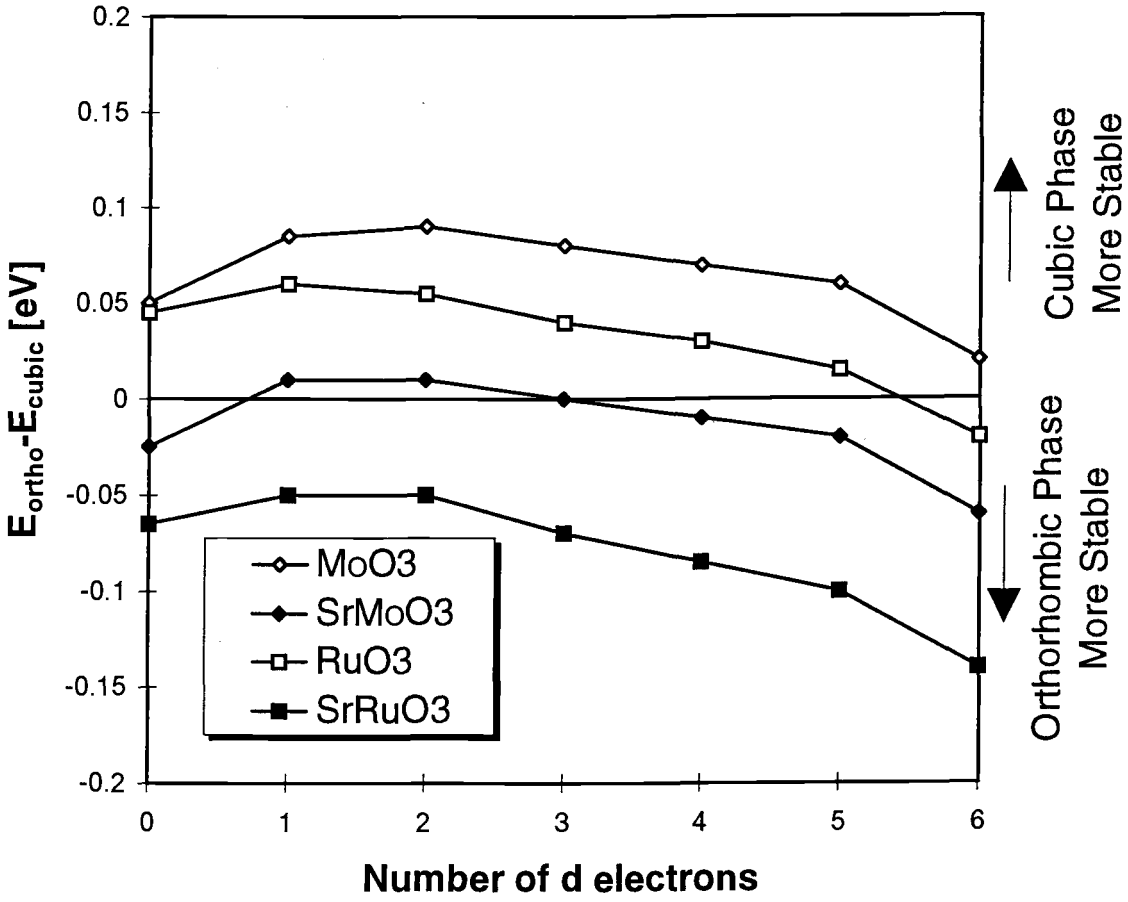

Figure 3.6 : The energy difference as calculated by the EHTB method between the cubic ($a^0a^0a^0$ tilt system) and the orthorhombic ($a^+b^-b^-$ tilt system) structures for $SrMO_3$ compounds. The open diamonds represent calculations on a MoO_3^{2-} lattice, the filled diamonds a $SrMoO_3$ lattice, the open squares a RuO_3^{2-} lattice, and the filled squares a $SrRuO_3$ lattice.

Even the simplest model would not predict that π bonding stabilization of the cubic structure will be the same for all transition metal perovskites. The energy, spatial extent, and filling of the d-orbitals on the octahedral ion all play a role in determining the M-O π bonding strength. Furthermore, the σ bonding orbitals on the A cation and the π bonding orbitals on the M cation are in direct competition for the same orbitals on oxygen (Goodenough, 1971; Choy, Park, Hong & Kim, 1994; Takano *et al.*, 1991). Include the changes in ionic lattice energy that accompany octahedral tilting distortions and a theoretical determination of the lowest energy structure becomes quite complicated. Nevertheless, the fact that all of these forces are in competition to determine the structure, also provides an excellent opportunity to compare their relative strengths. However, before such a comparison can be made the factors influencing M-O π bonding must be better understood.

Extended Hückel calculations were performed on an $a^0a^0a^0$ cubic $SrMO_3$ structure and an $a^+b^-b^-$ $SrMO_3$ structure. The M-O bond distance was 1.98Å in both structures and the tilt angles in the orthorhombic system were -5.9°, 6.1°, 6.1°. The calculations were carried out for both structures using the EHTB parameters of Mo for the M site cation and repeated using the EHTB parameters of Ru. The calculations were performed with Sr on the A site, and repeated for a MO_3^{2-} lattice. In each calculation the number of valence electrons was varied to simulate the presence of 0 to 6 electrons in the 4d orbitals of the M cation. The structures and atomic parameters used in these calculations were chosen to most closely approximate the actual structures of $SrMoO_3$ and $SrRuO_3$. These two compounds were chosen for analysis because even though $SrMoO_3$ has a smaller tolerance factor than $SrRuO_3$, the former compound is cubic while the latter is orthorhombic. Therefore, the energetic changes associated with M-O π bonding across the 4d series appear to be the structure determining forces in these compounds.

Figure 3.6 shows graphically the results of these calculations. It is encouraging that the calculations predict $SrMoO_3$ will be cubic, and $SrRuO_3$ will be orthorhombic. However, the trends apparent in figure 3.6 are more important than the absolute energy differences between structures, which are quite small. Three generalizations can be drawn from these calculations. First of all, the M-O π bonding stabilization of the cubic structure is largest for d^1 and d^2 octahedral cations, and decreases as the π^* band becomes increasingly populated. Secondly, the presence of Sr stabilizes the orthorhombic structure with respect to the cubic structure, even though Sr-O oxygen bonds show only a small degree of covalency. Finally, substitution of the more electronegative Ru, for Mo, stabilizes the orthorhombic structure, particularly in the presence of Sr or when the π^* band is nearly full.

The results in figure 3.6 can be understood in the following way. The immediate environment about the M cations, which is primarily responsible for determining the π and π^* energy levels, is the same for both the cubic and orthorhombic structures. On the other hand, the orbital overlap across M-O-M linkages, which allows electron delocalization, is better in the cubic structure. The former interaction, to a first approximation, dictates the position of the center of the π^* band, whereas the latter interaction determines the width of the π^* band. This leads to an orthorhombic π^* band which is more narrow than the cubic π^* band, but centered at approximately the same energy. Figure 3.7 depicts an exaggerated density of states band picture that corresponds this situation. As the π^* band begins to fill the total energy of the cubic structure will be lower than the orthorhombic structure. This is because the bottom of the cubic π^* band is at a lower energies than the bottom of the orthorhombic π^* band. If the two bands are centered at exactly the same energy, the maximum stabilization of the cubic structure will occur when the π^* band is half filled, corresponding to a d^3 octahedral cation. As the π^* band continues to fill the energy stabilization of the cubic structure will begin to decrease, until the band is completely filled, and the two structures once again have the same energy. If the center of the narrow band is at a slightly lower energy than the center of the broad band, the maximum stabilization will be shifted from a half filled band to a somewhat lesser degree of filling and the total energy of the completely filled narrow band will be lower than the total energy of the completely filled broad band. Both of these trends are observed in figure 3.6, indicating that the energy center of the orthorhombic π^* band has a slightly lower energy than the energy center of the cubic π^* band. The band centers are not at exactly the same energy because the oxygen cannot form perfect overlaps with both metal cations in the orthorhombic structure. This reduces the antibonding character of the π^* band (increases its nonbonding character), thus lowering its energy somewhat.

The effect of substituting ruthenium for molybdenum can also be explained in a straightforward manner. It is directly related to the fact that ruthenium is more electronegative than molybdenum, and the Ru 4d orbitals will therefore be lower in energy than the Mo 4d orbitals. To understand the effect of this change, consider the interaction between a metal orbital and a lower energy oxygen orbital to form a bonding orbital and an antibonding orbital, as depicted in figure 3.8. If the metal orbital is lowered in energy, by the amount ΔE_m, then the energy overlap of the two levels is improved. This results in a small increase in the stabilization of the bonding orbital and a destabilization of the antibonding orbital. If the interaction is somehow changed so that no bonding interaction occurs and only two nonbonding levels exist the only change will be a lowering of the upper level.

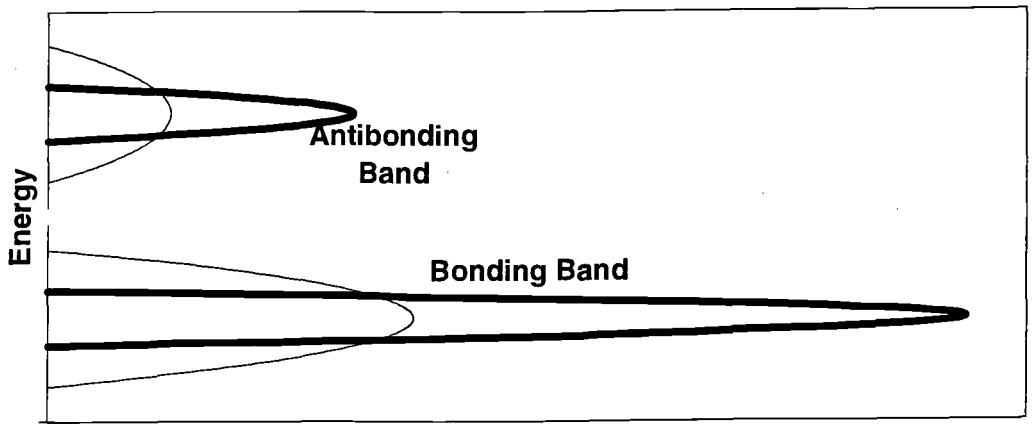

Figure 3.7 : An exaggerated representation of the density of electronic states associated with the π (bonding) and π^* (antibonding) bands in a perovskite. The thick line represents a poor M-O-M overlap which results in narrow bands. The fine line represents a good M-O-M overlap and broader bands.

Therefore, the energy difference between the antibonding and nonbonding levels, ΔE_1 and ΔE_2, will increase as the energy separation between the metal and oxygen energy levels decreases, due to the increased destabilization of the antibonding orbital. In other words, the relationship $\Delta E_1 < \Delta E_2$ will always hold. This analysis can be applied to the perovskite structure in the following way. Because, the spatial overlap of orbitals is reduced in the orthorhombic structure the π^* band has a larger metal t_{2g} nonbonding component than the same band in the cubic structure. Therefore, lowering the energy of the 4d orbitals in $SrRuO_3$ causes the center of the π^* band in the cubic structure to shift upward, relative to the center of the same band in the orthorhombic structure. This will result in a stabilization of the orthorhombic structure, relative to the cubic structure, especially as the π^* band becomes increasingly populated.

The prediction that the presence of Sr stabilizes the orthorhombic structure is consistent with the earlier analysis of covalent A-O interactions, which showed that covalent A-O bonding was optimized in the orthorhombic $a^+b^-b^-$ tilt system. However, these calculations contain two additional points of interest. First of all, in the case of $SrRuO_3$ the calculations only predict the orthorhombic structure to be more stable when Sr is included in the calculation. Secondly, the electronegativity of strontium is much smaller than that of yttrium, and Sr-O bonds have only a small degree of covalency. Yet the calculations suggest that even this weak covalent interaction is sufficient to stabilize the distorted structure over the cubic structure. Since the A cation σ bonding orbitals and M cation π bonding orbitals both overlap with the same orbitals on oxygen, the formation of covalent A-O bonds, will reduce the electron density in the M-O π and π^* bonds. Presumably, this will come primarily from the higher energy π^* band. In this way formation of A-O bonds may actually strengthen the M-O bonds. This effect should be most evident in the orthorhombic $a^+b^-b^-$ structure, which has already been shown to maximize the A-O covalent interactions. This might explain why the orthorhombic structure is favored over the rhombohedral structure. Of course the Madelung energy contribution also favors the orthorhombic and rhombohedral structures over the cubic structure. Another possibility, if the ionic contribution to the total energy is dominant, is that the Sr-O repulsion is large enough (the tolerance factor is greater than 1, yet the structure is distorted) to destabilize the rhombohedral structure with respect to the orthorhombic structure.

Equipped with a better understanding of M-O bonding interactions we are now prepared to analyze table 3.7. The compounds in table 3.7 can be grouped into three categories. The first eight compounds all have either Ba or Sr on the A site and one of the early 3d or 4d

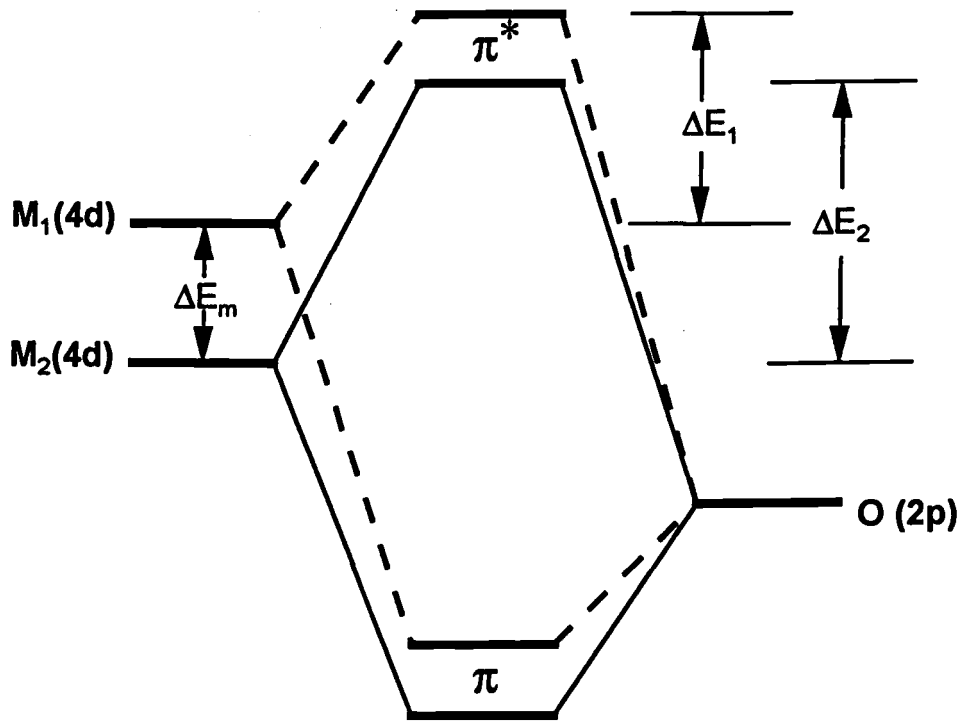

Figure 3.8 : A schematic representation of the effect that lowering the energy of the metal orbital, in a M(4d)-O(2p) interaction, has on the bonding and antibonding levels. The energy ΔE_1 is the difference in energy between the antibonding level and the nonbonding level before lowering the energy of the metal 4d orbital. The energy ΔE_2 is the same energy difference after lowering the energy of the metal 4d orbital, by ΔE_m.

transition metals on the M site. These compounds have all of the attributes which stabilize the cubic structure. The A cations here are quite basic, so that A-O covalency is expected to be small. The early transition metals have t_{2g} orbitals with a fairly large spatial extent, for good overlap with oxygen 2p orbitals. This is more true of the 4d transition metals than the 3d transition metals. Furthermore, all of these ions have t_{2g} orbitals that are less than half full. The exception is $SrRuO_3$, which is also the only compound of the eight that is not cubic. The forces that cause $SrRuO_3$ to be orthorhombic have been discussed in detail above. Because of its intermediate position between $SrMoO_3$ and $SrRuO_3$ it would be very interesting if $SrTcO_3$ could be synthesized and structurally characterized. The next two compounds have Ca on the A site and a 3d transition metal on the M site. Both of these compounds are orthorhombic, even though their tolerance factors are in the same range where cubic compounds were observed among the first eight compounds. There are two possible reasons for this change in structure. First of all calcium is more electronegative than either barium or strontium, resulting in increased covalency in the A-O bonds, and stabilizing the orthorhombic structure. Secondly, because of decreased spatial and energetic overlap between oxygen 2p and metal 3d orbitals the π bonding stabilization of the cubic structure will be smaller when M is a 3d transition metal, than when it is a 4d transition metal. However, when A=Ca and M is a 4d transition metal the tolerance factor is always smaller than 0.97, so it is unknown whether π bonding could be increased to the point where it stabilized the cubic structure, despite the presence of calcium on the A site. The last five compounds all have one of the larger lanthanide ions on the A site and one of the later elements from the 3d transition series on the M site. Once again this is the only combination, of lanthanides with transition metals, that leads to a tolerance factor larger than 0.98. The attributes of this group of compounds are well suited to the rhombohedral structure. All of the transition metals have filled t_{2g} shells so that π bonding stabilization of the cubic structure is negated. Furthermore, the trivalent cation on the A site maximizes the ionic interaction between the A site ion and oxygen. This interaction is optimized in the rhombohedral structure. Finally, the tolerance factor values fall into a range where repulsive forces between the A site ion and oxygen are not large enough to destabilize the rhombohedral structure. Not surprisingly all of these compounds adopt the rhombohedral structure.

3.5 Non-Equivalent A Site Tilt Systems

The tilt systems already discussed account for the majority of the known distorted perovskites. However, when the two A site cations become very different, such as an alkaline earth and a transition metal, the tilt systems with nonequivalent A sites become important. Tilt systems 17,18 (0+-) and 4-7 (++-) are similar in that half of the A cation sites become suitable for small cations, while the other half remain suitable for large A cations. The large cation site is described in table 3.1 as face centered trigonal prismatic. This description is meant to describe the coordination that would result if the A cation was moved from the center of a trigonal prism toward one of the rectangular faces. As with the eight coordinate site in the $a^+b^-b^-$ system, the distribution of bond distances is probably more important than the exact coordination geometry. The small A cation sites in these systems are distorted tetrahedral sites in tilt systems 17 and 18, and a 50:50 mixture of distorted tetrahedral and square planar sites in tilt systems 4-7. Excluding high temperature phases, the only compound known to adopt one of these six tilt systems is $CaFeTi_2O_6$ (Leinenweber & Parise, 1995). This compound has the expected distribution of cations with Ca^{2+} occupying the large A cation sites and Fe^{2+} occupying the smaller tetrahedral and square planar sites. Tilt systems 15,16 (0++) have a different distribution of A cation sites. In $a^0b^+b^+$ one half of the A sites are very similar to the A site coordination found in $a^0a^0c^+$, one quarter of the A sites are in a highly symmetrical eight coordinate cubic coordination, and the remaining A sites are square planar with a considerably smaller coordination sphere. Thus 75% of the A cation sites can accommodate large A cations and the other 25% are only suitable for smaller A cations.

The $a^+a^+a^+$ tilt system is interesting in part because even though it can be highly distorted from the ideal perovskite structure it is cubic ($Im\overline{3}$). In this structure, 25% of the A cation sites are coordinated by 12 equidistant anions in a geometry only slightly displaced from the cubo-octahedral geometry found in the undistorted perovskite structure. The remaining A cation sites have a considerably smaller first coordination sphere that is perfectly square planar. The $a^+b^+c^+$ (#1) and $a^+b^+b^+$ (#2) tilt systems have similar A cation site distributions. Of these five tilt systems (#1, #2, #3, #15 and #16) actual compounds are only observed for tilt system #3, $a^+a^+a^+$ (see table 3.2). Many of the compounds found in this space group including $CaFe_3Ti_4O_{12}$ (Leinenweber & Parise, 1995), $CaCu_3Ge_4O_{12}$ (Ozaki, Ghedira, Chenevas, Joubert & Marezio, 1977), $CaCu_3Mn_4O_{12}$ (Chenevas, Joubert, Marezio & Bochu, 1975), and $NaMn_3Mn_4O_{12}$ (Marezio, Dernier, Chenevas & Joubert, 1973) were synthesized under high pressure where ¾ of the A cations are smaller transition metals (Fe and Mn) and

¼ of the A cations are larger alkali, alkaline earth, or rare earth metals. In this structure the transition metals occupy the square planar site, while the larger cations occupy the 12 coordinate site. Some of the compounds belonging to this tilt system were synthesized in air at ambient pressures, such as the ruthenates (Labeau, Bochu, Joubert, & Chenevas, 1980) and titanates (Bochu *et al.*, 1979) in table 3.2. All of these compounds have the Jahn-Teller ion Cu^{2+} on the square planar A cation sites. The Cu^{2+} ion occupies the square planar sites in preference to the octahedral sites, thus lifting the degeneracy of the copper based e_g orbitals. The list of $a^+a^+a^+$ compounds in table 3.2 is not exhaustive, but not surprisingly all compounds omitted from table 3.2 have a Jahn-Teller transition metal cation, such as Cu^{2+} or Mn^{3+}, on ¾ of the A cation sites. In general this tilt system should be quite stable whenever ¾ of the A cation sites are filled with cations that prefer square planar coordination, and the other ¼ of the A cation sites are filled by larger cations compatible with a cubo-octahedral coordination.

The information contained in tables 1 and 2 for tilt systems with non-equivalent A sites suggests that it is possible that many more of these compounds could be synthesized with the proper choice and ratio of ions. It seems reasonable to assume that the tilt system achieved will be directly dependent upon the ratio of large, A_L, to small cations, A_S, on the A site. When the A_L/A_S ratio is 3:1 tilt systems 15 and 16 (0++) should be favored, when the A_L/A_S ratio is 1:1 tilt systems 17 and 18 (0+-) or 4-7 (++-) should be favored, and when A_L/A_S is 1:3 tilt systems 1-3 (+++) should be favored. Of course, in order to get the small cations onto the A site high pressure synthesis may be necessary. In such a synthetic search POTATO could prove useful for predicting which combination of ions will have the proper size match to form a stable compounds.

3.6 Conclusions

The various tilt systems have been compared in terms of their A cation coordination and it has been shown that the tilt systems where all of the A cation sites remain crystallographically equivalent are strongly favored when there is a single ion on the A site. Of these tilt systems the orthorhombic $a^+b^-b^-$ tilt system has been shown to maximize A-O covalent bonding, and minimize repulsive A-O overlap. For these reasons the orthorhombic $GdFeO_3$ structure is found almost exclusively when the tolerance factor becomes smaller than 0.975, or when the A site cation becomes relatively electronegative, as is the case when A=Ca. Madelung energy calculations show the undistorted cubic $a^0a^0a^0$ tilt to be

unstable with respect to distorted tilt systems. This structure is stabilized only by ion-ion repulsion in the case of oversized A cations, and M-O π bonding interactions when M is an early transition metal cation. The rhombohedral $a^-a^-a^-$ tilt system is most commonly observed in those cases where the tolerance factor is in the range 0.975 to 1.02 and the ionic charge of the A site cation is large. These factors favor the rhombohedral structure because they maximize the A-O ionic interaction and keep the ion-ion repulsion from becoming too large. Tilt systems with nonequivalent A site environments will be favored in compounds where at least two A cations with different sizes and/or bonding preferences are present. The ratio of large to small cations will dictate the most stable tilt system.

3.7 References

Abrahams, S.C. & Bernstein, J.L. (1967). *J. Phys. Chem. Solids* **28**, 1685.

Ahtee, A., Ahtee, M., Glazer, A.M. & Hewat, A.W. (1976). *Acta Cryst.* B**32**, 3243.

Ahtee, M. & Darlington, C.N.W. (1980). *Acta Cryst.* B**36**, 1007.

Ahtee, M., Glazer, A.M. & Hewat, A.W. (1978). *Acta Cryst.* B**34**, 752.

Ahtee, M., Glazer, A.M. & Megaw, H. (1972). *Phil. Mag.* **26**, 995.

Aleksandrov, K.S. (1976). *Kristallografiya* **21**, 249.

Alter, E. (1974). *Z. Anorg. Allg. Chem.* **408**, 115.

Bartram, S.F. & Fryxell, R.E. (1970). *J. Inorg. Nucl. Chem.* **32**, 3701.

Battle, P.D., Gibb, T.C. & Lightfoot, P. (1990). *J. Solid State Chem.* **84**, 271.

Benner, G. & Hoppe, R. (1990). *J. Fluorine Chem.* **46** 283.

Bensch, W., Schmalle, H.W. & Reller, A. (1990). *Solid State Ionics* **43**, 171.

Bidaux, R. & Mériel, P. (1968). *J. Phys. Radium* **29**, 220.

Blasse, G. (1965). *J. Inorg. Nucl. Chem.* **27**, 993.

Bochu, B., Deschizeaux, N.N., Joubert, J.C., Collomb, A., Chenevas, J. & Marezio, M. (1979). *J.Solid State Chem.* **29**, 291.

Bouloux, J.-C. & Galy, J. (1976). *J. Solid State Chem.* **16**, 385.

Brese, N.E. & O'Keeffe, M. (1991). *Acta Cryst.* B**47**, 192.

Brixner, L.H. (1960). *J. Inorg. Nucl. Chem.* **14**, 225.

Brochu, R., Padiou, J. & Grandjean, D. (1970). *C.R. Acad. Sci. Ser.* C **271**, 642.

Brown, I.D. (1981). *Structure and Bonding in Crystals,* Vol. 2, edited by M. O'Keeffe & A. Navrotsky, pp. 1-30. New York: Academic Press.

Brynestad, J., Yakel, H.L. & Smith, G.P. (1966). *J. Chem. Phys.* **45**, 4652.

Burbank, R.D. (1970). *J. Appl. Cryst.* **3**, 112.

Burdett, J.K. (1980). *Molecular Shapes*, Chapter 2. New York: John Wiley & Sons.

Burdett, J.K. & Mitchell, J.F. (1993). *Chem. Mater.* **5**, 1465.

Bush, T.S. Catlow, C.R.A., Chadwick, A.V., Cole, M. Geatches, R.M., Greaves, G.N. Tomlinson, S.M. (1992). *J. Mater. Chem.* **2**, 309.

Bush, T.S., Gale, J.D., Catlow, R.A. & Battle, P.D. (1994). *J. Mater. Chem.* **4**, 831.

Buttner, R.H. & Maslen, E.N. (1988). *Acta Cryst.* C**44**, 1707.

Chenevas, J., Joubert, J.C., Marezio, M. & Bochu, B. (1975). *J. Solid State Chem.* **14**, 25.

Choy, J.-H., Park, J.H., Hong, S.-T. & Kim, D.K. (1994). *J. Solid State Chem.* **111**, 370.

Christoph, C.G., Larson, A.C., Eller, P.G., Purson, J.D., Zahrt, J.D., Penneman, R.A. & Rinehart, G.H. (1988). *Acta Cryst.* B**44**, 575.

Clearfield, A. (1963). *Acta Cryst.* **16**, 135.

Collomb, A., Samaras, D., Buevoz, J.L., Levy, J.P. & Joubert, J.C. (1983). *J. Magn. Magn. Mater.* **40**, 75.

Dann, S.E., Currie, D.B., Weller, M.T., Thomas, M.F. & Al Rawwas, A.D. (1994). *J. Solid State Chem.* **109**, 134.

Darlington, C.N.W. (1971). Thesis, Univ. of Cambridge.

Deblieck, R., Van Tendeloo, G., Van Landyt, J. & Amelinckx, S. (1985). *Acta Cryst.* B**41**, 319.

Demazeau, G., Parent, C., Pouchard, M. & Hagenmueller, P. (1972). *Mater. Res. Bull.* **7**, 913.

deRango, C., Tsoucaris, G. & Zelwer, C. (1966). *Acta Cryst.* **20**, 590.

Derighetti, B., Drumheller, J.E., Laves, F., Müller, K.A. & Waldner, F. (1965). *Acta Cryst.* **18**, 557.

Deschizeaux, M.N., Joubert, J.C., Vegas, A., Collomb, A., Chenevas, J. & Marezio, M. (1976). *J. Solid State Chem.* **19**, 45.

Dickens, P.G. & Powell, A.V. (1991). *J. Mater. Chem.* **1**, 137.

Diehl, R. & Brandt, G. (1975). *Mater. Res. Bull.* **10**, 85.

Diehl, R., Brandt, G. & Salje, E. (1978). *Acta Cryst.* B**34**, 1105.

Elemans, J.B.A., van Laar, B, van der Veen, K.R. & Loopstra, B.O. (1971). *J. Solid State Chem.* **3**, 238.

Ferretti, A., Rogers, D.B. & Goodenough, J.B. (1965). *J. Phys. Chem. Solids* **26**, 2007.

Fesenko, E.G., Razumovskaya, O.N., Shuvaeva, V.A., Gridneva, G.G. & Bunina, O.A. (1991). *Isv. Akad. Nauk SSSR, Neorg. Mater.* **27**, 1991.

Flocken, J.W., Guenther, R.A., Hardy, J.R. & Boyer, L.L. (1986). *Phys. Rev. Lett.* **56**, 1738.

Flocken, J.W., Guenther, R.A., Hardy, J.R. & Boyer, L.L. (1986). *Phys. Rev. B Cond. Matter* **56**, 1738.

Forquet, J.E., Renou, M.F., De Pape, R., Theveneau, H., Man, P.P., Lucas, O. & Pannetier, J. (1983). *Solid State Ionics* **9**, 1011.

Galasso, F.S. (1969). *Structure, Properties, and Preparation of Perovskite Type Compounds* Oxford: Pergammon Press.

Gale, J.D. (1992-1994). GULP. General Utility Lattice Program. Royal Institution and Imperial College, London.

Geller, S. & Wood, E.A. (1956). *Acta Cryst.* **9**, 563.

Glazer, A.M. & Megaw, H. (1972). *Phil. Mag.* **25**, 1119.

Glazer, A.M. (1972). *Acta Cryst.* B**28**, 3384.

Goldschmidt, V.M. (1926). *Naturwissenschaften* **14**, 477.

Goodenough, J.B. (1963). *"Magnetism and the Chemical Bond,"* New York, Interscience and Wiley.

Goodenough, J.B. (1967). *Phys. Rev.* **164**, 785.

Goodenough, J.B. (1971) *Prog. Solid State Chem.* **5**, 145.

Goodenough, J.B. & Kafalas, J.A. (1972). *J. Solid State Chem.* **6**, 493.

Greedan, J.E., Willmer, K.L. & Gibbs, H.F. (1992). *Eur. J. Solid State Chem.* **29**, 505.

Hägg, G. (1935). *Z. Phys. Chem.* B**29**, 192.

Hemley, R.J., Cohen, R.E., Yeganeh-Haeri, A., Mao, H.K., Weidner, D.J. & Ito, E. (1989). *Geophysical Monographs, Vol. 45 (Perovskite - A Structure of Great Interest to Geophysics and Materials Science)*, edited by A. Navrotsky & D. Weidner, pp. 35-44. Washington D.C.:American Geophysical Union.

Hepworth, M.A., Jack, K.H., Peacock, R.D. & Westland, G.J. (1957). *Acta Cryst.* **10**, 63.

Hoffmann, R. (1963). *J. Chem. Phys.* **39**, 1397.

Hoffmannn, R. (1988). *Solids and Surfaces: A Chemist's View of Bonding in Extended Structures.* New York: VCH Publishers.

Hohnstedt, C. & Meyer, G. (1993). *A. Anorg. Allg. Chem.* **619**, 1374.

Hönle, W., Miller, G. & Simon, A. (1988). *J. Solid State Chem.* **75**, 147.

Hönle, W. & Simon, A. (1986). *Z. Naturf. B. Anorg. Chem. Organ. Chem.* **41**, 1391.

Horowitz, A., Amit, M., Makovsky, J., Ben Dor, L. & Kalman, Z.H. (1982). *J. Solid State Chem.* **43**, 107.

Huang, T.C. Parrish, W., Toraya, H., Lacorre, P. & Torrance, J.B. (1990). *Mater. Res. Bull.* **25**, 1091.

Hyde, B.G. & Andersson, S. (1988). *Inorganic Crystal Structures*, Chapter XI. New York: Wiley Interscience.

Jacobson, A.J., Tofield, B.C. & Fender, B.E.F. (1972). *Acta Cryst.* B**28**, 956.

Jirak, Z., Pollert, E., Andersen, A.F., Grenier, J.-C. & Hagenmuller, P. (1990). *Eur. J. Solid State Inorg. Chem.* **27**, 421.

Jones, C.W., Battle, P.D., Lightfoot, P. & Harrison, W.T.A. (1989). *Acta Cryst.* C**45**, 365.

Kamata, K., Nakamura, T. & Sata, T. (1975). *Chem. Lett.* **1**, 81.

Keller, H.L., Meier, K.H., Müller-Buschbaum, H. (1975). *Z. Naturf.* **30**, 277.

Khattak, C.P. & Cox, D.E. (1977). *Mater. Res. Bull.* **12**, 463.

Kijima, N., Tanaka, K. & Marumo, F. (1981). *Acta Cryst.* B**37**, 545.

Kijima, N., Tanaka, K. & Marumo, F. (1983). *Acta Cryst.* B**39**, 557.

Kohn, K., Inoue, K., Horie, O. & Akimoto, S.-I. (1976). *J. Solid State Chem.* **18**, 27.

Koopmanns, H.J.A., van de Velde, G.M.H., & Gellings, P.J. (1983). *Acta Cryst.* C**39**, 1323.

Labeau, M., Bochu, B., Joubert, J.C. & Chenevas, J. (1980). *J. Solid State Chem.* **33**, 257.

Lacorre, P., Torrance, J.B., Pannetier, J. Nazzal, A.I., Wang, P.W. & Huang, T.C. (1991). *J. Solid State Chem.* **91**, 225.

Leinenweber, K. & Parise, J. (1995). *J. Solid State Chem.* **114**, 277.

Liu, G., Zhao, X. & Eick, H.A. (1992). *J. Alloys Comp.* **187**, 145.

Loopstra, B.O. & Rietveld, H.M. (1969). *Acta Cryst.* B**25**, 1420.

Luetgert, B. & Babel, D. (1992). *Z. Anorg. Allg. Chemie* **616,** 133.

Mackrodt, W.C. (1984). *Solid State Ionics* **12**, 175.

MacLean, D.A., Ng, H.-K. & Greedan, J.E. (1979). *J. Solid State Chem.* **30**, 35.

Marezio, M., Dernier, P.D. & Remeika J.P. (1972). *J. Solid State Chem.* **4**, 11.

Marezio, M., Dernier, P.D., Chenevas, J. & Joubert, J.C. (1973). *J. Solid State Chem.* **6**, 16.

Marezio, M., Remeika, J.P. & Dernier, P.D. (1970). *Acta Cryst.* B**26**, 2008.

Marx, D.T., Radaelli, P.G., Jorgensen, J.D., Hitterman, R.L., Hinks, D.G., Pei, S. & Dabrowski, B. (1992). *Phys. Rev. B Cond. Matter* **46**, 1144.

Megaw, H.D. (1968). *Acta Cryst.* A**24**, 583.

Megaw, H.D. & Darlington, C.N.W. (1975). *Acta Cryst.* A**31**, 161.

Menyuk N., Dwight, K. & Raccah, P.M. (1967). *J. Phys. Chem. Solids* **28**, 549.

Michel, C., Moreau, J.-M., Achenbach, G., Gerson, R. & James, W.J. (1969). *Solid State Commun.* **7**, 701.

Miller, G. (1990). NEW5. Extended Hückel band structure calculation program. Iowa State University.

Minkiewicz, V.J., Fujii, Y. & Yamada, Y. (1970). *J. Phys. Soc. Japan* **28**, 443.

Miyata, N., Tanaka, K. & Marumo, F. (1983). *Acta Cryst.* B**39**, 561.

Morin, F.J. (1961). *J. Appl. Phys.* **32**, 2195.

Müller, J., Haouzi, A., Laviron, C., Labeau, M. & Joubert, J.C. (1986). *Mater, Res. Bull.* **21**, 1131.

Navrotsky, A. (1989). *Geophysical Monographs, Vol. 45 (Perovskite - A Structure of Great Interest to Geophysics and Materials Science)*, edited by A. Navrotsky & D. Weidner, pp. 67-69. Washington D.C.:American Geophysical Union.

Noël, H., Padiou, J. & Prigent (1975). *C.R. Acad.Sci. Ser.* C **280**, 123.

Odenthal, R.H. & Hoppe, R. (1971). *Monatsh. Chem.* **102**, 1340.

O'Keeffe, M. (1989). *Struct. Bonding (Berlin)*, **71**, 162.

O'Keeffe, M. (1992). Eutax. Program for calculating bond valences. EMLab Software, Phoenix, Arizona.

O'Keeffe, M. & Hyde, B.G. (1977). *Acta Cryst.* B**33**, 3802.

Ozaki, Y., Ghedira, M., Chenevas, J., Joubert, J.C. & Marezio, M. (1977) *Acta Cryst.* B**33**, 3615.

Parise, J.B., McCarron III, E.U. & Sleight, A.W. (1987). *Mater. Res. Bull.* **22**, 803.

Pauling, L. (1929). *J. Am. Chem. Soc.* **51**, 1010.

Poeppelmeier, K.R., Leonowicz, M.E., Scanlon, J.C., Longo, J.M. & Yelon, W.B. (1982). *J. Solid State Chem.* **45**, 71.

Quezel-Ambrunaz, S. (1968). *Bull. Soc. Franc. Minér. Crist.* **91**, 339.

Randall, C.A., Bhalla, A.S., Shrout, T.R. & Cross, L.E. (1990). *J. Mater. Res.* **5**, 829-834.

Rey, M.J., Dehaudt, P.H., Joubert, J.C., Lambert-Andron, B., Cyrot, M. & Cyrot-Lackmann, F. (1990). *J. Solid State Chem.* **86**, 101.

Ritter, H., Ihringer, J., Maichle, J.K., Prandl, W., Hoser, A. & Hewat, A.W. (1989). *Z. Physik* **B75**, 297.

Rodier, N., Julien, R. & Tien, V. (1983). *Acta Cryst.* C**39**, 670.

Rodier, N. & Laruelle, P. (1970). *C.R. Acad. Sci.* **270**, 2127.

Roth, R.S. (1957). *J. Research N.B.S.* **58**, 75.

Saiki, A., Seto, Y., Seki, H., Ishizawa, N., Kato, M. & Mizutani, N. (1991). *J. Chem. Soc. Japan* (1), 25.

Salje, E. (1977). *Acta Cryst.* B**33**, 574.

Sasaki, S. Prewitt, C.T. & Liebermann, R.C. (1983). *Am. Miner.* **68**, 1189.

Sasaki, S., Prewitt, C.T., Bass, J.D. & Schulze, W.A. (1987). *Acta Cryst.* C**43**, 1668.

Sato, M., Jin, T., Hama, Y. & Uematsu, K. (1993). *J. Mater. Chem.* **3**, 325.

Shannon, R.D. (1976). *Acta Cryst.* A**32**, 751.

Shimizu, Y., Syono, Y. & Akimoto, S. (1970). *High Temp. High Press.* **2**, 113.

Sleight, A.W. & Prewitt, C.T. (1973). *J. Solid State Chem.* **6**, 509.

Smith, A.J. & Welch, A.J.E. (1960). *Acta Cryst.* **13**, 653.

Svensson, C. & Stahl, K. (1988). *J. Solid State Chem.* **77**, 112.

Svensson, G. & Werner, P.-E. (1990). *Mater. Res. Bull.* **25**, 9.

Takano, M. Nasu, S., Abe, T., Yamamoto, K. Endo, S. Takeda, Y. & Goodenough, J.B. (1991) *Phys. Rev. Lett.* **67**, 3267.

Takano, M., Okita, T., Nakayama, N. Bando, Y., Takeda, Y., Yamamoto, O. & Goodenough, J.B. (1988). *J. Solid State Chem.* **73**, 140.

Thomas, N.W. & Beitollahi, A. (1994). *Acta Cryst.* B**50**, 549.

Thomas, N.W. (1996). *Acta Cryst.* B**52**, 16.

Thornton, G. & Jacobson, A.J. (1976). *Mater. Res. Bull.* **11**, 837.

Thornton, G., Tofield, B.C. & Hewat, A.W. (1986). *J. Solid State Chem.* **61**, 301.

Tornero, J.D., Cano, F.H., Fayos, J. & Martinez-Ripoll, M. (1978). *Ferroelectrics* **19**, 123.

Unoki, J. & Sakudo, T. (1967). *J. Phys. Soc. Japan* **23**, 546.

Vegas, A., Vallet-Regi, M., Gonzales-Calbet, J.M. & Alario-Franco, M.A. (1986). *Acta Cryst.* B**42**, 167.

Wang, Y., Lu, X., Gao, G.D., Lieberman, R.C. & Dudley, M. (1991). *Mater. Sci. Eng.* A**132**, 13.

Whangbo, M-H., Evain, M., Canadell, E. & Ganne, M. (1989). *Inorg. Chem.* **28**, 267.

Whangbo, M.-H. & Hoffmann, R. (1978). *J. Am. Chem. Soc.* **100**, 6093.

Wiseman, P.J. & Dickens, P. (1973). *J. Solid State Chem.* **3**, 374.

Wiseman, P.J. & Dickens, P. (1976). *J. Solid State Chem.* **17**, 91.

Woodward, P.M., Sleight, A.W. & Vogt, T. (1995) *J. Phys. Chem. Solids* **56**, 1305.

Yamada, K., Funabiki, S., Horimoto, H., Matsui, T., Okuda, T. & Ichiba, S. (1991). *Chem. Lett.* 801.

Zhao, C., Feng, S. Zhicheng, C., Shi, C. Xu, R. & Ni, J. (1996). *Chem. Commun.* 1641.

Zubkov, V.G., Berger, I.F., Pesina, Z.M., Bazuev, G.V. & Shveikin, G.P. (1986). *Sov. Phys. Dokl.* **31**, 459.

Zunger, A. (1980). *Phys. Rev. B* **23**, 5839.

Chapter 4

X-ray and Neutron Diffraction Studies of Ordered Perovskites

4.1 Introduction

Chapter two discussed distortions from the ideal perovskite structure. One of the significant results of that chapter was table 2.4 where space group predictions were made for all 23 Glazer tilt systems in the presence of cation ordering. In this chapter structural characterization of double perovskite, $A_2MM'O_6$, compounds will be discussed. Four compounds, Sr_2AlTaO_6, Sr_2CrTaO_6, Ca_2CrTaO_6, and Sr_2YTaO_6, each belonging to a different Glazer tilt system have been synthesized and structurally characterized using both X-ray and neutron diffraction. The identification of the proper tilt system from either X-ray and neutron diffraction, or from X-ray diffraction alone will be considered. The structural features exhibited by these compounds will be discussed in terms of the predictions of chapter two.

4.2 Identification of the Tilt System from Diffraction Patterns

It was shown in chapter 2 that ordered perovskites with the ideal perovskite structure belong to the cubic space group $Fm\bar{3}m$, and that all structures derived from the ideal structure by octahedral tilting distortions belong to lower symmetry space groups. In principle this reduction in symmetry can have three effects on the diffraction patterns: splitting of the peaks, introduction of previously unobserved peaks, and changes in the intensities of the peaks.

The first effect, peak splitting, can be the most direct way to tell if octahedral tilting has occurred, but there are many potential pitfalls associated with using this method independently. To begin with perovskites always have a high degree of pseudo-symmetry, and the observed dimensions of the unit cell often indicate a higher degree of symmetry than is actually present. The most common examples of this effect are the ordered monoclinic perovskites, which belong to tilt system $a^+b^-b^-$. Calculations using POTATO indicate that for perfectly regular octahedra the lattice constants for this system are

$a^0a^0a^0$ Cubic	$a^0a^0c^-$ Tetragonal	$a^-a^-a^-$ Rhombohedral	$a^+b^-b^-$ Pseudo-Orthorhombic†	$a^+b^-c^-$ Pseudo-Monoclinic‡
200	002 (1) 110 (2)	011	110 (2) 002 (1)	110 (2) 002 (1)
220	112 (2) 200 (1)	112 (1) $01\bar{1}$ (1)	020 (1) 112 (4) 200 (1)	020 (1) $11\bar{2}$ (2) 112 (2) 200 (1)
222	202	222 (1) 002 (3)	022 (1) 202 (1)	022 (2) $20\bar{2}$ (1) 202 (1)
400	004 (1) 220 (2)	022	220 (2) 004 (1)	220 (2) 004 (1)
420	114 (1) 222 (1) 310 (1)	123 (1) $1\bar{1}2$ (1)	130 (1) 222 (2) 114 (2) 310 (1)	130 (1) $22\bar{2}$ (1) 222 (1) $11\bar{4}$ (1) 114 (1) 310 (1)
422	204 (1) 312 (2)	233 (1) 013 (2) $11\bar{2}$ (1)	132 (2) 024 (1) 204 (1) 312 (2)	$13\bar{2}$ (2) 132 (2) 024 (2) $20\bar{4}$ (1) 204 (1) $31\bar{2}$ (2) 312 (2)

Table 4.1 : The peak splitting patterns for commonly observed tilt systems. The numbers in parenthesis give the approximate intensity ratio of the individual peaks. The unit cells used for indexing are a doubled cubic cell for $a^0a^0a^0$, a $\sqrt{2}$ cell for $a^0a^0c^-$, $a^+b^-b^-$, and $a^+b^-c^-$, and a rhombohedral cell with $a \cong \sqrt{2}a_p$, $a \cong 60°$. Details of the unit cell dimensions for each space group can be found in appendix 3. This table is similar to the one produced by Kupriyanov and Filip'ev (Kupriyanov & Filip'ev, 1963). †The true symmetry of the $a^+b^-b^-$ tilt system is monoclinic. ‡The true symmetry of the $a^+b^-c^-$ tilt system is triclinic.

orthorhombic, and in practice most compounds in this tilt system have unit cells which are orthorhombic within experimental error. However, the true symmetry of the $a^+b^-b^-$ structure is monoclinic. This has led to many errors in assignment of the crystal system, particularly in the older literature. This has been pointed out and treated in comprehensive treatment of tilt systems $a^0a^0a^0$ and $a^+b^-b^-$ in the presence of random and ordered cation distributions (Anderson *et al.*, 1993). Another practical difficulty with using peak splitting to determine the

	Random M/M' Cation Distribution			Ordered M/M' Cation Distribution		
Tilt System	**Crystal System**	**Z**	**Reflection Conditions**	**Crystal System**	**Z**	**Reflection Conditions**
#1,#2	Orthorhombic	4	hkl: h+k+l=2n	Orthorhombic	4	0kl: k+l=2n h0l:h+l=2n hk0:h+k=2n
#3	Cubic	4	hkl: h+k+l=2n	Cubic	4	0kl: k+l=2n h0l: h+l=2n hk0: h+k=2n
#4, #6	Orthorhombic	4	hk0: h+k=2n	Monoclinic	4	hk0: h+k=2n
#5, #7	Tetragonal	4	hk0: h+k=2n hhl : l=2n	Tetragonal	4	hk0: h+k=2n 00l: l=2n
#8, #9	Monoclinic	2	0k0: k=2n	Triclinic	2	none
#10,#11	Orthorhombic	2	0kl : k+l=2n hk0: h=2n	Monoclinic	2	hk0: h+k=2n 00l: l=2n
#12	Triclinic	4	face centered conditions	Triclinic	4	face centered conditions
#13	Monoclinic	2	hkl: h+k+l=2n h0l: h,l=2n	Triclinic	4	face centered conditions
#14	Rhombohedral	1R	hhl: l=2n	Rhombohedral	1R	none
#15	Orthorhombic	4	hkl: h+k+l=2n	Orthorhombic	4	0kl: k+l=2n h0l:h+l=2n hk0:h+k=2n
#16	Tetragonal	4	hkl: h+k+l=2n	Tetragonal	4	hk0: h+k=2n 0kl: k+l=2n 00l: l=2n
#17,#18	Orthorhombic	4	hkl: h+k=2n h0l: h,l=2n	Monoclinic	4	hkl: h+k=2n h0l: h,l=2n
#19	Monoclinic	2	hkl: h+k+l=2n	Triclinic	2	hkl: h+k+l=2n
#20	Orthorhombic	2	hkl: h+k+l=2n hk0: h,k=2n	Monoclinic	2	hkl: h+k+l=2n
#21	Tetragonal	1T	0kl: k=2n h00: h=2n	Tetragonal	2	0kl: k+l=2n hhl: l=2n h00: h=2n
#22	Tetragonal	2	hkl: h+k+l=2n 0kl: k,l=2n	Tetragonal	2	hkl: h+k+l=2n
#23	Cubic	½S	none	Cubic	4	face centered conditions

Table 4.2 : Unit cell descriptions and reflection conditions for $A_2MM'O_6$ perovskites in all 23 Glazer tilt systems, both with and without 1:1 octahedral cation ordering. The size of the unit cell can be inferred from the Z value. If a_p is the dimension of the small cubic unit cell then $a \cong b \cong c \cong 2a_p$ when Z=4, two cell parameters are approximately $\sqrt{2}a_p$ and one $2a_p$ when Z=2, $a \cong \sqrt{2}a_p$ and $\alpha \cong 60°$ when Z=1R, $a=b \cong \sqrt{2}a_p$ and $c \cong a_p$ when Z=1T, and $a=b=c=a_p$ when Z=½S. Full details can be found in appendix 3. The reflection conditions were taken from *International Tables for Crystallography, Vol. A* (Hahn, 1983). Face centered conditions are all indices either odd or even, that is hkl: h=2n,k=2n,l=2n or hkl: h=2n+1,k=2n+1,l=2n+1.

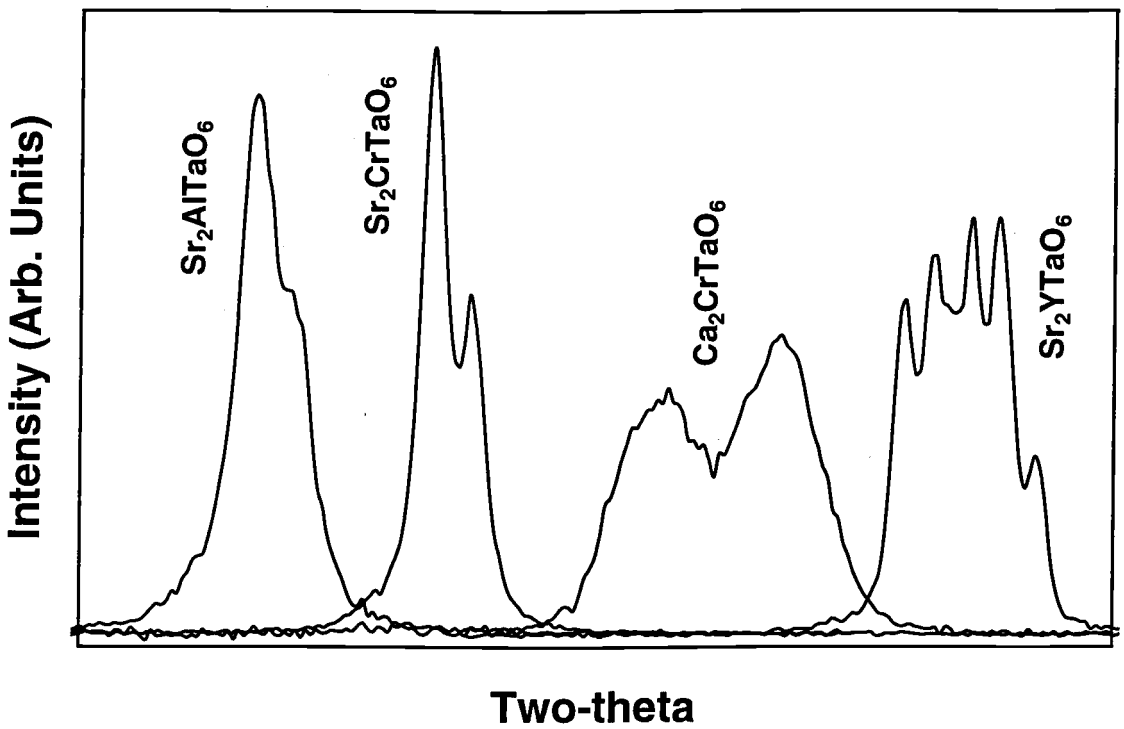

Figure 4.1 : The cubic (422) peak in Sr_2AlTaO_6, Sr_2CrTaO_6, Ca_2CrTaO_6, and Sr_2YTaO_6. The peak positions have been shifted in two theta to achieve the even spacing present in the figure, but the overall scale (4° two theta) is the same for all curves. Both Kα1 and Kα2 peaks are present. The Kα1/ Kα2 splitting is visible in the Sr_2AlTaO_6 and Sr_2CrTaO_6 patterns, where no splitting of the (422) reflection is observed.

crystal system is the fact that in many cases the distortion is quite small and splitting of the peaks is difficult to quantify or in some cases even detect. Peak splitting is particularly difficult to detect if the peaks are broadened by size and/or strain effects. Nonetheless, if these pitfalls are taken into consideration, a proper analysis of the peak splitting is the first step in assigning the proper tilt system. Table 4.1 gives the peak splitting patterns of the first six subcell reflections in the most commonly observed tilt systems. Figure 4.1 shows the peak splitting of the cubic (422) peak in the X-ray diffraction patterns of Sr_2AlTaO_6, Sr_2CrTaO_6, Ca_2CrTaO_6, and Sr_2YTaO_6. Notice that no splitting can be observed in Sr_2CrTaO_6 even though the true symmetry, as will be shown later, is tetragonal rather than cubic.

The next step in identifying the tilt system is to index the peaks. Matching the observed splitting pattern with those found in table 4.1, and using the values for the approximate unit cell constants in table A2.2 (appendix 2) it should be possible to determine a unit cell which will index all of the peaks in the diffraction pattern. Table 4.2 contains the unit cell description and extinction conditions for all 23 Glazer tilt systems for both random and ordered cation distributions. Using this information one should be able to narrow the list of possible tilt systems down to a single or at least a very short list of possibilities. In practice the vast majority of compounds belong to one of the following four tilt systems: $a^0a^0a^0$ (#23), $a^0a^0c^-$ (#22), $a^-a^-a^-$ (#14), and $a^+b^-b^-$ (#10). These four tilt systems result in compounds which are commonly referred by their crystal symmetry, that is cubic, tetragonal, rhombohedral, and orthorhombic/monoclinic respectively. Proper identification of each of these four tilt systems is discussed in greater detail below.

In cases where peak splitting is either absent or undetectable all of the peaks can be indexed with a single cubic lattice constant, a_c. In order to index the peaks in all cases the doubled lattice constant of the ordered cubic structure (~8Å) should be used initially. If the all of the peaks index according to face centered cubic extinction conditions, h,k,l either all odd (i.e. 111, 311) or all even (i.e. 222, 400), then the structure is the ordered cubic perovskite structure, tilt system $a^0a^0a^0$, and space group $Fm\bar{3}m$. If only peaks with h,k, and l all even are present then the structure is the simple cubic structure, tilt system $a^0a^0a^0$, and space group $Pm\bar{3}m$. Although not commonly observed there is one other tilt system which can lead to a cubic space group, $a^+a^+a^+$. Compounds which belong to this tilt system adopt either the $Pn\bar{3}$ (ordered octahedral cation distribution) or $Im\bar{3}$ space group (random octahedral cation distribution). The extinction conditions of these space groups are given in table 4.2. If the observed peaks violate the extinction conditions for these four space

groups, the true symmetry must be lower than cubic, even though the unit cell may be dimensionally cubic.

For simple perovskites and double perovskites with a random distribution of cations the cubic $a^0a^0a^0$ (#23), tetragonal $a^0a^0c^-$ (#22), and rhombohedral $a^-a^-a^-$ (#14) tilt systems can be differentiated based on their extinction conditions. However, in the presence of cation ordering this situation is more complicated. Both cation ordering and octahedral tilting reduce the translational symmetry of the simple cubic perovskite structure. This leads to the appearance of superstructure reflections in the diffraction pattern. If the peak splitting is too small to be detected, this combination can lead to ambiguities in assigning the correct tilt system. Under these conditions (cation ordering, no apparent peak splitting) the cubic $a^0a^0a^0$ (#23), tetragonal $a^0a^0c^-$ (#22), and rhombohedral $a^-a^-a^-$ (#14) tilt systems all give diffraction patterns which contain the same set of peaks. The only way to distinguish between these three tilt systems is a careful analysis of the superstructure peak intensities. Further complicating the problem is the fact that the structures corresponding to all three tilt systems differ from each other only in the positions of the oxygen ions. Because the metal ions typically dominate the X-ray scattering, and the superstructure peak intensities are dependent upon both the degree of cation ordering and the octahedral tilting, these three tilt systems are nearly indistinguishable from analysis of X-ray diffraction data alone. In these cases Rietveld analysis of neutron diffraction data is essential to determine the structure accurately, and assign the correct tilt system. This has undoubtedly lead to several incorrect structure determinations in the literature. Such is the case for Sr_2CrTaO_6 whose correct structure as given later in this chapter is tetragonal (tilt system $a^0a^0c^-$) rather than cubic as originally thought (Choy, Park, Hong & Kim, 1994).

The most commonly occurring tilt system is $a^+b^-b^-$ (#10) which leads to an orthorhombic or monoclinic (pseudo-orthorhombic) structure, for random and ordered cation distributions respectively. Compounds in this tilt system usually display peak splitting sizable enough to identify the lattice symmetry, but in some cases such as Sr_2ScTaO_6, Sr_2InTaO_6, (see chapter 5) and $SrSnO_3$ (Vegas *et al.*, 1986) the apparent unit cell is essentially cubic and peak splitting is negligible. In these cases the only indication of monoclinic/orthorhombic symmetry is the appearance of peaks that can be indexed with the large cubic lattice constant, a_c, but are not allowed in any of the cubic tilt system space groups. Usually the largest of these extra peaks is the cubic (210) peak (orthorhombic (111) peak). Not only is this peak not allowed in any of the cubic structure tilt systems, but is also absent in tetragonal ($a^0a^0c^-$) and rhombohedral ($a^-a^-a^-$) perovskites. Therefore, the presence of this peak is a strong indication that the symmetry is orthorhombic/monoclinic (tilt system $a^+b^-b^-$). Once the tilt system has been established as $a^+b^-b^-$, the distinction between ordered

(monoclinic) and disordered (orthorhombic) structures can be made by looking for the cubic (111) peak (orthorhombic (011) peak) and/or the cubic (221) peak (orthorhombic (021) peak). If the cubic (111) or (221) peaks are present, at least partial ordering between octahedral cations is implied, and the ordered monoclinic structure (space group $P2_1/n$) is confirmed*. If both the cubic (111) and (221) peaks are absent the disordered orthorhombic structure (space group Pbnm) is more likely.

The above discussion is meant to be a guide which can be used to eliminate most tilt systems from consideration, and in certain cases identify a unique tilt system. In all cases refinement of the both the X-ray and neutron diffraction patterns is recommended if at all possible. However, a good starting model is a prerequisite for successful structure determination using the Rietveld method. Using the concepts presented above, one should be able to identify the tilt systems which agree with the observed peak splittings and extinction conditions. Once this has been done the program POTATO (appendix 1) can be used to generate starting models in the appropriate tilt systems. Finally, based on comparison of refinement results a correct determination of the structure and corresponding identification of the tilt system should be possible.

4.3 Synthesis

Both Sr_2CrTaO_6 and Ca_2CrTaO_6 were synthesized using conventional ceramic techniques from Cr_2O_3 (Baker Analyzed Reagent), Ta_2O_5 (99.9% Johnson Matthey), and either $Sr_2(NO_3)_2$ (Baker Analyzed Reagent), or $Ca_2(NO_3)\cdot 4H_2O$ (Baker Analyzed Reagent). After grinding a stoichiometric mixture of the reagents in a mortar and pestle, the starting materials were heated to 750°C to decompose the nitrates. This was followed by additional grinding and heating to the final annealing temperature for 1 hour. After another grinding using the mortar and pestle the compounds were heated to the final annealing temperature for 8-24 hours. The final annealing temperatures were 1500°C for Sr_2CrTaO_6 and 1400°C for Ca_2CrTaO_6. Both Sr_2AlTaO_6 and Sr_2YTaO_6 were made using the flux/anneal route, in a molten $SrCl_2$ flux. This procedure has been previously described in the literature (Woodward, Hoffman & Sleight, 1994). The same reagents were used with the exception

* In tilt systems #1, #2, #3, #5, #7, #10, #11, #13, #14, #20, #21, #22, #23 the cubic (111) peak cannot be attributed to octahedral tilting. In these tilt systems the presence of this peak is a clear indication of cation ordering. Because the vast majority of perovskite compounds belong to one of these tilt systems, it is usually safe to take the observance of

that chromium oxide was replaced with Al_2O_3 (99.8% Aldrich) and Y_2O_3 (99.999% Atomergic) respectively. For Sr_2YTaO_6 the final annealing temperature used was 1500°C, while the two samples of Sr_2AlTaO_6 had final annealing temperatures of 900°C and 1500°C.

4.4 Structure Refinement

The following sections describe the results of Rietveld refinements performed on $A_2MM'O_6$ double perovskite compounds Sr_2AlTaO_6, Sr_2CrTaO_6, Ca_2CrTaO_6, and Sr_2YTaO_6. Using both X-ray and neutron diffraction results it will be shown that each compound belongs to a different tilt system. All refinements were performed using the 1991 release of the RIETAN software package (Izumi, 1989; Izumi, 1993). This Rietveld program is uniquely suited for analysis of these compounds because it allows the subcell and superstructure peaks to be refined separately. This is necessary in compounds where partial cation ordering creates antiphase boundaries, because these extended defects cause the superstructure peaks to broaden and shift to smaller d-spacing values (Woodward, Hoffman & Sleight, 1994). This anisotropy in the peak broadening, which is clearly apparent in the X-ray diffraction patterns, necessitates a refinement where the optimal profile coefficients (and in some cases lattice constants) are refined separately for the two sets of peaks. All other parameters are set to be equivalent for both classes of reflections. This refinement procedure is described in greater detail elsewhere (Woodward, Hoffmann & Sleight, 1994). In the neutron diffraction patterns the superstructure peaks were also observed to be somewhat broader than the subcell peaks, but the anisotropy in peak widths was much smaller than found with X-rays. This is due partially to the decreased resolution of the neutron diffractometer, and in part to the mixed character (cation ordering and octahedral tilting) of the superstructure reflections.

X-ray diffraction patterns were collected using a Siemens D5000 diffractometer, equipped with a Kevex, Peltier cooled Si(Li) energy dispersive detector, and a copper $K\alpha$ radiation source. Measurements for Rietveld analysis were collected from 2-150° two-theta, using a step size of 0.02°, a count time of 3-6 seconds per step, and a 0.05mm detector slit. Neutron data collection was performed at the high flux beam reactor (HFBR) at Brookhaven National Laboratory (BNL). The Sr_2AlTaO_6 samples were analyzed on the H4S beam line, using a wavelength of 1.358Å, and a step size of 0.1°. Diffraction patterns for the other

---

this peak as an indication that at least partial cation ordering is present. However, it should be remembered that certain rare exceptions to this rule exist.

three samples were collected on the high resolution neutron powder diffractometer (HRNPD) at BNL, using a wavelength of 1.8857Å, and a step size of 0.02°.

The use of both X-ray and neutron data to determine a structure is very useful. Because of the differences in atomic scattering powers, instrument resolution, and sampling depth each technique is sensitive to different features of the structure. However, combining the two refinements to obtain one result is not necessarily trivial. The GSAS software package (Larson & Von Dreele, 1994) allows simultaneous refinement of X-ray and neutron patterns, as does the latest version of RIETAN (Izumi, 1993). However, neither of these two programs can accommodate the superstructure peak broadening complication discussed above, only the 1991 release of RIETAN can correctly model this feature of the patterns. Unfortunately, this version of RIETAN is not capable of simultaneous X-ray and neutron refinements. Therefore, the X-ray and neutron patterns were refined separately, and the agreement between the two refinements was found to be in general quite good. As indicated by the standard deviations, the long range order parameter and lattice constants are more accurately determined using the X-ray data, and the oxygen positions, bond distances, and thermal parameters are more accurately determined using the neutron data. In those compounds where both cation ordering and octahedral tilting were present, the broadening of the superstructure lines was apparent in the X-ray diffraction patterns (except for Sr_2YTaO_6) but absent in the neutron patterns. Therefore, determination of the ordered domain size was carried out only on the X-ray data. Because of the increased accuracy of the oxygen positions, bond distances and bond valences were calculated using only the results of the neutron refinement.

4.4.1 Sr_2AlTaO_6

X-ray refinement results for Sr_2AlTaO_6 have been reported in detail elsewhere (Woodward, Hoffmann & Sleight, 1994). Neutron diffraction was carried out to confirm the cubic symmetry and to more accurately ascertain the oxygen position. Neutron diffraction patterns were collected on two Sr_2AlTaO_6 samples using the H4S beamline of the high flux beam reactor (HFBR) at Brookhaven National Laboratory (BNL). Both samples were prepared using the flux/anneal synthesis, but the final annealing temperature was 900°C for the first sample and 1500°C for the second. This resulted in one sample with a high degree of long range order and one with a much lower degree of long range order. Rietveld refinement results of the neutron and X-ray diffraction patterns are given in tables 4.3 and

4.4 respectively. The interatomic distances and angles, polyhedral volumes, and bond valences were calculated from the neutron refinement results of the 1500°C sample and are given in table 4.5. The observed and difference patterns for both the X-ray and neutron refinement are shown in figure 4.2, while the structure is shown in figure 4.3. Notice that the superstructure reflections are much stronger in the X-ray pattern than they are in the neutron pattern. As mentioned previously both cation ordering and octahedral tilting give rise to superstructure reflections, but neutron diffraction will be more sensitive than X-ray diffraction to octahedral tilting distortions. This is due to the neutron scattering length of oxygen being comparable to or in some cases greater than the scattering length of the metal ions. On the other hand, in this compound the scattering powers of aluminum and tantalum are such that X-ray diffraction is much more sensitive to changes in the long range order parameter. Therefore, the very weak superstructure reflections in the neutron pattern and the excellent fit achieved using the cubic space group Fm3m, both indicate that the true symmetry is actually cubic. Refinements in tilt systems $a^0a^0c^-$ (#22) and $a^-a^-a^-$ (#14) did not lead to an improvement in the quality of the fit.

Previous X-ray refinements on this compound made under a variety of synthesis conditions had in many cases given negative thermal parameters for the octahedral site cation (Woodward, Hoffmann & Sleight, 1994). One possible explanation for this is a deviation from the ideal stoichiometry. Since both neutron and X-ray data sets have been collected there is enough information available to justify a refinement of the stoichiometry. Beginning with the neutron pattern (1500°C sample) where all four elements have comparable scattering lengths (b_{Sr}=0.69, b_{Ta}=0.70, b_{Al}=0.345, b_O=0.575) (Ibers & Hamilton, 1974), the occupancies of the individual sites were all refined separately. The R_{wp} parameter decreased from 10.12% to 9.87%, 10.06%, and 10.02% upon refining the occupancy of the Sr, Al/Ta, and O sites respectively. Clearly the effect of varying the occupancy of the Al/Ta and O sites does not have a significant effect on the diffraction pattern. However, by decreasing the electron density on the strontium site there is a noticeable improvement in the quality of fit. Applying a Hamilton significance test reveals that the refinement with strontium vacancies is significantly better at the 75% confidence level (Hamilton, 1965). To maintain overall charge neutrality strontium vacancies would need to be accompanied either by interstitial cations, oxygen vacancies ($Sr_{2-x}AlTaO_{6-x}$), or excess tantalum on the octahedral site ($Sr_{2-x}Al_{1-x}Ta_{1-x}O_6$). Because of the high packing density of the perovskite structure a significant concentration of interstitial ions can be ruled out. Refinements of the neutron diffraction pattern showed little sensitivity to either of the latter two charge compensation mechanisms. Refining the X-ray patterns it was possible to

lower the R_{wp} term from 8.9% to roughly 8.4% with either charge compensation mechanism. However, when the latter mechanism was used the occupancy of the strontium site showed good agreement with the value obtained from the neutron refinement. Application of the Hamilton test on the residuals from the X-ray refinements suggests that the strontium vacancy model gives a significantly better refinement at the 95% confidence level. Based on these results all four refinements were done using the $Sr_{2-x}Al_{1-x}Ta_{1+x}O_6$ model.

Compound	**Sr_2AlTaO_6 (900°C)**	**Compound**	**Sr_2AlTaO_6 (1500°C)**
Diffraction Method	**Neutron**	**Diffraction Method**	**Neutron**
Space Group	**Fm3m (A-225)**	**Space Group**	**Fm3m (A-225)**
Z	**4**	**Z**	**4**
Cell Parameters		**Cell Parameters**	
a (Subcell)	**7.8104(3)Å**	**a (Subcell)**	**7.8004(2)Å**
a (Supercell)	**7.791(9)Å**	**a (Supercell)**	**7.792(4)Å**
Order Parameter	**54%**	**Order Parameter**	**78%**
Wavelength	**1.358Å**	**Wavelength**	**1.358Å**
2-Theta Range	**5-120°**	**2-Theta Range**	**5-120°**
# of Reflections	**41**	**# of Reflections**	**41**
# of Parameters	**20**	**# of Parameters**	**24**
R_{WP}	**10.94%**	**R_{WP}**	**9.89%**
χ^2	**1.35**	**χ^2**	**1.29**
R_I (Subcell)	**1.36%**	**R_I (Subcell)**	**1.17%**
R_I (Supercell)	**2.19%**	**R_I (Supercell)**	**1.05%**

Atom	Site	x	y	z	Occ	B (Å^2)
900°C Sample						
Sr	8c	¼	¼	¼	0.97(2)	0.9(1)
Al1	4a	0	0	0	0.74(12)	0.5(1)
Ta1	4a	0	0	0	0.26	0.5
Ta2	4b	½	½	½	0.80	0.5
Al2	4b	½	½	½	0.20	0.5
O	24e	0.2459(9)	0	0	1.0	0.70(6)
1500°C Sample						
Sr	8c	¼	¼	¼	0.96(2)	0.69(7)
Al1	4a	0	0	0	0.85(4)	0.4(1)
Ta1	4a	0	0	0	0.15	0.4
Ta2	4b	½	½	½	0.93	0.4
Al2	4b	½	½	½	0.07	0.4
O	24e	0.2465(7)	0	0	1.0	0.71(4)

Table 4.3 : Results of Rietveld refinements of neutron powder diffraction data for Sr_2AlTaO_6 samples prepared using the flux/anneal method at 900°C and 1500°C. The long range order parameters were calculated using the formula, S=Occ(Al1)+Occ(Ta2)-1. Details of the refinement are given in the text.

Figure 4.2 : Observed and difference patterns for selected regions of the a) X-ray and b) neutron diffraction patterns of Sr_2AlTaO_6. The two-theta scales have been chosen so that the d-spacing range is approximately equal in X-ray and neutron patterns. The asterisks represent a small $Sr_5Ta_4O_{15}$ impurity.

Figure 4.3 : The structure of Sr_2AlTaO_6. In part a) the atoms are represented as spheres with black spheres representing the aluminum rich site, shaded spheres the tantalum rich site, large open spheres representing strontium, and the small open spheres oxygen. The atomic radii of the oxygen atoms have been made very small for clarity while the other atoms are shown at one half their normal radii. In part b) only the AlO_6 and TaO_6 octahedra are shown. The rock salt superstructure and doubling of the simple unit cell in all three dimensions are apparent in this figure.

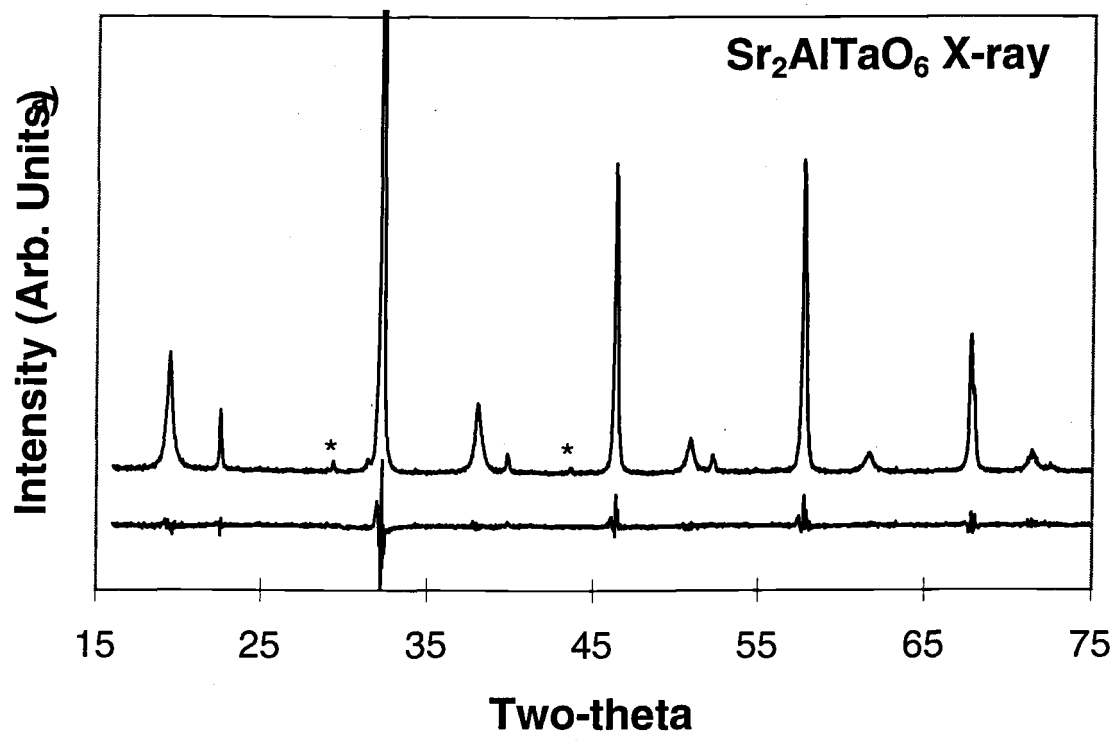
Sr2AlTaO6 X-ray
Intensity (Arb. Units)
15
25
35
45
55
65
75
Two-theta

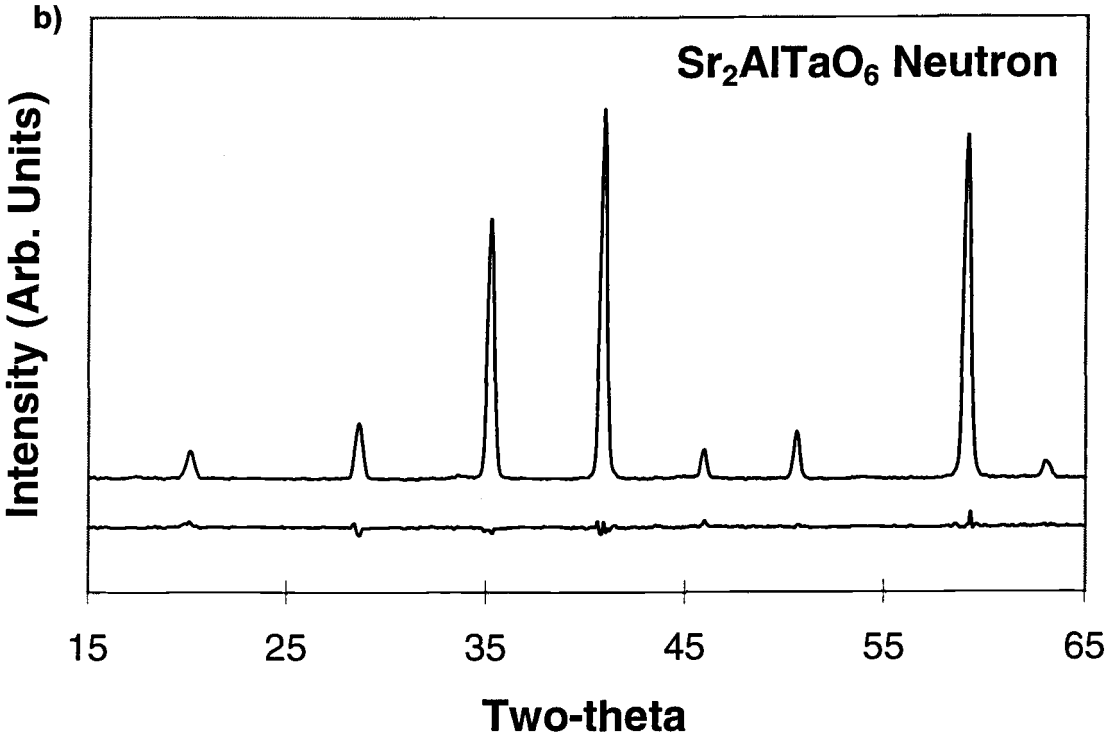
b)
Sr2AlTaO6 Neutron
Intensity (Arb. Units)
15
25
35
45
55
65
Two-theta

Figure 4.2

a)

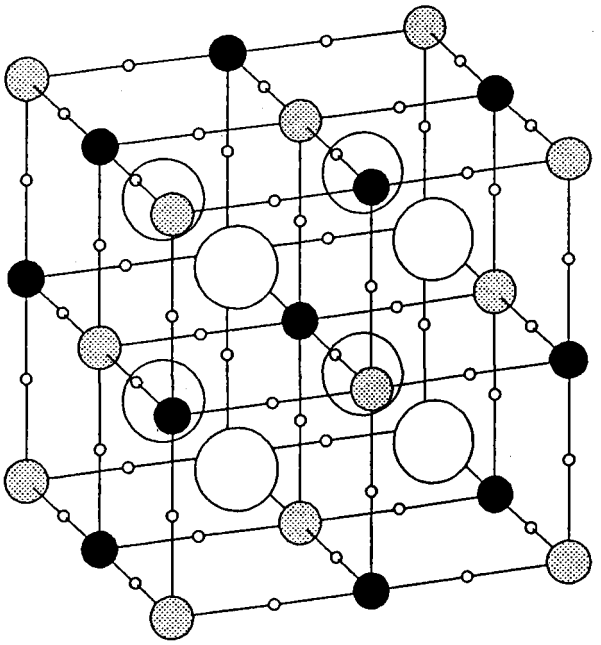

b)

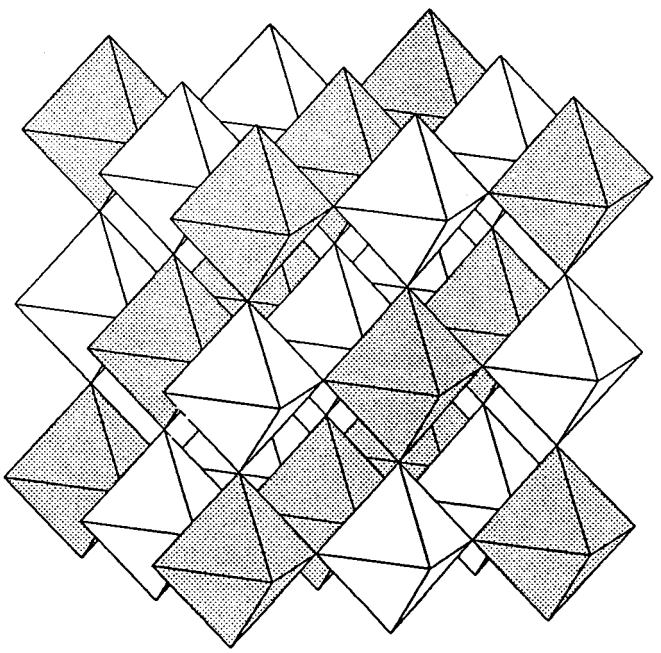

Figure 4.3

Compound	**Sr_2AlTaO_6 (900°C)**	**Compound**	**Sr_2AlTaO_6 (1500°C)**
Diffraction Method	**X-ray**	**Diffraction Method**	**X-ray**
Space Group	**Fm3m (A-225)**	**Space Group**	**Fm3m (A-225)**
Z	**4**	**Z**	**4**
Cell Parameters		**Cell Parameters**	
a (Subcell)	**7.8092(1)Å**	**a (Subcell)**	**7.79767(7)Å**
a (Supercell)	**7.793(1)Å**	**a (Supercell)**	**7.7929(4)Å**
Order Parameter	**66%**	**Order Parameter**	**84%**
Ordered Domain Size	**88Å**	**Ordered Domain Size**	**206Å**
Radiation	**Cu Kα**	**Radiation**	**Cu Kα**
Two-Theta Range	**2-150°**	**Two-Theta Range**	**2-150°**
# of Reflections	**40**	**# of Reflections**	**40**
# of Parameters	**23**	**# of Parameters**	**23**
R_{WP}	**8.33%**	**R_{WP}**	**8.39%**
χ^2	**1.33**	**χ^2**	**1.33**
R_I (Subcell)	**2.01%**	**R_I (Subcell)**	**1.78%**
R_I (Supercell)	**1.29%**	**R_I (Supercell)**	**2.73%**

Atom	Site	x	y	z	Occ	B (Å^2)
900°C Sample						
Sr	8c	¼	¼	¼	0.972(6)	0.9(1)
Al1	4a	0	0	0	0.80(1)	0
Ta1	4a	0	0	0	0.20	0
Ta2	4b	½	½	½	0.86	0
Al2	4b	½	½	½	0.14	0
O	24e	0.241(3)	0	0	1.0	0.4(3)
1500°C Sample						
Sr	8c	¼	¼	¼	0.964(4)	0.62(9)
Al1	4a	0	0	0	0.88(1)	0
Ta1	4a	0	0	0	0.12	0
Ta2	4b	½	½	½	0.96	0
Al2	4b	½	½	½	0.04	0
O	24e	0.2468(8)	0	0	1.0	0.3(3)

Table 4.4 : Results of Rietveld refinements of X-ray powder diffraction data for Sr_2AlTaO_6 samples prepared using the flux/anneal method at 900°C and 1500°C. The long range order parameters were calculated using the formula, S=Occ(Al1)+Occ(Ta2)-1. Ordered domain sizes were determined from a Williamson-Hall plot of the superstructure peaks. Details of the refinement are given in the text.

	Sr	M	M'	O
M-O Bond Distance (Å)	2.755(4)	1.921(1)	1.975(1)	
Polyhedral Volume ($Å^3$)	49.3	9.5	10.3	
Bond Valence	2.15	2.89	5.17	2.06

Table 4.5 : Bond distances, MO_n polyhedral volumes, and bond valences for Sr_2AlTaO_6, based on the structure determined from refinement of the neutron diffraction pattern of the 1500°C sample. Polyhedral volumes were calculated using IVTON (Zunic & Vickovic, 1996) and bond valences were calculated using EUTAX (O'Keeffe, 1992). M represents the Al rich site, and M' the Ta rich site. Bond valences were calculated by taking the M and M' sites to be fully occupied by Al and Ta respectively.

4.4.2 Sr_2CrTaO_6

The structure of Sr_2CrTaO_6 was recently determined from the Rietveld refinement of an X-ray powder diffraction pattern to be a partially ordered cubic perovskite (Choy, Park, Hong & Kim, 1994). Refinements based on X-ray diffraction data carried out in that study showed no indication that the structure was not cubic. However, the compound Sr_2GaTaO_6 under most synthesis conditions also appears to be a partially ordered cubic perovskite. Nonetheless, when Sr_2GaTaO_6 is heated to 1600°C, the superstructure reflections due to cation ordering become very weak and diffuse exposing weak, yet sharp superstructure reflections that can only be attributed to octahedral tilting. Rietveld refinements show that Sr_2GaTaO_6 is in fact a tetragonal perovskite, tilt system $a^0a^0c^-$, rather than a cubic perovskite. The small octahedral tilting distortion is normally masked in the X-ray diffraction pattern by the presence of cation ordering. Unlike Sr_2GaTaO_6 the long range cation order in Sr_2CrTaO_6 remains fairly constant from its formation up to at least 1600°C (see chapter 6), so that one can never hope to unambiguously differentiate between the cubic and tetragonal structures using X-ray diffraction data alone. However, the tolerance factors (0.999 for Sr_2GaTaO_6 and 0.998 for Sr_2CrTaO_6) suggest that the two compounds should be isostructural. In order to confirm or deny this hypothesis a neutron powder diffraction pattern of Sr_2CrTaO_6 was collected for Rietveld analysis.

Compound	Sr_2CrTaO_6 (1500°C)	**Compound**	Sr_2CrTaO_6 (1500°C)
Diffraction Method	Neutron	**Diffraction Method**	X-ray
Space Group	I4/m (A-87)	**Space Group**	I4/m (A-87)
Z	2	**Z**	2
Cell Parameters		**Cell Parameters**	
a	5.5742(2)Å	**a**	5.57197(5)Å
c	7.8816(6)Å	**c**	7.8854(1)Å
Order Parameter	60%	**Order Parameter**	64%
Ordered Domain Size	----	**Ordered Domain Size**	102Å
Wavelength	1.8857Å	**Radiation**	Cu Kα
Two-Theta Range	15-154°	**Two-Theta Range**	2-150°
# of Reflections	76	**# of Reflections**	132
# of Parameters	21	**# of Parameters**	21
R_{WP}	9.83%	**R_{WP}**	10.97%
χ^2	2.74	**χ^2**	1.45
R_I	3.39%	**R_I (Subcell)**	3.71%
		R_I (Supercell)	2.16%

Atom	Site	x	y	z	Occ	B (Å^2)
Neutron Diffraction						
Sr	4d	0	½	¼	1.0	0.9(1)
Cr1	2a	0	0	0	0.80(9)	0.6(2)
Ta1	2a	0	0	0	0.20	0.6
Ta2	2b	½	½	0	0.80	0.6
Cr2	2b	½	½	0	0.20	0.6
O1	8h	0.235(1)	0.735	0	1.0	1.0(1)
O2	4e	0	0	0.25	1.0	1.0
X-ray Diffraction						
Sr	4d	0	½	¼	1.0	0.59(6)
Cr1	2a	0	0	0	0.820(9)	0.00(5)
Ta1	2a	0	0	0	0.180	0.00
Ta2	2b	½	½	½	0.820	0.00
Cr2	2b	½	½	½	0.180	0.00
O1	8h	0.235(4)	0.745	0	1.0	0.2(2)
O2	4e	0	0	0.268(7)	1.0	0.2

Table 4.6 : Results of Rietveld refinements of neutron and X-ray powder diffraction data for Sr_2CrTaO_6. The long range order parameters were calculated using the formula, S=2×Occ(Cr1)-1. Ordered domain sizes were determined from a Williamson-Hall plot of the superstructure peaks. Details of the refinement are given in the text.

Figure 4.4 : The difference pattern from refinement of the Sr_2CrTaO_6 neutron powder pattern, using cubic (Fm3m) and tetragonal (I4/m) models. To emphasize the poor fit of the cubic pattern to the superstructure reflections, the intensity of the difference curves have been set to zero in all regions of the spectrum where no superstructure reflections are present. The peak indices refer to the cubic unit cell.

Figure 4.5 : Observed and difference patterns for selected regions of the a) X-ray and b) neutron diffraction patterns of Sr_2CrTaO_6. The two-theta scales have been chosen so that the d-spacing range is approximately equal in X-ray and neutron patterns. The asterisks represent a small $Sr_5Ta_4O_{15}$ impurity.

Figure 4.6 : The structure of Sr_2CrTaO_6. In part a) the atoms are represented as spheres with the black spheres representing the chromium rich site, the shaded spheres tantalum rich site, the large open spheres strontium, and the small open spheres oxygen. The atomic radii of the oxygen atoms have been made very small for clarity while the other atoms are shown at one half their normal radius. In part b) only the CrO_6 and TaO_6 octahedra are shown.

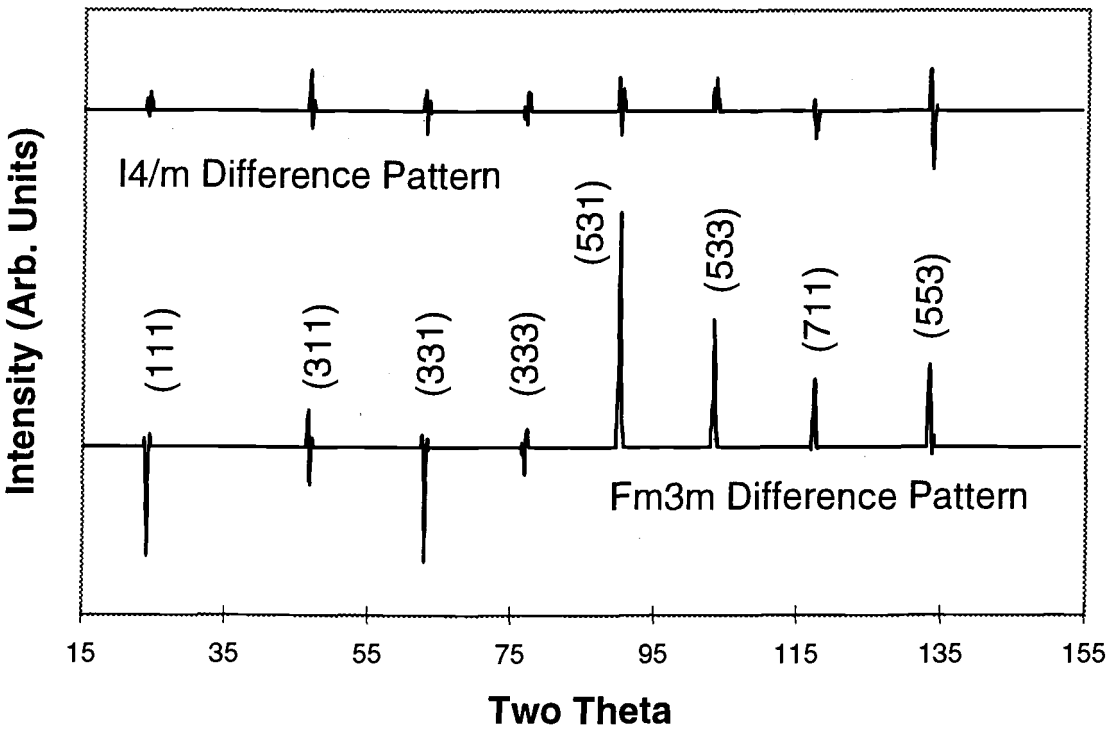
I4/m Difference Pattern
Fm3m Difference Pattern
(111)
(311)
(331)
(333)
(531)
(533)
(711)
(553)
Intensity (Arb. Units)
15
35
55
75
95
115
135
155
Two Theta

Figure 4.4

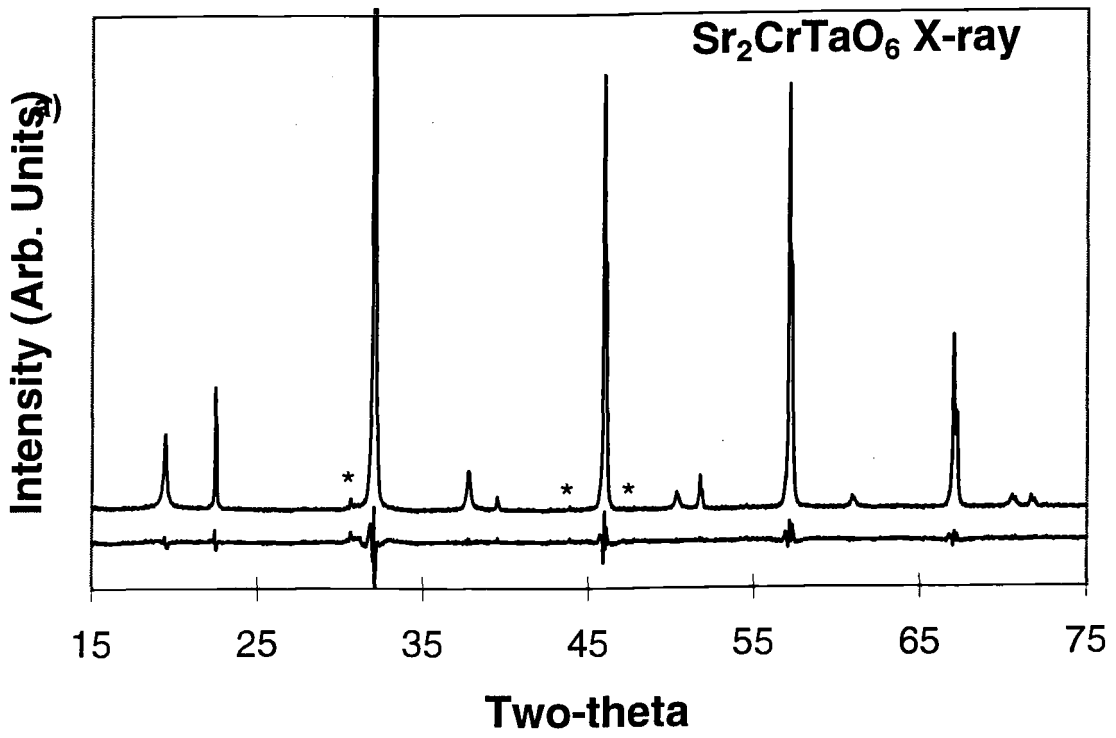
a)
Sr_2CrTaO_6 X-ray
Intensity (Arb. Units)
*
*
*
15
25
35
45
55
65
75
Two-theta

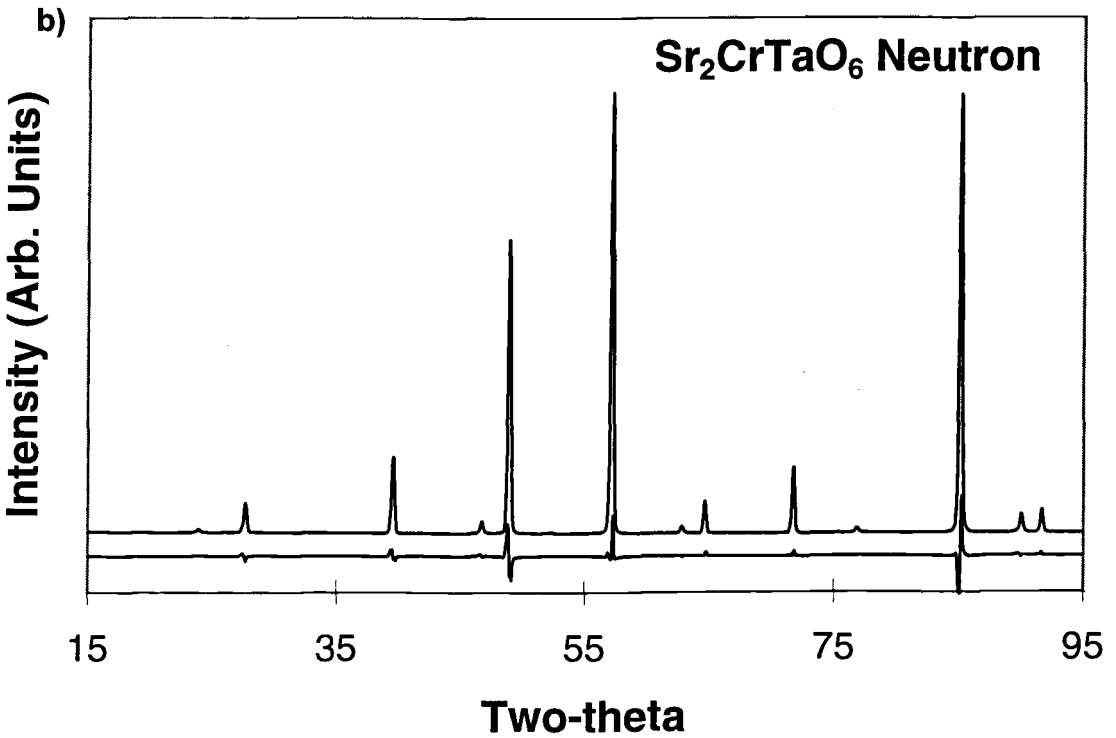
b)
Sr_2CrTaO_6 Neutron
Intensity (Arb. Units)
15
35
55
75
95
Two-theta

Figure 4.5

a)

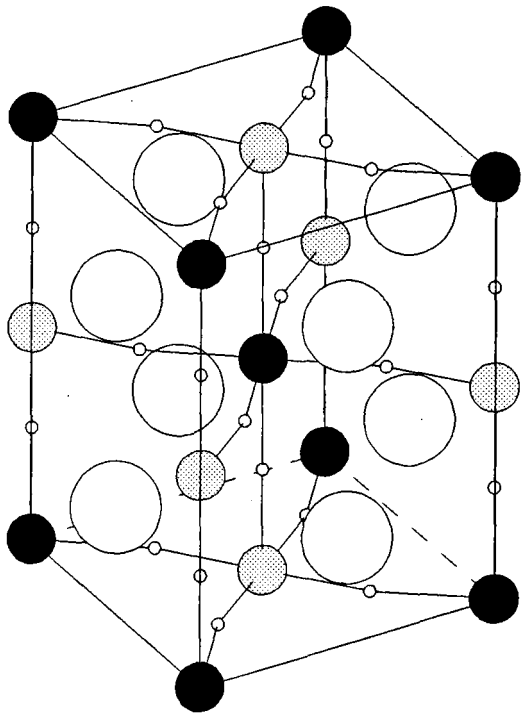

b)

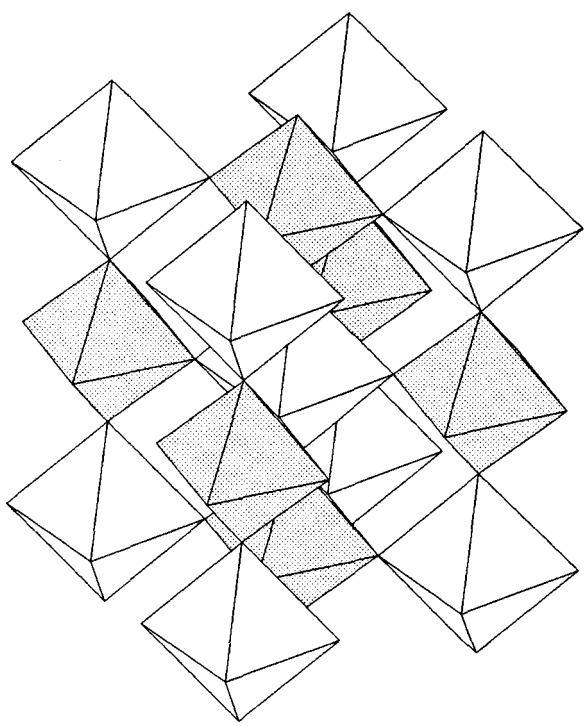

Figure 4.6

Bond Distances (Å)			
Sr-O1	4×2.705(3)	M/M'-O1	4×1.921(4)
	4×2.872(3)	M/M'-O2	2×1.970(1)
Sr-O2	4×2.787(3)		
Bond Angles			
M-O1-M'	173.1(6)°	O1-M-O1	90°
M-O2-M'	180°	O1-M-O2	90°
Polyhedral Volumes ($Å^3$)		*Bond Valences*	
Sr	51.0	Sr	2.00
Cr	10.2	Cr	3.06
Ta	10.2	Ta	5.20
		O	2.04

Table 4.7 : Bond distances, angles, MO_n polyhedral volumes, and bond valences for Sr_2CrTaO_6, based on the structure determined from the neutron powder diffraction refinement. Calculations performed as in table 4.5. M represents the Cr rich octahedral site and M' the Ta rich site.

Comparison of the neutron pattern of Sr_2CrTaO_6 (figure4.4) with the one presented earlier for Sr_2AlTaO_6 (figure 4.2) shows that the superstructure reflections, while still weak, are now clearly visible. However, the neutron scattering lengths of the aluminum and chromium, 0.345 cm and 0.352 cm respectively (Ibers & Hamilton, 1974), are nearly identical. Therefore, any increase in the superstructure peak intensity must be due either to a dramatic increase in the long range cation order or to an octahedral tilting distortion. X-ray measurements indicate that the long range order in Sr_2CrTaO_6 is smaller than it is in Sr_2AlTaO_6, leading to the conclusion that an octahedral tilting distortion is present in Sr_2CrTaO_6. Rietveld refinements of the neutron diffraction pattern in both $a^0a^0a^0$ and $a^0a^0c^-$ tilt systems confirm this distortion. The weighted R factor drops from 11.76% to 9.83% upon lowering the symmetry from cubic to tetragonal. This is in contrast to refinements using X-ray diffraction data where both models give essentially equivalent fits to the diffraction pattern. Figure 4.4 shows the difference patterns for the superstructure reflections using both cubic and tetragonal models for refinement. This figure clearly illustrates the superior fit of the tetragonal model. The neutron data were also refined using the rhombohedral tilt system $a^-a^-a^-$ as a starting model. The rhombohedral model refined to a weighted R value of 9.97%. This value is not much higher than the residual obtained using tetragonal model, but one of the superstructure reflections, the cubic (531) reflection, fits much better in the tetragonal space group. Based on these results one can confidently assign Sr_2CrTaO_6 to the $a^0a^0c^-$ tilt system. The neutron and X-ray refinement results are given in table 4.6, while

the bond distances, polyhedral volumes, and bond valences are contained in table 4.7. Figure 4.5 shows the observed and difference patterns for both the X-ray and neutron diffraction analyses, figure 4.6 shows the structure.

One unusual feature of the neutron refinement was the tendency for oxygen to remain equidistant from both the chromium and tantalum rich sites. The values reported in table 4.6 were obtained by fixing the oxygen positional parameters so that equivalent distances to both octahedral sites were maintained. The refinement could also be carried out in the absence of this constraint, but no improvement in the R_{wp} was observed when this done, nor did the oxygen ions move closer to either of the two octahedral sites. This did however, cause the standard deviations on the oxygen parameters to go up significantly. This behavior is undoubtedly due to the partial cation ordering and the similar ionic radii of Ta^{5+} and Cr^{3+}.

4.4.3 Ca_2CrTaO_6

Like Sr_2CrTaO_6, the structure of Ca_2CrTaO_6 was recently reported by Choy *et al.* (Choy, Park, Hong & Kim, 1994). Based on Rietveld refinements of X-ray diffraction data, they found Ca_2CrTaO_6 to be a partially ordered monoclinic perovskite. Refinements of neutron and X-ray powder patterns in this study confirm their conclusion. The results of these refinements are included in this discussion to illustrate the increased accuracy with which the structure can be determined using both X-ray and neutron methods. A very accurate structure determination is essential in order to study subtle changes in bonding between two similar structures, as Choy and coworkers were attempting to do. In the discussion section some of their conclusions will be revisited in light of the improved structural data.

Table 4.8 contains the results of X-ray and neutron refinements carried out on Ca_2CrTaO_6. Figure 4.7 shows the observed and difference curves for both X-ray and neutron diffraction patterns. The line splitting and appearance of several superstructure peaks in the low angle region of the spectrum are clear indications of the $a^+b^-b^-$ monoclinic perovskite structure. Because the oxygen ions are now significantly displaced from their positions in the cubic structure, many more peaks are present in the diffraction patterns. This is particularly evident in the neutron diffraction pattern which is much more complex than the corresponding patterns for Sr_2AlTaO_6 and Sr_2CrTaO_6. The structure is shown in figure 4.8 and the tilting about all three Cartesian axes is evident in the final orientations of the octahedra. Table 4.9 contains the pertinent geometrical analysis of the structure,

Compound (1400°C)	Ca_2CrTaO_6	**Compound (1400°C)**	Ca_2CrTaO_6
Diffraction Method	**Neutron**	**Diffraction Method**	**X-ray**
Space Group	**$P2_1/n$ (A-14-2)**	**Space Group**	**$P2_1/n$ (A-14-2)**
Z	**2**	**Z**	**2**
Cell Parameters		**Cell Parameters**	
a	**5.42340(7)Å**	**a**	**5.4245(1)Å**
b	**5.49657(6)Å**	**b**	**5.4981(1)Å**
c	**7.7149(1)Å**	**c**	**7.7163(2)Å**
β	**90.006(4)°**	**β**	**90.02(3)°**
Order Parameter	**60%**	**Order Parameter**	**66%**
Wavelength	**1.8857Å**	**Radiation**	**Cu Kα**
Two-Theta Range	**15-160°**	**Two-Theta Range**	**2-150°**
# of Reflections	**266**	**# of Reflections**	**473**
# of Parameters	**33**	**# of Parameters**	**41**
R_{WP}	**6.77%**	**R_{WP}**	**7.39%**
χ^2	**2.12**	**χ^2**	**1.69**
R_I	**2.98%**	**R_I (Subcell)**	**1.77%**
		R_I (Supercell)	**2.05%**

Atom	Site	x	y	z	Occ	B ($Å^2$)
Neutron Diffraction						
Ca	4e	0.506(1)	0.5384(8)	0.256(3)	1.0	1.2(1)
Cr1	2d	½	0	0	0.82(4)	0.26(7)
Ta1	2d	½	0	0	0.18	0.26
Ta2	2c	0	½	0	0.82	0.26
Cr2	2c	0	½	0	0.18	0.26
O1	4e	0.214(2)	0.211(2)	-0.043(2)	1.0	0.7(3)
O2	4e	0.298(2)	0.706(2)	-0.037(2)	1.0	0.4(3)
O3	4e	0.4232(7)	-0.0194(6)	0.249(2)	1.0	0.7(1)
X-ray Diffraction						
Ca	4e	0.502(1)	0.539(1)	0.242(2)	1.0	0.6(1)
Cr1	2d	½	0	0	0.829(3)	0
Ta1	2d	½	0	0	0.171	0
Ta2	2c	0	½	0	0.829	0
Cr2	2c	0	½	0	0.171	0
O1	4e	0.239(2)	0.218(4)	-0.044(5)	1.0	0
O2	4e	0.307(4)	0.707(5)	-0.033(7)	1.0	0
O3	4e	0.420(3)	-0.022(4)	0.245(5)	1.0	0

Table 4.8 : Results of Rietveld refinements of neutron and X-ray powder diffraction data for Ca_2CrTaO_6. The long range order parameters were calculated using the formula, S=2×Occ(Cr1)-1. The thermal parameters for Cr, Ta, and O tended to go slightly negative in the X-ray refinement, and were therefore, fixed at zero.

Bond Distances (Å)	Neutron Refinement	X-ray Refinement	Choy, Park, Hong & Kim
M-O1	2×1.97(1)	2×1.89(1)	2×1.89(3)
M-O2	2×1.97(1)	2×1.94(3)	2×1.91(3)
M-O3	2×1.97(1)	2×1.94(4)	2×1.97(3)
M'-O1	2×2.00(1)	2×2.05(1)	2×2.07(2)
M'-O2	2×1.99(1)	2×2.03(2)	2×2.05(3)
M'-O3	2×1.98(1)	2×2.02(4)	2×1.90(2)
Ca-O1	2.65(2)	2.85(2)	2.72(4)
	2.52(2)	2.47(2)	2.61(4)
	2.45(2)	2.53(2)	2.38(4)
Ca-O2	2.64(2)	2.54(5)	2.40(4)
	2.50(2)	2.35(4)	2.38(4)
	2.55(2)	2.78(4)	2.27(4)
Ca-O3	2.305(6)	2.45(2)	2.34(2)
	2.407(7)	2.32(2)	2.46(1)
Bond Angles			
O1-M-O2	88.8(5)°	M-O1-M'	154.3°
O1-M-O3	88.3(5)°	M-O2-M'	153.4°
O2-M-O3	88.8(5)°	M-O3-M'	154.9°
O1-M'-O2	87.5(5)°		
O1-M'-O3	89.9(5)°		
O2-M'-O3	90.0(5)°		

Polyhedral Volumes ($Å^3$)		*Bond Valences*	
Ca (8 coord.)	25.8	Ca	1.97
Ca (difference)	47.1	Cr	3.10
Cr	10.2	Ta	4.96
Ta	10.5	O1	2.00
		O2	1.93
		O3	2.06

Table 4.9 : Bond distances, angles, MO_n polyhedral volumes, and bond valences for Ca_2CrTaO_6. Bond distances are reported for the structure determined from the neutron refinement, the X-ray refinement, and the values in the literature. All other parameters are based only on the neutron refinement. Polyhedral volumes were calculated using IVTON (Zunic & Vickovic, 1996) and bond valences were calculated using EUTAX (O'Keeffe, 1992). M represents the Cr rich octahedral site and M' the Ta rich site. The bond valences were calculated by taking the M and M' sites to be fully occupied by Cr and Ta respectively. The polyhedral volume for Ca was calculated in two ways, once in IVTON using a coordination number of eight, and again by subtracting the Cr and Ta polyhedral volumes from the total unit cell volume.

Figure 4.7 : Observed and difference patterns for selected regions of the a) X-ray and b) neutron diffraction patterns of Ca_2CrTaO_6. The two-theta scales have been chosen so that the d-spacing range is approximately equal in X-ray and neutron patterns. The asterisks represent a small $Ca_3Ta_2CaO_9$ impurity.

Figure 4.8 : The structure of Ca_2CrTaO_6. In part a) the atoms in the unit cell are represented as spheres with black spheres representing the chromium rich site, shaded spheres the tantalum rich site, large open spheres represent calcium, and the small open spheres oxygen. The atomic radii of the oxygen atoms have been made very small for clarity while the other atoms are shown at one half their normal radii. In part b) only the CrO_6 and TaO_6 octahedra are shown.

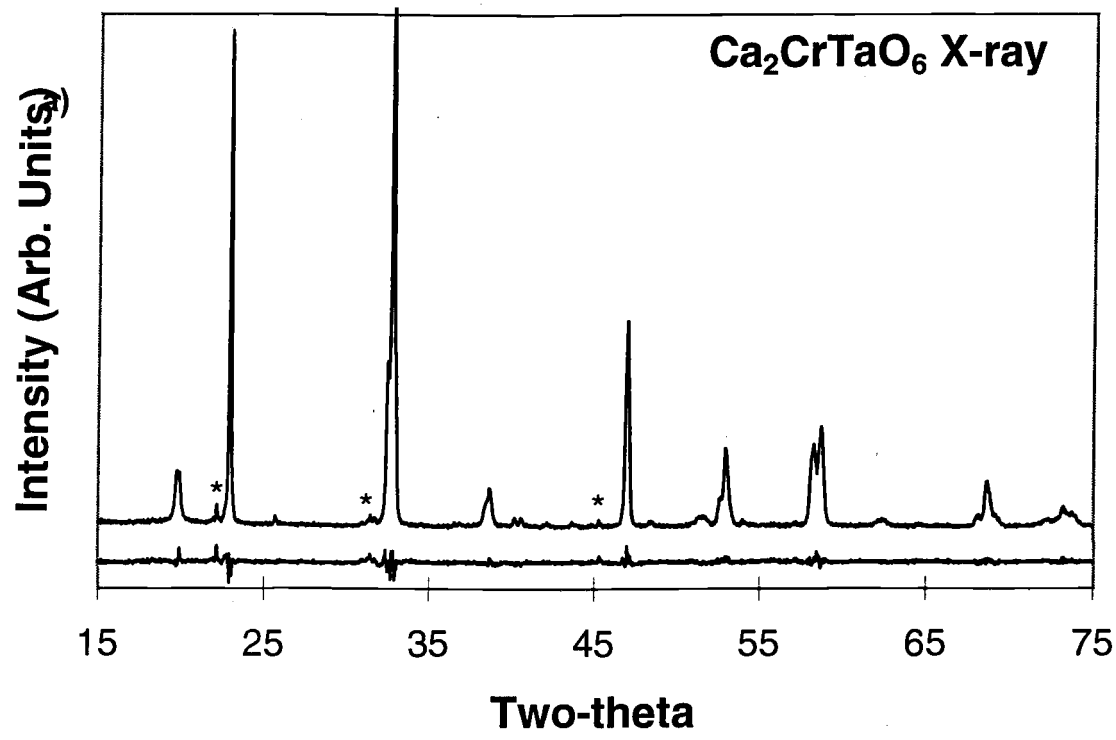
a)
Ca2CrTaO6 X-ray
Intensity (Arb. Units)
*
*
*
15
25
35
45
55
65
75
Two-theta

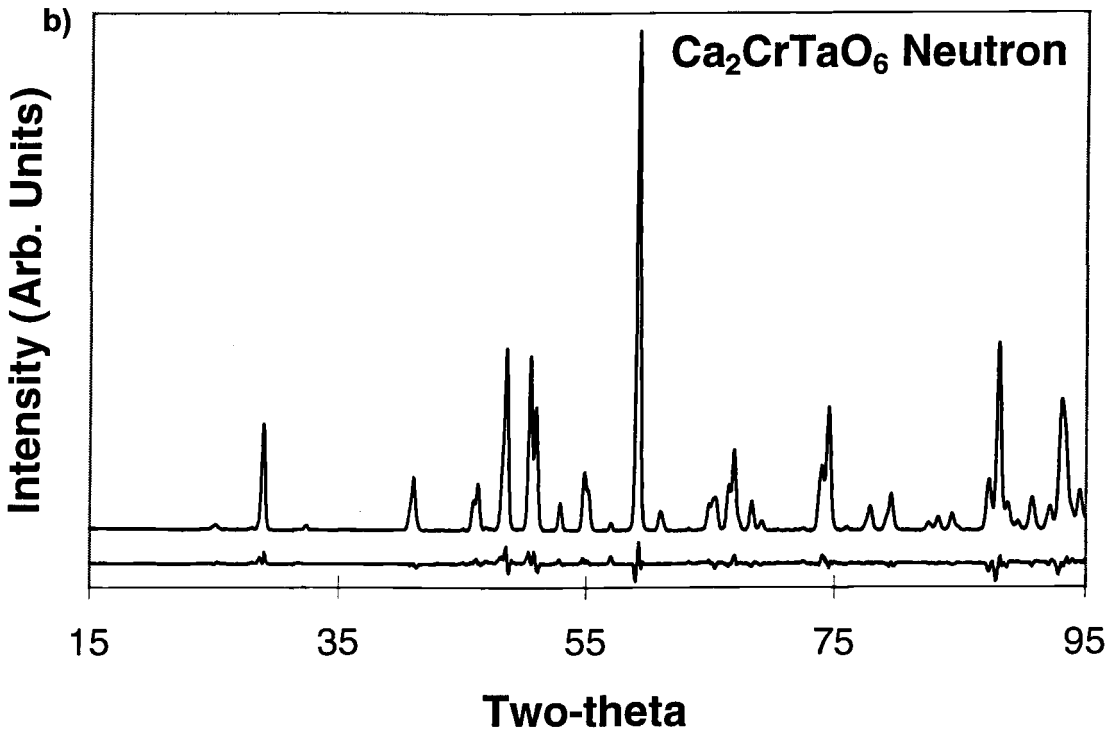
b)
Ca2CrTaO6 Neutron
Intensity (Arb. Units)
15
35
55
75
95
Two-theta

Figure 4.7

a)

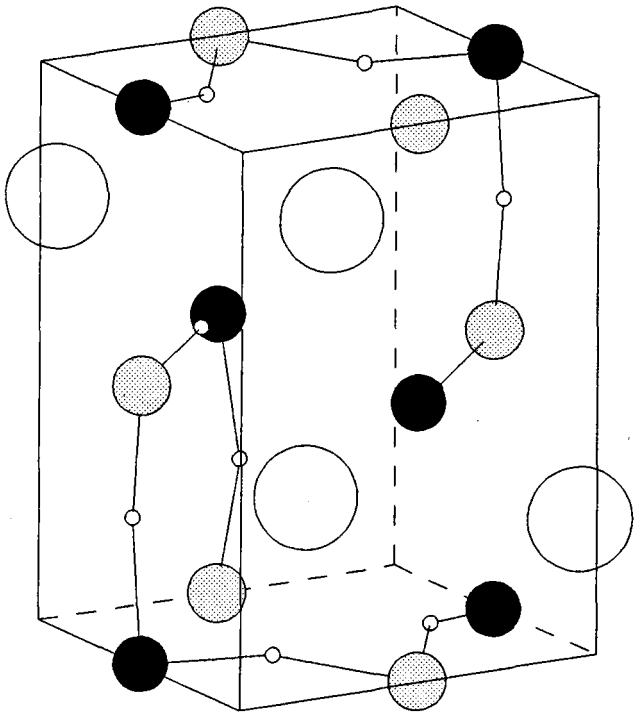

b)

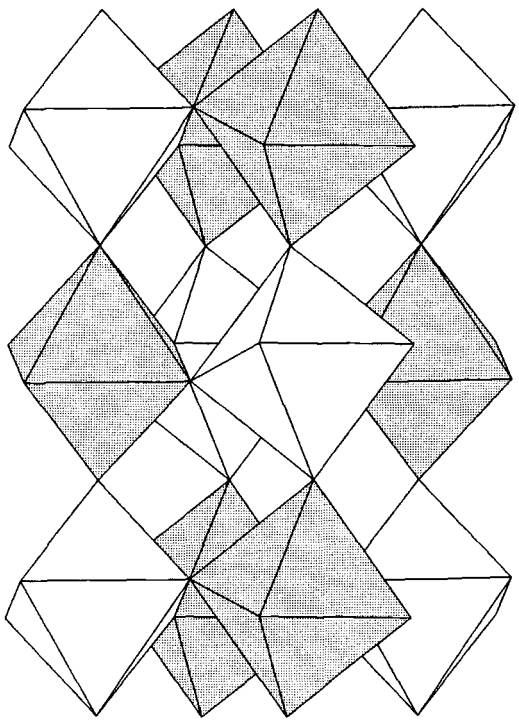

Figure 4.8

including a comparison of the bond distances determined by Choy and coworkers, with the bond distances determined in this study. Notice that the structure determined from neutron diffraction shows negligible distortion of the octahedral units, and bond valences which are very close to the ideal bond values for each ion. In contrast both X-ray structure determinations find significant anisotropy in the metal-oxygen bond distances. This comparison gives a measure of the accuracy with which bond distances can be determined using powder X-ray diffraction in pseudo cubic perovskites. Accurately determining the oxygen positions is particularly difficult in low symmetry crystal systems such as monoclinic and triclinic, where the number of free positional parameters is large, but the number of independently resolved peaks has not increased in a proportional manner.

4.4.4 Sr_2YTaO_6

Kupriyanov and Filip'ev reported Sr_2YTaO_6 to be a rhombohedrally distorted perovskite which transformed to cubic symmetry at 640°C, but no structural refinement was carried out (Kupriyanov & Filip'ev, 1963). Since there are relatively few examples of double perovskites with the rhombohedral unit cell, this compound appeared to be an interesting candidate for further structural studies. Unexpectedly, the X-ray powder diffraction pattern showed a complex peak splitting which could not be indexed using the rhombohedral unit cell reported in the literature. Furthermore, the pattern of peak splitting was different than that observed for Ca_2CrTaO_6 and could not be indexed using a pseudo-orthorhombic cell. Finally, the pattern was indexed using a monoclinic cell with approximate lattice constants of: a=5.86Å, b=5.81Å, c=8.24Å, and α=89.86°. However, all attempts to refine the structure in space group $P2_1/n$ (tilt system $a^+b^-b^-$) were unsatisfactory. Eventually, a satisfactory fit of the X-ray data was obtained using space group $P\bar{1}$, but the standard deviations on the oxygen positions were still quite high, and the bond distances were somewhat unrealistic. Therefore, a large sample was prepared and neutron diffraction data was collected on the HRNPD at Brookhaven National Laboratory. Table 4.10 contains the results of both the X-ray and the neutron refinements, and the pertinent structural details have been tabulated in table 4.11. Figure 4.9 shows the observed and difference patterns for both the X-ray and neutron refinements.

The structure of Sr_2YTaO_6 is shown in figure 4.10. It is quite similar to the structure of Ca_2CrTaO_6 but the octahedral tilting arrangement is slightly different. Ca_2CrTaO_6 belongs to

Table 4.10 : Results of Rietveld refinements of neutron and X-ray powder diffraction data for Sr_2YTaO_6. The long range order parameters were calculated using the formula, S=2×Occ(Y1)-1.

Table 4.11 : Bond distances, angles, MO_n polyhedral volumes, and bond valences for Sr_2YTaO_6, based on the structure determined from neutron powder diffraction. Polyhedral volumes were calculated using IVTON (Zunic & Vickovic, 1996) and bond valences were calculated using EUTAX (O'Keeffe, 1992).

Figure 4.9 : Observed and difference patterns for selected regions of the a) X-ray and b) neutron diffraction patterns of Sr_2YTaO_6. The two-theta scales have been chosen so that the d-spacing range is approximately equal in X-ray and neutron patterns. The asterisks represent a small Y_2O_3 impurity.

Figure 4.10 : The structure of Sr_2YTaO_6. In part a) the atoms are represented as spheres with the black spheres representing yttrium, the shaded spheres tantalum, the large open spheres strontium, and the small open spheres oxygen. The atomic radii of the oxygen atoms have been made very small for clarity while the other atoms are shown at one half their normal radii. In part b) only the YO_6 and TaO_6 octahedra are shown.

Compound	Sr_2YTaO_6 (1500°C)	Compound	Sr_2YTaO_6 (1500°C)
Diffraction Method	Neutron	Diffraction Method	X-ray
Space Group	$P\bar{1}$ (A-2)	Space Group	$P\bar{1}$ (A-2)
Z	2	Z	2
Cell Parameters		Cell Parameters	
a	5.85553(8)Å	a	5.85705(7)Å
b	5.80864(8)Å	b	5.80946(7)Å
c	8.2403(1)Å	c	8.2415(1)Å
α	89.854(1)°	α	89.857(1)°
β	90.016(4)°	β	90.044(2)°
γ	89.974(2)°	γ	89.995(2)°
Order Parameter	100%	Order Parameter	100%
Wavelength	1.8857Å	Radiation	Cu Kα
Two-Theta Range	5-157°	Two-Theta Range	2-150°
# of Reflections	646	# of Reflections	1159
# of Parameters	49	# of Parameters	55
R_{WP}	11.41%	R_{WP}	11.48%
χ^2	3.40	χ^2	2.09
R_I	5.78%	R_I	3.65%

Atom	Site	x	y	z	Occ	B ($Å^2$)
Neutron Diffraction						
Sr1	2i	0.527(2)	0.514(2)	0.250(3)	1.0	0.65(8)
Sr2	2i	0.970(2)	0.999(3)	0.751(3)	1.0	0.65
Y1	1c	0	½	0	1.0	0.22(6)
Y2	1f	½	0	½	1.0	0.22
Ta1	1d	½	0	0	1.0	0.22
Ta2	1g	0	½	½	1.0	0.22
O1	2i	0.223(3)	0.194(3)	-0.036(3)	1.0	0.8(1)
O2	2i	0.273(3)	0.694(4)	0.455(3)	1.0	0.8
O3	2i	0.282(2)	0.730(3)	0.039(2)	1.0	0.6(1)
O4	2i	0.176(2)	0.221(3)	0.537(2)	1.0	0.6
O5	2i	0.490(2)	0.071(3)	0.236(3)	1.0	0.6(1)
O6	2i	-0.029(3)	0.418(3)	0.260(3)	1.0	0.6
X-ray Diffraction						
Sr1	2i	0.522(1)	0.493(1)	0.248(2)	1.0	0.36(4)
Sr2	2i	0.961(1)	0.991(1)	0.750(2)	1.0	0.36
Y1	1c	0	½	0	1.0	0.00(2)
Y2	1f	½	0	½	1.0	0.00
Ta1	1d	½	0	0	1.0	0.00
Ta2	1g	0	½	½	1.0	0.00
O1	2i	0.18(1)	0.213(9)	-0.028(8)	1.0	0.0(4)
O2	2i	0.282(8)	0.80(1)	0.553(7)	1.0	0.0
O3	2i	0.230(9)	0.71(2)	-0.028(8)	1.0	0.0
O4	2i	0.205(8)	0.21(1)	0.534(9)	1.0	0.0
O5	2i	0.498(9)	0.885(8)	0.259(7)	1.0	0.0
O6	2i	0.023(9)	0.413(9)	0.247(7)	1.0	0.0

Table 4.10

Bond Distances (Å)			
Sr1-O1	2.73(3)	Sr2-O1	2.68(3)
O2	2.65(3)	O1	2.78(3)
O2	2.89(3)	O2	2.70(3)
O3	2.70(2)	O3	2.63(3)
O3	2.90(3)	O4	2.59(3)
O4	2.79(2)	O4	2.79(3)
O5	2.61(2)	O5	2.51(2)
O6	2.43(2)	O6	2.53(3)
Y1-O1	2×2.23(2)	Y2-O2	2×2.25(2)
O3	2×2.15(1)	O4	2×2.31(1)
O6	2×2.21(2)	O5	2×2.21(3)
Ta1-O1	2×2.00(2)	Ta2-O2	2×1.99(2)
O3	2×2.05(2)	O4	2×1.94(2)
O5	2×1.99(2)	O6	2×2.03(2)
Bond Angles			
O1-Y1-O3	93.8(7)°	O2-Y1-O4	91.6(7)°
O1-Y1-O6	90.3(7)°	O2-Y1-O5	91.9(7)°
O3-Y1-O6	92.4(7)°	O4-Y1-O5	90.3(6)°
O1-Ta1-O3	92.9(7)°	O2-Ta1-O4	94.5(8)°
O1-Ta1-O5	90.2(8)°	O2-Ta1-O6	88.8(9)°
O3-Ta1-O5	90.9(7)°	O4-Ta1-O6	90.1(7)°
Ta1-O1-Y1	155.1(5)°	Ta2-O2-Y2	153.2(6)°
Ta1-O3-Y1	158.4(6)°	Ta2-O4-Y2	151.3(5)°
Ta1-O5-Y2	157.1(6)°	Ta2-O6-Y1	152.4(7)°
Polyhedral Volumes ($Å^3$)			
Sr1(8 coord.)	32.4	Y1	14.1
Sr2 (8 coord.)	30.5	Y2	15.3
Sr (ave. diff.)	57.4	Ta1	10.8
		Ta2	10.5
Bond Valences			
Sr1	1.71	O1	1.94
Sr2	1.99	O2	1.98
Y1	3.69	O3	1.99
Y2	3.12	O4	2.02
Ta1	4.69	O5	1.99
Ta2	5.00	O6	2.04

Table 4.11

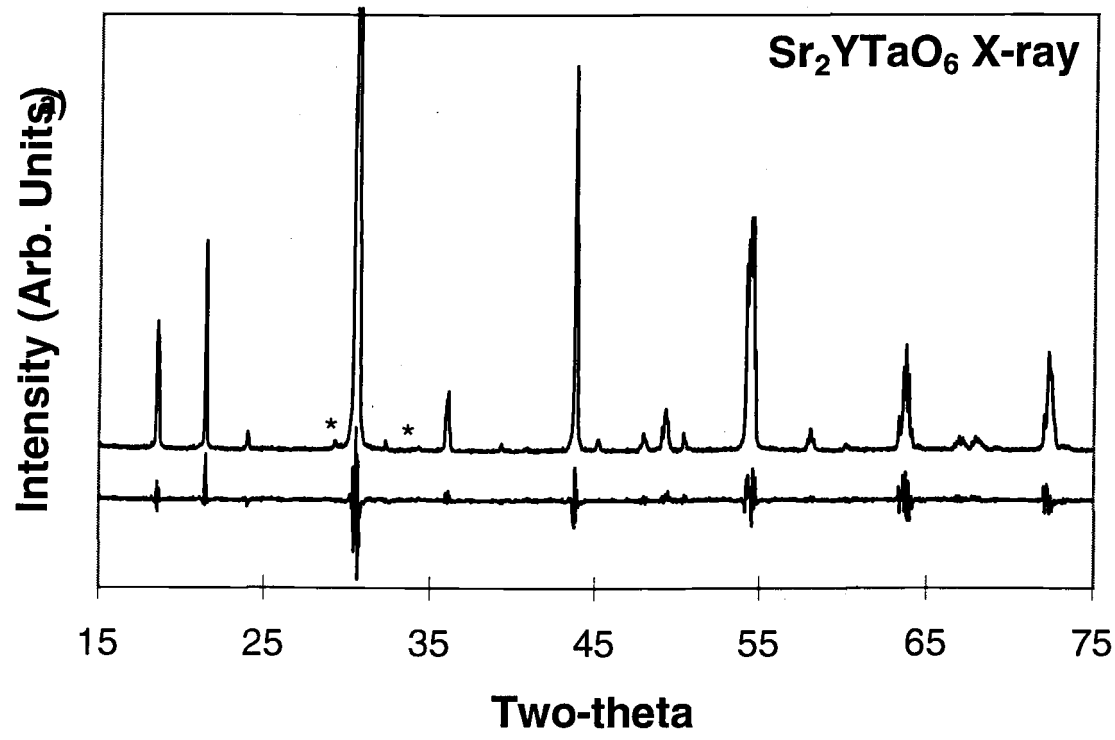
a)
Sr_2YTaO_6 X-ray
Intensity (Arb. Units)
*
*
15
25
35
45
55
65
75
Two-theta

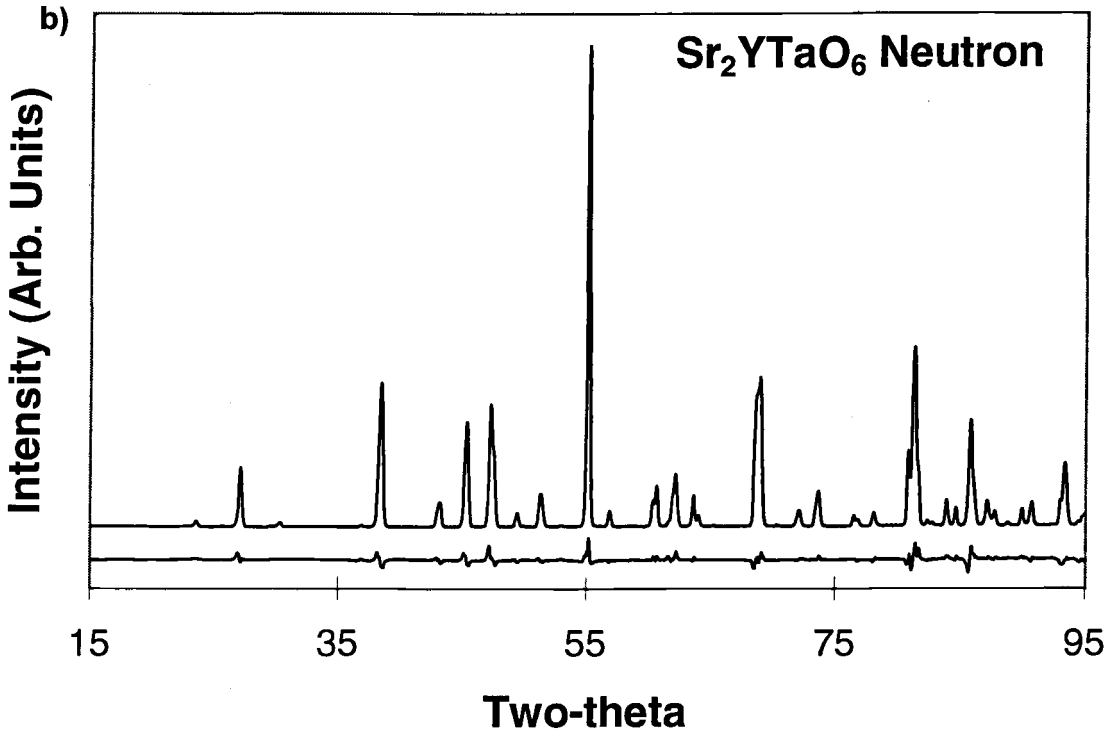
b)
Sr_2YTaO_6 Neutron
Intensity (Arb. Units)
15
35
55
75
95
Two-theta

Figure 4.9

a)

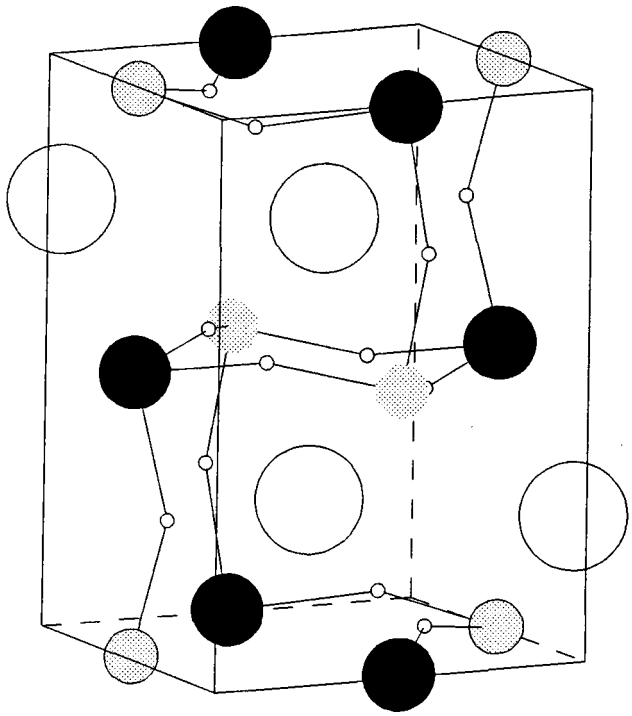

b)

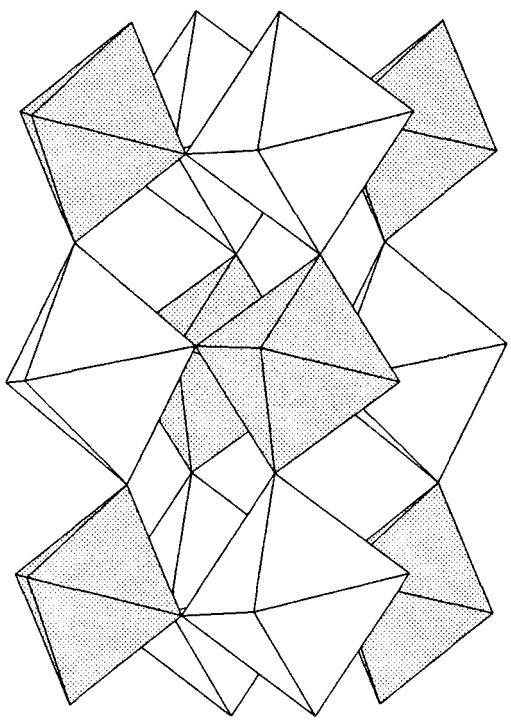

Figure 4.10

tilt system $a^+b^-b^-$ (#10) which is the most commonly observed tilt system among distorted perovskites, while Sr_2YTaO_6 belongs to the rarely observed $a^+b^-c^-$ (#8) tilt system. The triclinic symmetry of Sr_2YTaO_6 is in agreement with the predictions in chapter two for tilt system $a^+b^-c^-$. The different tilting arrangements of Ca_2CrTaO_6 and Sr_2YTaO_6 will be discussed in more detail later in the discussion section.

4.5 Discussion

The results of the structural analysis on these four compounds show that for each compound the structural distortion can truly be described as tilting of essentially rigid octahedra. In Sr_2AlTaO_6, Sr_2CrTaO_6, and Ca_2CrTaO_6 the octahedral distortions are negligible, within experimental error. In Sr_2YTaO_6 the octahedra are slightly distorted, but the extent of this distortion is still relatively small. The relationship between the structure and the tilt system can easily be seen by viewing the structure parallel to the directions along which the octahedra share corners. For the large (Z=4) cell those directions are parallel to the Cartesian axes [100], [010], and [001]. The equivalent directions in the $\sqrt{2}$ cell with long axis running in the c direction are [$\bar{1}$ 10], [110], and [001]. Figure 4.11 shows a view of Sr_2AlTaO_6 and Sr_2CrTaO_6 looking down the [001] direction. Here one can see that the octahedra have rotated slightly about this axis in Sr_2CrTaO_6 ($\cong$3.5°), and the rotations are in opposite directions in adjacent layers. This is consistent with the tilt system $a^0a^0c^-$. Figure 4.12 shows the polyhedral representations of Ca_2CrTaO_6 and Sr_2YTaO_6 looking down the [$\bar{1}$ 10], [110], and [001] directions. In each structure the tilts are out of phase (in opposite directions in adjacent layers) in two directions and in phase in the third direction. The subtle difference between the two structures is in the directions of the tilts. Considering the axes about which out of phase tilting occurs in Ca_2CrTaO_6, the tilt direction and magnitude are the same for both axes. This can be seen by examining the upper left octahedron of figures 4.12a and 4.12b and observing that it tilts in a clockwise sense in both the [$\bar{1}$ 10] and [110] directions. A similar examination of Sr_2YTaO_6 shows that each octahedron is tilted in the opposite direction in figure 4.12e from its orientation in 4.12d. To further check this each structure was simulated using POTATO and the bond distances determined in the structural analysis. The results of the POTATO modeling are as given in table 4.12. The results confirm that the out of phase tilt angles in Sr_2YTaO_6 are in opposite directions. This change in the tilt orientations is responsible for lowering the symmetry from $P2_1/n$ to $P\bar{1}$.

Figure 4.11 : Polyhedral representations looking down the [001] direction of a) Sr_2AlTaO_6 and b) Sr_2CrTaO_6. The white polyhedra represent the tantalum rich octahedra, while the shaded polyhedra represent the aluminum and chromium rich octahedra respectively. The open spheres represent strontium.

Figure 4.12 : The polyhedral representations of Ca_2CrTaO_6 looking down the a) [110] direction, b) [$\bar{1}$10] direction, and c) [001] direction. The second half of the figure is a polyhedral representation of Sr_2YTaO_6 looking down the d) [110] direction, e) [$\bar{1}$10] direction, and f) [001] direction. The white polyhedra represent the tantalum rich octahedra, while the shaded polyhedra represent the chromium rich and yttrium octahedra respectively. The open spheres represent calcium and strontium respectively.

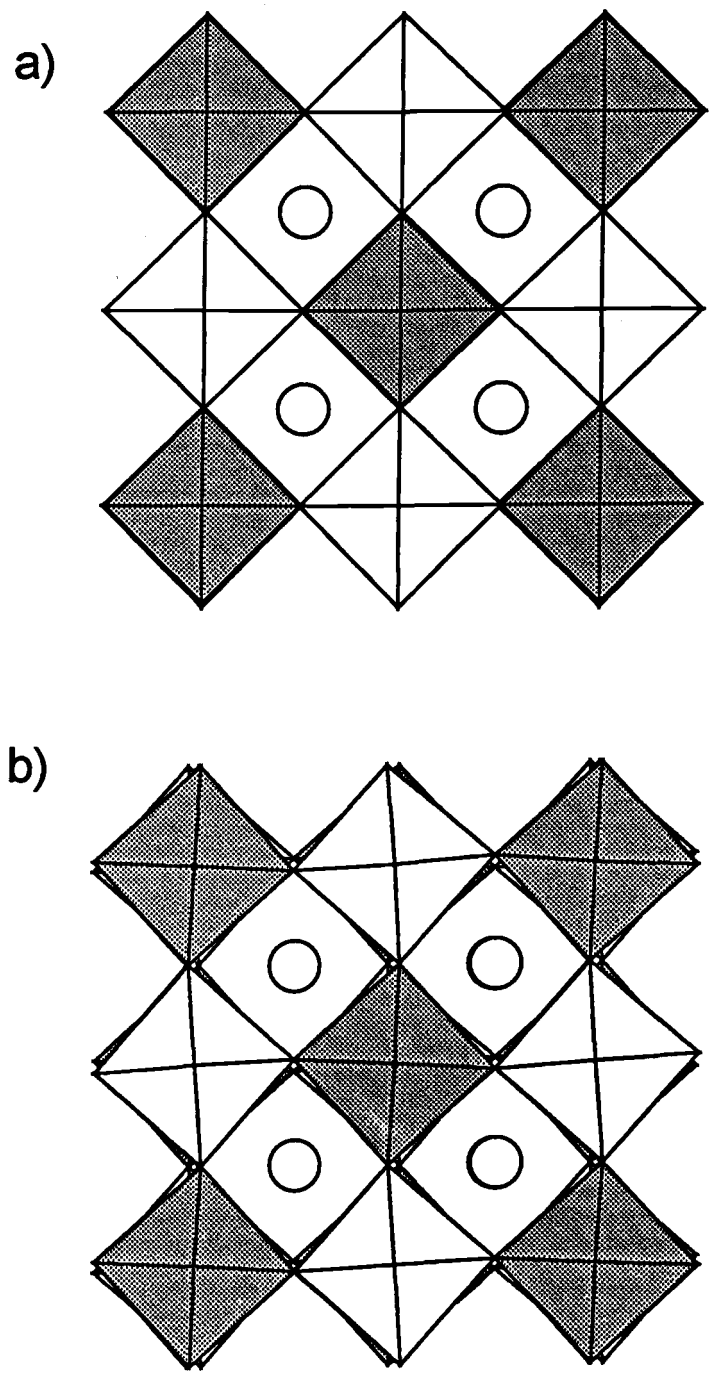

Figure 4.11

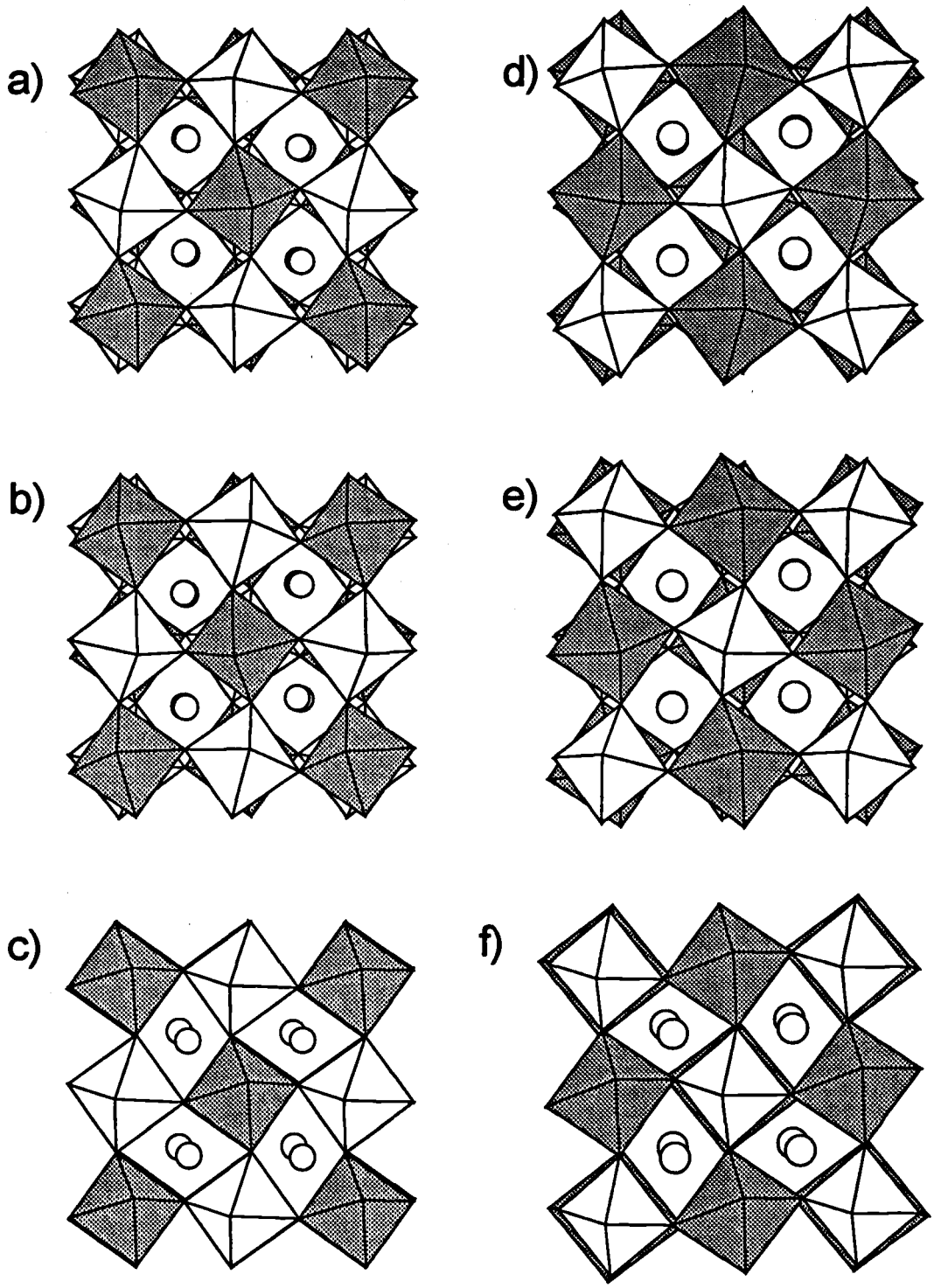

Figure 4.12

Compound	Tilt System	Approximate Tilt Angles
Sr_2AlTaO_6	$a^0a^0a^0$	0°,0°,0°
Sr_2CrTaO_6	$a^0a^0c^-$	0°,0°,3.5°
Ca_2CrTaO_6	$b^-b^-a^+$	-9.2°,-9.2°,9.0°
Sr_2YTaO_6	$a^-b^-c^+$	-7.5°,8.0°,9.5°

Table 4.12 : Approximate tilt angles of A_2MTaO_6 compounds in Glazer notation.

Table 2.4 indicates that five tilt systems can lead to triclinic perovskites, $a^0b^-c^-$ (#19), $a^-b^-b^-$ (#13), $a^-b^-c^-$ (#12), $a^+a^-b^-$ (#9), and $a^+b^-c^-$ (#8). These tilt systems are related by the fact that perpendicular to two of the three Cartesian axes the tilt angles are of different magnitudes and out of phase, $(a^{+/-/0})b^-c^-$. A search of the inorganic crystal structure database (ICSD) reveals three double perovskite compounds with triclinic symmetry. Those compounds are Ba_2LaRuO_6 (Battle, Goodenough & Price, 1983), $Ba_2LaRu_{.5}Sb_{.5}O_6$ (Almaer *et al.*, 1993), and Ca_2LaRuO_6 (Battle, 1981).

All three compounds have been assigned to space group $I\bar{1}$, which is the predicted symmetry for tilt system $a^0b^-c^-$ (#19). A visual inspection of these structures reveals out of phase tilting about two axes in opposite directions (clockwise and counterclockwise) and no tilting about the third axis. Therefore, Sr_2YTaO_6 appears to be the first structurally characterized member of tilt system $a^+b^-c^-$.

The driving force which causes the two tilt out of phase tilt angles to be in opposite directions is at this time unclear. However, among this limited set of compounds the common feature is a tolerance factor in the range $0.93 < t < 1.0$, and a large mismatch in the ionic radii of the two octahedral cations. No other structurally determined perovskite compounds with this combination of ionic radii could be found in the literature. Interestingly though some studies of lattice constants behavior, in compounds where a large mismatch in the ionic radii of the octahedral cations exists, have indicated unusual behavior. In 1966 Filip'ev and Fesenko studied a series of compounds with the formula A_2LnMO_6, where A was Sr or Ba, Ln was a rare earth, and M was either Nb or Ta (Filip'ev & Fesenko, 1966). When A was Ba they claimed that for Ln=La, Pr, Nd, or Sm they observed a rhombohedrally distorted perovskite, and for Ln=Eu,Gd,Tb,Dy,Ho,Er,Tm,Yb, or Lu the structure was cubic. Whereas, when A was Sr the structure was monoclinic for rare earth ions from La to Er, and of unknown pseudo-cubic symmetry for R=Tm and Lu. The same trends were observed for both Nb and Ta. The errors associated with assigning symmetry based on lattice constants

has been well documented in this chapter, and it seems likely that the true symmetry is lower. Recall that Kupriyanov and Filip'ev originally assigned rhombohedral symmetry to Sr_2YTaO_6 (Kupriyanov & Filip'ev, 1963). More recently Trunov, Sirotinkin, and Evdokimov also studied the series Sr_2LnTaO_6 and Sr_2LnNbO_6 by powder x-ray diffraction. In both series of compounds they found an abrupt change in the unit cell volume on going from Ln=Er to Ln=Tm. Based on the lattice constants they assigned monoclinic symmetry to those compounds containing a larger rare earth, and orthorhombic symmetry when Ln=Tm, Yb, or Lu (Trunov, Sirotinkin & Evdokimov, 1983). Once again because of the high pseudo-symmetry of in distorted perovskites these assignments could easily be incorrect. Based on the lattice constant behavior and the combination of ionic radii found in these compounds, full structure determination in these compounds would probably enlarge the scope of triclinic perovkites.

The compositional and structural similarity of these four compounds provide a good opportunity to examine the effect of cation substitution on the structure and bonding in perovskites. From the ionic radii of these compounds[†] the tolerance factors for Sr_2AlTaO_6, Sr_2CrTaO_6, Ca_2CrTaO_6, and Sr_2YTaO_6 are calculated to be 1.018, 0.998, 0.962, and 0.931 respectively. In agreement with what was observed for simple perovskites in chapter 3 as the tolerance factor decreases the number of tilt axes increases. As with simple perovskites the driving force for the tilting distortion is to optimize the A-O interaction. In Sr_2AlTaO_6 the bond valence for strontium is 2.15 indicating that Sr-O distances are sufficient to completely satisfy the valency requirements of strontium. Repulsive interactions between strontium and oxygen presumably prevent further shortening of the Sr-O bonds, which would occur if octahedral tilting were present. In Sr_2CrTaO_6 substituting chromium for aluminum expands the corner sharing octahedral network, causing a slight increase in the Sr-O bond distance in the idealized cubic structure. It was shown in chapter three that all other things being equal, tilting of the octahedra always increases the Madelung energy with respect to the cubic structure. Apparently in Sr_2CrTaO_6 the increased size of chromium lengthens the Sr-O bonds enough so that the Madelung energy gain associated with a small tilting distortion outweighs the increase in Sr-O repulsive interactions. In Ca_2CrTaO_6 and Sr_2YTaO_6 the tolerance factor is small enough that large tilts about all three Cartesian axes are necessary to maintain a reasonable coordination environment for the A cation.

The average Ta-O bond distances for Sr_2AlTaO_6, Sr_2CrTaO_6, Ca_2CrTaO_6, and Sr_2YTaO_6 are 1.97Å, 1.97Å, 1.99Å, and 2.00Å respectively. Across the same series the average M^{3+}-O

bond distances are 1.93Å, 1.97Å, 1.97Å, and 2.23Å. With the exception of aluminum these values are in excellent agreement with the bond distances that would be calculated by summing ionic radii (Shannon, 1976). Thus it appears that the position of the oxygen ion is driven by the ionic radii rather than the charge of the octahedral cations. The ionic radii themselves are dictated by a variety of factors which include both covalent and ionic interactions. Therefore, if one were to conclude that because the Cr-O bond distances were shorter than the Ta-O bond distances in Sr_2CrTaO_6, the Cr-O bonding must be stronger. Would that logic not also lead to the conclusion that the Al-O bonding must be stronger than either Cr-O or Ta-O bonding? Such a line of reasoning is clearly not valid. On the other hand information about how the Ta-O bond distances change across a series of compounds could give some insight into the way in which the other ions compete with tantalum to form bonds with oxygen. Unfortunately, the partial ordering between Cr/Ta and Al/Ta complicate such an analysis.

The increased Al-O bond distance (with respect to the predicted value of 1.885Å) can be attributed to two factors. First of all, there is some disorder between aluminum and tantalum and the presence of the larger tantalum ion on the aluminum site will cause a slight increase in the average bond distance. Secondly, because the tolerance factor is larger than unity the strontium ion is actually too large for the corner sharing octahedral framework. In order to accommodate the strontium ion the octahedral bonds must be stretched to some extent. The "overstuffing" of the lattice by strontium may also help to explain the observed deviation in stoichiometry. The refined stoichiometry, $Sr_{1.92}Ta_{1.08}Al_{0.92}O_6$, contains two features which help to relieve the strain caused by the oversized strontium ion. The substitution of tantalum for aluminum increases the average size of the octahedral cations, thereby expanding the octahedral framework. and the presence of strontium vacancies allows oxygen ions to relax away from occupied strontium sites. This nonstoichiometry may also explain why antiphase boundaries (APB) are so prevalent in this compound, despite the relatively high degree of long range order. A model which places excess tantalum at the APB's is consistent with several experimental facts. An extensive study of this compound found that after annealing at high temperatures the long range order parameter reached a maximum value of approximately 90% (Woodward, Hoffmann & Sleight, 1994). With a vacancy parameter of x=0.08, this corresponds to a stoichiometry of $Sr_{1.92}(Ta_{0.99}Al_{0.01})(Ta_{.09}Al_{0.91})O_6$. Hence, the order has nearly reached its maximum value due to the fact that the Al:Ta ratio is not 1:1. Furthermore, even in these samples the superstructure peaks are still broadened

---

† Ionic radii of Sr=1.44Å, Ca=1.34Å, Al=0.535Å, Cr=0.615Å, Y=0.900Å, Ta=0.64Å and O=1.35Å are taken from Shannon, using coordination numbers of 12 for the A cation, 6 for

considerably by APB's. If such defects are caused by nonstoichiometry then it is not surprising that they cannot be annealed out. Finally, the observation that a lattice expansion occurs at the APB is consistent with a model which places an excess of the larger tantalum ion at the APB. Since the samples are synthesized in a molten $SrCl_2$ flux which is then washed away, it is possible that some aluminum is lost during this process which would help to explain how the nonstoichiometry occurs.

4.6 Conclusions

All of the perovskite compounds synthesized agree with the space group symmetry predictions for double perovskites in chapter two. The structure of Sr_2AlTaO_6 has been shown to be cubic, tilt system $a^0a^0a^0$. Nonstoichiometry of the form $Sr_{2-x}Ta_{1+x}Al_{1-x}O_6$ has also been determined from refinement of both the X-ray and neutron diffraction patterns. This nonstoichiometry may explain the high concentration of antiphase boundaries observed in this compound. Sr_2CrTaO_6 has been shown to be tetragonal, tilt system $a^0a^0c^-$, instead of cubic as had previously been proposed (Choy, Park, Hong & Kim, 1994). The tetragonal symmetry cannot be assigned using X-ray data alone. Neutron diffraction is necessary to ascertain the true structure. Other perovskite compounds listed in the literature as cubic may also have true symmetries which are either tetragonal or rhombohedral. In particular compounds with tolerance factors less than one should be analyzed by neutron diffraction before confident assignment of cubic symmetry can be made. The structures of Ca_2CrTaO_6 and Sr_2YTaO_6 have been determined to be monoclinic ($a^+b^-b^-$) and triclinic ($a^+b^-c^-$) respectively. The structures of the two compounds are quite similar, but the out of phase tilting angles have the same direction and magnitude in Ca_2CrTaO_6, and different directions in Sr_2YTaO_6.

4.7 References

Almaer, S.A., Battle, P.D., Lightfoot, P., Mellen, R.S. & Powell, A.V. (1993). *J. Solid State Chem.*, **102**, 375.

Anderson, M.T., Greenwood, K.B., Taylor, G.A. & Poeppelmeier, K.R. (1993). *Prog. Solid State Chem.* **22,** 197.

---

the octahedral cation, and 2 for the oxygen (Shannon, 1976).

Battle, P.D. (1981). *Mater. Res. Bull.* **16**, 397.

Battle, P.D., Goodenough, J.B. & Price, R. (1983). *J. Solid State Chem.*, **46**, 234.

Choy, J.-H., Park, J.-H., Hong, S.-T., Kim, D.K. (1994). *J. Solid State Chem.*, **111**, 370.

Filip'ev, V.S. & Fesenko, E.G. (1966). *Sov. Phys. Crystallogr.*, **10**, 532.

Hahn, T. Ed. (1983). *International Tables for Crystallography, Vol. A*, Reidel Pub. Co., Boston.

Hamilton, W.C. (1965). *Acta Cryst.* **18**, 502.

Ibers, J.A. & Hamilton, W.C. (1974). *International Tables for Crystallography, Vol. IV*, Kynoch Press, Birmingham, U.K.

Izumi, F. (1989). *Rigaku J.*, **6**, 10.

Izumi, F. (1993). *The Rietveld Method*, ed. R.A. Young, Oxford University Press, Oxford, Ch. 13.

Kupriyanov, M.F. & Filip'ev, V.S. (1963). *Sov. Phys. Crystallogr.*, **8**(3), 278.

Larson, A.C. & Von Dreele, R.B. (1994). *LANSCE*, Los Alamos National Laboratory, Los Alamos, NM.

O'Keeffe, M. (1992). Eutax. Program for calculating bond valences. EMLab Software, Phoenix, Arizona.

Powell, A.V., Gore, J.G. & Battle, P.D. (1993). *J. Alloys Comp.*, **201**, 73.

Shannon, R.D. (1976). *Acta Cryst.*, A**32**, 751.

Trunov, V.K., Sirotinkin, V.P. & Evdokimov, A.A. (1983). *Russ. J. Inorg. Chem.*, **28**(3), 349.

Vegas, A., Vallet-Regi, M., Gonzales-Calbet, J.M., Alario-Franco, M.A. (1986). *Acta. Cryst.*, **B42**, 167.

Woodward, P.M., Hoffmann, R.-D. & Sleight, A.W. (1994). *J. Mater. Res.* **8**, 2118.

Zunic, T.B. & Vickovic, I. (1996). *J. Appl. Cryst.* **29**, 305.

Chapter 5

Synthesis and Structural Characterization of $A_2MM'O_6$ Perovskites

5.1 Introduction

The previous chapter considered structural characterization of four $A_2MM'O_6$ perovskites using both X-ray and neutron diffraction. It was shown that using both techniques highly accurate structure determinations could be carried out. Unfortunately, because of the relatively few places equipped to perform neutron diffraction it is not practical to carry out neutron diffraction on all samples. However, the results of the last chapter also show that it is possible in many cases to obtain good structures using X-ray diffraction independently. The key to this approach is to keep in mind the limitations of the technique. Specifically, all results must be interpreted in light of the following two considerations. First of all, in the presence of cation ordering the cubic ($a^0a^0a^0$), tetragonal ($a^0a^0c^-$), and rhombohedral ($a^-a^-a^-$) structures cannot easily be distinguished from X-ray refinements. Secondly, as the symmetry is lowered and the number of free positional parameters increases, the accuracy with which the oxygen positions are determined will decrease. This will correspondingly decrease the accuracy of the bond distances. Keeping these points in mind the following chapter will describe the synthesis and structural characterization of 30 double perovskite compounds. Most of these compounds have been previously synthesized and reported in the literature, primarily in the 1960's, but structural characterizations have never been carried out. The motivation to revisit these compounds is twofold. The discussion of chapter three was based on understanding the structure determining forces in ternary perovskites. However, as will be shown there are some differences in the behavior of quaternary perovskites. In order to develop an understanding of this behavior, analogous to the results of chapter three, a larger database of structurally characterized double perovskites is needed. The interest in these compounds also stems from a desire to understand the cation ordering behavior in perovskite compounds. For this reason the formal oxidation states of the octahedral cations differ by two in the majority of compounds synthesized. This class of perovskites is chosen because among its members the degree of cation order varies from disordered to completely ordered, with many compounds

displaying partial order. A consideration of the ordering behavior in these compounds is considered in detail in chapter six.

5.2 Synthesis

Most of the compounds presented in this chapter were prepared using conventional ceramic techniques from stoichiometric mixtures of the appropriate oxides, nitrates, and carbonates (nitrates and carbonates were generally only used as a source of the A cation). Usually at least three annealing steps were carried out. After grinding stoichiometric mixtures of the appropriate reagents in a mortar and pestle, the starting materials were heated to a relatively low temperature (750°C-1000°C) to decompose the nitrates and/or carbonates. This was followed by additional grinding and heating cycles at higher temperatures until the product was either single phase or nearly single phase. The dwell time at the final annealing temperature varied from 8 hours to 1 week. In a few instances the synthesis had to be carried out using a molten $SrCl_2$ flux in a platinum crucible, followed by later annealing at higher temperature. This procedure is called the flux/anneal technique and has been described in greater detail elsewhere (Woodward, Hoffman & Sleight, 1994). Synthesis of La_2MgHfO_6 and Na_2ZrTeO_6 as single phase products could not be achieved using the above methods. To overcome this two different approaches were employed. For La_2MgHfO_6 formation of the pyrochlore phase $La_2Zr_2O_7$ at high temperatures was problematic. Therefore, lanthanum nitrate, magnesium nitrate, and hafnium oxychloride were dissolved in water. The water was then driven off by heating while stirring the solution. After the water had completely evaporated, the white paste left behind was transferred to a crucible for annealing. For Na_2ZrTeO_6 reduction of hexavalent tellurium at temperatures over 850°C limited the final annealing temperature. However, at these low temperatures it was difficult to get ZrO_2 to react completely. Therefore, Na_2CO_3 and ZrO_2 were prereacted at 1050°C to form $NaZrO_3$. This product was then mixed with TeO_2 and heated to 700°C to synthesize the desired perovskite phase. This approach has previously been used in the synthesis of quaternary tellurates (Choisnet, Rulmont & Tarte, 1989). Final annealing temperatures, synthesis routes, and impurity phases present in each compound are given in table 5.1. All annealing steps were done in air, with the exception of Sr_2VTaO_6 which was annealed in a flowing 10% H_2/90% N_2 atmosphere.

Compound	Final Annealing Temp. (°C)	Synthesis Route	Impurities
Ba_2FeTaO_6	1100	Conventional	$Ba_4Ta_2O_9$, $Ba_5Ta_4O_{15}$
Ba_2ScTaO_6	1600	Conventional	Trace
Sr_2AlNbO_6	1400	Flux/Anneal	2.2% $Sr_5Nb_4O_{15}$
Sr_2AlTaO_6	1500	Conventional	$Sr_5Ta_4O_{15}$
Ba_2InTaO_6	1400	Conventional	2.6% In_2O_3
Sr_2CrSbO_6	1400	Conventional	$Sr_3SbO_{5.5}$, ?
Sr_2GaSbO_6	1400	Conventional	4.1% $Sr_3SbO_{5.5}$
Sr_2MnSbO_6	1600	Conventional	3.1% $Sr_3SbO_{5.5}$
Sr_2CoTaO_6	1200	Conventional	None
Sr_2GaTaO_6	1400	Conventional	Trace
Ba_2ScBiO_6	1000	Conventional	$(Ba_{0.4}Bi_{0.6})BiO_{2.8}$
Sr_2VTaO_6	1400	Conventional/H_2	Trace
Sr_2FeTaO_6	1200	Conventional	1.4% $Sr_5Ta_4O_{15}$
Sr_2MnTaO_6	1400	Conventional	None
Pb_2ScTaO_6	1000	Conventional	4.6% $Pb_3Ta_2O_8$
Sr_2CrTaO_6	1500	Conventional	None
Sr_2MgWO_6	1350	Conventional	None
Na_2ZrTeO_6	700	$NaZrO_3$+TeO_2	Trace
Sr_2ScTaO_6	1600	Conventional	None
Ca_2FeTaO_6	1100	Conventional	None
Ca_2MnTaO_6	1400	Conventional	None
Ca_2AlTaO_6	1400	Conventional	$Ca_3(CaTa_2)O_9$
Sr_2InTaO_6	1400	Flux/Anneal	6.0% In_2O_3
Sr_2YTaO_6	1400	Conventional	6.6% Y_2O_3
Ca_2ScTaO_6	1400	Conventional	None
La_2MgHfO_6	1500	Solution Route	1.3% La_2O_3, 0.1%$La_2Hf_2O_7$
Ca_2CrTaO_6	1500	Conventional	$Ca_3(CaTa_2)O_9$
Ca_2GaTaO_6	1400	Conventional	Unknown
Ca_2YTaO_6	1400	Conventional	Y_2O_3
$SrNaCrTaO_6$	1400	Conventional	None
$SrNaFeTaO_6$	1200	Conventional	None

Table 5.1 : Synthesis conditions for $A_2MM'O_6$ compounds. Details of the synthesis routes are discussed in the text. In many cases the impurities were refined as second phases in the Rietveld refinement. The percentage numbers in the final column represent the mass fraction of the impurity phase determined in this manner. Impurities that were not refined had peak intensities which suggest that their concentrations are also in the same range, 1-5%. Trace refers to impurity peaks in the XRD pattern too weak to identify.

5.3 Structure Refinement

X-ray diffraction patterns were collected using a Siemens D5000 diffractometer, equipped with a Kevex, Peltier cooled Si(Li) energy dispersive detector, and a copper Kα radiation source. Measurements for Rietveld analysis were collected from 2-150° two-theta, using a step size of 0.02°, a count time of 3-6 seconds per step, and a 0.05mm detector slit. All refinements were performed using the 1991 release of the RIETAN software package (Izumi, 1989; Izumi, 1993). This Rietveld program is uniquely suited for analysis of these compounds because it allows subcell and supercell peaks to be refined separately. This is necessary in partially ordered perovskites as discussed in chapter four. All bond valence calculations were performed using the program EUTAX (O'Keeffe, 1992).

5.4 Overview of Structure Refinement Results

Table 5.2 summarizes the basic attributes of perovskite compounds synthesized. Of the literature references to these compounds only Sr_2AlTaO_6, Sr_2AlNbO_6, (Woodward, Hoffmann & Sleight, 1994) Sr_2CrTaO_6, and Ca_2CrTaO_6 (Choy, Park, Hong & Kim, 1994) involved actual structure determinations. With the exception of Sr_2AlNbO_6 these compounds have been discussed in the previous chapter. All other reports in the literature refer only to the lattice constants and symmetry of the unit cell. All of the compounds in table 5.2 belong to one of the tilt systems discussed in chapter four. The compounds marked with a † cannot be assigned to a given tilt system with absolute certainty. These compounds all show partial cation order, and undetectable splitting of the diffraction lines. As discussed in chapter four when a compound has this combination of attributes, neutron diffraction is needed to unambiguously determine the structure and assign the tilt system. The assignments made in table 5.2 are based on how well the different structure models fit the supercell reflections in the X-ray pattern, and some knowledge about the tolerance factor. These assignments are tentative and neutron diffraction is necessary to confirm them. No line splitting could be detected in Sr_2MnTaO_6, Sr_2GaTaO_6, Sr_2ScTaO_6, and Sr_2InTaO_6 either. However, in these compounds the appearance of very weak "extra" reflections could be detected in the diffraction pattern. These reflections are systematically absent in the cubic perovskite structure ($Fm\bar{3}m$ or $Pm\bar{3}m$), and may only be accounted for by lowering the symmetry of the lattice. Assignment of symmetry in such situations was discussed in detail in chapter four.

Table 5.2 : A summary of the structure types, tilt systems, and long range order parameters of perovskites synthesized in this work. Tolerance factors are calculated from the ionic radii of Shannon and Prewitt (Shannon, 1976). The volume/Z numbers are calculated by dividing the volume of the unit cell by the number of simple perovskite, AMO_3, formula units. The cube root of this number would be the cell edge of a simple cubic perovskite unit cell. References for compounds in the table are as follows: 1] Sleight (1964), 2] Filip'ev & Fesenko (1966), 3] Galasso, Layden & Flinchbaugh (1966), 4] Brandle & Fratello (1990), 5] Blasse (1965), 6] Geguzina, Fesenko & Devlikanova (1976), 7] Shuvaeva & Fesenko (1970), 8] Bernier, Chauvel & Kahn (1974), 9] Nomura & Nakagawa (1971), 10] Nakagawa & Nomura (1966), 11] Bell (1968), 12] Kupriyanov & Filip'ev (1963), 13] Choy, Park, Hong & Kim (1994), 14] Bayer (1969), 15] Fesenko, Filip'ev & Kupriyanov (1964), 16] Filip'ev & Fesenko (1965).

* These compounds have shown some tendency to deviate from the ideal stoichiometry (see discussion toward the end of the chapter)

† The tilt system and structure assignments for these compounds are made from refinements of X-ray data and are therefore tentative.

‡ These samples have some disorder between the large M site cation (M^{3+}) and the A site cation.

Microprobe and diffraction measurements indicate that the stoichiometry of this compound is actually $(Sr_{1.29}Na_{.39})(Ta_{1.19}Cr_{.61}Sr_{.21})O_6$ with vacancies on the A site.

$ Microprobe and diffraction measurements indicate that the stoichiometry of this compound is actually $(Sr_{1.29}Na_{.44})(Ta_{1.11}Fe_{.71}Sr_{.18})O_6$.

Compound	Space Group	Tilt System	Tol. Factor	Volume /Z ($Å^3$)	Long Range Order Parameter	Reference
Ba_2FeTaO_6	$Pm3m^{\dagger}$	$a^0a^0a^0$	1.051	66.8	0%	1
$Ba_2ScTaO_6^*$	$Fm3m^{\dagger}$	$a^0a^0a^{0\dagger}$	1.025	69.5	72-96%	1,2,3
Sr_2AlNbO_6	$Fm3m^{\dagger}$	$a^0a^0a^{0\dagger}$	1.018	59.1	63-97%	1,2,4
$Sr_2AlTaO_6^*$	Fm3m	$a^0a^0a^0$	1.018	59.3	68-96%	1,2,4
$Ba_2InTaO_6^*$	$Fm3m^{\dagger}$	$a^0a^0a^{0\dagger}$	1.011	70.9	79-100%	1,2,3
Sr_2CrSbO_6	$P2_1/n$	$a^+b^-b^-$	1.008	60.8	97-96%	1,5
Sr_2GaSbO_6	I4/m	$a^0a^0c^-$	1.007	60.7	96-97%	1
$Sr_2MnSbO_6^*$	I4/mcm	$a^0a^0c^-$	1.000	61.6	0%	5
Sr_2CoTaO_6	I4/mcm	$a^0a^0c^-$	0.999	61.7	0%	6
$Sr_2GaTaO_6^*$	I4/m	$a^0a^0c^-$	0.996	61.5	48-82%	1,4
$Ba_2ScBiO_6^*$	$Fm3m^{\dagger}$	$a^0a^0a^{0\dagger}$	0.995	73.5	0-83%	7
Sr_2VTaO_6	I4/m	$a^0a^0c^{-\dagger}$	0.991	62.2	52%	8
$Sr_2FeTaO_6^*$	I4/mcm	$a^0a^0c^-$	0.990	62.5	0%-Low	1,9,10,11,12
Sr_2MnTaO_6	I4/mcm	$a^0a^0c^-$	0.990	62.6	0%	12
$Sr_2CrTaO_6^*$	I4/m	$a^0a^0c^-$	0.983	61.3	60-70%	1,9,13
Ca_2AlTaO_6	$P2_1/n$	$a^+b^-b^-$	0.982	55.5	90-92%	4,16
Sr_2MgWO_6	I4/m	$a^0a^0c^-$	0.981	61.8	99%	2
Na_2ZrTeO_6	$P2_1/n$	$a^+b^-b^-$	0.974	59.5	100%	14
$Sr_2ScTaO_6^*$	$P2_1/n$	$a^+b^-b^-$	0.966	65.3	93-99%	15
Ca_2FeTaO_6	$P2_1/n$	$a^+b^-b^-$	0.955	58.7	0%	16
Ca_2MnTaO_6	$P2_1/n$	$a^+b^-b^-$	0.955	59.6	0%	16
$Sr_2InTaO_6^*$	$P2_1/n$	$a^+b^-b^-$	0.953	66.3	100%	1
Sr_2YTaO_6	P-1	$a^+b^-c^-$	0.931	70.3	60-100%	12
Ca_2ScTaO_6	$P2_1/n$	$a^+b^-b^-$	0.930	61.1	97-95%	none
La_2MgHfO_6	$P2_1/n$	$a^+b^-b^-$	0.928	65.9	10%	none
Ca_2CrTaO_6	$P2_1/n$	$a^+b^-b^-$	0.921	53.5	66-67%	13
Ca_2GaTaO_6	$P2_1/n$	$a^+b^-b^-$	0.919	58.1	50%	4
$Ca_2YTaO_6^{\ddagger}$	$P2_1/n$	$a^+b^-b^-$	0.897	65.4	100%	16
$SrNaCrTaO_6^{\#}$	I4/mcm	$a^0a^0c^-$	***	61.2	0%	none
$SrNaFeTaO_6^{\$}$	I4/mcm	$a^0a^0c^-$	***	62.1	0%	none

Table 5.2

Consistent with the findings in chapters three and four the number of tilt axes (0 for $a^0a^0a^0$, 1 for $a^0a^0c^-$, 3 for $a^+b^-b^-$) increases as the tolerance factor decreases. There are some exceptions to this trend however, most notably when M'=Sb. This will be discussed in greater detail in the discussion section. Primarily to study their ordering behavior, many compounds in table 5.2 were synthesized more than one time (over 80 different samples of Sr_2AlTaO_6 were made during the course of this work). This is reflected in the long range order parameter being reported as a range for several of the entries in table 5.2. Although almost all compounds synthesized were refined, only the best refinements, on samples with the lowest possible impurity levels are discussed in this chapter. Details of the refinements on each compound are given in the sections that follow.

5.5 Cubic Perovskites

The ideal simple cubic perovskite structure is the starting point from which all other perovskite structures are derived. The visualization of this structure has already been described and need not be reiterated here. Crystallographically the structure belongs to the space group $Pm\bar{3}m$ (A-221) and the atoms are all located in fixed positions: the A cation at ½,½,½; the M cation at 0,0,0; and the oxygen at ½,0,0. Excluding background and profile functions, refinements of compounds with this structure involve only five variables: the scale factor, lattice constant and thermal parameters for each type of atom.

Ordering of octahedral cations in substituted perovskites leads to the ordered cubic perovskite structure. This structure belongs to the space group $Fm\bar{3}m$ where the A, M, M', and O atoms are all found in different special positions. A comparison of the atomic positions in the ordered and disordered structures is given in table 5.3. Refinement of a fully ordered compound only introduces three additional variables: the oxygen position x, the ratio of M and M' ions on the octahedral sites, and one additional thermal parameter (for M'). Because of the correlation between occupancies and thermal parameters constraints were placed on certain variables. Due to these constraints only one thermal parameter and the long range order parameter, S^*, were refined for the M and M' sites. Using the above mentioned constraints only two additional variables are introduced upon moving from the

---

* The long range order parameter is determined by refining the parameter x in the structure model $A_2(M_{1-y}M'_y)(M_yM_{1-y})O_6$, where y can vary between 1 (fully ordered) and 0.5 (disordered). The long range order parameter is then defined as S=2y-1. This results in a parameter which scales from 0% to 100%.

disordered to the ordered structure: the long range order parameter, S; and the oxygen position, x.

	Disordered Structure	Ordered Structure
Space Group	$Pm\bar{3}m$	$Fm\bar{3}m$
A Site	(1b) ½,½,½	(8c) ¼,¼,¼
M Site	(1a) 0,0,0	(4a) 0,0,0 (4b) ½,½,½
O Site	(3d) ½,0,0	(24e) x,0,0

Table 5.3 : Atomic positions in the simple cubic and ordered cubic perovskite structures.

As the degree of long range order decreases both the structure and the refinement become more complex. As discussed briefly in chapter four and in more detail in the literature (Woodward, Hoffmann & Sleight, 1994) antiphase boundaries are formed which broaden the supercell reflections and often times shift the positions of the subcell reflections. In order to accurately fit the peaks in such compounds, separate lattice constants and profile functions were used to fit each class of reflections, while the scale factor, atomic positions, and thermal parameters were kept the same. The results of Rietveld refinements on representative samples of each cubic perovskite compound synthesized are shown in table 5.4. Table 5.5 gives the results of geometry and bond valence calculations on the refined structures from table 5.4.

5.6 Tetragonal Perovskites

5.6.1 Jahn-Teller Effect

In compounds exhibiting octahedral tilts, the octahedra do not remain completely rigid and distortions from the ideal octahedral units are observed. Nonetheless, these types of deviations are usually small and can be treated as a perturbation on the tilting of rigid octahedra. This assumption is not generally valid if a Jahn-Teller ion is present on the octahedral site. A first order Jahn-Teller effect describes the phenomenon of the ideal lattice distorting to lower the symmetry about a given ion in order to remove the degeneracy of

Compound	R_{WP} %	Subcell/Supercell R_I %	Cell Edge(Å)	LRO %	Oxygen Pos.	Thermal Parameters A	M/M'	O
Ba_2FeTaO_6	14.08	4.16	4.0566(2)	0	0.5	0.4(2)	0.1(2)	0.5(6)
Sr_2AlNbO_6	12.30	1.81 3.00	7.7858(1) 7.7834(2)	94(1)	0.245(2)	0.6(1)	0.0(1)	0.3(2)
Sr_2AlTaO_6	9.38	1.44 4.83	7.7866(1) 7.7859(1)	89(1)	0.246(2)	0.5(1)	0.0	0.2(3)
Ba_2BiScO_6	16.01	4.05 5.04	8.3660(1) 8.3609(4)	75(2)	0.246(2)	0.4(1)	0.0(1)	0.3(5)
Ba_2ScTaO_6	12.08	3.01 3.30	8.2200(4) 8.2198(2)	91(2)	0.256(3)	0.1(1)	0.0	0.4(6)
Ba_2InTaO_6	9.24	1.86	8.2814(4)	79(3)	0.258(2)	0.3(1)	0.0(1)	0.3(2)

Table 5.4 : Refinement values for cubic perovskites. Both R.I and the cell edge have two values for most compounds. The first one is from refinement of the subcell reflections the second set of values is from refinement of the supercell reflections. This was necessary in most cases because of the broadening and shifting of the supercell reflections. Compounds with the M/M' thermal parameter fixed at zero were refined in a manner that allowed stoichiometric deviations. However, none of the samples in this table showed a tendency to deviate from ideal stoichiometry. In all cases the trivalent cation was at (0,0,0) and the pentavalent ion at (½,½,½).

Compound	Density (g/cc)	Bond Distance (Å) A-O	M-O	M'-O	Bond Valences A	M	M'	O
Sr_2AlNbO_6	5.50	2.75	1.91	1.99	2.16	3.00	4.91	2.04
Sr_2AlTaO_6	6.74	2.75	1.92	1.98	2.16	2.94	5.13	2.04
Ba_2FeTaO_6	7.56	2.87	2.03	2.03	2.51	2.90	4.48	2.07
Ba_2ScBiO_6	7.09	2.96	2.06	2.13	1.97	3.41	5.03	2.07
Ba_2ScTaO_6	7.13	2.91	2.10	2.01	2.27	3.01	4.76	2.05
Ba_2InTaO_6	7.79	2.93	2.14	2.00	2.14	3.18	4.78	2.04

Table 5.5 : Bond distances and bond valences in cubic perovskite compounds. In partially ordered compounds the M site is rich in the trivalent ion, and the M' site is rich in the pentavalent ion. Bond valences were calculated by assuming complete order between M and M'.

partially filled orbitals on the ion (Albright, Burdett & Whangbo, 1985). More specifically, for perovskites the Jahn-Teller effect becomes important when the octahedral cation has an odd number of electrons in the e_g orbitals (d_{z2} and d_{x2-y2}). For transition metal ions there are three separate cases in which an odd number of electrons are present in the e_g orbitals: d^4 (high spin) ions, d^7 (low spin) ions, and d^9 ions. Ions which correspond to the above spin states include Cu^{2+}, Ni^{+}, and the high spin ions Cr^{2+}, Mn^{3+}, and Fe^{4+}. The degeneracy between the e_g orbitals is lifted by lengthening two bonds on opposite sides of the octahedron. This results in a coordination about the central cation of two long and four short bonds. In the simple perovskite structure all of the long bonds are found in the xy plane in alternating directions. This leads to a tetragonal distortion of the ideal structure with a/c>1 (Galasso, 1969).

In double perovskites, $A_2MM'O_6$ there are two situations which can arise. If both ions on the M cation sublattice are Jahn-Teller ions then the lattice distortion should be similar to a Jahn-Teller distortion of a simple perovskite. However, if the cations are ordered and only one cation is a Jahn-Teller ion, it has been observed that all of the long M-O bonds are now directed along the c axis instead of along a and b (Blasse, 1965; Sleight & Ward, 1962). This results in a "ferromagnetic" Jahn-Teller distortion where the where the microscopic distortions align cooperatively, and the relationship between lattice parameters now becomes a/c<1. The effect of the Jahn-Teller ion on the lattice constants is less clear when the M and M' cations are disordered. The Jahn-Teller distortions in simple and double perovskites are illustrated in figure 5.1.

5.6.2 Possible Tetragonal Perovskite Structures

Depending upon the type of distortion, $a^0a^0c^+$ tilting, $a^0a^0c^-$ tilting, or a Jahn-Teller distortion, and the presence or absence of cation ordering there are at least six possible tetragonal perovskite structures which could possibly result, each one belonging to a different space group. Table 5.8 lists the space group and atomic positions of each of the six structures. All structures have the $\sqrt{2}$ unit cell described in chapter two, but the disordered $a^0a^0c^+$ structure has a c axis which is not doubled (see appendix 2 for more complete structural descriptions).

As long as the scattering powers of the M and M' cations are not too similar, and the degree of order is not too low, it is a simple matter to differentiate between the ordered and disordered structures from the x-ray diffraction pattern. Ordered structures will have a (101)

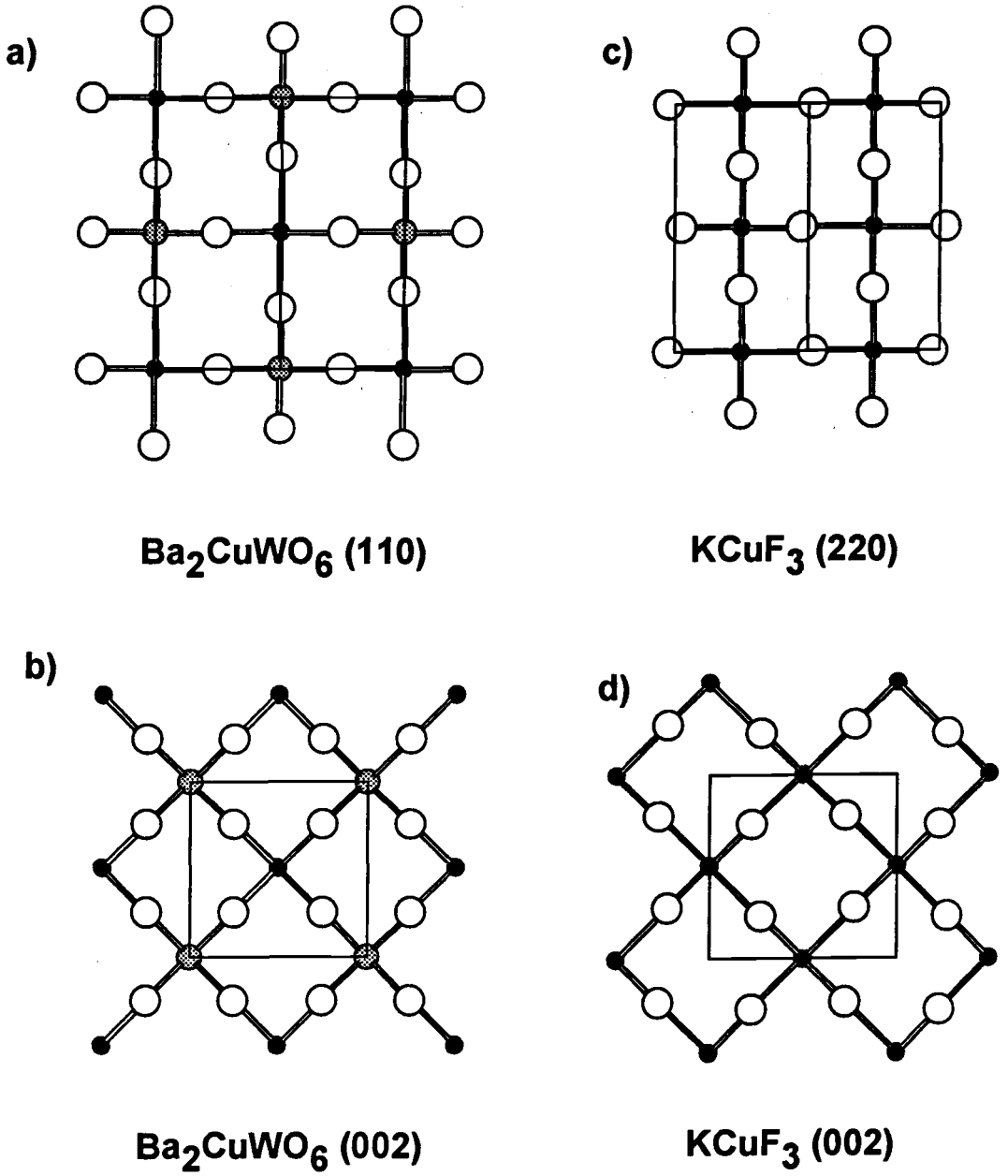

Figure 5.1 : Typical Jahn-Teller distortions in AMO_3 and $A_2MM'O_6$ perovskites. In Ba_2CuWO_6 (Reinen & Weitzel, 1976) the long Cu-O bonds align cooperatively in the c direction, as seen in the views of the a) (110), and b) (002) planes. In $KCuF_3$ (Okazaki & Suemune, 1961) the long Cu-O bonds alternate directions in the xy plane, as evident in the c) (220), and d) (002) planes. The Cu atoms are represented as black circles, the oxygens as white circles, and the tungstens as shaded circles. The A cations have been omitted for clarity.

reflection present (cubic (111)), while this reflection is absent for disordered compounds. Differentiating between the three possible structures for both ordered and disordered compounds is more subtle. For simplicity the discussion will be limited to the disordered case but the same principles may be applied when comparing ordered structures. Comparison of the three possible disordered structures reveals that the cations have not moved off of their ideal sites and are in identical positions in all three structures, only the oxygens have moved off of their ideal sites. For the $a^0a^0c^+$ case the octahedra connected along the c axis all tilt in phase so that oxygen sublattice is identical in each M-O sheet, (001) plane, and no doubling of the c axis is necessary. In the $a^0a^0c^-$ case these tilts are now out of phase and the displacements of the oxygens cause a doubling of the lattice constant in the c direction (see figure 2.1). Finally, in the case of a pure Jahn-Teller distortion no tilting occurs, but the octahedra are elongated in the [110] direction. The direction of the long M-O bonds alternates from the [110] direction in a given octahedra to the $[\bar{1}10]$ direction in the neighboring octahedra (see figure 5.1). This also results in a doubling of the unit cell in the c-direction.

Because the three structure types discussed above only differ by the position of the oxygen atoms their x-ray diffraction patterns are very similar. Calculations using the program LAZY/PULVERIX (Yvon, Jeitschko & Parthe, 1977) show that the subcell peaks (present in the cubic pattern) have the same intensities in the I4/mcm and P4/mbm space groups, and a similar but slightly different intensity distribution in the I4/mmm space group. This difference in peak intensity is very subtle, however, and cannot be detected visually. Fortunately, in the case of a disordered cation distribution the three structures can usually be differentiated, due to the different reflection conditions associated with each space group. Table 5.9 shows the LAZY/PULVERIX calculations for Sr_2FeTaO_6 using all three structure models. All three space groups allow the peaks that were present in the cubic space group. The I4/mmm structure also allows all reflections where h+k+l=2n. The extinction conditions for the I4/mcm structure are almost the same except that the h0k peaks , when h=2n+1, are absent [(101), (103), and (301)]. The P4/mbm structure on the other hand has a different set of weak peaks present in its pattern. Using the differences in extinction conditions and a carefully collected diffraction pattern one may in theory eliminate two of the structures and correctly identify the correct structure through a visual inspection of the powder pattern. In practice the extra lines are often very weak and can easily be missed if care is not taken in the data collection and interpretation.

The situation becomes more complicated when long range ordering between the octahedral cations exists. When this occurs the c axis is doubled in all three possible space

groups (P4/mnc, I4/m, and I4/mmm) and cation ordering usually leads to strong peaks for indices with h+k=2n+1 and l=2n+1. The primitive space group P4/mnc may still be identified by the presence of peaks with indices h+k+l=2n+1, but now the two body centered space groups have the same extinction conditions and refinement of the structure is the only way to differentiate between the two space groups. Furthermore, as discussed in chapter four, if the peak splitting is negligible (a/c≅1) an ordered cubic model will also give peaks in the exact same positions with very similar intensities.

Tilt System/ Ordering	Space Group	A Site Position	M Site Position	Oxygen Position
$a^\circ a^\circ c^+$ Disordered	P4/mbm A-127	(2c) ½,0,½	(2a) 0,0,0	(4g) x,½+x,0 (2b) 0,0,½
$a^\circ a^\circ c^-$ Disordered	I4/mcm A-140	(4b) ½,0,¼	(4c) 0,0,0	(8h) x,½+x,0 (4a) 0,0,¼
Jahn-Teller* Disordered	I4/mmm A-139	(4d) ½,0,¼	(2a) 0,0,0 (2b) 0,0,½	(8h) x,x,0 (4e) 0,0,z
$a^\circ a^\circ c^+$ Ordered	P4/mnc A-128	(4d) ½,0,¼	(2a) 0,0,0 (2b) 0,0,½	(8h) x,y,0 (4e) 0,0,z
$a^\circ a^\circ c^-$ Ordered	I4/m A-87	(4d) ½,0,¼	(2a) 0,0,0 (2b) 0,0,½	(8h) x,y,0 (4e) 0,0,z
Jahn-Teller* Ordered	I4/mmm A-139	(4d) ½,0,¼	(2a) 0,0,0 (2b) 0,0,½	(8h) x,x,0 (4e) 0,0,z

Table 5.6 : Space groups and atomic positions for the six most likely tetragonal perovskite structures. For small distortions the approximate lattice constants of the last five structures are $a=b\approx\sqrt{2}*A_p$, $c\approx 2*A_p$ where A_p is simple ideal perovskite lattice constant (~4Å). The first structure has approximate lattice constants of $a=b\approx\sqrt{2}*A_p$, $c\approx A_p$. For ordered structures the two different octahedral positions are occupied by different cations: M and M'. For disordered structures all of the octahedral positions are occupied by a random distribution of cations. * The structures attributed to a Jahn-Teller distortion assume only a lengthening of the axial bond lengths about the Jahn-Teller ion. No tilting of the octahedra is used to obtain the symmetry listed.

Peak Indices (hkl)				Intensity		
Cubic	**P-Tetr**	**I-Tetr**	**2-Theta**	**P4/mbm**	**I4/mcm**	**I4/mmm**
		101	19.36			**6.2**
100	110	110	22.37	59.8	59.8	67.2
100	001	002	22.42	32.1	32.1	31.1
110	200	200	31.85	526.3	526.3	509.5
110	111	112	31.88	1000	1000	1000
	210		35.73	**4.0**		
		211	37.54		**6.8**	1.5
		103	37.60			.9
111	201	202	39.30	10.8	10.8	10.4
	211		42.59	**4.4**		
200	220	220	45.66	325.6	325.6	315.2
200	002	004	45.76	168.5	168.5	163.1
		301	50.03			2.5
		213	50.08		2.4	.5
210		310	51.42		13.8	9.3
210	221	222	51.44	9.0	9.0	8.7
210	112	114	51.51	10.8	10.8	11.9
211	311	312	56.77	412.2	412.2	371.2
211	202	204	56.83	203.8	203.3	196.8

Table 5.7 : Results of a LAZY/PULVERIX (Yvon, Jeitschko & Parthe) calculation for three hypothetical disordered tetragonal structures of Sr_2FeTaO_6 (a=5.615Å, c=7.925). The intensities in bold are important peaks for differentiating between the three structures.

5.6.3 Tetragonal Structure Refinements

Eleven compounds were synthesized that crystallized with tetragonal symmetry: Sr_2MnSbO_6, Sr_2CoTaO_6, Sr_2FeTaO_6, $SrNaFeTaO_6$, Sr_2GaTaO_6, Sr_2MnTaO_6, $SrNaCrTaO_6$, Sr_2MgWO_6, Sr_2CrTaO_6 and Sr_2GaSbO_6. Out of this group five compounds Sr_2GaSbO_6, Sr_2GaTaO_6, Sr_2CrTaO_6, Sr_2VTaO_6 and Sr_2MgWO_6 showed supercell reflections indicative of long range order. The other compounds showed no indication of long range order, with the exception of Sr_2FeTaO_6 which in some cases showed very broad and weak supercell reflections, however, these reflections were too broad to accurately refine. The refinement of Sr_2CrTaO_6 was discussed in detail in the previous chapter and will not be repeated here. Visual inspection of the x-ray diffraction patterns allowed classification of each sample as ordered or disordered. In addition, in all cases the reflections present in the pattern were consistent with a body centered tetragonal lattice and not a primitive tetragonal lattice. For the disordered compounds the presence of a small peak where the (211) reflection was expected coupled with the absence of a (101) reflection indicated I4/mcm was the correct space group. In order to be sure of the correct space group Rietveld refinements of the observed patterns were performed using each of the three possible structure types as a starting model. The results of the refinements were compared to give confirmation of the correct structure type. The best fit of the three starting models was chosen based on three criteria: the intensity residual, R_i, of the perovskite phase, the thermal parameter of the oxygens (both oxygens were constrained to have the same thermal parameter), and the standard deviation of the positional parameter of the oxygens in the (001) plane. These criteria were chosen because if the symmetry of the oxygen sublattice was incorrectly modeled not only would the residual increase but the thermal parameter and uncertainty in the oxygen position should also increase. The results of these refinements are summarized in table 5.8. Based on the results of the refinements, and in agreement with the observed extinction conditions, the structure resulting from an $a^oa^oc^-$ tilt combination can be assigned as the true structure for all compounds studied. Table 5.9 summarizes the results of Rietveld refinements using the space groups I4/mcm and I4/m, while table 5.10 lists the bond distances and bond valences for these compounds. It is important to notice in table 5.9 that Sr_2MnSbO_6, $SrNaCrTaO_6$, and $SrNaFeTaO_6$ have deviated from their ideal stoichiometry. Deviations in stoichiometry in these compounds as well as others are discussed in more detail later in this chapter.

Compound/Parameter	I4/mcm	P4/mbm	I4/mmm
$SrNaCrTaO_6$			
R_i	3.11	3.26	3.63
Oxygen Pos. (O1)	.229(5)	.230(7)	.25(1)
Oxygen B Value	1.5(4)	1.6(4)	2.0(3)
Sr_2CoTaO_6			
R_i	3.50	3.55	3.67
Oxygen Pos. (O1)	.23(1)	.24(2)	.25(60)
Oxygen B Value	0.6(7)	0.9(7)	1.1(6)
Sr_2FeTaO_6			
R_i	3.30	3.62	3.82
Oxygen Pos. (O1)	.218(3)	.231(5)	.236(5)
Oxygen B Value	0.3(3)	1.0(3)	1.2(2)
$SrNaFeTaO_6$			
R_i	4.34	4.41	4.51
Oxygen Pos. (O1)	.219(5)	.229(8)	.25(371)
Oxygen B Value	1.9(5)	2.4(6)	3.0(5)
Sr_2MnTaO_6			
R_i	3.69	3.71	3.94
Oxygen Pos. (O1)	.222(5)	.24(1)	.25(12)
Oxygen B Value	1.0(4)	1.6(5)	1.9(4)
Sr_2MnSbO_6			
R_i	3.71	3.85	3.84
Oxygen Pos. (O1)	.226(5)	.25(18)	.25(25)
Oxygen B Value	1.2(5)	2.0(5)	2.0(5)
	I4/m	**P4/mnc**	**I4/mmm**
Sr_2GaSbO_6			
R_i	3.01	3.20	3.20
Oxygen x Pos. (O1)	.217(5)	.25(10)	.246(4)
Oxygen y Pos. (O1)	.721(7)	.76(10)	
Oxygen B Value	0.2(4)	1.3(3)	1.3(3)
Sr_2GaTaO_6			
R_i	2.00	2.05	*******
Oxygen x Pos. (O1)	.229(5)	.23(1)	Not
Oxygen y Pos. (O1)	.718(4)	.72(1)	Stable
Oxygen B Value	0.1(2)	0.1(7)	*******
Sr_2MgWO_6			
R_i	2.24	2.36	2.44
Oxygen x Pos. (O1)	.289(6)	.275(6)	.258(3)
Oxygen y Pos. (O1)	.771(6)	.759(7)	
Oxygen B Value	0.6(4)	1.3(4)	1.6(4)

Table 5.8 : A comparison of Rietveld refinement results for tetragonal perovskites as a function of structure type.

			Subcell/Supercell			Thermal Parameters (B)		
Compound	R_{WP} %	R_I %	Cell Edges a,c (Å)	LRO %	Oxygen Position	A	M/M'	O
$SrNaCrTaO_6$*	9.27	3.11	5.57119(4) 7.88908(9)	0	O1 x=.229(5)	0.4(1)	-0.09(5)	1.5(4)
Sr_2CoTaO_6	11.58	3.52	5.5865(1) 7.9098(4)	0	O1 x =.23(1)	0.7(1)	0.0(1)	0.6(7)
Sr_2FeTaO_6	10.37	3.49	5.6067(1) 7.9491(3)	0	O1 x=.220(3)	0.8(1)	0.09(5)	0.4(3)
$SrNaFeTaO_6$*	10.65	4.35	5.59011(6) 7.9426(1)	0	O1 x=.219(5)	0.7(1)	0	1.9(5)
Sr_2MnTaO_6	9.73	3.69	5.6135(1) 7.9510(3)	0	O1 x=.223(5)	1.0(1)	0.12(7)	1.0(4)
Sr_2MnSbO_6 *Sb Occ=.44(2)*	17.34	3.72	5.5336(1) 8.0482(2)	0	O1 x=.226(5)	0.8(1)	0.0(2)	1.3(5)
Sr_2GaSbO_6	14.80	3.01	5.54765(9) 7.8884(2)	96(2)	O1 x=.217(5) O1 y=.721(7) O2 z=.254(5)	0.34(6)	0.06(7)	0.2(3)
Sr_2VTaO_6	8.88	2.61 1.51	5.5978(1) 7.9413(2) 5.601(9) 7.94(2)	52(2)	O1 x=.226(5) O1 y=.726(5) O2 z=0.25(1)	0.8(1)	0.2(1)	0.4(4)
Sr_2GaTaO_6	14.80	2.00 4.59	5.57846(5) 7.8962(1) 5.575(4) 7.90(1)	63(2)	O1 x=.229(5) O1 y=.718(4) O2 z=.235(9)	0.69(7)	0	0.0(2)
Sr_2MgWO_6	11.85	2.24	5.57946(4) 7.93838(9)	99(1)	O1 x=.289(6) O1 y=.771(6) O2 z=.263(4)	0.55(8)	0.05(6)	0.6(4)

Table 5.9 : Rietveld refinement results on tetragonal perovskites. For Sr_2GaTaO_6 the subcell reflections and supercell reflections were refined with different lattice constants and profile parameters. The R.I and lattice constants are listed first for the subcell reflections and then for the supercell reflections. *These two compounds appear to have much more complicated stoichiometries than those listed. The true compositions are discussed at the end of the chapter.

The bond valences in table 5.10 all appear to be quite reasonable. The bond distances are also in the range of what would be expected from ionic radii arguments. Unlike the cubic case the bond valences for the A site cation are all quite close to the expected value, because now 2/3 of the oxygen atoms are free to move in order to optimize their distance from the A cation without changing the M-O distances. From the bond distances in table 5.10 one can see that half of the oxygens on the O1 site (x,x+½,0 or x,y,0) move closer to a given A ion, while the other half move farther away from the same ion. This gives four short A-O interactions (2.61-2.69Å), four medium A-O interactions (2.77-2.81Å), and four long A-

O interactions (2.91-2.98Å). The regularity of the A cation bond valence illustrates the importance of the A-O interaction in determining the symmetry of these compounds.

		Bond Distances(Å)			Bond Valences					
Comp	Dens. (g/cc)	A-O	M-O	M'-O	A	M	M'	O	Tilt Angle	a/c
SNCT	5.96	4×2.67 4×2.79 4×2.91	4×1.98 2×1.97		1.44	3.04	5.17	1.85 1.85	4.80°	.999
SCoT	6.88	4×2.69 4×2.79 4×2.91	4×1.98 2×1.98		1.98	2.82	5.10	1.99 1.98	4.55°	.999
SFT	6.75	4×2.64 4×2.80 4×2.97	4×2.00 2×1.99		1.98	3.18	4.92	2.02 2.00	6.85°	1.002
SNFT	5.94	4×2.63 4×2.80 4×2.98	4×1.99 2×1.99		1.44	3.22	4.97	1.85 1.84	7.05°	.995
SMT	6.73	4×2.66 4×2.81 4×2.96	4×2.00 2×1.99		1.95	3.19	4.92	2.01 2.00	6.15°	.999
SMS	6.04	4×2.68 4×2.77 4×2.94	4×1.97 2×2.01		2.00	3.31	5.41	2.17 2.03	5.50°	.972
SGS	6.33	4×2.61 4×2.77 4×2.96	4×1.96 2×2.00	1.99 1.94	2.14	3.10	5.50	2.14 2.16	7.05°	.995
SVT	6.72	4×2.67 4×2.80 4×2.94	4×1.99 2×1.99	1.99 1.99	1.96	3.10	5.00	2.01 1.99	5.49°	.997
SGT	7.05	4×2.65 4×2.79 4×2.94	4×1.86 2×1.94	1.94 2.09	2.04	3.22	5.04	2.09 1.99	6.05°	.999
SMgW	6.44	4×2.64 4×2.79 4×2.97	4×2.06 2×2.09	1.92 1.88	2.03	2.18	6.28	2.08 2.11	6.85°	.994

Table 5.10 : Results of bond valence and geometry calculations on tetragonal perovskite structures. For the A-O distances the long and short bonds are to O1 and the intermediate length bonds are to O2. For the M-O distances and oxygen bond valences the top number corresponds to O1 (x,x+½,0 or x,y,0) and the lower number corresponds to O2 (0,0,¼ or 0,0,z). The octahedral tilting angle was calculated from the M-O-M' angle, and the a/c ratio is for the pseudocubic FCC tetragonal lattice constants (not the BCC tetragonal cell).

The assignment of tetragonal symmetry to Sr_2GaTaO_6 is somewhat uncertain. The peak splitting is so small that it is not detectable and refinements of most samples using both cubic and tetragonal structures give very similar residuals (for example R_{wp} of 9.66 for the cubic structure and 9.61 for the tetragonal structure). Under most conditions Sr_2GaTaO_6 is

partially ordered and the (103) peak (the cubic (311) peak) is present due to long range cation ordering regardless of the symmetry. However, for an SGT sample formed initially in a $SrCl_2$ flux and then heated to 1600°C the supercell peaks become weak and very broad, except for the cubic (311) peak which is decreased in intensity but not broadened. This confirms tetragonal symmetry for that sample. This observation coupled with the determination of tetragonal symmetry for Sr_2CrTaO_6 makes it quite likely that Sr_2GaTaO_6 is tetragonal under other synthesis conditions as well. Neutron diffraction of this compound should be done to remove all doubts about the lattice symmetry.

5.6.4 Jahn-Teller Ions and the Observed Structures

It has already been discussed that a distortion from cubic to tetragonal can result from either the presence of a Jahn-Teller ion or tilting of the octahedra, or both. In 1:1 ordered perovskites where only one of the two octahedral cations is a Jahn-Teller ion, both effects will cause the a/c ratio to become smaller than unity (Blasse, 1965; Glazer, 1972). In table 5.10 Sr_2MnSbO_6, Sr_2MnTaO_6, and $SrNaFeTaO_6$ are the only compounds containing Jahn-Teller ions (Mn^{3+} and Fe^{4+}) yet they crystallize in space group I4/mcm not I4/mmm as do all of the other disordered compounds in table 5.11. Inspection of the structures confirms that all of compounds undergo $a^oa^oc^-$ tilting, including those compounds containing Jahn-Teller ions. The magnitude of the tilting is in roughly the same range for all of the compounds in table 5.12, 4°-7° from their cubic alignment. If octahedral tilting and Jahn-Teller distortions are both present then the degree of tetragonal distortion is not a good indicator of the local distortion around the Jahn-Teller ion, rather differences in M-O1 and M-O2 bond distances are more useful because they can directly give information about the local distortion. Examining the metal-oxygen distances in the three compounds where a Jahn-Teller distortion is expected shows that only in Sr_2MnSbO_6 is the Jahn-Teller distortion apparent around the M ion. Furthermore, Sr_2MnSbO_6 is the only one to show an a/c ratio significantly different than one. The lack of a significant distortion from cubic symmetry in either the macroscopic lattice constants or the observed interatomic distances for both Sr_2MnTaO_6 and $SrNaFeTaO_6$ may be a result of the disorder present on the octahedral site. The disorder between Mn (Fe) and Ta seems to randomize the direction of the long Mn-O (Fe-O) bonds. This would explain the small deviation from cubic symmetry and the M-O distances observed. Conversely, the lattice constants of Sr_2MnSbO_6 suggest a high degree of short range order between Sb and Mn despite the fact that no long range order is present.

5.7 Monoclinic Perovskites

5.7.1 Monoclinic or Orthorhombic Unit Cell

The orthorhombic distortion of the cubic perovskite cell was first described by Geller in 1955 for $GdFeO_3$ (Geller, 1955), and was subsequently expanded to the related perovskites, $AFeO_3$ (A=Eu, Sm, Nd, Pr, La) and YMO_3 (M=Fe, Cr, Al) (Geller & Wood, 1956). Since that time many compounds have been found to adopt this structure type. In Galasso's book, "Structure, Properties, and Preparation of Perovskite Type Compounds", there are 170 $A_2M^{3+}M^{5+}O_6$ compounds listed and 42, nearly 25%, of them are listed as either orthorhombic or monoclinic (Galasso, 1969). The tilt system corresponding to this structure is $a^+b^-b^-$, and as discussed in chapter three, this structure type is favored when the fit of the A cation in the cubic network of corner sharing octahedra is poor. For substituted perovskites $A_2MM'O_6$ this type of distortion is generally seen when the tolerance factor becomes too small ($t \leq 0.97$).

	Disordered Orthorhombic Structure	**Ordered Monoclinic Structure**
Space Group	Pbnm (#62)	$P2_1/n$ (#14)
A Position	(4c) x,y,¼	(4e) x,y,z
M Position	(4b) ½,0,0	(2d) ½,0,0 (2c) 0,½,0
O1 Position	(8d) x,y,z	(4e) x,y,z (4e) x,y,z
O2 Position	(4c) x,y,¼	(4e) x,y,z

Table 5.11 : The crystallographic descriptions of the ordered monoclinic and disordered orthorhombic structures. Pbnm is a nonstandard setting of space group A-62. Pnma is the standard setting. $P2_1/n$ is the second setting of space group #14 $P2_1/c$.

Ignoring the symmetry of the structure for a moment and considering only the dimensions of the unit cell. The lattice constants of the pseudocubic cell parameters will be $a=c\neq b$, $\beta\neq 90°$ (Glazer, 1972; Burns & Glazer, 1990). Therefore, at first inspection it appears as though the unit cell has distorted from cubic to monoclinic, and in many early literature reports complex perovskites which had undergone this type of distortion were indexed as monoclinic with $a\approx b\approx c\approx 2*A_p$ and $\beta\approx 90°$ (Náray-Szabó, 1943). Other literature references

recognized the fact that only the 3 and 4-fold axes had been destroyed and assigned orthorhombic symmetry to the lattice. In many cases orthorhombic symmetry was assigned for simple perovskites (Geller & Wood, 1956; Galasso, 1969), where it is correct, and for ordered perovskites (Filip'ev & Fesenko, 1965), where it is incorrect. As discussed in chapter two, ordering of the octahedral cations destroys mirror and glide planes and reduces the true symmetry of the ordered structure to monoclinic. Table 5.11 compares the space group and atomic positions of both the orthorhombic and monoclinic structures. The lack of a mirror plane in the monoclinic structure gives the A site cation more freedom to displace from its ideal position and the 8 equivalent oxygens in the orthorhombic structure are split into two sets of four equivalent oxygens in the monoclinic structure. A detailed consideration of correctly assigning the symmetry of the lattice, orthorhombic or monoclinic, has been given in the literature (Anderson, Greenwood, Taylor & Poeppelmeier, 1993).

5.7.2 Monoclinic Structure Refinements

Several different monoclinic perovskite compounds were synthesized in this work. The refinement results of representative samples are given in tables 5.12 and 5.13. Table 5.13 lists the R factors, lattice constants, and long range order parameters of these compounds, while the atomic positional parameters are given in table 5.13. All compounds were refined using the space group $P2_1/n$.

All of the compounds, except Sr_2ScTaO_6 and Sr_2InTaO_6, possessed lattice constants which were essentially orthorhombic. Calculations using POTATO confirm that this is as expected for a distortion involving rigid octahedral units. Multiplying the a and b lattice constants by $\sqrt{2}$ to convert back to the cubic cell reveals that Sr_2ScTaO_6 and Sr_2InTaO_6 have lattice constants that are essentially cubic. The appearance of extra lines in the diffraction patterns and not line splitting showed the monoclinic symmetry of these two compounds. The last three compounds in table 5.13 show deviations from the ideal stoichiometry. Refinements indicated some exchange between Ca and Y in Ca_2YTaO_6. A more accurate formula for this compound would be $(Ca_{.935}Y_{.065})_2(Y_{.87}Ca_{.13})TaO_6$. The relative sizes of Ca^{2+}, Y^{3+}, and Ta^{5+} (1.14Å, 1.04Å, and 0.78Å respectively for a coordination number

Compound/ Sample	R_{wp} %	R_i %	Lattice Const. (Å)	LRO (%)	Thermal Parameters A	M/M'	O
Ca_2MnTaO_6	10.41	3.90	5.4574(1) 5.5664(1) 7.7166(2) 90.00(3)	0	0.8(1)	0.05(4)	0.4(3)
Ca_2FeTaO_6	10.50	4.22	5.4498(1) 5.5482(1) 7.7591(2) 90.072(4)	0	0.5(1)	0.01(4)	0
Ca_2AlTaO_6	9.91	3.01 2.66	5.3798(1) 5.4160(1) 7.6275(2) 90.088(7)	90.0(4)	0.45(8)	0.04(3)	0
Ca_2CrTaO_6	7.39	1.77 2.05	5.4245(1) 5.4981(1) 7.7163(2) 90.02	65.8(6)	0.6(1)	-0.04(3)	0
Ca_2GaTaO_6	10.12	2.16 7.24	5.4321(1) 5.5122(1) 7.7249(2) 89.958(3)	50(1)	0.69(8)	-0.01(2)	0
Sr_2CrSbO_6	15.93	4.49	5.57664(8) 5.55526(9) 7.8451(1) 90.00(1)	96(1)	0.30(4)	-0.02(4)	0
Na_2ZrTeO_6	9.69	2.45	5.49899(8) 5.53952(7) 7.8138(1) 90.014(9)	100	1.4(1)	0.34(2)	0.6(2)
La_2MgHfO_6	14.89	5.91	5.6672(2) 5.7666(2) 8.0648(3) 89.95(4)	10(1)	0.5(1)	0	0
Ca_2ScTaO_6	10.24	1.98	5.50505(8) 5.64621(9) 7.8679(1) 89.985(4)	95.0(6)	0.1(1)	-0.07(3)	0.0(2)
Ca_2YTaO_6 Ca Occ=.93 Y Occ=.07	9.87	2.42	5.59049(6) 5.80831(6) 8.0545(1) 89.973(2)	100	0.6(1)	0.14(3)	0.0(2)
Sr_2ScTaO_6 Ta Occ=.53 Sc Occ=.47	9.41	2.48 3.68	5.6925(5) 5.6924(4) 8.0590(2) 89.951(3)	98.5(2)	0.53(5)	0	0
Sr_2InTaO_6 Ta Occ=.56 In Occ=.44	8.49	2.65	5.7170(3) 5.7126(3) 8.0942(2) 89.893(3)	100	0.60(6)	0.03(3)	0

Table 5.12 : Results of refinements on monoclinic perovskite compounds. In some cases the supercell peaks were refined separately (second R_I value), but in others the increased number of lattice constants prevented independent refinement of the supercell reflections.

Comp.	x	y	z	Comp.	x	y	z
CMT				**SCrS**			
Ca	.511(3)	.5466(9)	.252(5)	**Sr**	.498(3)	.498(2)	.2507(8)
O1	.219(9)	.23(1)	-.042(5)	**O1**	.223(8)	.23(1)	-.014(9)
O2	.325(8)	.692(8)	-.041(6)	**O2**	.243(8)	.76(1)	-.024(6)
O3	.416(3)	-.027(4)	.25(2)	**O3**	.467(6)	0	.246(3)
CFT				**CST**			
Ca	.516(2)	.544(1)	.248(5)	**Ca**	.518(2)	.547(1)	.249(1)
O1	.21(1)	.233(9)	-.056(6)	**O1**	.200(3)	.217(3)	-.054(4)
O2	.29(1)	.705(7)	-.040(6)	**O2**	.290(3)	.696(3)	-.054(4)
O3	.410(3)	-.028(4)	.247(9)	**O3**	.411(3)	-.029(3)	.254(2)
CAT				**CYT**			
Ca	.4962(6)	.526(2)	.2360(8)	**Ca**	.515(2)	.5524(7)	.2459(8)
O1	.237(2)	.225(9)	-.024(2)	**O1**	.182(3)	.221(3)	-.067(3)
O2	.311(3)	.71(1)	-.038(7)	**O2**	.388(3)	.683(3)	-.050(3)
O3	.433(3)	-.019(6)	.243(4)	**O3**	.386(3)	-.053(3)	.266(3)
CCrT				**SST**			
Ca	.502(1)	.539(1)	.242(2)	**Sr**	.5081(4)	.5131(7)	.2468(9)
O1	.239(2)	.218(4)	-.044(5)	**O1**	.201(4)	.238(7)	.000(7)
O2	.307(4)	.707(5)	-.033(7)	**O2**	.250(3)	.745(5)	-.025(5)
O3	.420(3)	-.022(4)	.245(5)	**O3**	.421(3)	-.006(5)	.255(8)
CGT				**SIT**			
Ca	.507(1)	.540(1)	.250(3)	**Sr**	.511(1)	.5147(9)	.248(2)
O1	.226(3)	.211(4)	-.055(5)	**O1**	.19(1)	.19(1)	-.015(7)
O2	.297(4)	.721(5)	-.031(6)	**O2**	.26(1)	.75(1)	-.028(6)
O3	.418(3)	-.026(4)	.247(5)	**O3**	.47(1)	-.015(6)	.276(4)
LMgH				**NZTe**			
La	.509(1)	.5417(5)	.249(2)	**Na**	.501(5)	.519(2)	.253(3)
O1	.22 (1)	.21 (1)	-.04(1)	**O1**	.225(4)	.209(5)	-.034(8)
O2	.27(1)	.72 (1)	-.069(8)	**O2**	.291(4)	.724(4)	-.039(7)
O3	.394(6)	-.035(5)	.25(1)	**O3**	.423(3)	-.015(4)	.238(6)

Table 5.13 : Atomic positions of monoclinic perovskite compounds as refined from X-ray diffraction patterns. The trivalent cation (M) is located in position 2d at ½,0,0, and the pentavalent cation (M') is in position 2c at 0,½,0.

Compound	Density (g/cc)	Bond Valence A	M	M	O
Ca_2MnTaO_6	5.84	2.01	3.12	4.81	1.98 1.92 2.07
Ca_2FeTaO_6	5.85	2.00	3.14	4.85	2.01 1.98 2.01
Ca_2AlTaO_6	5.74	2.12	3.17	4.81	1.99 2.05 2.08
Ca_2CrTaO_6	5.90	2.04	3.52	4.42	1.96 1.98 2.06
Ca_2GaTaO_6	6.13	2.00	3.44	4.42	1.94 1.96 2.04
Sr_2CrSbO_6	6.08	2.14	3.09	5.41	2.16 2.11 2.12
Na_2ZrTeO_6	5.03	1.07	4.27	5.91	2.07 2.03 2.06
La_2MgHfO_6	7.27	2.91	2.05	3.77	1.82 1.96 2.03
Ca_2ScTaO_6	5.46	1.91	3.11	4.93	1.97 1.99 1.97
Ca_2YTaO_6	5.66	1.84	3.20	4.96	1.93 2.02 1.98
Sr_2ScTaO_6	6.32	1.91	3.02	5.33	2.11 2.01 1.97
Sr_2InTaO_6	7.12	1.91	3.59	5.21	2.00 2.05 2.26

Table 5.14 : Bond valence calculations for monoclinic perovskites.

	Ca_2FeTaO_6 Orthorhombic Pnma	Ca_2FeTaO_6 Monoclinic $P2_1/n$	Ca_2MnTaO_6 Orthorhombic Pnma	Ca_2MnTaO_6 Monoclinic $P2_1/n$
R_{wp}	11.51	10.50	11.06	10.41
R_i	4.92	4.22	4.31	3.90
a	5.4498(2)	5.4498(1)	5.4574(1)	5.4574(1)
b	7.7586(2)	5.5482(1)	7.7165(2)	5.5664(1)
c	5.5476(2)	7.7591(2)	5.5664(1)	7.7166(2)
β	90	90.072(4)	90	90.00(3)
Ca B Value	1.4(2)	0.5(1)	1.4(2)	0.8(1)
M/Ta B Value	-0.06(2)	0.01(4)	0.0	0.05(4)
O B Value	0.0	0.0	0.9(4)	0.4(3)

Table 5.15 : A comparison of the refinements of the disordered perovskites Ca_2FeTaO_6 and Ca_2MnTaO_6 using both orthorhombic and monoclinic space groups.

of 6) suggest that disorder between the Ca and Y sites is more likely than disorder between Y and Ta. Both Sr_2ScTaO_6 and Sr_2InTaO_6 appear to be somewhat Ta rich. Stoichiometry deviations are discussed in more detail in the next section.

Bond valence, lattice energy and geometry calculations were performed on these structures and a partial listing of the results is given in table 5.14. The bond distances and angles are not shown because the accuracy of these parameters (and the bond valences for that matter) is somewhat questionable. There are now 12 positional parameters to refine as opposed to one and three respectively in cubic and tetragonal perovskites and with x-ray diffraction it is difficult to accurately determine the oxygen positions. This problem was illustrated in the refinement of Ca_2CrTaO_6 presented in the previous chapter. The insensitivity of the pattern to small changes in the oxygen positions is probably also responsible for the thermal parameters of the oxygens refining negative in many cases. (When the oxygen B values went negative they were fixed at 0.0 , which was quite common as evidenced in table 5.12).

In the absence of long range cation order, it is reasonable to expect that complex perovskite $A_2MM'O_6$ compounds will belong to the Pnma space group. Contrary to this expectation, two disordered compounds, Ca_2MnTaO_6 and Ca_2FeTaO_6, are included in tables 5.12-5.14. Because the (101) reflection (cubic (111) reflection) was absent, signifying a random distribution of octahedral cations, Pnma was initially assumed to be the correct space group. After refinements using Pnma were complete, $P2_1/n$ was also used to refine both compounds. The results given in table 5.15 indicate that the monoclinic space group $P2_1/n$ gives a noticeably better fit to the observed pattern. Furthermore, a close inspection

of the patterns shows the presence of peaks (in particular the (021) reflection) which are forbidden in the Pnma space group. This confirms the monoclinic symmetry of the structure. Nonetheless, it is unclear why these compounds possess monoclinic rather than orthorhombic symmetry, in the absence long range cation order. Perhaps there is sufficient short range order to give rise to monoclinic symmetry.

5.8 Deviations from Ideal Stoichiometry

Although in most cases the Rietveld refinements gave very acceptable results that suggested nothing out of the ordinary, in some cases the B value for the octahedral site became negative. Although the thermal parameter for this site was rather small in all cases, because of the possible correlation between thermal parameters and occupancies, negative thermal parameters were treated as cause for further investigation. The first step was to fix the thermal parameter for the octahedral site to be zero and then let the occupancy on the octahedral site vary. In some cases the M:M' ratio did not vary from 1:1 even when the thermal parameter was fixed at zero. The original refinement values were used for such compounds. In other cases the refinements showed an M to M' ratio different from unity. These compounds were assumed to have deviated from the ideal stoichiometry and were refined as described below. Deviations from stoichiometry in compounds containing tantalum on the octahedral site inevitably showed an excess of tantalum. Since at this point no chemical analysis has been performed, the compounds were refined in one of two ways. Compounds with transition metal ions that can easily change oxidation state were generally refined with the $A_2M_{1-x}M'_{1+x}O_6$ model. When both ions were in stable oxidation states the compounds were refined with the $A_{2-x}M_{1-x}M'_{1+x}O_6$ model. In the latter model the excess Ta is compensated by vacancies of the A site (see also chapter four), while in the first model the transition metal, M, is assumed to be able to change its oxidation state in order to maintain a charge balance. Table 5.16 details the refinement results for all compounds that showed a tendency to deviate from the ideal composition. Notice that the Sr_2InTaO_6 samples and the one Sr_2CrTaO_6 sample (KS-1000°C) have lattice constants which vary appreciably from one compound to the next. This would be expected if significant deviations in stoichiometry exist from one sample to the next.

Some of the samples where refinements suggested a deviation from stoichiometry were analyzed by electron microprobe analysis (EMPA) to obtain an independent estimate of their true composition. Table 5.17 shows the refinement and EMPA results together. The EMPA

results are useful in a qualitative way, but proper standards were not used to justify using them quantitatively in the X-ray refinements.

Examining tables 5.16 and 5.17 one can see that the compounds $SrNaCrTaO_6$ and $SrNaFeTaO_6$ have both deviated significantly from their beginning stoichiometries. The loss of sodium from these samples is not too surprising, $SrNaFeTaO_6$ was annealed at 1000°C for 48 hours, but shows small amounts of Na/Fe/O impurity phases in both the XRD and EMPA results, and $SrNaCrTaO_6$ had to be annealed at 1400°C to get a single phase product. Under these conditions sodium could easily be lost due to volatilization. The loss of Cr and Fe from these samples is more perplexing, but perhaps volatile Na/Fe and Na/Cr oxide phases formed and were vaporized. Certainly with the chromium sample, and to a lesser extent with the iron containing sample, such phases are present at lower temperatures and shorter annealing times, but diminish or disappear with additional annealing. Both samples have excess Ta on the M site and a considerable concentration of vacancies on the A site. In both cases the oxidation state of the first row transition metal (Fe, Cr), assuming no oxygen vacancies is approximately 4.35. This oxidation state is higher than might be expected for iron and suggests that oxygen vacancies may be present.

The antimonate sample Sr_2MnSbO_6 appears to have lost antimony. The Rietveld refinements and microprobe results both indicate a loss of antimony. Further supporting this is the fact that at 1400°C the perovskite phase formed with a significant amount of an Sr/Sb phase (approximately $Sr_3SbO_{5.5}$) as an impurity. Upon heating to 1600°C the impurity level significantly decreased, but the lattice constants for the perovskite phase were unchanged. Consistent with the above observations Sb_2O_5 sublimes at 1550°C suggesting that volatilization is a real possibility. Unlike the tantalates, refinements of this compound suggest vacancies on the octahedral site.

Although the SIT and SGT samples analyzed with EMPA were made in a $SrCl_2$ flux, where the net stoichiometry has the possibility of changing while washing away the flux, the other tantalates were made by direct annealing methods. It is puzzling how elements such as Al, Sc, and Ta could be lost in these samples. Also the Sr/Ta ratio is consistently close to 2.15 in many of these samples. This may suggest that the electron microprobe calibration was slightly off and perhaps these deviations from stoichiometry are much smaller than implied by the EMPA results. Certainly the Sr/Ta ratio determined from microprobe analysis for Sr_2AlTaO_6 does not agree with the same ratio determined by combined X-ray and neutron diffraction (chapter four). In conclusion the results of this section indicate that stoichiometric deviations are possible, but more research is needed to understand the type and concentration of such defects and in many cases to confirm their presence.

Compound Sample	Synthesis Conditions	Deviation from Ideal Composition	Avg.Cell Edge (Å)	Impurities (Mole %)
Sr_2ScTaO_6		**$Sr_{2-x}Sc_{1-x}Ta_{1+x}O_6$**		
SST-2	DA1-1600°C	x=0.01	8.055	None
SST-3	KS-1600°C	x=0.03	8.053	None
Ba_2ScTaO_6		**$Ba_{2-x}Sc_{1-x}Ta_{1+x}O_6$**		
BST-1	DA1-1600°C	x=0.0	8.220	Traces
BST-2	KS-1600°C	x=0.02	8.223	None
Sr_2CrTaO_6		**$Sr_{2-x}Cr_{1-x}Ta_{1+x}O_6$**		
SCrT-1	1400°C	x=0.01	7.882	None
SCrT-2	1400°C	x=0.01	7.882	None
SCrT-3	1500°C	x=0.0	7.884	None
SCrT-4	KS-1000°C	x=0.08	7.894	32% $SrCrO_4$
SCrT-4	KS-1200°C	x=0.03	7.886	None
SCrT-4	KS-1400°C	x=0.01	7.883	None
SCrT-4	KS-1600°C	x=0.02	7.882	None
Sr_2FeTaO_6		**$Sr_2Fe_{1-x}Ta_{1+x}O_6$**		
SFT-1	Flux-1000°C	x=0.05	7.936	0.8% $Sr_5Ta_4O_{15}$
SFT-3	KS-1200°C	x=0.0	7.936	0.6% $Sr_5Ta_4O_{15}$
Sr_2InTaO_6		**$Sr_{2-x}In_{1-x}Ta_{1+x}O_6$**		
SIT-1	1400°C	x=0.04	8.086	25% In_2O_3
SIT-2	F/A-1400°C	x=0.07	8.104	6% In_2O_3
SIT-3	1400°C	x=0.04	8.092	10% In_2O_3
Ba_2InTaO_6		**$Ba_{2-x}In_{-x}Ta_{1+x}O_6$**		
BIT-1	1400°C	x=0.01	8.281	3% In_2O_3
BIT-2	1400°C	x=0.01	8.276	1% In_2O_3
Ca_2YTaO_6		**$(Ca_{2-x}Y_x)TaY_{1-x}Ca_xO_6$**		
CYT-1	KS-1400°C	x=0.13	8.057	Y_2O_3
$SrNaCrTaO_6$		**$Sr_{2-x}Na_xCrTaO_6$**		
SNCT-1	KS-1000°C	x=1.34	7.885	$SrCrO_4$,Cr_2O_3,Na_2CrO_4
SNCT-1	KS-1200°C	x=1.16	7.882	$SrCrO_4$,Cr_2O_3,Na_2CrO_4
SNCT-1	KS-1400°C	x=1.0	7.882	None
$SrNaFeTaO_6$		**$Sr_{2-x}Na_xFeTaO_6$**		
SNFT-1	KS-1000°C	x=0.94	7.917	$NaFeO_2$
SNFT-1	KS-1200°C	x=0.92	7.918	None
Sr_2MnSbO_6		**$Sr_2Mn_{1+x}Sb_{1-x}O_6$**		
SMS-1	KS-1400°C	x=0.12	7.899	54% $Sr_3SbO_{5.5}$
SMS-1	KS-1600°C	x=0.12	7.899	3% $Sr_3SbO_{5.5}$

Table 5.16 : Rietveld refinements of compounds where the diffraction data showed a tendency to deviate from the ideal stoichiometry. The average cubic cell edges were calculated from the cube root of the pseudocubic unit cells. The impurity concentrations are calculated from refinements. Flux denotes synthesis in a $SrCl_2$ flux, F/A denotes the flux/anneal synthesis route, KS denotes samples which were progressively heated to higher temperatures for annealing times of 24-48 hours at each temperature (1000°C, 1200°C, 1400°C, 1600°C).

Compound	Synthesis Conditions	Refinement Stoichiometry	Electron Microprobe Results
SNCT-1	KS-1400°C	$SrNaCrTaO_6$	Cr/Ta=0.51 Na/Sr=0.26 Sr/Ta=1.25
SNFT-1	KS-1000°C	$Sr_{1.06}Na_{.94}FeTaO_6$	Fe/Ta=0.64 Na/Sr=0.30 Sr/Ta=1.32
SMS-1	KS-1600°C	$Sr_2Mn_{1.12}Sb_{.88}O_6$	Mn/Sb=1.05 Sr/Sb=2.17
SMT-2	KS-1400°C	Sr_2MnTaO_6	Mn/Ta=0.92 Sr/Ta=2.14
SST-3	KS-1600°C	$Sr_{1.97}Sc_{.97}Ta_{1.03}O_6$	Sc/Ta=0.98 Sr/Ta=2.16 Al/Ta=0.04
SAT-31	DA1-1400°C	Sr_2AlTaO_6	Al/Ta=0.95 Sr/Ta=2.12
SIT-2	F/A-1400°C	$Sr_{1.93}In_{.93}Ta_{1.07}O_6$	In/Ta=0.97 Sr/Ta=1.95
SGT-9	F/A-1400°C	$Sr_{1.97}Ga_{.97}Ta_{1.03}O_6$	Ga/Ta=0.89 Sr/Ta=2.05

Table 5.17 : Refinement and electron microprobe results for compounds analyzed for chemical composition by microprobe analysis.

Tilt System	Compound	Cation Dist.	Tol. Factor	$\lvert R_M-R_{M'}\rvert$ (Å)	Reference
3-Tilt Systems					
$a^+b^-c^-$ (#8), $a^+a^-c^-$ (#9)	Sr_2YTaO_6	Ordered	0.931	0.260	This Work
$a^+b^-b^-$ (#10), $a^+a^-a^-$ (#11)	**Sr_2CrSbO_6**	**Ordered**	**1.008**	**0.015**	**This work**
	Sr_2FeSbO_6	**Ordered**	**1.000**	**0.045**	**1**
	(BaNd)$SbNiO_6$	**Ordered**	**0.989**	**0.090**	**2**
	Ca_2AlTaO_6	Ordered	0.982	0.105	This work
	(SrLa)$NiSbO_6$	**Ordered**	**0.975**	**0.090**	**18**
	Na_2ZrTeO_6	**Ordered**	**0.974**	**0.160**	**This work**
	(SrLa)$CoRuO_6$	Ordered	0.970	0.180	3
	Sr_2ScTaO_6	Ordered	0.966	0.105	This work
	(SrLa)$CuSbO_6$	**Ordered**	**0.965**	**0.130**	**4**
	(SrLa)$FeSnO_6$	**Random**	**0.964**	**0.045**	**18**
	(SrPr)$LiTeO_6$	**Ordered**	**0.958**	**0.200**	**5**
	La_2NiRuO_6	Ordered	0.956	0.070	6
	Sr_2LuRuO_6	Ordered	0.956	0.296	7
	La_2NiIrO_6	Ordered	0.955	0.065	8
	Ca_2MnTaO_6	Random	0.955	0.005	This work
	Ca_2FeTaO_6	Random	0.955	0.005	This work
	Sr_2InTaO_6	Ordered	0.953	0.160	This work
	Sr_2ErRuO_6	Ordered	0.950	0.325	9
	Sr_2YRuO_6	Ordered	0.947	0.335	10
	La_2MgIrO_6	Ordered	0.947	0.095	8
	La_2LiSbO_6	Ordered	0.944	0.160	11
	La_2CoIrO_6	Ordered	0.942	0.120	8
	La_2ZnIrO_6	Ordered	0.943	0.115	8
	(SrEu)$LiTeO_6$	**Ordered**	**0.943**	**0.200**	**19**
	(CaPr)$LiTeO_6$	**Ordered**	**0.940**	**0.200**	**5**
	Ba_2CeBiO_6	**Random**	**0.938**	**0.025**	**20**
	Ca_2ScTaO_6	Ordered	0.930	0.105	This work
	La_2MgHfO_6	Ordered	0.928	0.010	This Work
	Ca_2CrTaO_6	Ordered	0.921	0.025	This work, 12
	Ca_2GaTaO_6	Ordered	0.919	0.020	This work
	Nd_2MgTiO_6	Ordered	0.921	0.115	13
	Sr_2CaIrO_6	Ordered	0.912	0.375	14
	Ba_2SrUO_6	Ordered	0.908	0.450	15
	Ca_2YTaO_6	Ordered	0.897	0.260	This work
	Ca_2NdRuO_6	Ordered	0.895	0.418	9
	(CaLa)$CaRuO_6$	Ordered	0.895	0.435	17
	Sr_2CaUO_6	Ordered	0.891	0.270	15
	Sr_2NdBiO_6	**Ordered**	**0.888**	**0.223**	**21**
	(CaNd)$CaRuO_6$	Ordered	0.880	0.435	9
	Ca_2CaUO_6	Ordered	0.859	0.270	16
$a^-a^-a^-$ (#14)	**Ba_2YbBiO_6**	**Ordered**	**0.967**	**0.108**	**20**
	Ba_2BiBiO_6 (32-627°C)	**Ordered**	**0.932**	**0.270**	**22**
	$Ba_2(Ba_{.18}Bi_{.82})BiO_6$	Ordered			23
	$Ba_2(Ba_{.28}Bi_{.72})BiO_6$	Ordered			23

Table 5:18

Table 5:18 (Continued)

2-Tilt Systems					
$a^0b^-c^-$ (#19)	**$Ba_2LaRu_{.5}Sb_{.5}O_6$**	**Ordered**	**0.971**	**0.450**	**24**
	Ba_2LaRuO_6	Ordered	0.975	0.465	17
	$(BaLa)CoIrO_6$	Ordered	0.999	0.175	25
$a^0b^-b^-$ (#20)	**Ba_2TlSbO_6**	**Random**	**1.000**	**0.285**	**26**
	Sr_2NiTeO_6	**Ordered**	**0.999**	**0.130**	**27**
	Ba_2SbBiO_6 (4.2 K)	**Ordered**	**0.967**	**0.430**	**28**
	Ba_2TbBiO_6	**Ordered**	**0.951**	**0.018**	**20**
	Ba_2NdBiO_6	**Ordered**	**0.942**	**0.223**	**20**
	Ba_2PrBiO_6	**Ordered**	**0.934**	**0.060**	**20**
	Ba_2BiBiO_6 (<32°C)	**Ordered**	**0.932**	**0.270**	**22,28**
	$Ba_2(Bi_{1.33}Ru_{.67})O_6$	Ordered			29
1-Tilt Systems					
$a^0a^0c^-$ (#22)	**Sr_2GaSbO_6**	**Ordered**	**1.007**	**0.020**	**This work**
	Sr_2MnSbO_6	**Random**	**1.000**	**0.045**	**This work**
	Sr_2CoTaO_6	Random	0.999	0.030	This work
	Sr_2GaTaO_6	Ordered	0.996	0.020	This work
	Sr_2VTaO_6	Ordered	0.991	0.000	This work
	Sr_2FeTaO_6	Random	0.990	0.005	This work, 31
	Sr_2MnTaO_6	Random	0.990	0.005	This work
	Sr_2NiWO_6	Ordered	0.989	0.090	32
	Sr_2CuTeO_6	Ordered	0.989	0.170	30
	Sr_2CrTaO_6	Ordered	0.983	0.025	This work
	Sr_2MgWO_6	Ordered	0.981	0.120	This work
	Sr_2CuWO_6	Ordered	0.979	0.130	30
0-Tilt Systems					
$a^0a^0a^0$ (#23)	Ba_2NiWO_6	Ordered	1.049	0.090	33
	Ba_2CoWO_6	Ordered	1.035	0.145	33
	Ba_2MnReO_6	Ordered	1.026	0.280	34
	Sr_2AlTaO_6	Ordered	1.018	0.105	This Work
	Ba_2RuYO_6	Ordered	1.005	0.335	7
	Ba_2RuLuO_6	Ordered	0.986	0.295	7
	Ba_2BiBiO_6 (>627°C)	**Ordered**	**0.932**	**0.270**	**35**

Table 5.18 : A partial summary of the tilt systems for structurally determined double perovskite compounds. Not all $a^+b^-b^-$ compounds in the literature are listed. Only cubic compounds whose structures have been determined from neutron diffraction are included in tilt system $a^0a^0a^0$. The compounds with bold tolerance factors contain a high valent main group ion (Sb^{5+}, Te^{6+}, Bi^{5+}) on one of the octahedral sites. References for compounds in the table are as follows: 1] Battle *et al.* (1995), 2] Alvarez *et al.* (1993), 3] Kim & Battle (1995), 4] Attfield *et al.* (1992a), 5] Lopez *et al.* (1993a), 6] Seinen *et al.* (1987), 7] Battle & Jones (1989), 8] Currie *et al.* (1995), 9] Battle, Jones & Studer, 10] Battle & Macklin (1984), 11] Lopez *et al.* (1992), 12] Choy, Park, Hong & Kim (1994), 13] Groen, van Berkel & IJdo (1986), 14] Jung & Demazeau (1995), 15] Groen & IJdo, 16] van Duivenboden & IJdo (1986), 17] Battle, Goodenough & Price (1983), 18] Attfield *et al.* (1992b), 19] Lopez *et al.* (1993b), 20] Harrison *et al.* (1995), 21] Lenz & Mueller-Buschbaum (1990), 22] Cox & Sleight (1975), 23] Reis, Jacobson & Nicol (1993), 24] Almaer *et al.* (1993), 25] Powell, Gore & Battle (1993), 26] Subramanian *et al.*, 27] Koehl, Schultze-Rhonhof & Reinen (1970), 28] Thornton & Jacobson (1978), 29] Darriet *et al.* (1993), 30] Reinen & Weitzel (1976), 31] Nakagawa & Nomura (1966), 32] Köhl (1973), 33] Cox, Shirane & Frazer (1967), 34] Khattak, Cox & Wang (1975), 35] Sakuma, Hashizume & Yamanaka (1990).

5.9 Incidence of Ordered Octahedral Tilt Systems

Most of the known AMO_3 perovskite compounds have been structurally characterized and upon examination of their structure can easily be assigned to one of the 23 Glazer tilt systems. These compounds were cataloged according to tilt systems in tables 3.2 and 3.3, and served as the basis for much of the discussion in chapter three. Combining the results of this chapter and the previous chapter with the results of a literature search a similar data set can be constructed for double perovskite compounds. This compilation is contained in table 5.18. No representatives of tilt systems 1-7, 12, 13, 15-18 and 21 were found, hence these tilt systems are not contained in the table. Because of the potential to mistakenly assign cubic symmetry from X-ray data, only cubic structures which had been determined using neutron diffraction are included in table 5.18. Because of the large number of compounds found for tilt system $a^+b^-b^-$ (#10)/$a^+a^-a^-$ (#11) only a representative sampling of these compounds is given in table 5.18.

5.10 Discussion

5.10.1 Relationship between the Polyhedral Volumes and the Unit Cell Volume

It has been suggested by Thomas that distortions in perovskites can be understood in terms of the polyhedral volumes of the A and M cation (Thomas, 1996). In the undistorted cubic structure the polyhedra fill space in such a way that the volume of the M cation octahedron and the A cation dodecahedron combine to occupy the entire unit cell volume (Thomas, 1989):

$$V_U = Z(V_A + V_M) \qquad (5.1)$$

In distorted perovskites the octahedra remain regular, but the A cation coordination becomes distorted, significantly in some cases. Because of this distortion the volume of the A cation polyhedron becomes somewhat ill defined. However, if one assumes that the combined polyhedral volumes still occupy the entire volume of the unit cell, and that the octahedra remain perfectly rigid the apparent volume of the A cation polyhedron, V_A, can be determined from the following formula:

$$V_A = (V_U/Z) - 1.33\times(d_{M\text{-}O})^3 \qquad (5.2)$$

where $d_{M\text{-}O}$ is the octahedral bond distance. This can easily be extended to double perovskites where one obtains the formula:

$$V_A = (V_U/Z) - 0.667\times[(d_{M\text{-}O})^3+(d_{M'\text{-}O})^3]. \qquad (5.3)$$

The bond distances can either be obtained from the experimentally determined structure, or alternatively, can be estimated from ionic radii. Inaccuracies in the structure determination and partial cation order are two effects which complicate the use of experimentally determined bond distances. On the other hand, the ionic radii of all elements are easy to obtain and have been accurately compiled (Shannon, 1976). Furthermore, the results of chapter four indicated excellent agreement between ionic radii of the octahedral cations and the observed bond distances. Therefore, the bond distances will be calculated based on ionic radii for the remainder of this chapter. Using equation 5.3 with the experimentally determined unit cell volumes and the ionic radii of the constituent ions, apparent A cation volumes were calculated for the those compounds in table 5.18, with A=Ca, Sr, or Ba[†]. The results are plotted in figure 5.2. Figure 5.2a shows how the apparent A cation volume varies, while figure 5.2b shows the $V_A/V_{M/M'}$ ratio changes, both as a function of the average volume of the octahedral cation. In figure 5.2b those compounds with M'=Sb^{5+} or Te^{6+} have been excluded for reasons which will be discussed later.

Inspection of figure 5.2a shows that the apparent A cation volume increases as expected moving from calcium to strontium to barium. The other immediately apparent feature is the fact that the apparent A cation volume is not constant, but rather increases as the octahedral volume increases. For cubic compounds this effect can be attributed to the compressibility of the A-O bonds, as the "chemical pressure" is changed. For noncubic compounds the increase in the apparent volume of the A cation polyhedron, as the octahedral volume increases, can be at least in part attributed to the increased distortion of this polyhedron. It

[†] The six coordinate cation radii and two coordinate anion radii of Shannon and Prewitt (Shannon, 1976) were used with the exception of tungsten. The W^{6+}-O bond distance, if calcuated using the tabulated radii, comes out to 1.95Å. However, if the average tungsten oxygen distance in perovskite compounds is typically much shorter (Filip'ev, Shatalova, & Fesenko, 1974). For the calculations in this paper a value of 1.89Å was used. This value was obtained by averaging the W-O distances in Sr_2MgWO_6, Ba_2MgWO_6, Sr_2NiWO_6, Ba_2ZnWO_6, Ba_2NiWO_6, Ba_2CoWO_6, Sr_2CuWO_6, and Pb_2MgWO_6.

is a well established trend that as the distortion of an MX_n polyhedron increases the average M-X bond distances also increases[‡]. Here as the sizes of the octahedra increase the average tilt angle will also increase in order to maintain an optimal A-O interaction. What is perhaps surprising is that the apparent A cation volume can be modeled very well using a single linear fit for each A cation, regardless of the tilt system. This suggests that the magnitude of the tilting distortion is dependent primarily on the properties of the A cation (electronegativity, ionic radius) and the ionic radii of the M, M' and O ions. Performing linear regression for the three sets of compounds in figure 5.2 gives the following equations for the apparent A cation volume:

$$V_{Ca} = 2.1V_{M/M'} + 26, \tag{5.4}$$

$$V_{Sr} = 2.4V_{M/M'} + 26, \tag{5.5}$$

$$V_{Ba} = 2.5V_{M/M'} + 29, \tag{5.6}$$

$$V_{M/M'} = 1.333((r_M + r_O)^3 + (r_{M'} + r_O)^3). \tag{5.7}$$

These equations can also be used with equation 5.1 to calculate the expected unit cell volume from ionic radii of the octahedral cations. The slope values of these equations give a measure of how easily the A cation coordination sphere is either expanded/compressed or distorted upon changing bond lengths in the $MM'O_6$ octahedral framework. Any covalent character in the A-O interaction will favor direction specific bonding and discourage distortion of the coordination environment. This will result in a decrease in the value of the slope term, found in equations 5.4-5.6, relative to an A cation which has a smaller covalent interaction with oxygen. This parameter provides an estimate of the strength of the A-O interaction. Among calcium, strontium, and barium the trend in the value of the slope term, is consistent with the increasing electronegativity of the A cation, upon moving from calcium to barium.

[‡] The explanation for this effect is related to the anharmonicity of the M-X interaction potential. If this interaction is modeled using the concept of bond valence, with the constraint that the central ion must maintain a constant valence as the polyhedral distortion occurs, it is observed that the long bond distances increase at a faster rate than the short bond distances decrease. This is due to the exponential dependence between the bond valence and the bond distance (Brown & Altermatt, 1985; Brese & O'Keeffe, 1991).

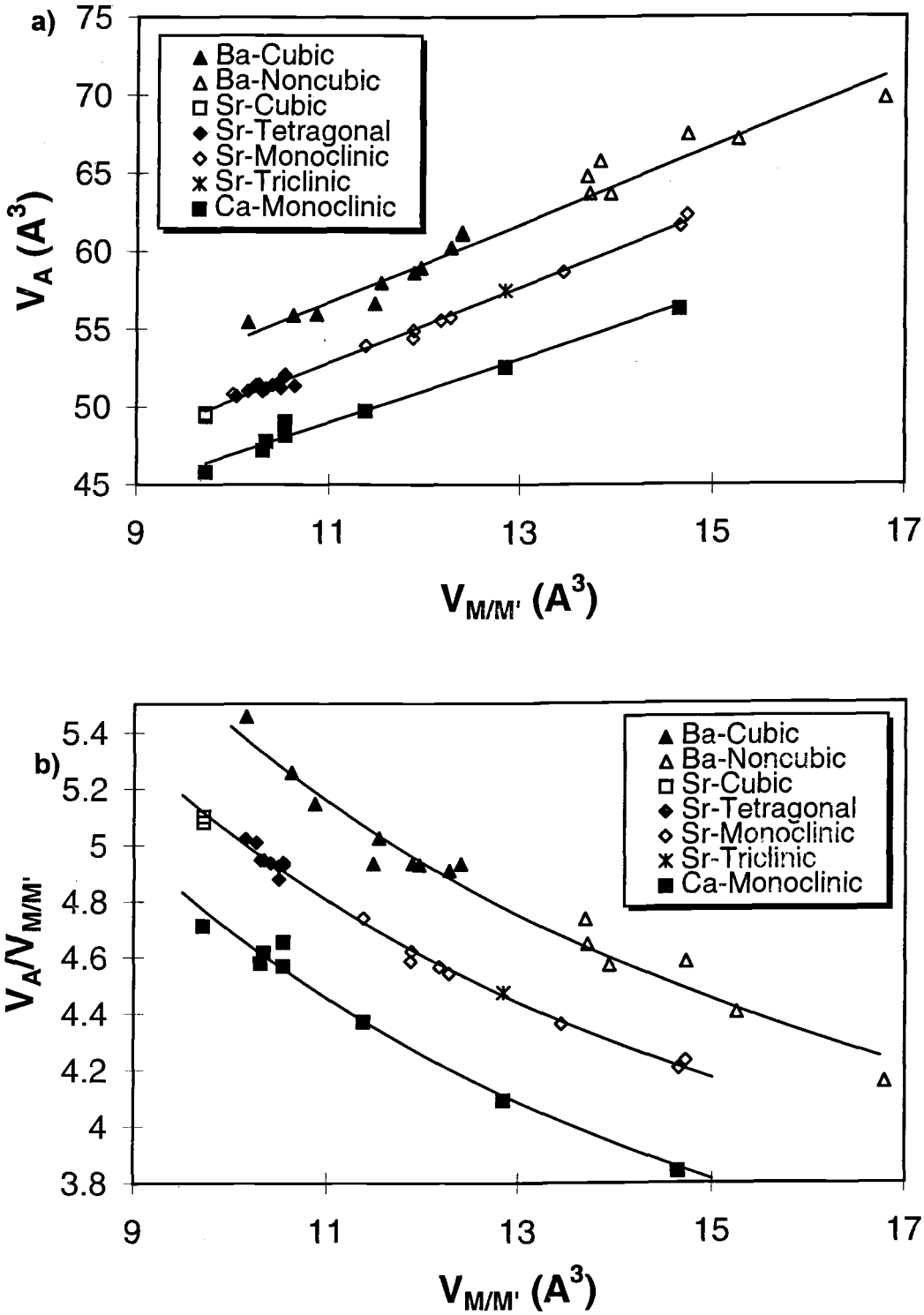

Figure 5.2 : A plot of the relationship between the average octahedral volume and a) the apparent A cation polyhedral volume, and b) the ratio of the A cation polyhedral volume to the average octahedral volume in $A_2MM'O_6$ perovskites with A=Ca, Sr, or Ba.

5.10.2 Prediction of Tilt System from the $V_A/V_{M/M'}$ Ratio

Thomas has examined in detail the relationship between structure and the V_A/V_M ratio in AMO_3 perovskites (Thomas, 1996; Thomas & Beitollahi, 1994; Thomas, 1989). He has shown that in the ideal cubic structure the V_A/V_M ratio is exactly 5.0, and this value decreases when octahedral tilting distortions occur. He also concludes that as this ratio decreases the number of axes about which tilting occurs, and the average tilt angle both increase (Thomas, 1996). The approach taken in this work differs from Thomas' methodology in that the polyhedral volumes are estimated based solely on the observed unit cell volume and the ionic radii of the octahedral cations (and oxygen), rather than on an analysis of the exact crystal structure. While a certain amount of accuracy is lost in using the ionic radii, the advantage of this approach is its simplicity and ease of use. In this way this approach may be thought of as combination of the polyhedral volume concepts of Thomas with the classical tolerance factor arguments of Goldschmidt (Goldschmidt, 1926). Examination of figure 5.2b confirms the general conclusion that as the V_A/V_M ratio decreases tilting distortions are more likely to occur. However, based strictly on this ratio no quantitative conclusions can be reached. For example when V_A/V_M is approximately 4.95 the strontium containing compounds are tetragonal ($a^0a^0c^-$) while the barium containing compounds are cubic ($a^0a^0a^0$). If on the other hand the data are segregated by A cation type, as is done in figure 5.2b, then the utility of this approach for separating the different tilt systems is clearly evident. Using equations 5.4-5.6 one can easily generate expressions which express the $V_A/V_{M/M'}$ ratio as a function of the octahedral volume, $V_{M/M'}$. The equations that result for each A cation are:

$$V_A/V_{M/M'} = 2.5 + 29/V_{M/M'} \qquad A=Ba, \qquad (5.8)$$

$$V_A/V_{M/M'} = 2.4 + 26/V_{M/M'} \qquad A=Sr, \qquad (5.9)$$

$$V_A/V_{M/M'} = 2.1 + 26/V_{M/M'} \qquad A=Ba. \qquad (6.0)$$

Using these equations and the ionic radii of the octahedral cations it is possible to estimate the polyhedral ratio for any compound containing calcium, strontium, or barium as the A site cation.

From the data in figure 5.2b stability ranges for each tilt system can be estimated. For A=Ba, cubic compounds are observed for $V_A/V_{M/M'} > 4.9$, and noncubic compounds for $V_A/V_{M/M'} < 4.8$. The noncubic compounds belong to the tilt systems: $a^0b^-b^-$ (#20), $a^0b^-c^-$

(#19), $a^-a^-a^-$ (#14), and $a^+b^-b^-$ (#10). There are not enough representatives of these tilt systems at this time to justify any further separation of tilt systems when A=Ba[§]. For A=Sr, either monoclinic or triclinic symmetry is found for $V_A/V_{M/M'} < 4.8$, tetragonal symmetry for $4.85 < V_A/V_{M/M'} < 5.05$, and cubic symmetry presumably for $V_A/V_{M/M'} > 5.05$. When A=Ca, monoclinic symmetry is always observed. The fact that the boundaries which separate different tilt systems vary from one A cation to the next is not unexpected. Even in an alkaline earth-oxygen bond there is some degree of covalency. Increasing covalency in the A-O interaction will favor the lower coordination numbers found in the distorted perovskite structures over the dodecahedral 12 coordinate environment found in the cubic structure. To a simple approximation the degree of covalency in the A-O bonds will be proportional to the electronegativity of the A cation. Therefore, as the electronegativity of the A cation is increased the $V_A/V_{M/M'}$ ratios which separate the cubic/tetragonal and tetragonal/monoclinic regions are expected to shift to larger values. This is what is observed upon going from barium to strontium. Although no cubic or tetragonal $Ca_2MM'O_6$ compounds were found in the literature, one can estimate that the tetragonal structure will probably not be stabilized below $V_A/V_{M/M'} \cong 5$. If this estimate is used together with equation 5.8 calculations indicate that to obtain a tetragonal $Ca_2MM'O_6$ compound the average M/M'-O bond distance would need to be approximately 1.84Å. This small value (Al^{3+}-O bond distances are 1.885Å) suggests that it is highly unlikely to form a double perovskite with A=Ca that is either tetragonal or cubic at ambient conditions.

This technique shows great promise as a tool to predict symmetries of unknown perovskites. Furthermore, as indicated in the previous chapter and earlier in this chapter when cation ordering is present it can be very difficult to distinguish certain tilt systems based on refinements of x-ray data. However, the approach outlined above can be used as a guide to indicate the tilt systems which are most likely to be observed. The advantage of this approach over a simple calculation of the tolerance factor is that the electronegativity of the A cation, which was shown in chapter three to play an important role in determining the tilt system, is now taken into account. Therefore, further work should be undertaken to establish $V_A/V_{M/M'}$ vs. $V_{M/M'}$ relationships for other A cations in order to expand the utility of this approach.

[§] Compounds where more than two types of ions occupy the octahedral site have not been included in figure 5.15. Included in this list are compounds such as $Ba_2(Tb^{3+}Tb^{4+})(Bi^{5+}Bi^{3+})O_6$ (Harrison *et al.*, 1995) which display mixed valency.

5.10.3 p Block Elements in High Oxidation States on the Octahedral Site

The discussion up to this point has completely ignored the effect of the octahedral cation-anion bonding. The treatment of the previous section showed that for many compounds the tilting behavior can be described quite well without any consideration of M-O bonding. However, when one of the octahedral cations is a small highly charged main group element, such as Sb^{5+} or Te^{6+}, the M-O bonding must be considered. M-O bonding plays an important role when these ions are present because formation of strong metal oxygen bonds is dependent upon the M' cation effectively polarizing the electron cloud surrounding oxygen. The 180° M-O-M' bond angle found in the cubic structure, is the least favorable geometry for optimizing oxygen polarization. This is because the oxygen electron cloud is being pulled in exact opposite directions by the M and M' ions. For this reason these compounds typically undergo octahedral tilting distortions to reduce the M-O-M' angle. Even when arguments based on ionic radii suggest that the A cation is a good fit to the cubic lattice. In table 5.18 there are several examples of this type of behavior. Their tolerance factors are marked in bold. This effect is particularly evident among the $a^+b^-b^-$ compounds in table 5.18. Excluding Ca_2AlTaO_6 (the electronegativity effect of calcium was discussed in the previous section) all of the monoclinic perovskites in this tilt system with tolerance factors greater than 0.97, have either Sb^{5+} or Te^{6+} as one of the octahedral cations. In these compounds the octahedral tilting is not driven by A cation coordination, but rather by M-O and M'-O bonding interactions. This effect is not observed in compounds containing transition metals in high oxidation states, because they have empty d-orbitals available for pi bonding. In contrast to anion polarization, pi bonding is optimized in the 180° M-O-M' geometry. The bonding differences between transition metals (Nb^{5+}/ Ta^{5+}) and main group elements (Sb^{5+}/Bi^{5+}), and the effect they have on the observed crystal structure are discussed in detail in the literature (Goodenough & Kafalas, 1973; Blasse, 1965). We will see in the next chapter that this effect also has important implications with respect to the ordering behavior in double perovskites.

5.11 Conclusions

Approximately thirty $A_2MM'O_6$ compounds have been synthesized and structurally characterized using the Rietveld method to refine the X-ray powder diffraction patterns. Although most of the compounds had previously been reported, structural determinations

had never been performed in most cases. In contrast to the AMO_3 perovskites the tetragonal $a^0a^0c^-$ tilt system appears to be favored rather than the rhombohedral $a^-a^-a^-$ tilt system for slight distortions from the cubic structure. The number of structurally characterized members of this tilt system has been greatly expanded as a result of this work. A method for predicting the most stable tilt system for a compound based on the ionic radii of the M and M' cations and the identity of the A cation has been proposed. This classification scheme has been shown to be very effective when the A cation is calcium, strontium, or barium. Compounds containing p block cations, such as Sb^{5+} and Te^{6+}, are found to be commonly distorted to a greater extent than would be expected from their tolerance factor. This effect can be understood in terms of the bonding preferences of these cations.

5.12 References

Albright, T.A., Burdett, J.K. & Whangbo, M.-H. (1985). *Orbital Interactions in Chemistry*, Wiley, New York.

Almaer, S.A., Battle, P.D., Lightfoot, P., Mellen, R.S. & Powell, A.V. (1993). *J. Solid State Chem.*, **102**, 375.

Altermatt, C. & Brown, I.D. (1987). *Acta Cryst.* A**43**, 125.

Alvarez, I., Lopez, M.L., Gonzales, C., Jerez, A., Veiga, M.L. & Pico, C. (1993). *Solid State Ionics* **63**, 609.

Attfield, M.P., Battle, P.D., Bollen, S.K., Gibb, T.C. & Whitehead, R.J. (1992b). *J. Solid State Chem.* **100**, 37.

Attfield, M.P., Battle, P.D., Bollen, S.K., Kim, S.H., Powell, A.V. & Workman, M. (1992a). *J. Solid State Chem.* **96**, 344.

Battle, P.D. & Jones, C.W. (1989). *J. Solid State Chem.* **78**, 108.

Battle, P.D. & Macklin, W.J. (1984). *J. Solid State Chem.* **52**, 138.

Battle, P.D., Gibb, T.C., Herod, A.J. & Hodges, J.P. (1995). *J. Mater. Chem.*, **5**(1), 75.

Battle, P.D., Goodenough, J.B. & Price, R. (1983). *J. Solid State Chem.* **46**, 234.

Battle, P.D., Jones, C.W. & Studer, F. (1991). *J. Solid State Chem.*, **90**, 302.

Bayer, G. (1969). *Fortschr. Miner.* **46**, 42.

Bell, R.O. (1968). *J. Phys. Chem. Solids*, **29**, 1.

Bernier, J.-C., Chauvel, C. & Kahn, O. (1974). *J. Solid State Chem.* **11**, 265.

Blasse, G. (1965). *J. Inorg. Nucl. Chem.*, **27**, 993.

Brandle, C.D. & Fratello, V.J. (1990). *J. Mater. Res.*, **5**(10), 2160.

Brese, N.E. & O'Keeffe (1991). *Acta Cryst.* B**47**, 192.

Choisnet, J., Rulmont, A. & Tarte, P. (1989). *J. Solid State Chem.* **82**, 272.

Choy, J.-H. Park, J.-H., Hong, S.-T. & Kim, D.-K. (1994). *J. Solid State Chem.*, **111**, 370.

Cox, D.E. & Sleight (1979). A.W. *Acta Cryst.*, **B35**, 1.

Cox, D.E., Shirane, G. & Frazer, B.C. (1967). *J. Appl. Phys.* **38**, 1459.

Currie, R.C., Vente, J.F., Frikkee, E. & IJdo, D.J.W. (1995). *J. Solid State Chem.*, **116**, 199.

Darriet, J., Bontchev, R., Dussarrat, C., Weill, F. & Darriet, B. (1993). *Eur. J. Solid State Chem.* **30**, 273.

Fesenko, E.G., Filip'ev, V.S. & Kupriyanov, M.F. (1964). *Izv. Akad. Nauk SSSR, Ser. Fiz.*, **28**, 669.

Filip'ev, V.S. & Fesenko, E.G. (1965). *Sov. Phys. Crystallogr.*, **10**(3), 243.

Filip'ev, V.S. & Fesenko, E.G. (1966). *Sov. Phys. Crystallogr.*, **10**(5), 532.

Filip'ev, V.S., Shatalova, G.E. & Fesenko, E.G. (1974). *Kristalographiya* **19**, 236.

Galasso, F.S. (1969). *Structure, Properties, and Preparation of Perovskite Type Compounds*, Pergammon Press, Oxford.

Galasso, F.S., Layden, G.K. & Flinchbaugh, D.E. (1966). *J. Chem. Phys.*, **44**(7), 2703.

Geguzina, G.A., Fesenko, E.G. & Devlikanova, R.U. (1976). *Sov. Phys. Crystallogr.* **20**(4), 518.

Groen, W.A., & IJdo, D.J.W. (1987). *Acta Cryst.* C**43**, 1033.

Groen, W.A., van Berkel, F.P.F. & IJdo, D.J.W. (1986). *Acta Cryst.* C**42**, 1472.

Harrison, W.T.A., Reis, K.P., Jacobson, A.J., Schneemeyer, L.F. & Waszczak, J.V. (1995). *Chem. Mater.* **7**, 2161.

Izumi, F. (1989). *Rigaku J.*, **6**, 10.

Izumi, F. (1993). *The Rietveld Method*, ed. R.A. Young, Oxford University Press, Oxford, Ch. 13.

Jung, D.-Y. & Demazeau, G. (1995). *J. Solid State Chem.*, **115**, 447.

Khattak, C.P., Cox, D.E. & Wang, F.F.Y. (1975). *J. Solid State Chem.* **13**, 77.

Kim, S.H. & Battle, P.D. (1995). *J. Solid State Chem.*, **114**, 174.

Koehl, P., Schultze-Rhonhof & Reinen, D. (1970). *Z. Anorg. Allg. Chem.* **378**, 129.

Köhl, V.P. (1973). *Z. Anorg. Allg. Chemie,* **401**, 121.

Kupriyanov, M.F. & Filip'ev, V.S. (1963). *Sov. Phys. Crystallogr.*, **8**(3), 278.

Lenz, A., Mueller-Buschbaum, H. (1990). *J. Less Common Metals*, **161**, 141.

Lopez, M.L., Alvarez, I., Gaitan, M., Jerez, A., Pico, C. & Veiga, M.L. (1993b). *Solid State Ionics* **63**, 599.

Lopez, M.L., Jerez, A., Pico, C., Saez-Puche, R. & Veiga, M.L. (1993a). *J. Solid State Chem.* **105**, 19.

Lopez, M.L., Veiga, M.L., Rodriguez-Carvajal, J., Fernandez, F., Jerez, A. & Pico, C. (1992). *Mater. Res. Bull.* **27**, 647.

Nakagawa, T. & Nomura, S. (1966). *Japan J.Appl. Phys.*, **5**(7), 578.

Nomura, S. & Nakagawa, T. (1971). *J. Phys. Soc. Japan*, **30**(2), 491.

Okazaki, A. & Suemune, Y. (1961). *J. Phys. Soc. Jpn.* **16**, 176.

Powell, A.V., Gore, J.G. & Battle, P.D. (1993). *J. Alloys Comp.*, **201**, 73.

Reinen, C. & Weitzel, H. (1976). *Z. Anorg. Allg. Chem.* **424**, 31.

Reis, K.P., Jacobson, A.J. & Nicol, J.M. (1993). *J. Solid State Chem.* **107**, 428.

Sakuma, H. Hashizume, H. & Yamanaka, A. (1990). *Acta Cryst.* B**46**, 693.

Seinen, P.A., van Berkel, F.P.F., Groen, W.A. & IJdo, D.J.W. (1987). *Mater. Res. Bull.* **22**, 535.

Shuvaeva, E.T. & Fesenko, E.G. (1970). *Sov. Phys. Crystallography*, **14**(6), 926.

Sleight, A.W. (1964). Thesis--*Disertation Abstracts,* **24**, 64-3565, U. Connecticut--1963.

Sleight, A.W., Ward, R. (1962). *Inorg. Chem*, **1**(4), 790.

Subramanian, M.A., Ganguli, A.K., Willmer, K.L. & Greedan, J.E. (1991). *J. Solid State Chem.* **95**, 447.

Thomas, N.W. & Beitollahi, A. (1996). *Acta Cryst.* B**50**, 549.

Thomas, N.W. (1989). *Acta Cryst.* B**45**, 337.

Thomas, N.W. (1996). *Acta Cryst.* B**52**, 16.

Thornton, G. & Jacobson, A.J. (1978). *Acta Cryst.*, **B34**, 351.

van Duivenboden, J.C. & IJdo, D.J.W. (1986). *Acta Cryst.*, **C42**, 523.

Woodward, P.M., Hoffmann, R.-D. & Sleight, A.W. (1994). *J. Mater. Res.* **8**, 2118.

Yvon, K., Jeitschko, W. & Parthe, E. (1977). LAZY PULVERIX: A computer program for calculating X-ray and neutron diffraction powder patterns. *J. Appl. Cryst.* **10**, 73.

Chapter 6

Long Range Order in Double Perovskites

6.1 Introduction

The previous chapter contained a detailed study of octahedral tilting distortions in double perovskite compounds. This chapter describes a complimentary study of the long range ordering behavior in these compounds. The work was partially motivated by a desire to extend the techniques used to study cation ordering in Sr_2AlTaO_6 and Sr_2AlNbO_6 (Woodward, Sleight & Hoffmann, 1994) to double perovskites in general. However, before describing the detailed results of this study it is instructive to examine the findings of previous workers in this area.

It has been known for over thirty years that different types and degrees of long range order exist in complex perovskite compounds. During this time there have been several studies undertaken in which attempts were made to identify the factors controlling the ordering behavior (Galasso & Darby, 1962; Sleight, 1964; Patrat, Brunel & deBergevin, 1976; Wittman, Rauser & Kemmler-Sack, 1981; Randall, Bhalla, Shrout & Cross, 1990; Anderson, Greenwood, Taylor & Poeppelmeier, 1993). Furthermore, at least four different types of ordering have been observed depending upon the combination and ratio of ions present. The most common type of ordering observed is the 1:1 ordering of the octahedral M and M' cations previously described. When the ratio of octahedral cations is 1:1, as it is for all of the compounds studied in this thesis, this type of ordering results in a stoichiometric distribution of cations where the M and M' cations are separated on crystallographically distinct sites. However, this type of ordering can also occur when the ratio of M to M' is not 1:1. For example, the compounds $Sr_3MSb_2O_9$ (M=Mg,Ca,Co,Cu,Sr) all display 1:1 order (Blasse, 1965). In these compounds one of the two octahedral sites is occupied exclusively (or at least predominantly) by the octahedral cation in greater concentration, while the other site is occupied by the remainder of the octahedral cations. A more illustrative way of writing the formula for these compounds is $A_2(M_{2/3}M'_{1/3})M'O_6$. When 1:1 ordering occurs in compounds where the M:M' ratio is not 1:1 it is often called non-stoichiometric ordering (Randall, Bhalla, Shrout & Cross, 1990).

When the M:M' ratio is 2:1 another type of ordering may occur, where the M and M' ions order on (111) planes of the cubic structure. In this ordering arrangement, commonly called

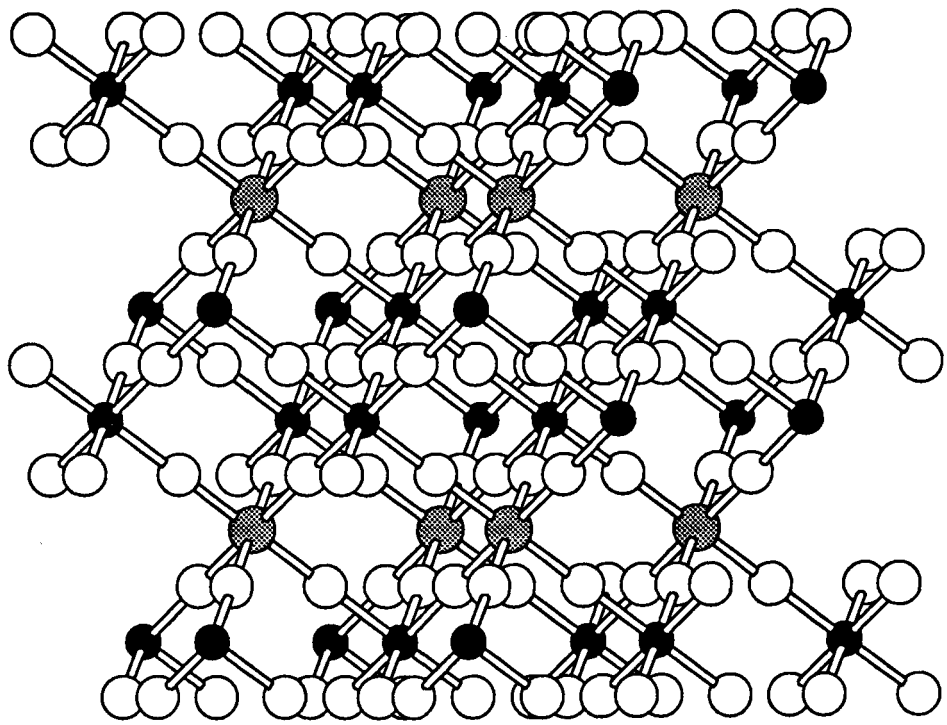

Figure 6.1 : The 2:1 ordered structure sometimes observed for $A_3M_2M'O_9$ compounds. The O ions are represented by open spheres, the M ions by black spheres, the M' ions by shaded spheres. The A cations have been omitted for clarity.

the 2:1 ordered structure, if the lattice is viewed along (111) planes there is a hexagonal close packing sequence of AO_3 layers and between these layers the M and M' cations fill the octahedral holes. The layering sequence is (AO_3-M'-AO_3-M'-AO_3-M-). Figure 6.1 shows the 2:1 ordered structure. Blasse noted that in $A_3MM'_2O_9$ compounds annealed between 1000°C and 1300°C only the compounds where A=Ba showed 2:1 ordering, but when A=Sr or Sr/La these compounds displayed 1:1 ordering even when the charge difference between M and M' was large (Blasse, 1965). He attributes this behavior to kinetic limitations in compound formation. Others have attributed the difficulty in achieving the 2:1 ordered structure to a poor local charge balance.

The final two types of ordering observed in perovskites are both relatively uncommon. In compounds such as $NaLaTi_2O_6$, $NaYTi_2O_6$, $NaBiTi_2O_6$, $LiLaTi_2O_6$ (Daleveld, Bruntich, Dotman & Blasse, 1973), $Pb_{1-x}Ca_xTiO_3$ (King, Goo, Yamamoto & Okazaki, 1988), and $Ba_{1-x}Pb_xTiO_3$ (Wang & Zhang, 1990) long range ordering has been observed between A site cations. It appears that different ordering arrangements can occur depending upon the cation ratio (Wang & Zhang, 1990), but this type of ordering phenomenon appears to be not completely characterized. The other type of ordering phenomenon observed in complex perovskites is the ordered layer structure (Anderson & Poeppelmeier, 1991). In this structure instead of ordering in a 1:1 face centered arrangement, the octahedral cations order along alternating cubic (100) planes. It appears that in order for this type of ordering to be favored, over the normal fcc 1:1 ordering scheme, the smaller octahedral cation has to be a Jahn-Teller ion, significantly different in size from the larger octahedral cation, and the charge difference between the cations must be two. The only compound known to adopt this structure is La_2CuSnO_6 (Anderson & Poeppelmeier, 1991). Of the four types of long range order discussed above 1:1 ordering is by far the most common and only 1:1 ordering was studied in this work. Therefore, any references to ordering throughout the rest of the text will understood to imply fcc 1:1 ordering of octahedral cations.

When considering the factors influencing ordering all reports in the literature agree that the most important factor driving the long range ordering process is the charge difference between M and M' ions. In general, when the charge difference is 0 or 1 no long range order exists between M and M', and when the charge difference is 3 or greater only the ordered structure is observed. In their comprehensive review of the literature Anderson, Greenwood, Taylor and Poeppelmeier (1993) found only three exceptions to this rule of thumb; the ordered compounds Ba_2PrPtO_6 (charge difference 0) (Amador, Hetherington,

Moran & Alario-Franco, 1992), $CaLaMnCoO_6$ (charge difference 1) (Vallet-Regi, Garcia & Gonzales-Calbet, 1988), and the disordered compound $SrLaCuRuO_6$ (charge difference 3) (Attfield *et al.,* 1992). In the case of Ba_2PrPtO_6 the large size difference between Pr^{4+} (0.85Å) and Pt^{4+} (0.625Å) is probably responsible for the ordering. In the latter two compounds the presence of transitions metals on both octahedral sites introduces some uncertainty into the assignment of oxidation states. In any case, in order to study variations in long range order most studies, including this one, consider primarily the class of compounds where the charge difference between octahedral cations is 2.

It has generally been accepted in the literature that following the difference in charge between M and M', the next most important factor in determining the long range order is the size difference between the two ions (Galasso & Darby, 1962; Anderson, Greenwood, Taylor & Poeppelmeier, 1993). Although the size difference is an important factor, a careful examination of the literature, as well as the results of this study, clearly shows that a model based solely on the charge and size differences between M and M' is too simplistic to accurately predict and explain the long range ordering behavior of many compounds. In his Ph.D. thesis, Sleight noted this and remarked that in Sr_2MTaO_6 perovskites there appeared to be no correlation between the M/Ta size difference and the observed degree of long range order (Sleight, 1964). He concluded that factors such as the degree of covalency in the M'-O bonding (increased covalency led to higher degrees of order), size of the A cation (smaller A cations promote higher degrees of order), crystal field stabilization (the presence of non-transition metals on the octahedral site results in higher degrees of order), and kinetic effects all influence the long range order (Sleight, 1964). Furthermore, to this author's knowledge Sleight's study is still the only one where the degree of long range order was determined for each compound[†] and they were not merely classified as either ordered or disordered (Randall, et. al. separate $Pb_2MM'O_6$ compounds into disordered, ordered with large coherent ordered domains, and ordered with short coherency, but do not estimate the degree of order beyond that classification (Randall, Bhalla, Shrout & Cross, 1990)). Another observation from the literature is that Sleight (1964) and Blasse (1965) both observe that Sr_2MSbO_6 compounds are in general more highly ordered than Sr_2MTaO_6 compounds.

---

[*] Charge difference is used throughout this chapter to imply differences in formal oxidation states, not actual charges. For a discussion of the differences between formal oxidation state and actual charge see Sleight (1989).

[†] The degree of long range order is defined as suggested by Sleight (1964) to be S=2x-1, where the stoichiometry is $A_2(M_xM'_{1-x})(M'_xM_{1-x})O_6$ and x>0.5. This gives a parameter which varies between 0% for a disordered compound and 100% for a completely ordered compound.

In general, a review of the literature shows that even though certain systems such as $Ba_4Bi_2O_9$ (Reis & Jacobson, 1993), Ln_2MCuO_6 (Anderson, Greenwood, Taylor & Poeppelmeier, 1993), and $Pb_2M_{1-x}M'_xO_6$ (Randall, Bhalla, Shrout & Cross, 1990) have been studied in some detail, an overall understanding of the factors which influence the ordering behavior of complex perovskites as a whole has not been developed. Furthermore, most studies have neglected the subtleties associated with partially ordered compounds. However, these subtleties (degree of order, ordered domain size, etc.) are, for relaxor ferroelectric applications in particular, directly related to the physical properties of interest. Probably the most comprehensive study was the Ph.D. work of Sleight, which was performed 31 years ago. In light of the importance of long range order in technologically important perovskites and the advances in powder diffraction analysis over the past 31 years, it was felt that a study aimed at developing a unified theory on the ordering behavior of perovskites could make an important contribution to our understanding of these materials.

6.2 Results

6.2.1 General Results for all $AA'MM'O_6$ Compounds

During the course of this work many compounds were synthesized, some in a variety of ways. The structures of these compounds were characterized by refining the powder diffraction patterns, using the Rietveld method. A more detailed description of the data collection and refinement procedure can be found in chapter five. Table 6.1 summarizes the results on all compounds synthesized in this work. This table contains all of the information pertinent to a discussion of the differences in long range ordering behavior, structural details for each compound are discussed in chapters five and six[‡]. Two important parameters were used to evaluate the long range order present in each compound, the long range order parameter, S, and the presence of antiphase boundaries. The presence of antiphase boundaries was confirmed by a broadening of the superstructure reflections to give an ordered domain size smaller than the overall crystallite size.

[‡] Pb_2ScTaO_6, Sr_2RhTaO_6 and Sr_2FeSbO_6 are not included in chapters five or six. The first two compounds appear to be cubic from analysis of the XRD data, but based on the relative ionic sizes lower symmetry is expected. In the absence of neutron data their inclusion in chapter six did not seem warranted. Sr_2FeSbO_6 is monoclinic (tilt system $a^+b^-b^-$, space group $P2_1/n$) and has been described in the literature (Battle, Gibb, Herod & Hodges, 1995).

Compound	Synthesis Cond.	Long Range Order Parameter	Detectable Antiphase Boundaries
Ca_2AlTaO_6	DA 1400-1500°C	90-92%	Yes
Sr_2AlTaO_6	DA 1400-1690°C	89-96%	Yes
Ca_2ScTaO_6	DA 1400-1600°C	95-97%	No
Sr_2ScTaO_6	DA 1400-1600°C	82-100%	Yes
Ba_2ScTaO_6	DA 1400-1600°C	72-96%	Yes
Pb_2ScTaO_6	DA 1000-1200°C	81-87%	Yes
Sr_2VTaO_6	DA 1400°C (H_2)	52%	Yes
Ca_2CrTaO_6	DA 1400-1500°C	56-67%	Yes
Sr_2CrTaO_6	DA 1200-1600°C	60-70%	Yes
$SrNaCrTaO_6$	DA 1200-1400°C	0%	---
Ca_2MnTaO_6	DA 1400°C	0%	---
Sr_2MnTaO_6	DA 1400°C	0%	---
Ca_2FeTaO_6	DA 1100°C	0%	---
Sr_2FeTaO_6	DA 1100-1200°C	0%-Low	Yes
$SrNaFeTaO_6$	DA 1000°C	0%	---
Ba_2FeTaO_6	DA 1100°C	0%	---
Sr_2CoTaO_6	DA 1100-1200°C	0%	---
Ca_2GaTaO_6	DA 1400°C	50%	Yes
Sr_2GaTaO_6	DA 1400-1600°C	48-64%	Yes
Ca_2YTaO_6	DA 1400°C	100%	No
Sr_2YTaO_6	DA 1200-1600°C	90-100%	No
Sr_2RhTaO_6	DA 1200°C	84%	Yes
Sr_2InTaO_6	DA 1400°C	100%	No
Ba_2InTaO_6	DA 1400°C	79-100%	No
Sr_2MgWO_6	DA 1350°C	99%	No
La_2MgHfO_6	Soln/Anneal 1500°C	10%	Yes
Na_2ZrTeO_6	Two Stage 700°C	100%	No
Sr_2CrSbO_6	DA 1400-1600°C	96-97%	No
Sr_2MnSbO_6	DA 1400-1600°C	0%	---
Sr_2FeSbO_6	DA 1000-1400°C	66-96%	Yes
Sr_2GaSbO_6	DA 1200-1400°C	96-97%	No
Ba_2ScBiO_6	DA 1000-1200°C	0-83%	Yes

Table 6.1 : Long range ordering results for several double perovskite compounds. DA, F/A, and Flux refer to direct anneal, flux/anneal, and flux ($SrCl_2$) synthesis techniques. Antiphase boundaries were assumed to be present when broadening of superstructure reflections, with respect to the subcell reflections, could be detected. For these compounds the superstructure reflections were too weak to easily ascertain if they were significantly broadened.

6.2.2 Kinetic Study

Although the results given in Table 6.1 are useful and can be used to draw many conclusions, it was felt that a more meaningful comparison could be made between different compounds if they had all been synthesized in the same manner. All compounds were prepared from appropriate mixtures of $A(NO_3)_2$ (BaO_2 in the case of Ba_2ScBiO_6), M_2O_3 and $M_2'O_5$. After grinding in a mortar and pestle each compound was heated to 1000°C for one hour. This was followed by an annealing treatment at 1000°C for 48 hours, and the collection of a subsequent x-ray diffraction pattern. The compounds were then heated to 1200°C and 1400°C for 24 hours at each temperature, taking a diffraction pattern after each annealing step. Finally, those compounds with ions that were stable at high temperatures were heated to 1600°C for 12 hours. By taking diffraction patterns after each annealing step it was hoped that the range over which the order parameter could vary would be determined for each compound. Table 6.2 summarizes the results of this study. There are not entries at each temperature for all compounds for a variety of reasons. Some compounds did not form the perovskite phase as a major phase at lower temperatures. Even among the entries in table 6.2 some of the samples had significant quantities of impurity phases present after the lower temperature annealing steps. At higher temperatures some entries are missing because the compound decomposed or converted to several different perovskite phases of varying composition. Most of the compounds studied either had 0% long range order at all temperatures or had a long range order parameter in the 90-100% range after annealing at the highest temperatures. Even those compounds that achieve a high degree of long range order can be divided into two different classes, those with antiphase boundaries and those without antiphase boundaries. However, there were some compounds that not only displayed intermediate degrees of order at all temperatures but also showed a decrease in the long range order at the highest temperatures, such as Sr_2CrTaO_6 and Sr_2GaTaO_6. It may be that for these two compounds the thermodynamic equilibrium state is a partially ordered structure, or at least that the kinetic processes associated with achieving the completely ordered structure are very slow. Sr_2FeTaO_6 showed a very broad and weak reflection where the first superstructure peak was expected. The peak was too broad to analyze but it would seem to indicate that some degree of long range order was present. The degree of long range order could not be quantified so it is simply listed as low in table 6.2. This is consistent with earlier studies of Sr_2FeTaO_6 (Sleight, 1964; Nomura & Nakagawa, 1971). Based on the behavior of compounds studied it would appear that the ordering behavior of complex perovskites can be divided into five different

Compound	Annealing Temperature (°C)	Long Range Order	Ordered Domain Size (Å)	Impurities (Mole %)
Ca_2ScTaO_6	1400°C	95.0(6)%	----	None
	1600°C	96.8(6)%	----	None
Sr_2ScTaO_6	1200°C	86(1)%	490	29% $Sr_4Ta_2O_9$ / 32% Sc_2O_3
	1400°C	91(1)%	760	9% $Sr_4Ta_2O_9$ / 7% Sc_2O_3
	1600°C	99(1)%	920	None
Ba_2ScTaO_6	1400°C	72(4)%	210	$Ba_4Ta_2O_9$ / $Ba_5Ta_4O_9$
	1600°C	96(3)%	420	None
Pb_2ScTaO_6	1000°C*	87(3)%	930	3% $Pb_3Ta_2O_8$
	1200°C*	81(3)%	840	7% $Pb_3Ta_2O_8$
Sr_2CrTaO_6	1000°C	37(3)%	80	32% $SrCrO_4$
	1200°C	60(4)%	160	None
	1400°C	70(2)%	490	None
	1600°C	67(3)%	420	None
$SrNaCrTaO_6$	1000°C	0%	-----	18% $SrCrO_4$ / Cr_2O_3 / Na_2CrO_4
	1200°C	0%	-----	$SrCrO_4$ / Cr_2O_3 / Na_2CrO_4 / ?
	1400°C	0%	-----	None
Sr_2MnTaO_6	1400°C	0%	-----	None
Sr_2FeTaO_6	1200°C	Low	-----	0.5% $Sr_5Ta_4O_{15}$
$SrNaFeTaO6$	1000°C	0%	-----	$NaFeO_2$
Sr_2CoTaO_6	1200°C	0%	-----	None
Sr_2GaTaO_6	1400°C	61(2)%	220	Trace
	1600°C	48(5)%	60	None
Ca_2YTaO_6	1400°C	100%	----	Y_2O_3
Sr_2YTaO_6	1000°C	60(2)%	----	35% Y_2O_3
	1200°C	90(1)%	----	19% Y_2O_3
	1400°C	98(1)%	----	14% Y_2O_3
	1600°C	98(1)%	----	4% Y_2O_3
Sr_2RhTaO_6	1200°C	84(4)%	280	0.8% $Sr_4Ta_2O_9$
Sr_2CrSbO_6	1400°C	96(1)%	----	$Sr_3SbO_{5.5}$ / ?
	1600°C	97(1)%	----	$Sr_3SbO_{5.5}$ / ?
Sr_2MnSbO_6	1400°C	0%	-----	54% $Sr_3SbO_{5.5}$
	1600°C	0%	-----	3% $Sr_3SbO_{5.5}$
Sr_2FeSbO_6	1000°C	67(3)%	?	3.1% $Sr_3SbO_{5.5}$
	1200°C	92(2)%	----	1.8% $Sr_3SbO_{5.5}$
	1400°C	96(2)%	----	3.1% $Sr_3SbO_{5.5}$
Sr_2GaSbO_6	1200°C	97(2)%	----	11% $Sr_3SbO_{5.5}$
	1400°C	96(2)%	----	4% $Sr_3SbO_{5.5}$
$Ba_2ScBiO6$	1000°C	75(2)%	262	None
	1200°C	0%	-----	None

Table 6.2 : Results of kinetic study. All samples were subjected to identical synthesis and annealing conditions. Some compounds didn't form major amounts of the perovskite phase until higher temperatures were reached, while other compounds separated into multiphase mixtures at higher temperatures. Impurity phase concentrations were determined through refinements of x-ray diffraction patterns. Ordered domain sizes are not listed if the compound was either disordered or the supercell peaks were not broadened, with respect to the subcell peaks.

categories: disordered (no long range order), very weakly ordered, partially ordered, highly ordered with antiphase boundaries, and highly ordered with no antiphase boundaries. Of course disordered compounds could probably be further divided into those possessing short range order and those without short range order, but no attempt to quantify the degree of short range order was made in this study.

6.2.3 Results of Substitution on the A Cation Site

Most of the studies on long range order in complex perovskite compounds have emphasized the role of the octahedral cations, focusing on the charge, size, and bonding differences between M and M' cations. But what effect if any does the properties of the A cation have on the long range ordering behavior of a compound? Sleight (1964) observed that in his studies it appeared as though smaller A cations promote a higher degree of long range order. He reasoned that this effect could be attributed to the smaller A cations forcing the octahedral cations closer together. By moving the M cations closer together charge and size differences between the two would be accentuated raising the energy of the disordered state and favoring the ordered structure. One could also speculate that changes in the strength of the A-O bonding influence the octahedral cation distribution. Patrat, Brunel and deBergevin (1976) reasoned that the A-O bonding interaction will be maximized when the oxygen ions are midway between M and M' cations, as they are on average in the disordered state. Therefore, increasing the electronegativity of the A cation, will increase the strength of the A-O interaction and favor the disordered state. In order to better understand the relationship between the properties of the A cation and the ordering behavior several $A_2MM'O_6$ systems were studied.

Table 6.3 contains pertinent information on the long range ordering behavior of several sets of compounds where different A cations have been substituted into the structure. In order to make meaningful comparisons the experimental conditions were kept constant among each set of compounds. To truly make an accurate comparison between two compounds they should both be studied over a wide temperature range to determine under what conditions equilibrium can be reached and the maximum long range order obtainable. Only under these conditions can the thermodynamic maximum long range order of the two compounds be compared. In the case of A_2ScTaO_6 and A_2YTaO_6 both series of compounds were included in the kinetic study and therefore, were studied over the temperature range 1000°C to 1600°C. In both of these cases the conditions under which

Compound	Synthesis	M^{3+}:M^{5+} Ratio	LRO Parameter	Antiphase Boundaries	Impurities
Ca_2AlTaO_6	DA 1400°C	50:50	90(1)%	Yes	$Ca_4Ta_2O_9$, + ?
Sr_2AlTaO_6	DA 1400°C	50:50	89(1)%	Yes	None
Ca_2ScTaO_6	DA 1600°C	50:50	95(1)%	No	None
Sr_2ScTaO_6	DA 1600°C	48:52	99(1)%	Yes	None
Ba_2ScTaO_6	DA 1600°C	48:52	96(3)%	Yes	None
Pb_2ScTaO_6	DA 1000°C	50:50	87(3)%	Yes	4.6% $Pb_3Ta_2O_8$
Ca_2CrTaO_6	DA 1500°C	50:50	67(1)%	Yes	$Ca_4Ta_2O_9$
$Ca_{1.6}Sr_{0.4}CrTaO_6$	DA 1500°C	50:50	71(1)%	Yes	$(Ca,Sr)_4Ta_2O_9$
$Ca_{1.2}Sr_{0.8}CrTaO_6$	DA 1500°C	50:50	70(1)%	Yes	$(Ca,Sr)_4Ta_2O_9$
$Ca_{0.8}Sr_{1.2}CrTaO_6$	DA 1500°C	50:50	66(1)%	Yes	$(Ca,Sr)_4Ta_2O_9$
$Ca_{0.4}Sr_{1.6}CrTaO_6$	DA 1500°C	50:50	64(1)%	Yes	$(Ca,Sr)_4Ta_2O_9$
Sr_2CrTaO_6	DA 1500°C	50:50	70(2)%	Yes	None
Ca_2FeTaO_6	DA 1100°C	50:50	0%	-----	None
Sr_2FeTaO_6	DA 1100°C	50:50	0%	-----	$Sr_5Ta_4O_{15}$
Ba_2FeTaO_6	DA 1100°C	50:50	0%	-----	$Ba_4Ta_2O_9$, $Ba_5Ta_4O_{15}$
Ca_2GaTaO_6	DA 1400°C	50:50	50(1)%	Yes	$Ca_4Ga_2O_4$?
Sr_2GaTaO_6	DA 1400°C	49:51	64(3)%	Yes	None
Ca_2YTaO_6	DA 1400°C	50:50*	100%	No	Y_2O_3
Sr_2YTaO_6	DA 1400°C	50:50	98(1)%	No	14% Y_2O_3
Sr_2InTaO_6	DA 1400°C	45:55	100%	No	11% In_2O_3
Ba_2InTaO_6	DA 1400°C	46:54	100%	No	1% In_2O_3

Table 6.3 : A comparison of the effect on the long range ordering behavior of A_2MTaO_6 compounds. The impurity percentages are mole percent values. The abbreviation DA stands for the direct anneal synthesis route, and LRO stands for long range order. Samples with a refined M^{3+}:M^{5+} ratio different than 50:50 are likely candidates for a deviation from the ideal stoichiometry. Changes in the M^{3+}:M^{5+} ratio will also affect the value of the refined long range order parameter. *The Ca_2YTaO_6 sample showed partial mixing between Ca and Y.

maximum long range order was obtained were the same for A=Ca,Sr,Ba and are listed in table 7.3. In separate attempt to attain equilibrium before making a comparison, the compounds A_2FeTaO_6 were held at 1100°C for 6 days before diffraction patterns were taken. In all cases, even if equilibrium was not obtained, by constraining the experimental conditions to be constant at least the ease with which the ordered structure could be formed was evaluated.

6.3 Discussion

6.3.1 Role of the A Cation

The results contained in table 6.3 seem to indicate that changing the A cation has little effect on the overall long range order of the compound. However, the importance of the A cation in determining the symmetry of perovskite compounds has been extensively discussed in earlier chapters. It is possible that the influence the A cation exerts in determining the symmetry is responsible for its lack of influence on the long range order. Only in the cubic system (and partially in the tetragonal system) are the M-O and M'-O distances forced to contract as the lattice constant decreases. In other systems reductions in the size of the A cation will be compensated for by increased tilting of the octahedra. This may minimize the squeezing effect described by Sleight when a smaller A cation is substituted for a larger A cation. Although the Coulombic repulsion between neighboring octahedral cations will not be reduced by tilting of octahedra at least bond distances can still adjust to approach their optimal values. Arguments based on A-O bonding are also nullified somewhat by the reduction in symmetry because the oxygen ions now have more freedom to position themselves in a position where A-O, M-O, and M'-O bonding can all be optimized. It is worth noting that no cubic $A_2MM'O_6$ compounds exist where the structure remains cubic upon substitution of a different A cation[§]. This structural subtlety was not fully appreciated in earlier studies because of difficulties in determining the true symmetry.

[§] It is not very likely any exceptions to the statement will be found (under ambient conditions). For example Ba_2FeTaO_6 has a tolerance factor (t=1.05) near the upper limit for the perovskite structure, yet Sr_2FeTaO_6 is tetragonal.

This study does not necessarily imply that the A cation has no affect on the M/M' site cation ordering**. However, it would seem to indicate that the effect is minor at best, and that the attributes of the M and M' cations dominate the long range ordering behavior. For this reason, the remainder of the discussion will focus on how the properties and characteristics of different octahedral cations affect the long range order of complex perovskite compounds. However, there are other relatively important consequences of this result. For example, from a technological point of view the ferroelectric properties of the $A_2MM'O_6$ perovskites with A=Pb are very important. On the other hand this study concentrates on double perovskites with A=Ca,Sr,Ba which do not typically have useful ferroelectric properties. However, because the ordering behavior is relatively insensitive to the A cation, the findings of this study should be applicable to the lead based perovskites.

6.3.2 Effect of Synthesis

Most of the compounds in table 6.2 show an increase in the long range order parameter and a decrease in the concentration of antiphase boundaries, with increasing annealing temperature. This is the same behavior displayed by Sr_2AlTaO_6 and Sr_2AlNbO_6 (Woodward, Hoffmann & Sleight, 1994) and is indicative of kinetic processes limiting the degree of long range order. Only Sr_2GaTaO_6, Pb_2ScTaO_6 and Ba_2BiScO_6 showed appreciable decreases in the long range order parameter with increasing temperature. The effect being the most dramatic in Ba_2BiScO_6. The behavior of Sr_2GaTaO_6 has been discussed elsewhere and the decrease in long range order at 1600°C is thought to be related to a thermodynamic limit on the long range order as the melting point is approached (Woodward, 1996). Defects in the structure and deviations from ideal stoichiometry may also play a role in depressing the melting point.

The effect of thermal annealing treatments on Pb_2ScTaO_6 was studied in some detail by Setter and Cross (1980). They found that by annealing pellets for anywhere from 24 to 103 hours at 1000°C they obtained a compound with a long range order parameter of 86%, which is very close to the value obtained in this study after a 48 hour anneal at 1000°C. They also observed a decrease in the long range order parameter, from 80% to 35%, in

** One trend that was observed was that the broadening of the supercell lines decreased slightly as the size of the A cation decreased. This effect may be due to larger ordered domains, but it is complicated by the combined contribution of cation ordering and octahedral tilting to the supercell peaks. Further research is necessary to deconvolute the two contributions in non-cubic compounds.

single crystals when they were annealed at 1400°C. These observations along with the results of this study would seem to indicate that the sample reaches equilibrium at 1000°C if it is annealed for a sufficient amount of time. If the sample is in equilibrium at 1000°C then thermodynamic considerations require that annealing at higher temperatures will result in a decrease in the long range order, due to the increased contribution of entropy. This is consistent with the results of both studies. Increased volatilization of PbO at higher temperatures may also play a role in the decrease of the long range order.

In the case of Ba_2ScBiO_6, the dramatic change in the long range order is almost certainly due to changes in the oxygen content and bismuth oxidation state. Ba_2BiO_3 was found to change cation distributions from the disordered $Ba(Ba_{1/3}Bi_{2/3})O_3$ to the 1:1 ordered $(Ba_{5/3}Bi_{1/3})BaBiO_3$ to the 2:1 ordered $Ba_3BaBi_2O_9$ merely upon changing the annealing conditions (Reis, Jacobson & Kulik, 1993).

6.3.3 Effect of Charge Difference

It has already been well established in the literature that the charge difference between octahedral cations is the most important factor in determining whether they will have an ordered or disordered distribution (Blasse, 1965; Sleight, 1964; Galasso & Darby, 1962; Anderson, Greenwood, Taylor & Poeppelmeier, 1993). Because of this almost all compounds synthesized were chosen so that the charge difference between M and M' was two. However, the few compounds made where the charge difference was different than two, gave no surprises. When the charge difference was increased, as in Sr_2MgWO_6 where the charge difference is four (Mg^{2+} and W^{6+}), a highly ordered compound with no antiphase boundaries was formed. The compounds $SrNaCrTaO_6$ and $SrNaFeTaO_6$ which appear to have a charge difference of only one, resulted in compounds with no evidence of long range order. However, detailed electron microprobe and x-ray diffraction studies of these two compounds show that the concentration of defects in these compounds is quite high and the M:M' ratio on the octahedral site is far from unity. On the other hand if the M^{3+} cation is reduced instead of oxidized the charge difference will increase and an ordered compound should result. One example of this is the compound $SrLaFeTaO_6$ (Fe^{2+}, charge difference 3) which is reported to be clearly ordered even though Sr_2FeTaO_6 is at best weakly ordered (Nakamura & Sata, 1971).

6.3.4 Effect of Size Difference

Table 6.4 lists the difference in ionic radii between octahedral cations and the long range ordering behavior of several compounds. All of the octahedral cation pairs synthesized in this work are represented in table 6.4. The compounds have been divided into three classifications, for reasons which will become apparent. Class 3 compounds are those which contain a main group element in a high oxidation state, such as Sb^{5+}, Bi^{5+} or Te^{6+}. Class 2 compounds are those which contain a first row transition metal as the lower valent cation. Finally, class 1 compounds are those which do not fall under one of the first two classifications.

It is immediately evident from inspection of this table that among class 2 and 3 compounds the degree of long range order present is not dependent upon the M/M' size difference. However, among class 1 compounds there is a fair correlation between the value of r_M-$r_{M'}$ and the maximum long range order obtained. One subtle trend that appears in table 6.4 is that for the same absolute difference in ionic radii, compounds where the lower valent cation is larger (i.e. Sr_2RhTaO_6, Sr_2ScTaO_6) have a slightly higher degree of long range order than those where the lower valent cation is smaller (Sr_2CrTaO_6, Sr_2AlTaO_6). This effect may be explained by considering the changes in Madelung energy as the oxygen is shifted between the two cations. To illustrate the magnitude of this term a Madelung energy calculation was done on a cubic $A_2^{2+}M^{3+}M^{5+}O_6$ perovskite with a cell edge of 7.79Å. The results are plotted in figure 6.2. In an ordered perovskite where the M^{3+} ion is smaller than the M^{5+} ion, the oxygen is located closer to the trivalent cation in the ordered structure, and equidistant from both cations in the disordered structure. In this case going from the ordered structure to the disordered structure shifts the oxygen closer to the pentavalent cation. This shift helps offset the Madelung energy lost through disordering of the cation and results in a decrease of roughly 50-100 kJ/mol in the Madelung energy. On the other hand if the M^{5+} cation is smaller than the M^{3+} ion, a transformation from the ordered to disordered structure results in a reduction of 150-225 kJ/mol in the Madelung energy. Of course bonding effects must also be considered but calculations based on a purely electrostatic model indicate the disordered structure is stabilized, with respect to the ordered structure, when the lower valent cation is smaller and destabilized when the lower valent cation is larger.

Compound	Difference in Radii r_{3+}-r_{5+} (Å)	Max. Long Range Order Obtained	Ordering Class
Class 1 Compounds			
Sr_2AlTaO_6	-0.105	91%	HB
Sr_2GaTaO_6	-0.020	61%	M
La_2MgHfO_6	+0.010	10%	L
Sr_2RhTaO_6	+0.025	84%	M
Sr_2ScTaO_6	+0.105	99%	HB
Sr_2InTaO_6	+0.160	100%	O
Sr_2YTaO_6	+0.260	100%	O
Class 2 Compounds			
Sr_2CoTaO_6	-0.030	0%	D
Sr_2CrTaO_6	-0.025	70%	M
Sr_2VTaO_6	0.000	52%	M
Sr_2FeTaO_6	+0.005	Low	L
Sr_2MnTaO_6	+0.005	0%	D
Class 3 Compounds			
Ba_2ScBiO_6	-0.015	83%	M
Sr_2CrSbO_6	+0.015	97%	O
Sr_2GaSbO_6	+0.020	97%	O
Sr_2FeSbO_6	+0.045	96%	O
Sr_2MnSbO_6	+0.045	0%	D
Na_2ZrTeO_6	+0.160	100%	O

Table 6.4 : The maximum long range order obtained between octahedral pairs studied in this work. The symbols used to represent the different ordering classes are: O-highly ordered with a low concentration of antiphase boundaries, HB-highly ordered with detectable antiphase boundaries, M-maximum long range order intermediate between poorly and highly ordered samples (50%<S<90%), L-low degree of long range order (0<S<50%), D-disordered, no long range order detectable. Ionic radii used are those of Shannon and Prewitt (Shannon, 1976).

6.3.5 Effect of Bonding

In table 6.4 most of the class three compounds display a higher degree of long range order than might be expected, based solely on the cationic radii of M and M'. The only exception to this trend is the compound Sr_2MnSbO_6 which has no long range order. However, Sr_2MnSbO_6 has a large tetragonal distortion as expected for a perovskite with the Jahn-Teller ion Mn^{3+} (see chapter 5), whereas, the tetragonal distortion in Sr_2MnTaO_6 is very small. This would seem to indicate that the short range order is much higher in the antimonate compound than it is in the tantalate, based on the assumption that short range order is necessary in order to achieve the cooperative Jahn-Teller distortion.

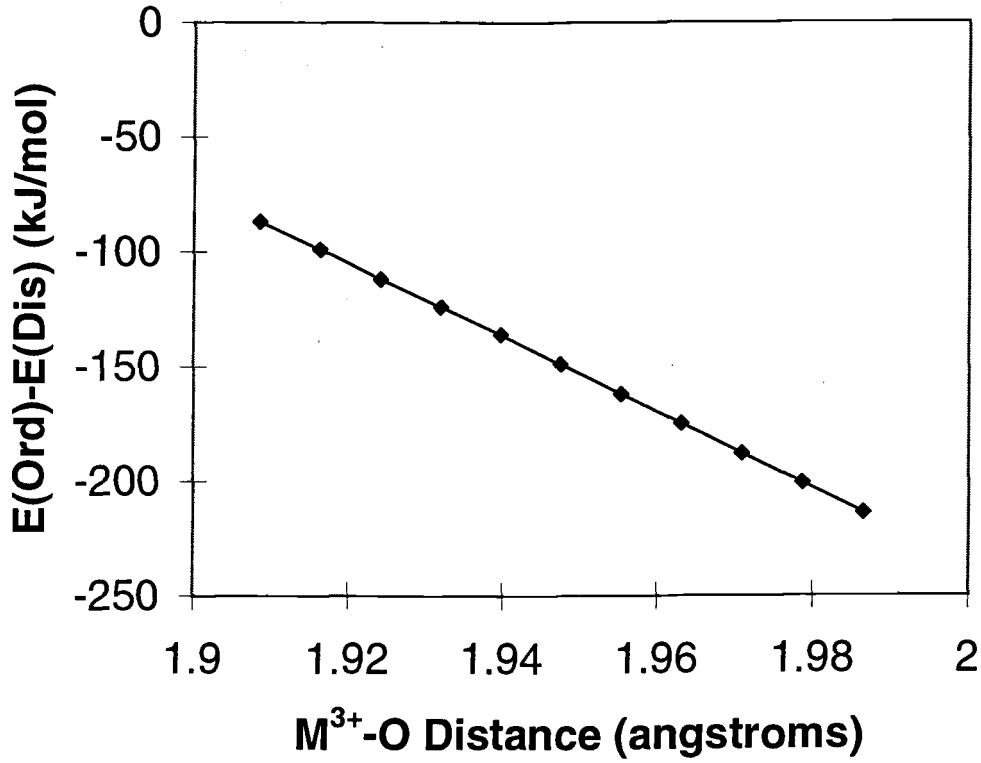

Figure 6.2 : The Madelung energy stabilization of an ordered, cubic $A_2M^{3+}M^{5+}O_6$ perovskite with respect to a disordered $A_2(M^{3+}M^{5+})O_6$ compound, as a function of the M^{5+}-O distance. The lattice constant was taken to be 7.79Å.

What causes these compounds to be more highly ordered than similar compounds containing transition metals such as tantalum, niobium, and hafnium? The answer can be found by examining the differences in the way main group and early transition metals bond to oxygen. One major difference between tantalum and antimony, or for that matter any early transition metal and a p block element, is presence of unfilled d-orbitals on the tantalum ion. The overlap of these empty d-orbitals with the filled 2p orbitals on oxygen forms pi-bonds between the metal ion and the oxygen. This pi interaction strengthens the metal-oxygen bonding. On the other hand the d-orbitals on antimony are completely filled and cannot participate in pi-bonding. Therefore, to maximize the bonding interaction it is particularly important in the case of main group elements to form a strong sigma bond. In

the case of highly charged cations, such as Sb^{5+}, the sigma bonding strength is to a large degree dependent upon the degree of anion polarization.

The differences in the way antimony and tantalum bond to oxygen become apparent when the crystal chemistry of the two elements are compared. Table 6.5 shows a comparison between antimony compounds and their tantalum analogs. In the first two examples, KMO_3 and Ba_2FeMO_6, antimony and tantalum form compounds with entirely different structures. The antimony compounds form in structures where 180° M-O-M bond angles are minimized, whereas the tantalum analogs have structures with exclusively 180° bond angles. This observation is as expected considering the fact that the pi-bonding overlap in an M-O-M linkage is optimized when the bond angle is 180°, but the anion polarization is at its weakest for a 180° bond angle. The polarization is weakest at a 180° angle because both cations are trying to polarize the anion in exactly opposite directions and they cancel each other out. This idea was first used by Blasse (1964) to understand differences in the between the crystal chemistry of Sb^{5+} and that of Ta^{5+} and Nb^{5+}. He concluded that the Sb^{5+} ion prefers structures which are more conducive to anion polarization, while Ta^{5+} and particularly Nb^{5+} favor structures in which it is favorable to form pi-bonds. This idea was also espoused by Goodenough and Kafalas (1973) to explain the crystal chemistry of $A^{+}M^{5+}O_3$ compounds.

Compounds	M = Ta	M = Sb
KMO_3	Cubic Perovskite Structure Corner Sharing Octahedra	Ilmenite Structure Edge & Corner Sharing Octahedra
Ba_2FeMO_6	Cubic Perovskite Structure Corner Sharing Octahedra	Hexagonal $BaTiO_3$ Structure Face & Corner Sharing Octahedra
Sr_2CrMO_6	Tetragonal Perovskite Structure Long Range Order = 70%	Monoclinic Perovskite Structure Long Range Order = 97%
Sr_2FeMO_6	Tetragonal Perovskite Structure Long Range Order = Low	Monoclinic Perovskite Structure Long Range Order = 70%
Sr_2MnMO_6	Tetragonal Perovskite Structure a/c Ratio = 0.999 Long Range Order = 0%	Tetragonal Perovskite Structure a/c Ratio = 0.972 Long Range Order = 0%
Sr_2GaMO_6	Tetragonal Perovskite Structure a/c Ratio = 0.999 Long Range Order = 84%	Tetragonal Perovskite Structure a/c Ratio = 0.995 Long Range Order = 97%

Table 6.5 : A comparison between tantalum and antimony oxide compounds.

The last four entries in table 6.5 compare compounds synthesized in this work. One observation can be made regarding the symmetry of these compounds. Sr_2CrTaO_6 and Sr_2FeTaO_6 are both tetragonal perovskites, whereas the antimony analogs are monoclinic. Sr_2MnMO_6 and Sr_2GaMO_6 form in the tetragonally distorted perovskite structure when M is either antimony or tantalum. However, the tetragonal distortion is much more pronounced in the antimony compounds. In all four compounds it appears that the bond angles deviate further from 180° in the antimony compounds than they do in the tantalum analogs. The symmetry lowering effects of Sb^{5+} and Te^{6+} are consistent with the ideas discussed in chapter five. The second observation that can be made about the last four entries in table 6.5 is that the antimony compounds appear to be more highly ordered. In Sr_2GaMO_6 and Sr_2CrMO_6 the antimony compounds both attain a highly ordered structure with a low concentration of antiphase boundaries, while the tantalum analogs are have only a moderate degree of long range order and a significant concentrations of antiphase boundaries. Even in the case of the two Sr_2MnMO_6 compounds, as previously discussed there is evidence that the short range order is much higher in the antimony compound than in the tantalum compound.

Both the symmetry and ordering differences between antimony and tantalum perovskites are consistent with the bonding effects discussed above. The Sb-O-M bond angles bend away from a linear 180° angle, in order to enhance the polarization of oxygen by the Sb^{5+} ion. Just as distortion from the cubic structure favors anion polarization, a highly ordered distribution of octahedral cations also favors anion polarization. In a perfectly ordered lattice all of the octahedral linkages will be of the Sb-O-M type, while a partially ordered or disordered lattice will also have some Sb-O-Sb and M-O-M linkages. The highly charged Sb^{5+} ion can more effectively polarize the oxygen ion than Cr^{3+}, Fe^{3+}, Ga^{3+}, and Mn^{3+} ions. Because of this in an Sb-O-M linkage the electron cloud around oxygen will be shifted toward the antimony ion strengthening the Sb-O bond. On the other hand in an Sb-O-Sb linkage the electron cloud around oxygen is pulled equally from each side and the anion polarization is weakened. Therefore, in order to minimize the number of Sb-O-Sb linkages and correspondingly maximize anion polarization and Sb-O bonding, complex perovskites containing the Sb^{5+} ion tend to form structures with a high degree of long range order. Similar arguments should also apply to other highly charged main group elements, such as Te^{6+}, Bi^{5+} and Sn^{4+}, but not to transition metal ions with empty d-orbitals, such as Ta^{5+}, Nb^{5+}, and Hf^{4+}. The effect should be more pronounced as the size of the ion decreases and the charge increases.

6.3.6 Effect of Oxidation State Stability

When considering the class 2 compounds in table 6.4, the oxidation state stability of the transition metal ion must be taken into consideration. If all of these ions are not in a single oxidation state it will introduce an additional component of disorder into the system, as will the presence of compensating defects (such as oxygen vacancies) which must accompany the change in oxidation state of the transition metal cation. The net effect of this change in the composition will be to frustrate the long range interactions which stabilize the ordered state. This will be particularly true if the charge and size differences between octahedral cations are small. Under these conditions the oxidation state stability of the transition metal will become the critical factor in determining of the long range ordering behavior. In such cases, synthesis and composition become critical. No unified theory can be developed to explain all such compounds, but rather each compound must be examined individually.

Sr_2VTaO_6 has previously been prepared between 1100-1200°C in an inert atmosphere (He), and found to be disordered (Bernier, Chauvel & Kahn, 1974). This result is not surprising considering the fact that Ta^{5+} and V^{3+} have identical ionic radii. However, synthesis in this study at 1400°C under flowing 10% H_2/90% N_2 resulted in a partially ordered distribution of tantalum and vanadium. The long range order parameter was approximately 50%. Apparently, either the higher synthesis temperature, which increases solid state diffusion, or the hydrogen atmosphere, to insure vanadium is found exclusively in the +3 oxidation state, are necessary to obtain a partially ordered sample. The fact that this compound orders, even partially, is irrefutable evidence that factors other than charge and size difference influence the ordering behavior.

Unlike the other transition metals ions considered in this study, for chromium the +3 oxidation state is strongly favored over both higher and lower oxidation states. This is evident by the fact that Sr_2CrTaO_6 can be obtained in nearly single phase form at 1200°C, but remains stable until at least 1600°C. Over this temperature range the long range order remains fairly constant, although it does appear to be decreasing slightly at 1600°C. This behavior is similar to Sr_2GaTaO_6 (Woodward, 1996) and Sr_2AlNbO_6 (Woodward, Hoffmann & Sleight, 1994) and may be due to the increased entropy term as the melting point is approached. Not surprisingly, due to the stability of Cr^{3+}, the long range order of this compound is the highest among class 3 compounds.

Sr_2FeTaO_6 was the only other class 3 compound which showed any sign of long range order, and the only indication of order was a very diffuse (101) peak (cubic (111)). Although

the peak was always quite broad its width was smallest after annealing at 1000°C. In samples annealed at higher temperatures this reflection was so diffuse, that it became difficult to quantify its position and width. The explanation as to why Sr_2VTaO_6 is more highly ordered than this compound is not completely understood at this time. Both divalent and tetravalent iron are known in perovskites so that disproportionation is a possibility. However, Fe^{3+} is known to be a stable ion in oxides, and furthermore, there have been several Mössbauer studies performed on this compound over the years, and no indication of either Fe^{2+} or Fe^{4+} was suggested in any of those studies (Nomura & Nakagawa, 1971; Bell, 1968). Assuming then that all of the iron is present as Fe^{3+}, the different ordering behaviors of Sr_2FeTaO_6 and Sr_2VTaO_6 can probably be attributed to differences in either kinetics or bonding[††].

Both Sr_2MnTaO_6 and Sr_2CoTaO_6 showed no signs of long range order at any temperature, nor did Sr_2MnSbO_6. In these compounds evidence exists to support the conclusion that neither manganese nor cobalt are present exclusively in the +3 oxidation state. In the case of Sr_2MnTaO_6, electron backscatter photographs taken during the course of electron microprobe analysis indicate the compound is compositionally inhomogeneous on the micron scale. Sampling of several crystallites found Mn:Ta ratios which varied from 0.85 to 0.97. Furthermore, a very broad signal can be detected in the room temperature EPR spectrum of this compounds. However, Mn^{3+} is a high spin d^4 ion and due to zero field splitting, caused by spin-orbit coupling, no EPR signal is expected for this ion. The observed signal is too broad to be attributed to Mn^{2+}, but may indicate the presence of Mn^{4+}. A broad EPR signal has been associated with Mn^{4+} in perovskites in other works (Hong, 1994). Both results suggest the loss of manganese, which is compensated by partial oxidation of the remaining manganese ions to give an average manganese oxidation state intermediate between +3 and +4.

In the case of Sr_2CoTaO_6 it was observed that the lattice constant, and to some extent the color, of this compound could be varied depending upon the atmosphere and cooling rate employed during synthesis. This is highly suggestive of deviations in the stoichiometry. Although refinements do not indicate cobalt deficiency, the partial reduction of Co^{3+} to Co^{2+} accompanied by oxygen deficiency seems a likely explanation for the behavior of this compound. Hong (1994) prepared the very similar compound Sr_2CoNbO_6 by a very similar route, and from titrations found the true stoichiometry to be $Sr_2Co^{2+}_{.14}Co^{3+}_{.86}NbO_{5.93}$. The

[††] Note that if Sr_2FeTaO_6 is heated at 1400°C (synthesis temperature of Sr_2VTaO_6) multiple perovskite phases are formed, presumably due to partial reduction of Fe^{3+} to Fe^{2+}. Perhaps if Fe^{3+} was stable at 1400°C a partially ordered phase could be formed, after all when prepared at 1200°C Sr_2VTaO_6 is disordered (Bernier, Chauvel & Kahn, 1974).

variability of the manganese and cobalt oxidation states in these compounds invariably disorders the octahedral cation distribution to such an extent that long range cation order is not obtained.

6.4 Conclusions

The long range ordering behavior of double perovskites has been examined. Five different classifications of ordering have been observed: highly ordered, highly ordered with the presence of antiphase boundaries, moderately ordered, weakly ordered, and disordered. For $A_2M^{3+}TaO_6$ compounds highly ordered compounds are only observed when the difference in ionic radii of the M^{3+} and Ta^{5+} ions is greater than 0.11Å, whereas the presence of antiphase boundaries has been shown to be prevalent when the size difference is smaller. The long range order parameter of moderately ordered compounds was observed to be relatively insensitive to the time and temperature of annealing treatments, suggesting that a partially ordered state is thermodynamically favored. In terms of predicting and/or understanding the ordering behavior of compounds based on the properties of the constituent ions, the following conclusions have been reached. The A cation has been shown to have little influence on the ordering behavior. Consistent with previous studies, the charge difference between M and M' cations is observed to be the primary factor influencing order, however, in compounds where the charge difference is two (or less) other factors can play an important role. In such compounds the presence of a highly polarizing main group cation, such as Sb^{5+} or Te^{6+}, promotes a high degree of ordering, regardless of the size difference between cations. Deviations from stoichiometry and the presence of octahedral site cations in more than one oxidation state stabilize the disordered state. In compounds where all ions are in stable oxidation states, and no highly charged main group ions are present, the degree of long range order and octahedral site cation size difference are correlated.

6.5 References

Amador, U., Hetherington, C.J.D., Moran, E. & Alario-Franco, M.A. (1992). *J. Solid State Chem.*, **96**, 132.

Anderson, M.T. & Poeppelmeier, K.R. (1991). *Chem. Nat.*, **3**, 476.

Anderson, M.T., Greenwood, K.B., Taylor, G.A. & Poeppelmeier, K.R. (1993). *Prog. Solid State Chem.* **22,** 197.

Attfield, M.P., Battle, P.D., Bollen, S.K., Kim, S.H., Powell, A.V. & Workman, M. (1992). *J. Solid State Chem.*, **96**, 344.

Battle, P.D., Gibb, T.C., Herod, A.J. & Hodges, J.P. (1995). *J. Mater. Chem.*, **5**(1), 75.

Bell, R.O. (1968). *J. Phys Chem. Solids* **29**, 1.

Bernier, J.-C., Chauvel, C., Kahn, O. (1974). *J. Solid State Chem.* **11**, 265.

Blasse, G. (1964). *J. Inorg. Nucl. Chem.* (1964). **26**, 1191.

Blasse, G. (1965). *J. Inorg. Nucl. Chem.*, **27**, 993.

Daleveld, E.W., Bruntich, D.J., Dotman, J.P. & Blasse, G. (1973). *J. Inorg. Nucl. Chem.*, **35**, 3928.

Galasso, F. & Darby, W. (1962). *J. Phys. Chem.* **66**, 131.

Goodenough, J.B. & Kafalas, J.A. (1973). *J. Solid State Chem.*, **6**, 493.

Hong, S.-T. (1994). Ph.D. Thesis, Seoul National Univ.

King, G., Goo, E., Yamamoto, T. & Okazaki, K. (1988). *J. Amer. Cer. Soc.*, **71**(6), 454.

Nakamura, T. & Sata, T. (1971). *J. Phys. Soc. Japan*, **30**, 1501.

Nomura, S. & Nakagawa, T. (1971). *J. Phys. Soc. Japan*, **30**(2), 491.

Patrat, G., Brunel, M. & deBergevin, F. (1976). *J. Phys. Chem. Solids* **37**, 285.

Randall, C.A., Bhalla, A.S., Shrout, T.R. & Cross, L.E. (1990). *J. Mater. Res.*, **5**(4), 829.

Reis, K.P. Jacobson, A.J. & Kulik, J. (1993). *Chem. Mater.*, **5**, 1070.

Setter, N. & Cross, L.E. (1980). *J. Appl. Phys.*, **51**(8), 4356.

Shannon, R.D. (1976). *Acta Cryst.*, **A32**, 751.

Sleight, A.W. (1964). Thesis--*Disertation Abstracts,* **24**, 64-3565, U. Connecticut--1963.

Sleight, A.W. (1988). *Proc. Welch Foundation Conf. Chem. Res. XXXII Valency* pp. 123.

Vallet-Regi, M., Garcia, E. & Gonzales-Calbet, J.M. (1988). *J. Chem. Soc. Dalton Trans.*, **3**, 775.

Wang, Q., Gu, B. & Zhang, S. (1990). *J. Phys.:Condens. Matter*, **2**, 9815.

Wittman, V.U., Rauser, G. & Kemmler-Sack, S. (1981). *A. Anorg. Allg. Chem.* **482**, 143.

Woodward, P.M., Hoffmann, R.-D. & Sleight, A.W. (1994). *J. Mater. Res.* **9**(8), 2118.

Woodward, P.M. (1996). Masters Thesis, Oregon State University.

Chapter 7

Structure Refinement of Triclinic δ-WO_3

7.1 Introduction

Tungsten trioxide is a simple compound in terms of stoichiometry, but it is complex in terms of structure and phase transitions. Its ideal structure is a three dimensional cubic network of corner sharing WO_6 octahedra, identical to the cubic perovskite structure in the absence of an A cation. The ideal cubic structure is adopted by ReO_3, but has never been observed for WO_3. Rather tungsten trioxide is found in a series of structures with the same connectivity as ReO_3, but distorted from the cubic symmetry of ReO_3. The symmetry of WO_3 is lowered from the ideal ReO_3 structure by two distortion mechanisms: tilting of WO_6 octahedra, and displacement of tungsten from the center of its octahedron. Variations in the details of these distortions give rise to several phase transitions. In that octahedral tilting distortions have been a major focus of this thesis, a study of the phase transitions in WO_3 seemed a natural extension of the work described thus far. Now however, the octahedral cation displacements add an increased degree of freedom, and level of complexity, to the structural distortion/phase transition behavior.

Phase	Symmetry	Space Group	Z	Temperature Range*	Reference
α-WO_3	Tetragonal	P4/nmm	2	1010-1170K	Kehl, Hay & Wahl (1952)
β-WO_3	Orthorhombic	Pmnb	8	600-1170K	Salje (1977)
γ-WO_3	Monoclinic	$P2_1/n$	8	290-600K	Tanisaki (1960) Loopstra & Rietveld (1969)
δ-WO_3	Triclinic	$P\bar{1}$	8	230-290K	Diehl, Brandt & Salje (1978)
ε-WO_3	Monoclinic	Pc	4	?-230K	Salje (1976)

Table 7.1 : Known polymorphs of tungsten trioxide. *The transition temperatures display large hysteresis effects and universal agreement is not found in the literature. The values in this table represent the best average values that could be found.

Tungsten trioxide adopts at least five distinct crystallographic modifications between absolute zero and its melting point at 1700K (Salje, & Viswanathan, 1975; Rao & Rao,

1974). Decreasing the temperature from the melting point, the crystallographic symmetry changes in the sequence: tetragonal-orthorhombic-monoclinic-triclinic-monoclinic. Most of the transitions appear to be first order and often display large hysteresis in the transition temperature (Salje, & Viswanathan, 1975; Rao & Rao, 1974). A summary of these transitions is given in table 7.1. Additionally DTA, heat capacity (Rosen, Banks & Post, 1956; Perri, Banks & Post, 1957) , and resistivity (Sawada, 1953) studies show discontinuities, indicative of phase transitions, in the tetragonal region at approximately 1170K and 1500K. Furthermore, capacitance and electrical resistivity measurements suggest phase transitions in the low temperature region of the phase diagram at 40K, 65K, and 130K (Lefkowitz, Dowell & Shields, 1975). However, structural refinements have not yet been performed in the necessary temperature intervals to determine if these anomalies in the physical properties, truly correspond to structural phase transitions of stoichiometric WO_3.

Since the advent of the Rietveld approach to refining structures from neutron powder diffraction data, γ–WO_3 has been used to demonstrate the power of this approach (Rietveld, 1966; Loopstra & Rietveld, 1969). This is the classic case of a heavy metal oxide where more accurate oxygen positions can sometimes be obtained with powder neutron diffraction data than with single crystal X-ray diffraction data. Furthermore, there are an abundance of overlapped peaks in the diffraction pattern of WO_3, thus challenging the Rietveld approach. With the availability of a new high resolution neutron powder diffractometer, it seemed appropriate to revisit the structure of δ-WO_3 using the Rietveld approach.

7.2 Synthesis and Data Collection

Reagent grade WO_3 was heated in air at 1200°C for 8 hours, cooled at 20°C/h to 800°C, and then cooled at 100°C/h to room temperature. An X-ray diffraction pattern was obtained on a Siemens D5000 diffractometer using Cu$K\alpha$ radiation. The peaks were very sharp with no indication of broadening from strain or crystallite size effects.

Data were obtained on the high-resolution neutron powder diffractometer (HRNPD) at beamline H1A of the high flux beam reactor (HFBR) at Brookhaven National Laboratory (BNL). The experimental details of the HRNPD have been described elsewhere (Woodward, Sleight & Vogt, 1995). The multichannel detector bank was moved in 0.02°

steps with integration times of roughly 5 minutes per step. Blocks of intensity and position data were then normalized with respect to both detector efficiency and positional errors.

7.3 Results

The initial neutron diffraction pattern obtained for WO_3 at 25°C was found to be a mixture of γ and δ–WO_3. The sample was therefore cooled in liquid nitrogen and allowed to warm to room temperature. Another neutron diffraction pattern was obtained at room temperature. This time the WO_3 pattern was that of pure δ–WO_3. The refinement of δ-WO_3 was initiated with the positional parameters reported for a single crystal X-ray diffraction refinement (Diehl, Brandt & Salje, 1978). Three different Rietveld refinement software packages were used and compared: GSAS (Larson & Von Dreele, 1994), Rietan (Izumi, 1993), and PROFIL (Cockcroft, ?). Table 7.2 gives the final R values, unit cell parameters and peak fitting parameters. Table 7.3 compares the refined positional parameters for oxygen atoms with those obtained from single crystal X-ray diffraction data. When the positional parameters for tungsten atoms were refined using our neutron data, the values obtained were within one standard deviation of the values reported from the single crystal X-ray diffraction study. The standard deviations for tungsten atomic positions were about twenty times higher for the neutron refinement than for the X-ray refinement. Thus, the tungsten atomic positions were fixed at the single crystal X-ray values when the oxygen thermal parameters were refined. The final profile fits are shown in figure 7.1. Attempts to refine δ–WO_3 as acentric did not lead to an improved fit to the data.

The thermal parameters obtained in each refinement are given in table 7.4. The thermal motion of the oxygen atoms was modeled with anisotropic thermal ellipsoids, while the tungstens were refined with isotropic thermal parameters. The thermal parameters obtained for tungsten in the single crystal determination indicated that the thermal vibrations of the tungsten atoms were nearly isotropic and practically identical for all four crystallographically distinct tungsten sites (Diehl, Brandt & Salje, 1978). Based on this observation, the use of a single isotropic thermal parameter for all four tungsten sites seems justified. To reduce the number of parameters for the oxygen anisotropic thermal motion, some constraints were used. The oxygens were divided into three different classes. Oxygens 1-4 have bonds to tungstens that are approximately parallel to the x-axis. Oxygens 5-8 form bonds with tungsten in the y-direction, and oxygens 9-12 form

Parameter	*RIETAN*	*GSAS*	*PROFIL*
R_{WP} (%)	8.81	7.89	9.59*
R_P (%)	6.55	5.82	----
χ^2	1.82	1.49	8.54*
R_E (%)	6.53	6.46	3.28*
R_I (%)	1.99	4.04	5.79
Data Points	7501	7501	7501
Reflections	999	999	994
Parameters	74	75	74
a	7.30939(4)	7.31261(6)	7.30994(5)
b	7.52173(5)	7.52521(7)	7.52245(6)
c	7.68574(5)	7.68937(7)	7.68630(7)
α	88.8474°(5)	88.847°(0)	88.8465°(5)
β	90.9117°(5)	90.912°(0)	90.9123°(6)
γ	90.9398°(4)	90.940°(0)	90.9399°(6)
Zero	0.6721(5)	0.747(3)†	0.686(4)
U	0.037(8)	0.00(3)†	0.0392(9)
V	-0.101(2)	-0.0113(3)†	-0.101(2)
W	0.108(1)	0.00(3)†	0.105(1)
P	----	0.0000(3)†	----
X	----	0.046(3)†	----
Y	----	0.000(4)†	----
Assymetry	0.03(1)	0.140(3)†	3.8(2)
γ (Gaussian Frac.)	0.71(1)	----	0.69(1)
δ ($\Gamma_{Gauss}/\Gamma_{Lor}$)	1.22(4)	----	1‡

Table 7.2 : Final parameters for pure δ-WO_3, as refined by three different Rietveld software packages.

* The R_{WP}, R_E and χ^2 calculated by PROFIL are actually 12.74%, 4.30% and 8.76% because this program subtracts the background before calculating the residuals. Its output also gives values without background correction which are listed in the table for ease of comparison with the other two programs.

† The GSAS program does calculations in centidegrees 2θ, therefore for comparison with the other programs the zero, X, Y, and asymmetry values have been divided by 100, and the U, V, W, and P values have been divided by 100^2.

‡ The peak shape function used PROFIL fixes this parameter at 1.0.

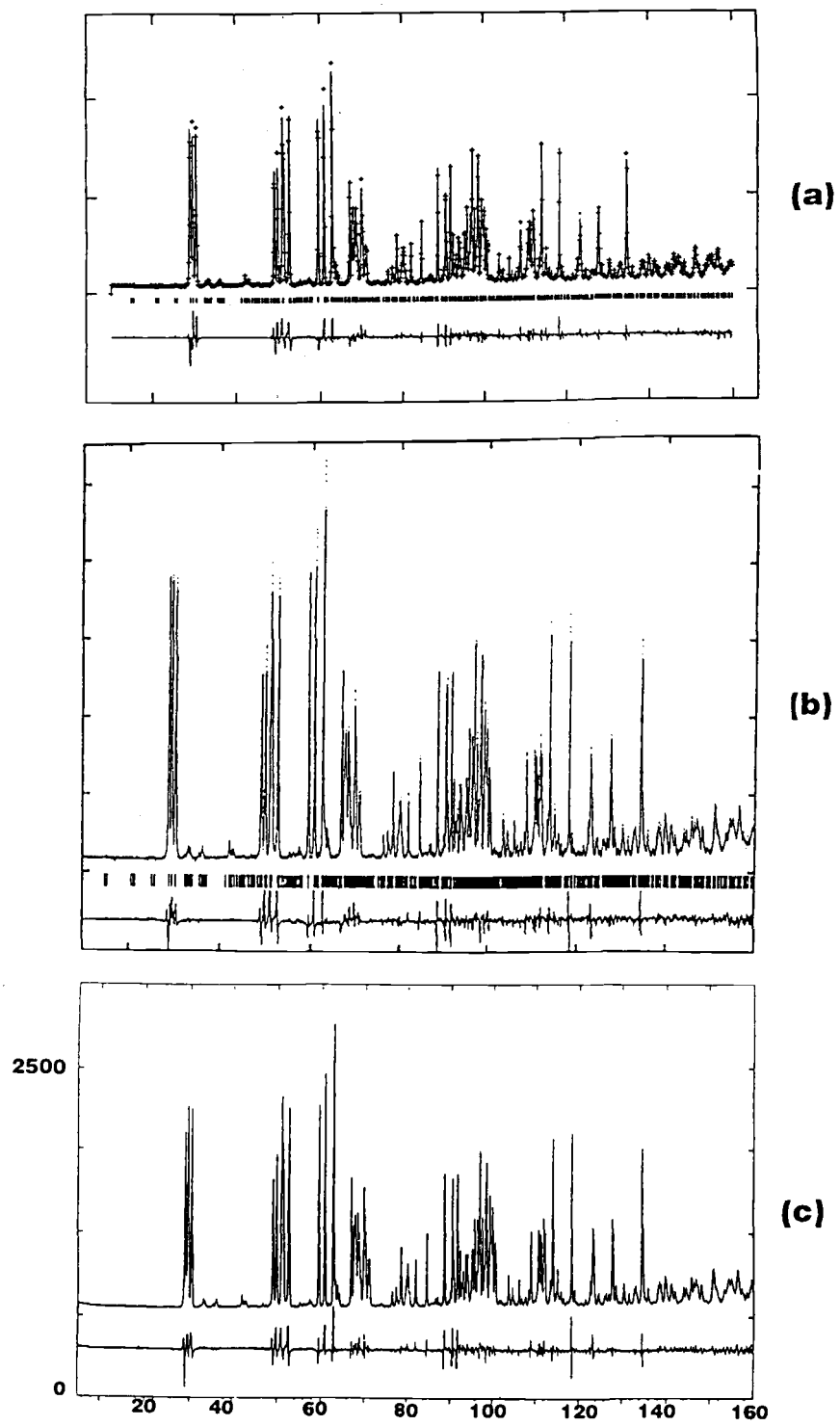

Figure 7.1 : Profile fits with a) GSAS, b) PROFIL, and c) RIETAN. Points in a) and b) are observed data which are not shown in c). Peak position markers are given in a) and b), but not c). Difference curves are given in all cases.

	X-ray single xtal	*RIETAN*	*GSAS*	*PROFIL*
O(1)				
x	0.001(3)	0.000(2)	0.0009(8)	0.0066(8)
y	0.039(3)	0.034(2)	0.0346(7)	0.0393(8)
z	0.210(3)	0.213(2)	0.2108(7)	0.2182(8)
O(2)				
x	0.504(3)	0.502(2)	0.5017(8)	0.5020(8)
y	0.536(3)	0.538(2)	0.5372(8)	0.5449(7)
z	0.218(3)	0.216(2)	0.2165(8)	0.2093(8)
O(3)				
x	0.008(3)	0.000(2)	0.0008(8)	0.0097(9)
y	0.466(3)	0.463(2)	0.4636(7)	0.4674(8)
z	0.288(3)	0.284(2)	0.2852(7)	0.2809(9)
O(4)				
x	0.497(3)	0.501(2)	0.5002(8)	0.4985(8)
y	0.964(3)	0.965(2)	0.9645(8)	0.9732(8)
z	0.288(3)	0.289(2)	0.2877(7)	0.2927(8)
O(5)				
x	0.285(3)	0.285(2)	0.2857(9)	0.2878(9)
y	0.257(3)	0.261(1)	0.2602(7)	0.2564(7)
z	0.287(3)	0.284(2)	0.2833(7)	0.2829(7)
O(6)				
x	0.220(3)	0.214(2)	0.2128(8)	0.2062(9)
y	0.763(3)	0.763(1)	0.7611(6)	0.7562(7)
z	0.223(3)	0.217(2)	0.2164(7)	0.2062(7)
O(7)				
x	0.219(3)	0.209(2)	0.2104(9)	0.210(1)
y	0.263(3)	0.258(1)	0.2586(7)	0.2630(8)
z	0.726(3)	0.727(2)	0.7278(7)	0.7304(8)
O(8)				
x	0.284(3)	0.288(2)	0.2860(9)	0.2738(9)
y	0.758(3)	0.760(1)	0.7608(6)	0.7631(7)
z	0.768(3)	0.774(2)	0.7737(7)	0.7685(8)
O(9)				
x	0.294(3)	0.288(2)	0.2872(8)	0.2920(9)
y	0.042(3)	0.042(2)	0.411(7)	0.0408(8)
z	0.000(3)	0.005(1)	0.0042(7)	0.0038(7)
O(10)				
x	0.297(3)	0.283(2)	0.2850(8)	0.2842(9)
y	0.545(3)	0.541(2)	0.5423(7)	0.5447(8)
z	0.498(3)	0.495(1)	0.4957(6)	0.4965(7)
O(11)				
x	0.297(3)	0.283(2)	0.2850(8)	0.2842(9)
y	0.545(3)	0.541(2)	0.5423(7)	0.5447(8)
z	0.498(3)	0.495(1)	0.4957(6)	0.4965(7)
O(12)				
x	0.209(3)	0.210(2)	0.2003(9)	0.2109(9)
y	0.983(3)	0.981(1)	0.9811(7)	0.9827(8)
z	0.505(3)	0.506(1)	0.5060(6)	0.5077(7)

Table 7.3 : Oxygen positional parameters in δ–WO_3. Tungsten positions were set to the values determined in the single crystal X-ray refinement: W1 (x=0.2566, y=0.0259, z=0.2850), W2 (x=0.2502, y=0.5280, z=0.2158), W3 (x=0.2438, y=0.0313, z=0.7817), W4 (x=0.2499, y=0.5338, z=0.7190) (Diehl, Brandt & Salje, 1978).

bonds with tungsten in the z-direction. The descriptions of bonds in either the x-, y-, or z-direction are approximate because of the slight deviation from orthogonality of the lattice vectors and the tilting of the octahedra. When the refinements were carried out, each of the three sets of oxygen ions were refined with a different set of anisotropic thermal parameters, and the thermal parameters were well behaved. In a few cases, one of the variables U11, U22 or U33 would go slightly negative. Because this has no physical significance, the value was reset to a small positive value and fixed.

The distances and angles given in table 7.5 are based on the GSAS refinement of pure δ–WO_3. If the standard deviations given by the GSAS refinement are considered meaningful, these distances and angles are more accurate than those reported from the single crystal X-ray study. However, this is only true because the atomic coordinates for tungsten were fixed at values obtained in the single crystal X-ray diffraction study. Furthermore, the estimated standard deviations calculated in traditional Rietveld programs are not necessarily directly comparable to those calculated in single crystal calculations. This will be discussed in more detail later.

Atom	*RIETAN*	*GSAS*	*PROFIL*
O(1-4)			
U11	8	10	9(8)
U22	92(14)	51(7)	50(8)
U33	190(15)	151(5)	95(9)
U12	0(11)	-2(5)	-3(8)
U13	-41(35)	3(5)	1(8)
U23	10(11)	4(5)	11(8)
O(5-8)			
U11	90(15)	51(7)	56(8)
U22	8(13)	10	7(8)
U33	204(15)	175(5)	102(8)
U12	4(12)	5(5)	-3(8)
U13	2(11)	0(5)	1(8)
U23	4(12)	1(5)	1(8)
O(9-12)			
U11	66(14)	47(6)	4(8)
U22	142(16)	113(7)	79(9)
U33	114(15)	77(7)	-4(8)
U12	4(11)	1(5)	10(8)
U13	-15(12)	-7(5)	4(8)
U23	-7(12)	2(5)	107(8)

Table 7.4 : Anisotropic oxygen thermal parameters ($\times 10^4$) in δ-WO_3.

W(1)-O(5)	1.948(6)	W(2)-O(6)	1.840(6)
W(1)-O(8)	1.847(6)	W(2)-O(7)	1.959(6)
W(1)-O(9)	1.772(5)	W(2)-O(9)	2.090(5)
W(1)-O(10)	2.090(5)	W(2)-O(10)	1.780(5)
W(1)-O(13)	2.175(5)	W(2)-O(14)	2.168(5)
W(1)-O(16)	1.763(5)	W(2)-O(15)	1.774(5)
O(5)-W(1)-O(8)	159.3(3)	O(6)-W(2)-O(7)	159.9(2)
O(5)-W(1)-O(9)	94 0(3)	O(6)-W(2)-O(9)	84.2(3)
O(5)-W(1)-O(10)	79.9(2)	O(6)-W(2)-O(10)	97.6(3)
O(5)-W(1)-O(13)	79.7(2)	O(6)-W(2)-O(14)	83.9(2)
O(5)-W(1)-O(16)	95.3(3)	O(6)-W(2)-O(15)	98.4(3)
O(8)-W(1)-O(9)	98.5(3)	O(7)-W(2)-O(9)	80.0(2)
O(8)-W(1)-O(10)	83.8(3)	O(7)-W(2)-O(10)	94.6(3)
O(8)-W(1)-O(13)	84.6(2)	O(7)-W(2)-O(14)	80.8(2)
O(8)-W(1)-O(16)	98.3(3)	O(7)-W(2)-O(15)	95.0(3)
O(9)-W(1)-O(l0)	164.8(2)	O(9)-W(2)-O(10)	165.4(2)
O(9)-W(1)-O(13)	87.0(2)	O(9)-W(2)-O(14)	78.8(2)
O(9)-W(1)-O(16)	101.5(2)	O(9)-W(2)-O(l5)	93.6(2)
O(lO)-W(l)-O(13)	78.3(2)	O(10)-W(2)-O(14)	86.9(2)
O(10)-W(1)-O(16)	92.9(2)	O(10)-W(2)-O(15)	100.5(2)
O(13)-W(1)-O(16)	170.4(2)	O(14)-W(2)-O(15)	171.8(2)
W(2)-O(5)	1.850(6)	W(4)-O(7)	1.833(6)
W(3)-O(8)	1.954(6)	W(4)-O(11)	2.086(5)
W(3)-O(11)	1.772(5)	W(4)-O(12)	1.782(5)
W(3)-O(12)	2.066(5)	W(4)-O(14)	1.740(5)
W(3)-O(13)	1.738(5)	W(4)-O(15)	2.147(5)
W(3) O(16)	2.170(5)		
O(5)-W(3)-O(8)	159.7(3)	O(6)-W(4)-O(7)	159.5(2)
O(5)-W(3)-O(11)	96.9(3)	O(6)-W(4)-O(11)	80.8(3)
O(5)-W(3)-O(12)	84.1(3)	O(6)-W(4)-O(12)	94.5(3)
O(5) W(3)-O(13)	98.4(3)	O(6)-W(4)-O(14)	96.0(3)
O(5)-W(3)-O(16)	83.5(2)	O(6)-W(4)-O(15)	80.8(2)
O(8)-W(3)-O(11)	94.0(3)	O(7) W(4)-O(11)	83.6(3)
O(6)-W(4)-O(7)	81.0(2)	O(7) W(4) O(12)	97.1(3)
O(8)-W(3)-O(13)	96.2(2)	O(7)-W(4) O(14)	98.3(3)
O(8)-W(3)-O(16)	80.0(2)	O(7)-W(4)-O(l5)	83.1(3)
O(ll)-W(3)-O(12)	164.8(3)	O(11)-W(4)-O(12)	164.5(3)
O(11)-W(3)-O(13)	101.3(3)	O(11)-W(4)-O(14)	94.0(2)
O(11)-W(3)-O(16)	86.8(2)	O(11)-W(4)-O(15)	78.3(2)
O(12)-W(3)-O(13)	93.6(2)	O(12)-W(4)-O(14)	101.3(3)
O(12)-W(3)-O(16)	78.2(2)	O(12)-W(4)-O(15)	86.3(2)
O(13)-W(3)-O(16)	171.4(2)	O(14)-W(4)-O(15)	172.0(2)

Table 7.5 : Interatomic distances (Å) and angles (°) from the GSAS refinement of δ-WO_3.

Based on Pauling's electrostatic valence rule (Pauling, 1929), one would expect that the four crystallographic tungsten atoms should be chemically equivalent and that the 12 crystallographically distinct oxygen atoms should be chemically equivalent. Bond valence calculations (Brown, 1978) were carried out using EUTAX and the coordinates from GSAS and the X-ray single crystal refinements. The average deviations from the average tungsten bond valence were 0.123 and 0.100 for the X-ray and neutron refinements, respectively. The average deviations from the average oxygen bond valence were 0.437 and 0.395 for the X-ray and neutron refinements, respectively. This further suggests that the neutron refinement has given more accurate oxygen positions because these data give four tungsten atoms and the twelve oxygen atoms which are closer to being chemically equivalent.

7.4 Discussion

Although the temperature of the transition between γ and δ–WO_3 is frequently given as 17°C, this is clearly not a thermodynamic equilibrium transition temperature. In fact, the equilibrium transition temperature appears to be higher than 25°C. On cooling WO_3 from high temperature, one normally obtains pure γ–WO_3 at 25°C. However, grinding WO_3 at 25°C results in a slow conversion to δ–WO_3 (Diehl, Brandt & Salje, 1978). If γ–WO_3 is cooled well below room temperature, for example to 0°C, it quickly converts completely to δ–WO_3. On warming δ–WO_3 to 25°C, it is stable indefinitely at room temperature. Thus, although γ–WO_3 is generally regarded as the room temperature stable form of WO_3, it appears that it is really δ–WO_3 that is the room temperature equilibrium form. To better understand the behavior of this phase transition it is instructive to examine how each polymorph is distorted from the ideal structure.

7.4.1 Octahedral Tilting and Tungsten Displacements in γ and δ-WO_3

Figure 7.2 shows the way in which the WO_3 octahedra are tilted in γ and δ–WO_3. Looking down both the x- and z-axes, the manner of tilting is the same for γ and δ–WO_3. However, when viewed down the y-axis, the different tilting arrangements of the two structures are apparent [figure 7.2(e) and (f)]. The tilts looking down the y-axis are in phase for γ–WO_3 and out of phase for δ–WO_3. In Glazer notation, γ–WO_3 belongs to the

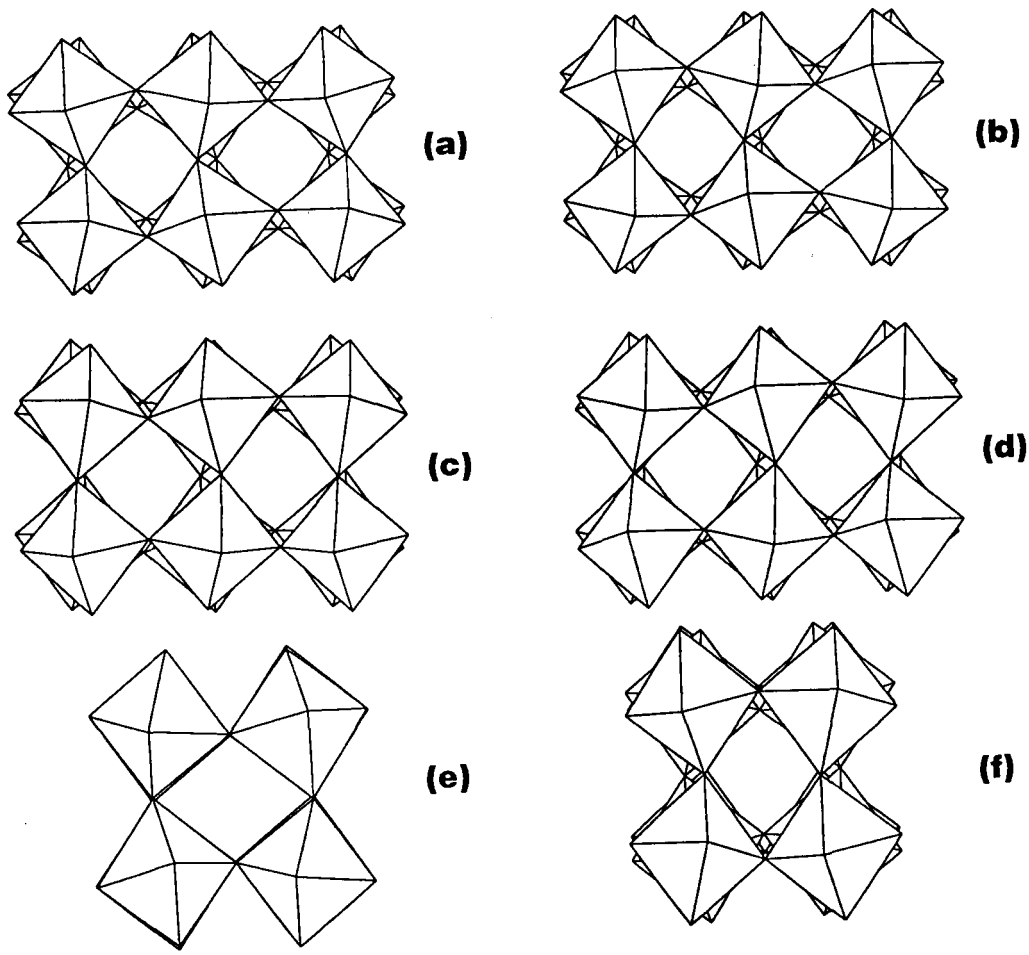

Figure 7.2 : Tilt patterns of WO_3 a) γ-WO_3 (001) projection, x-axis vertical; b) δ-WO_3 (001) projection, x-axis vertical; c) γ-WO_3 (100) projection, z-axis vertical; d) δ-WO_3 (100) projection, z-axis vertical; e) γ-WO_3 (010) projection, z-axis vertical; f) δ-WO_3 (010) projection, z-axis vertical.

three tilt system $a^+b^-c^-$, while δ–WO_3 belongs to the $a^-b^-c^-$ tilt system. In Glazer's (1972) original paper, the expected lattice constants and space group for each tilt system were predicted. For the $a^-b^-c^-$ system, the lattice constants are predicted to be approximately double the simple perovskite lattice constants (~4 Å) with $a \neq b \neq c$, $\alpha \neq \beta \neq \gamma \neq 90°$, and the atom positions are described by space group $F\bar{1}$. The $a^+b^-c^-$ system also has doubled lattice constants with $a \neq b \neq c$, $\beta \neq 90°$, and belongs to space group $P2_1/m$. Both of these descriptions are based on tilting of perfect octahedra with no displacement of cations.

The observed space group for γ–WO_3, $P2_1/n$, is different from the space group, $P2_1/m$, predicted by Glazer's system. Figure 7.2 shows that the sense of the tilting in phase looking down one axis and out of phase looking down the other two axes, is definitely known and correctly assigned. Of all the tilt systems with this sense of tilting: $a^+b^-c^-$, $a^+a^-c^-$, $a^+b^-b^-$ and $a^+a^-a^-$, only $a^+b^-c^-$ predicts that the a, b and c lattice constants will all be different. Examination of the experimentally determined lattice constants (a = 7.30Å, 6 = 7.54Å, c = 7.69Å) confirms that $a \neq b \neq c$. Therefore, assignment of the $a^+b^-c^-$ tilt system must be correct. The discrepancy between the observed and predicted symmetries must be due to distortion of the octahedra, displacement of the tungsten ions, or both. Inspection of figure 7.2 seems to indicate that the octahedra, as defined by the oxygen positions, are not significantly distorted. On the other hand based on the bond distances in table 7.5, the tungsten ions are definitely shifted from the centers of the octahedra. This suggests that cation displacements cause the symmetry to change from $P2_1/m$ to $P2_1/n$. Figure 7.3 shows the tungsten and oxygen positions defining the octahedra on the $z \cong 0.25$ level. In figure 7.3(a) the structure shown depicts the experimentally determined atomic positions for γ–$W0_3$, while figure 7.3(b) is an idealized structure where the atomic positions have been chosen to most closely match the experimentally determined positions but correspond to the symmetry constraints of space group $P2_1/m$. The mirror planes at y = 0.25 and y = 0.75 in $P2_1/m$ are evident in figure 7.3(b), but are missing in the actual structure shown in figure 7.3(a). Table 7.6 lists the positions of the atoms shown in figure 7.3 for both actual ($P2_1/n$) and ideal ($P2_1/m$) structures. In both figure 7.3 and table 7.6, it is apparent that the ions which have moved most from their ideal positions are the tungsten ions. It is the displacement of the tungsten ions primarily towards an edge of the octahedron that is the driving force in destroying the mirror symmetry and changing the space group from the ideal $P2_1/m$ to the observed $P2_1/n$. The displacements of tungsten atoms also result in a lower symmetry for δ–WO_3. For the $a^-b^-c^-$ tilt system Glazer predicted space group $F\bar{1}$ and a pseudocubic double unit cell ($a \cong b \cong c \cong 8$ Å and $\alpha \cong \beta$

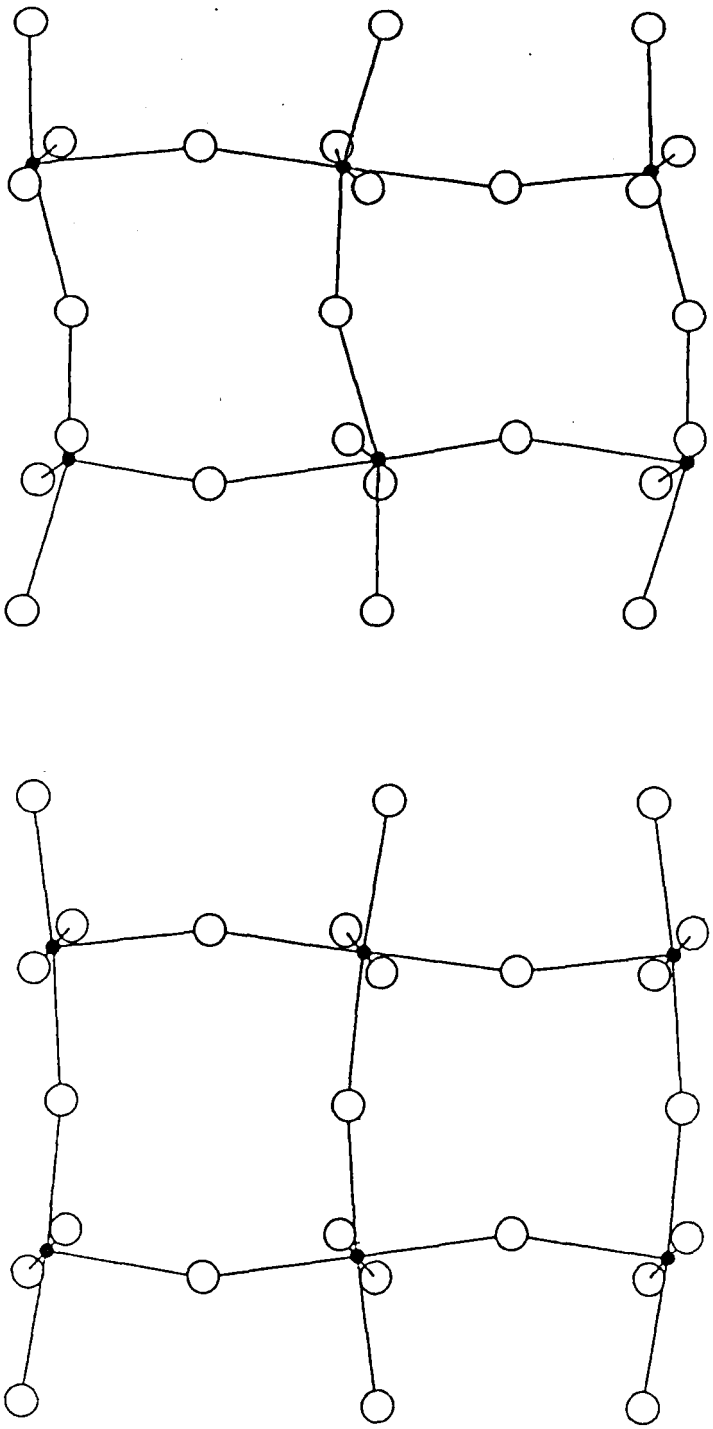

Figure 7.3 : Sections of γ-WO_3 in the (001) projection, with the x-axis vertical at $z \cong 0.25$. a) Real structure in $P2_1/n$ and b) idealized structure in $P2_1/m$.

	Actual structure ($P2_1/n$)			*Ideal structure ($P2_1/m$)*		
Atom	X	Y	Z	X	Y	Z
O(6)	2.08	3.656	-0.092	2.984	3.543	-0.04
W(1)	1.835	0.209	2.175	1.825	**0.000**	**1.894**
W(1)	1.816	3.978	1.614	1.825	**3.769**	**1.894**
O(1)	0.006	0.276	1.627	-0.007	0.143	1.646
O(1)	3.644	4.045	2.161	3.657	4.048	2.127
O(3)	2.059	1.962	2.175	2.059	1.885	2.175
O(5)	2.087	0.294	0.018	2.084	0.226	-0.04
O(5)	1.563	4.064	3.771	1.566	3.996	3.828
O(6)	2.080	-3.883	-0.092	2.084	-3.996	-0.041
W(1)	1.816	-3.561	1.614	1.825	**-3.769**	**1.894**
O(1)	3.644	-3.494	2.161	3.657	-3.491	2.127
O(2)	3.670	-0.277	2.124	3.657	-0.279	2.127
O(3)	1.591	-1.808	1.613	1.591	-1.885	1.613
O(5)	1.563	-3.475	3.771	1.566	-3.543	3.828
O(6)	1.570	-0.113	3.880	1.566	-0.226	3.828
O(5)	-2.087	-0.294	-0.018	-2.084	-0.226	0.04
W(2)	-1.811	-0.258	1.708	-1.825	**0.000**	**1.951**
W(2)	- 1.839	- 4.027	2.193	- 1.825	**-3.769**	**1.951**
O(1)	-3.656	-3.494	2.275	-3.643	-3.491	2.241
O(2)	-0.020	-4.047	1.664	-0.007	-3.913	1.646
O(2)	-3.630	-0.277	2.237	-3.643	-0.279	2.241
O(4)	-1.538	-1.962	2.093	-1.54	-1.885	2.093
O(5)	-1.563	-4.064	3.919	-1.566	-3.996	3.862
O(6)	-2.080	-3.656	0.092	-2.084	-3.543	0.040
W(2)	-1.839	3.512	2.193	-1.825	**3.769**	**1.951**
O(1)	-3.656	4.045	2.275	-3.643	4.048	2.241
O(2)	-0.020	3.492	1.664	-0.007	3.626	1.646
O(4)	-2.112	1.808	1.809	-2.110	1.885	1.809
O(5)	-1.563	3.475	3.919	-1.566	3.543	3.862
O(6)	-2.080	3.883	0.092	-2.084	3.996	0.040
O(6)	-1.570	0.113	3.809	-1.566	0.226	3.862

Table 7.6 : A comparison of the real and idealized atomic positions in γ-WO_3. All distances are listed in angstroms in Cartesian coordinates. Those distances in the ideal structure that deviate from the actual positions by more than 0.2Å are shown in bold.

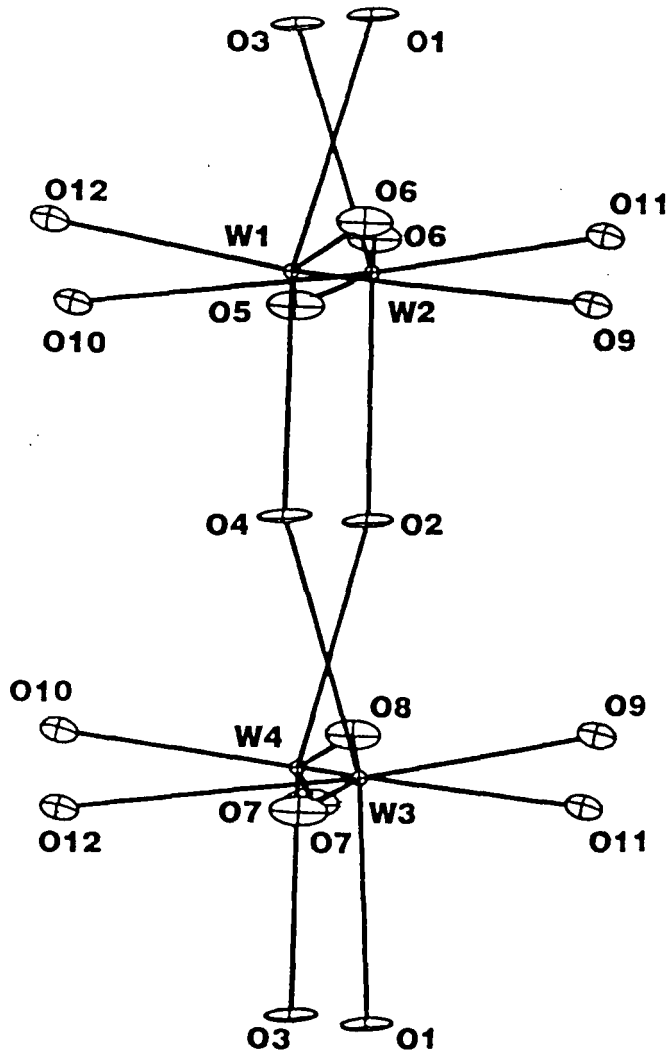

Figure 7.4 : Thermal ellipsoids in δ-WO_3. The view depicted in this figure is a (010) projection, with the z-axis vertical.

$\cong \gamma \cong 90°$). δ-WO_3 has a unit cell consistent with this prediction, but the symmetry corresponds to space group $P\bar{1}$.

In both δ and γ–WO_3, all tungsten atoms are displaced from the center of their octahedra in essentially the same manner. The displacement is approximately toward one edge of the octahedron. This leads to each tungsten atom having two short, two intermediate and two long bonds to oxygen (table 7.5 and figure 7.3). The average W-O distances are essentially the same in γ and δ–WO_3. The slightly higher density observed for δ–WO_3 can, therefore, be attributed to a better packing efficiency with its tilt system.

An ORTEP (Johnson, 1976) drawing of the thermal ellipsoids obtained in the GSAS refinement is shown in figure 7.4. The thermal motions of oxygen atoms 01-08 are roughly what might be expected. The primary directions of vibration are perpendicular to the W-O bonds. Both sets of atoms have a somewhat larger component of vibration in the z-direction than in the other perpendicular direction, y for 0(1)-0(4), and x for 0(5)-0(8) (see also table 7.4), but the results for these atoms are qualitatively as expected. In contrast the thermal ellipsoids for atoms 0(9)-0(12) have a significant magnitude in the z-direction, which is roughly parallel to the W-O bonds. Whether this result is meaningful or not is uncertain; however, it is a characteristic of all three refinements of the data and is reproducible from several different starting points. Inspection of the bond distances in table 7.5 shows that for all of the octahedra, both the shortest and the longest W-O bonds involve an oxygen in the group 0(9)-0(12). Therefore, these atoms are the ones involved in the most extreme O-W-O long-short bond distance alternation. Taking this fact into account, this result may be attributed to one of two causes. Either the long W-O distance on one side of the oxygen (2.14-2.18 Å) allows a larger thermal vibration of oxygen in that direction, or there is some disorder in the long-short bond alternation.

7.4.2 Comparison of RIETAN, GSAS and PROFIL

Inspection of tables 7.2-7.4 indicate that the three Rietveld software packages yield slightly different results. Table 7.2 shows some variation in residuals, lattice constants, and profile functions. GSAS has the lowest R_{WP} and apparently does the best job of fitting the observed pattern, followed by RIETAN and then PROFIL. The values of R_I are difficult to compare from one program to the next because of differences in the way each program defines the intensity of each hkl reflection. The difference between the R_E and $\chi^2 = (R_{WP}/R_E)^2$ calculated in PROFIL and the other two programs is not understood because

all three programs appear to calculate these parameters in the standard manner (Young, Prince & Sparks, 1982). A comparison of the lattice constants shows that RIETAN and PROFIL have similar zero points and their lattice constants agree to three places past the decimal point, but not nearly to within their standard deviations. With the exception of the c lattice constant, the lattice parameters determined by RIETAN and PROFIL are in excellent agreement with the values obtained in the single crystal determination. On the other hand GSAS gives a significantly different zero point and then not surprisingly different values for a, b and c.

All three programs use a pseudo-Voigt function to model the broadening of the reflections due to instrumental and sample effects. The pseudo-Voigt function has been shown to be one of the most satisfactory profile functions for Rietveld analysis (Young & Wiles, 1982; Young, 1993). However, all three use different pseudo-Voigt functions. PROFIL uses a simple pseudo-Voigt where:

$$\Gamma_{Lor}\,\Gamma_{Gauss} = [U\tan\theta + V\tan\theta + W]^{1/2}$$

$$p\text{-}V = \gamma G + (1-\gamma)L.$$

Γ symbolizes the full width at half maximum (FWHM), γ is the mixing term between pure Gaussian and pure Lorentzian profiles (γ = 0: Lorenztian; γ= 1: Gaussian), and U, V and W are refinable parameters that describe the broadening of peaks, as a function of θ. Rietan uses a very similar function, but incorporates an additional variable δ, that allows the FWHM of the Lorentzian function to differ from that of the Gaussian function:

$$\Gamma_{Gauss} = \delta\,\Gamma_{Lor}.$$

The GSAS program uses a profile function developed in part by D. E. Cox and is generally referred to as a modified Thompson-Cox-Hastings pseudo-Voigt (TCHpV) function (Thompson, Cox & Hastings, 1987; Young, 1993). In this function:

$$\Gamma_{Lor} = X\tan\theta + Y/\cos\theta$$

$$\Gamma_{Gauss} = [U\tan\theta + V\tan\theta + W + P/\cos\theta]^{1/2},$$

$$\gamma = 1.36603(\Gamma_{Lor}/\Gamma_{Gauss}) - 0.47719(\Gamma_{Lor}/\Gamma_{Gauss})^2 + 0.11116(\Gamma_{Lor}/\Gamma_{Gauss})^3$$

$$\Gamma = [(\Gamma_{Gauss})^5+2.69269(\Gamma_{Gauss})^4\,\Gamma_{Lor}+2.42843(\Gamma_{Gauss})^3(\Gamma_{Lor})^2+4.47163(\Gamma_{Gauss})^2(\Gamma_{Lor})^3 +0.07842\,\Gamma_{Gauss}(\Gamma_{Lor})^4+(\Gamma_{Lor})^5]^{1/5}$$

where X, Y and Z are additional refinable parameters. Not only do Γ_{Lor} and Γ_{Gauss} change differently with θ, but the mixing coefficient γ also varies with θ. The use of different peak profile functions undoubtedly leads to slightly different fits to the experimental pattern. Rietan and PROFIL have very similar functions and table 7.2 shows that the values of U, V, W and γ are very similar for the two refinements. Furthermore, the fact that γ is 0.7 indicates a significant amount of Lorentzian character is needed to obtain the best fit. This is not usually the case for neutrons (Young & Wiles, 1982) and may be a consequence of the high resolution capabilities of the HRNPD. The profile function used by GSAS is significantly different from those used by RIETAN and PROFIL, and this may be the source of differences in the zero-point and lattice constants between GSAS and the other two programs. The values of R_{WP} suggest that, at least for this sample, the modified TCHpV function fits the peaks better than the simple pseudo-Voigt functions. A problem, however, with the TCHpV function is that it is more prone to divergence during the refinements. One advantage usually attributed to the TCHpV function is that information on crystallite size and strain can easily be extracted, but such information can also be obtained using the simple pseudo-Voigt functions (Thompson, Cox & Hastings, 1987).

Comparing the positional parameters in table 7.3 the most striking difference between the different refinements is that the size of the estimated standard deviations (esd's) for the RIETAN refinement are 2-3 times larger than the other two refinements. Examination of the user's manuals revealed that RIETAN calculates its esd's differently from GSAS and PROFIL. The latter two programs calculate their esd's in the standard way by setting the standard deviation, σ, of the ith variable equal to:

$$\sigma(pi) = (A_{ii}^{-1}\chi^2)^{1/2}$$

where A_{ii}^{-1} is the appropriate diagonal element of the inverse of the matrix of the normal equations, and χ^2 is the goodness of fit ($\chi^2 = R_{WP}/R_E$) (Young, 1993). The RIETAN program uses a method proposed by Scott (1983) to calculate esd's, where:

$$\sigma(pi) = (A_{ii}^{-1}\chi_i^2)^{1/2}$$

where now χ_I^2 is a measure of the quality not of the entire fit, but only of the Bragg intensities ($\chi_I^2=R_I/N_B - P_c$) where N_B = no. of reflections, and P_c = no. of refinable structural parameters. In this way, the esd's may give a measure of the accuracy of the model and not just the statistics of fitting the data. These esd's should also be more meaningful for comparison with single crystal esd's. Keeping this in mind and examining table 7.3, we see that for almost all of the positional parameters the RIETAN data agrees within one standard deviation of the GSAS and single crystal data. The differences in positional parameters from one program or the next are in most cases much larger than the small esd's given by GSAS and PROFIL. Therefore, it appears that the RIETAN program gives a more reasonable estimate of the standard deviation of structural parameters than do the other two programs.

7.5 Conclusions

The thermodynamically stable form of WO_3 at room temperature has been shown to be triclinic δ-WO_3. The structure of δ-WO_3 has been obtained for the first time using neutron data, and this structure appears to be somewhat more accurate than that obtained from single crystal X-ray diffraction data. The tilt systems for γ and δ-WO_3 have been shown to be $a^+b^-c^-$ and $a^-b^-c^-$ respectively. The observed space groups are different than predicted by Glazer (1972) and in chapter two, due to displacements of tungsten ions roughly toward an edge in each octahedron. Despite this distortion the oxygen octahedra remain quite regular.

The Rietveld programs RIETAN, GSAS, and PROFIL have been compared. All three programs have their advantages and disadvantages. GSAS uses the most complex profile function and apparently achieves the best fit to the experimental data (for high resolution neutron diffraction data). This will presumably lead to a more accurate determination of the structural parameters of interest. Both Rietan and PROFIL appear to give better estimates of the lattice constants than does GSAS. RIETAN appears to give the most realistic values of the estimated standard deviations for structural parameters, but there is no significant difference between the three programs in terms of esd's for the lattice constants. PROFIL is the only program which calculates residuals after background subtraction, thus, giving R values more comparable to single crystal R values.

7.6 References

Brown I. D. (1978). *Chem. Soc. Rev.* **7**, 359.

Diehl R., Brandt G. and Salie E. (1978). *Acta Cryst.* B**34**, 1105.

Glazer, A. M. (1972). *Acta Cryst.* B**28**, 3385.

Johnson, C.K. (1976). *ORTEP-II.* Report ORNL-5138, Oak Ridge National Laboratory, TN.

Kehl W. L, Hay R G. and Wahl D. (1952). *J. Appl. Phys.* **23**, 212.

Larson, A.C. & Von Dreele, R.B. (1994). *LANSCE*, Los Alamos National Laboratory, Los Alamos, NM.

Lefkowitz, I., Dowell, & M.B. Shields, M.A. (1975). *J. Solid State Chem.* **15**, 24.

Loopstra B. O. and Rietveld H. M. (1969). *Acta Cryst.* B**25**, 1420.

Pauling, L., (1929). *J. Am. Chem. Soc.* **51**, 1010.

Perri J. A., Banks E. and Post B. (1957). *J. Appl. Phys.* **28**, 1272.

Rao, C.N.R. & Rao, B.V.S. (1974). *Natl. Stand. Ref. Data Ser. Natl. Bur. Stand.* **49**, 117.

Rietveld H. M. (1966). *Acta Cryst.* **22**, 151.

Rietveld, H.M. (1966). *Acta Cryst.* **22**, 151.

Rosen, C., Banks, E. & Post, B. (1957). *Acta Cryst.* **9**, 475.

Salje, E. & Viswanathan, K. (1975). *Acta Cryst.* A**31**, 356.

Salje, E. (1976). *Ferroelectrics*, **12**, 215.

Salje, E. (1977). *Acta Cryst.* B**33**, 547.

Sawada, S. (1956). *J. Phys. Soc. Jpn.* **11**, 1237.

Scott, H.G. (1983). *J. Appl. Cryst.* **16**, 159.

Tanisaki S. (1960). *J. Phys. Soc. Jpn.* **15**, 573.

Thompson R, Cox D. E. and Hastings J. B. (1987). *J. Appl. Crystallogr.* **20**, 79.

Woodward, P.M., Hoffmann, R.-D. & Sleight, R.D. (1994). *J. Mater, Res.* **9**, 2118.

Woodward, P.M., Sleight, A.W. & Vogt, T. (1995). *J. Phys. Chem. Solids* **56**, 1305.

Young, R.A. (Ed.) (1993). *The Rietveld Method*, IUCr Monographs on Crystallography, **5**, Oxford University Press, Oxford, pp. 1-38.

Young, R.A., Prince, E. & Sparks, R. (1982). *J. Appl. Cryst.* **15**, 430.

Chapter 8

Structure Refinement of Ferroelectric ε-WO_3

8.1 Introduction

The structure and phase transition behavior of tungsten trioxide near room temperature were discussed in the previous chapter. In this temperature region and above, rather subtle changes in physical properties accompany the subsequent phase transitions of WO_3. Tanisaki (1960) observed a small broad endothermic peak in the DTA curve and a slight decrease in the electrical resistivity (from 0.7 Ω-cm to 0.4 Ω-cm) upon heating crystals through the δ-WO_3 to γ-WO_3 phase transition, near 290K. Salje and Viswanathan (1975) found the resistivity to decrease from approximately 2.0 Ω-cm to 0.2 Ω-cm upon heating from 293K to 1123K. The optical band gap (2.58 eV at room temperature) is found to gradually decrease and become increasingly diffuse as the temperature is raised to 773K (Salje, 1974).

In contrast the physical properties change drastically upon cooling through the δ-WO_3 to ε-WO_3 phase transition at ≅ 230K. An abrupt 20 to 30 fold increase in the resistivity occurs at this transition (Salje & Viswanathan, 1975; Tanisaki, 1960). The optical band gap increases from 2.6 eV to an unknown value > 2.85 eV, resulting in a color change from pale green to bluish-white (Salje and Viswanathan, 1975). Tanisaki (1960) observed a sharp exothermic peak in the DTA curve (endothermic upon heating) and a rather large volume contraction (≅ 1%) upon cooling through the transition temperature. Salje and Viswanathan (1975) observed the onset of piezoelectricity upon transforming to the ε-phase. Hysteresis loops in the dielectric behavior at low temperatures have been observed in sintered pellets of WO_3 (Lefkowitz, Dowell, & Shields, 1975; Matthias & Wood, 1951), and single crystals specimens (Bihan & Vacherand, 1970), indicating the presence of ferroelectricity

Taking all of the physical property measurements into account it is clear that a definite change in the electronic band structure accompanies the δ-WO_3 to ε-WO_3 phase transition. Above this transition WO_3 is a semiconductor with an optical band gap in the visible region of the spectrum, Furthermore, conductivity measurements show the electron mobility to be quite high (for a metal oxide), and although the electrical conductivity is too high to accurately measure the dielectric properties structural studies

indicate antiferroelectric shifts of the ions. Below the transition WO_3 is a piezoelectric insulator with an optical band gap in the UV. The electron mobility is reduced by at least an order of magnitude and dielectric studies, although inconclusive, indicate the presence of ferroelectricity. In addition, when ε-WO_3 is slightly reduced, to introduce charge carriers, the electrical transport is found to be highly anisotropic ($\sigma_{ab}/\sigma_c > 100$) (Gehlig & Salje, 1983). Furthermore, if the measurements are performed in the dark bipolaronic transport is observed (Gehlig & Salje, 1983; Salje, 1995). Clearly the physical properties of the ε-phase are remarkably distinct from the properties of the other four WO_3 polymorphs, which it could be argued, make ε-WO_3 the most interesting form of tungsten trioxide.

From a theoretical, as well as a practical, point of view a thorough knowledge of the structure is a prerequisite for understanding the physical properties of the ε-phase, as well as the striking property changes which accompany the δ to ε transition. Surprisingly, the structure of the ε-phase is the least accurately know of all of the WO_3 polymorphs. The lattice constants were first determined by Tanisaki (1960). Sixteen years later Salje later refined approximate tungsten positions, but made no attempt to refine oxygen positions because his crystal was highly twinned upon cooling through the phase transition (Salje, 1976). In general the large volume contraction associated with the phase transition and the high degree of pseudosymmetry in the ε-phase make it nearly impossible to obtain good quality, untwinned single crystals of ε-WO_3. Salje also looked at powdered samples but did not pursue this route, because these samples showed incomplete, and sometimes almost no transition to the ε-phase even at 133K (Salje, 1976). However, with the advances made in powder diffraction over the past 20 years, and recent availability of a high resolution constant wavelength diffractometer, another attempt at accurately determining the structure of ε-WO_3 seemed appropriate, if not overdue.

8.2 Experimental

The sample used in this experiment was the same sample that was used for an earlier investigation of the δ-WO_3. Experimental details of its preparation are described in chapter seven. Data collection was performed on the high-resolution neutron powder diffractometer (HRNPD) at beamline H1A of the high flux beam reactor (HFBR) at Brookhaven National Laboratory (BNL). The experimental details of this diffractometer have been described previously (Woodward, Sleight & Vogt, 1995). Low temperature

spectra were collected using a two-stage Air Products displex for temperature control. Upon cooling a data set was collected at 200K and at 15K. After the data collection at 15K was complete, spectra were recorded upon warming at 50K, 100K, 150K, and 200K. The multibank detector array was moved in 0.02° steps for the 15K and 200K data sets, collected on cooling, and 0.05° steps for other data sets collected on warming. Integration times for all runs were roughly 5 minutes per step. Low temperature x-ray diffraction measurements were performed on the same sample at 20K and 50K, at beamline X7A of the national synchrotron light source (NSLS) at BNL. The sample was cooled in a two-stage Air Products displex using flat plate geometry. A point detector was used and due to the sharpness of the lines a step size of 0.003° was chosen. The sample was rocked about the theta position in an attempt to minimize preferred orientation. To obtain a highly monochromatic beam the incoming beam was passed through a Ge(111) monochromater and a Ge(220) crystal analyzer. The X7A experimental setup is discussed in greater detail elsewhere (Cox, 1992).

8.3 Structure Refinement

Initially, a neutron powder diffraction pattern was collected at 200K. However, upon inspection the diffraction pattern was found to contain at least two phases of WO_3 in significant quantities, making it unsuitable for structure refinement. With the goal of obtaining a single phase pattern another diffraction pattern was collected, this time at 15K. This pattern appeared to be single phase, although subsequent refinements showed the presence of a small amount of another WO_3 phase. The second phase had lattice constants similar to δ-WO_3 but the peaks were too weak to refine the structure. With the exception of the very weak second phase peaks, all of the reflections in the 15K pattern could be indexed using the lattice constants reported for ε-WO_3 in the literature (Tanisaki, 1960; Salje, 1976). At this point the peak intensities were extracted using the program EXTRA (Altomere, *et al.*, 1995). The EXTRA software package fits the entire pattern beginning from the space group and lattice constants and extracts the intensity of each peak using the method of LeBail (LeBail, Duroy, & Forquet, 1988). The extracted peak intensities were then used as input for the direct methods program SIRPOW (Altomere, *et al.*, 1994). From the extracted peak intensities SIRPOW was able to find all eight atoms in the asymmetric unit and gave an R(F) of 7.18% and an $R(F^2)$ of 9.99%. The atomic positions from SIRPOW were then used as the starting point for a Rietveld

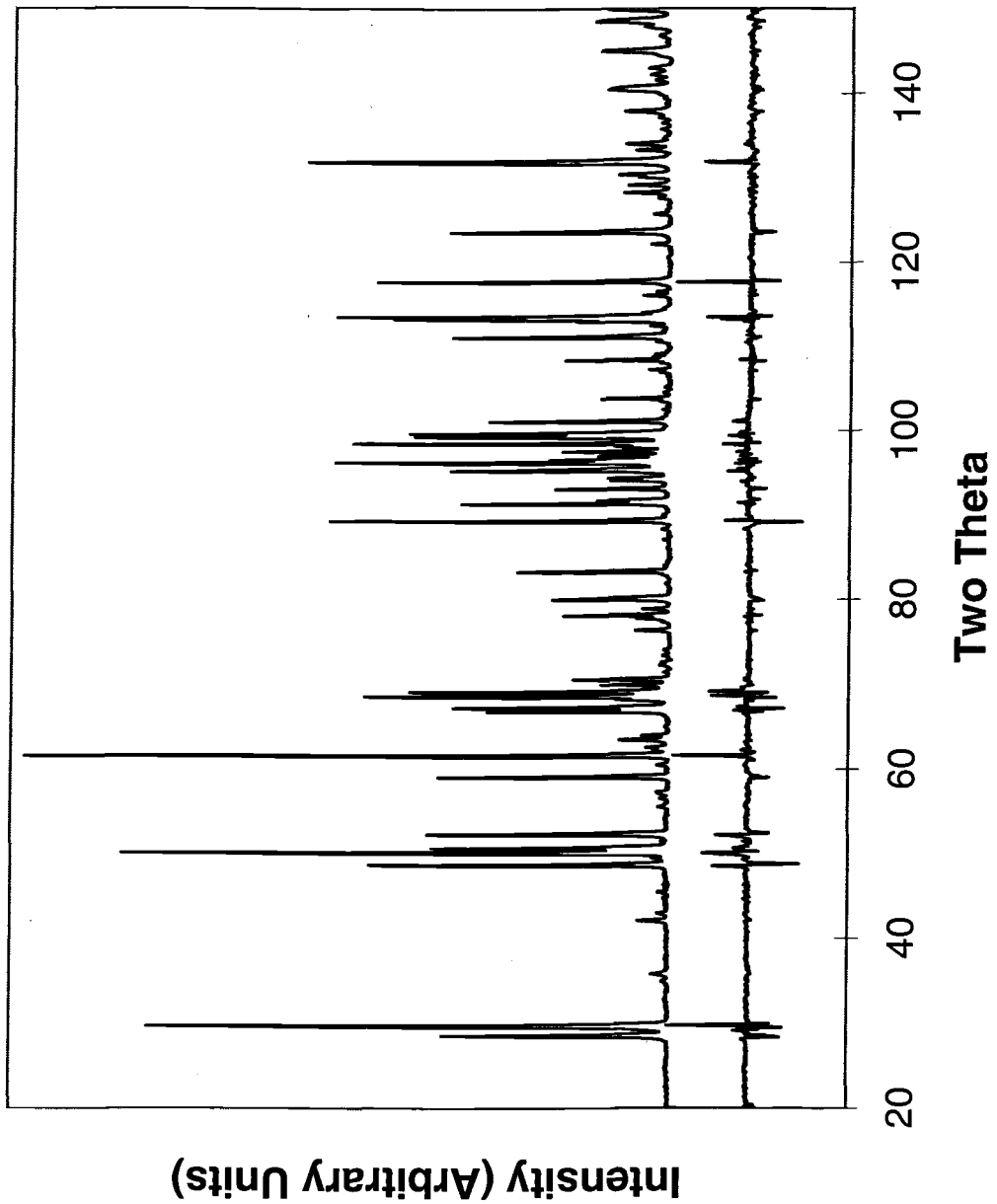

Figure 8.1 : The observed and difference patterns for the final GSAS refinement of the 15K neutron diffraction pattern.

***Space Group* =**		Pc		***a* =**	5.27792(3) Å
R_{wp} =		9.92%		***b* =**	5.15594(3) Å
R_p =		7.54%		***c* =**	7.66392(4) Å
χ^2 =		2.22		β =	91.762(1)°
$R(F^2)$ =		6.21		***Volume* =**	208.46 Å^3
***# of Reflections* =**		237		***Density* =**	7.39 g/cm^3
***# of Variables* =**		32		***Z* =**	4
Atom	***Site***	***x***	***y***	***z***	U_{iso}
W1	2a	0.000(1)	-0.015(1)	-0.0286(8)	-0.0012(4)
W2	2a	0.512(1)	0.473(1)	0.0478(9)	-0.0012
O3	2a	0.222(1)	0.713(1)	-0.0277(6)	0.0005(2)
O4	2a	0.294(1)	0.210(1)	0.0500(6)	0.0005
O5	2a	0.713(1)	0.793(1)	-0.0204(5)	0.0005
O6	2a	0.800(1)	0.289(1)	0.0582(5)	0.0005
O7	2a	0.005(1)	0.077(1)	0.7595(7)	0.0005
O8	2a	0.510(1)	0.426(1)	0.7737(7)	0.0005

Table 8.1 : Final results of the GSAS structural refinement of the 15K neutron diffraction pattern.

refinement using the program GSAS (Larson & Von Dreele, 1994). After addition of δ-WO_3 as a second phase to the refinement the refinement quickly converged to the structure given in table 8.1. The observed and difference patterns are shown in figure 8.1. Selected bond distances and angles are given in table 8.2. Because of the very weak intensity of even the strongest δ-WO_3 peaks only the lattice constants and phase fraction of the minority phase were refined. The profile coefficients and thermal parameters were fixed at the values obtained for the ε-phase and the atomic positions were set equal to the atomic positions found in the literature (Woodward, Sleight & Vogt, 1995). Even though it is uncertain if the true identity of the second phase is δ-WO_3, this approach seemed to fit observed second phase peaks fairly well. Refinement of the positional parameters of this phase were not attempted to minimize correlations with the ε-phase parameters.

Refinements were also carried out in space group P1, using the monoclinic structure as a starting model. When this was done the R_{wp} factor was found to drop from 9.92% to 9.74%. Applying the Hamilton significance test (Hamilton, 1965) to these two values indicates that even at the 50% confidence level the triclinic refinement is not statistically better than the monoclinic refinement. Furthermore, neither α nor γ refines statistically away from 90°, nor does any one peak or region of the spectrum appear to be fit

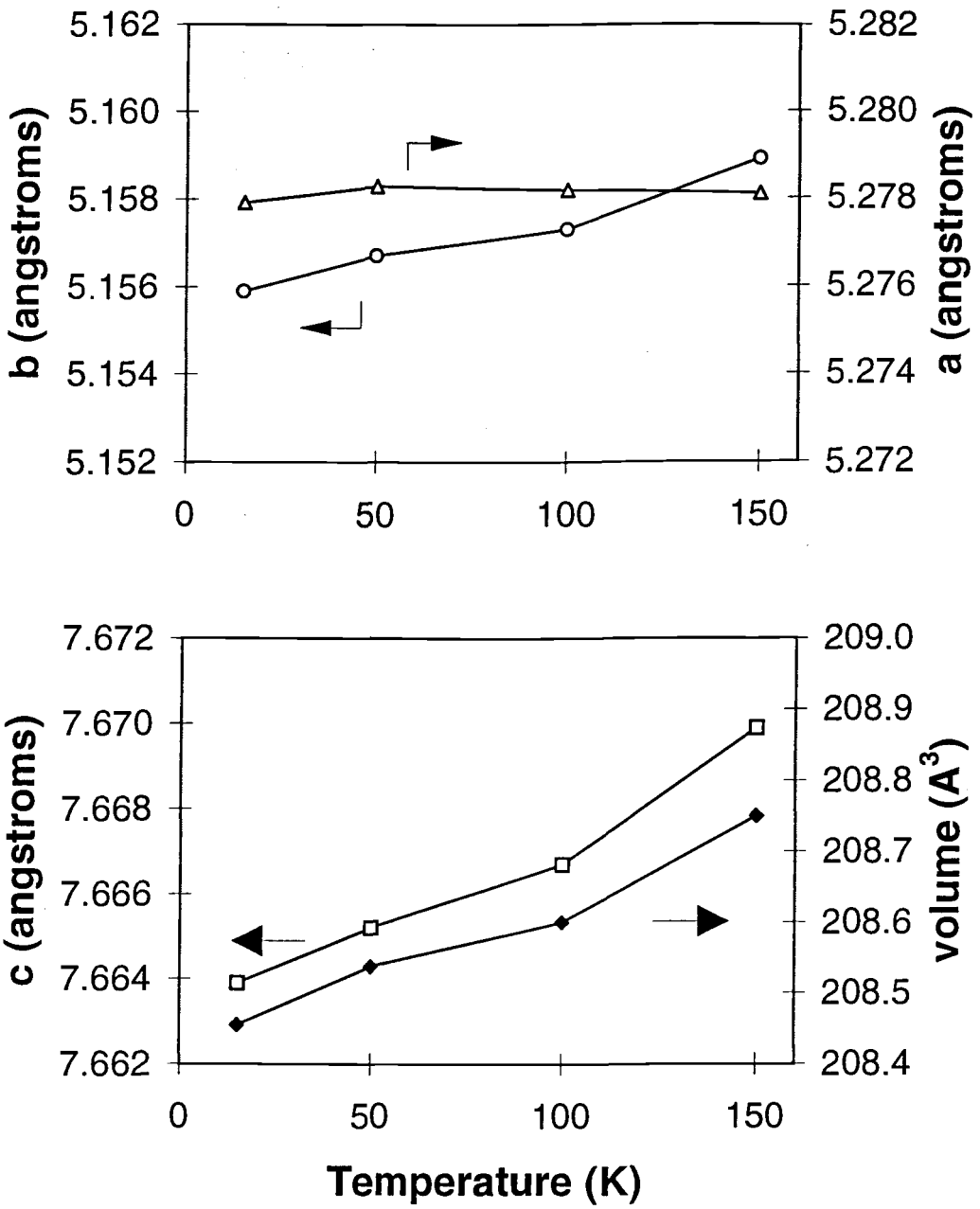

Figure 8.2 : The a, b, and c lattice constants unit cell volumes of ε-WO_3 as a function of temperature.

W1-O3	1.842(6)Å	W2-O3	2.025(7)Å
W1-O4	2.023(6)Å	W2-O4	1.775(7)Å
W1-O5	1.821(7)Å	W2-O5	2.048(6)Å
W1-O6	1.999(6)Å	W2-O6	1.781(8)Å
W1-O7	1.694(7)Å	W2-O8	2.131(8)Å
W1-O7	2.218(7)Å	W2-O8	1.804(7)Å
W1-O3-W2	162.0(2)°	W1-O6-W2	150.0(3)°
W1-O4-W2	156.5(1)°	W1-O7-W1	156.9(3)°
W1-O5-W2	152.0(3)°	W2-O8-W2	155.1(3)°

Table 8.2 : Selected bond distances in angles for WO_3 at 15K.

significantly better in the triclinic refinement. From these observations we conclude that the true symmetry is monoclinic, space group Pc. This is in agreement with Salje's findings based on photographs of twinned single crystals (Salje, 1976).

Based on capacitance and resistivity anomalies Lefkowitz, Dowell, and Shields (1975) suggested that below room temperature WO_3 undergoes phase transitions at 40K, 65K, 130K, 220K, and 260K. The latter two transitions appear to correspond to the γ to δ, and δ to ε phase transitions respectively, but the first three temperatures suggest phase transitions which have not yet been observed. To look for such transitions neutron diffraction patterns were collected at 50K, 100K, and 150K upon warming from 15K. A visual inspection of the patterns showed them all to be quite similar. No abrupt change of in the patterns can be observed. Nonetheless, all of the patterns were refined to look for subtle changes in the structure. Table 8.3 contains a summary of these refinements. Figure 8.2 shows the change in the lattice constants and unit cell volume of ε-WO_3.

In order to confirm the structural refinement from neutron data, low temperature synchrotron X-ray data sets were collected at 20K and 50K. Fairly crude qualitative data sets over a limited range were also collected at 50K intervals beginning at 250K upon cooling from room temperature. Unfortunately, texture effects (a few large crystals dominate the scattering) skew the peak intensities so that the data is unsuitable for structure refinement. However, from the peak positions alone several important features can be inferred. First of all, no peak splitting is observed and all peaks can be indexed with the unit cell described in table 8.1. This adds further weight to the conclusion that Pc is truly the correct space group, as suggested in the literature (Salje, 1976) and deduced

Parameter	50K	100K	150K
R_{wp}	11.04%	10.87%	13.03%
R_p	8.38%	8.18%	10.03%
χ^2	4.11	4.03	5.77
a	5.27829(8)Å	5.27821(5)Å	5.2781(1)Å
b	5.15666(8)Å	5.15728(5)Å	5.1589(1)Å
c	7.6652(1)Å	7.66669(7)Å	7.6699(1)Å
β	91.758(1)°	91.750(1)°	91.727(2)°
Volume	208.54 $Å^3$	208.60 $Å^3$	208.75 $Å^3$
Minority Phase Fraction	2.7%	2.4%	4.2%
Tungsten U_{iso}	0.0026(6)	0.0032(6)	0.0046(8)
Oxygen U_{iso}	0.0062(4)	0.0061(3)	0.0082(5)

Table 8.3 : Partial refinement results for neutron data sets collected upon warming from 15K. The detector step size was 0.05° two-theta rather than 0.02° two-theta used for the 15K data set. The difference in step size is partially responsible for the higher values of R_{wp} observed in these samples.

from the neutron diffraction data. Secondly, the minority WO_3 phase which appears in the neutron diffraction pattern is also clearly visible in the x-ray diffraction pattern, and the lattice constants of this phase are seen to smoothly evolve from those of the δ-phase above the transition temperature.

Although no transitions were observed between 15K and 150K some unusual effects were noted at 200K. Upon cooling the neutron diffraction pattern was found to be multiphase. Attempts to refine the pattern as a two phase mixture of δ-WO_3 and ε-WO_3 did not succeed in accurately fitting the pattern. Upon warming from low temperature the peak intensities of the minority phase noticeably increase at 200K, even though this is below the reported ε to δ phase transition temperature. The qualitative x-ray diffraction patterns obtained on cooling also indicate unusual behavior near this temperature. Deciphering this behavior is difficult, because the diffraction patterns always contain at least two (probably three or more) phases in this intermediate temperature region. Nonetheless, a more thorough study using both x-ray and neutron diffraction is already in progress. Hopefully, future work will be able to confirm or deny the presence of a new tungsten trioxide phase(s) between 150K and 250K.

8.4 Discussion

8.4.1 Comparison with the δ-Phase

Both tilting of the oxygen octahedra and displacement of tungsten from the center of those octahedra are responsible for lowering the symmetry of WO_3 from the cubic ReO_3 structure. Changes in either one or both of these distortion mechanisms are responsible for all of the phase transitions in WO_3. Upon cooling from high temperature tetragonal α-WO_3 to triclinic δ-WO_3 a change in the octahedral tilt system accompanies each phase transition. The easiest way to observed such a change in tilt system is to view a polyhedral representation of the structure down each of the three directions along which the octahedra share corners. Figure 8.3 shows such a view of the ε-WO_3 structure. One can readily see that octahedral tilting is out of phase down each of the three Cartesian axes. Neglecting the magnitudes of the tilts this corresponds to a --- Glazer tilt system, which as shown in the chapter seven, is also observed in δ-WO_3. Therefore, unlike the other phase transitions of WO_3, no significant change in the octahedral tilting arrangement is associated with the δ to ε phase transition.

To further examine the structural differences between δ and ε phases, the ε-phase was first transformed back to the large (Z=8) cell. Next the symmetry of each structure was reduced to P1 and the program IVTON (Zunic & Vickovic, 1996) was used to determine the volume center of each octahedron, as well as the direction and magnitude of each tungsten ion shift (with respect to the octahedral center of volume). Table 8.4 lists the position of the center of volume for each of the eight octahedra present in the large cell. For ease of comparison the positions are given in actual distances rather than fractional coordinates. A Cartesian coordinate system is used and both structure have been shifted so that the origin is located at the volume center of the first octahedron (the tilting sense of this octahedron is the same in both structures). The fact that only very small differences are observed between the two structures is additional proof that the oxygen ion positions do not change significantly through the phase transition.

If a change in the octahedral tilting arrangement does not drive the δ to ε transition, as it does the γ to δ transition, then shifts in the tungsten positions must be the driving force for the phase transition. The tungsten shifts, for the octahedra contained in table 8.4, are tabulated in table 8.5, and shown graphically in figures 8.4 and 8.5. One can immediately

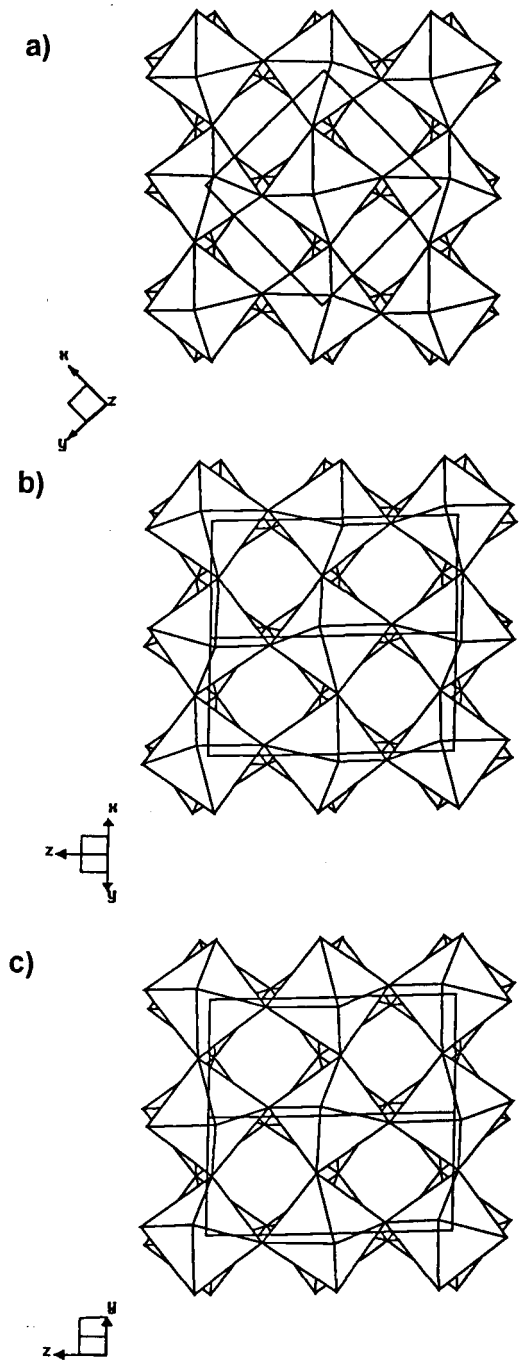

Figure 8.3 : A polyhedral representation of the ε-WO_3 structure looking down the a) [001] direction, b) [$\bar{1}$ 10] direction, and c) [110] direction. The bold lines represent the unit cell.

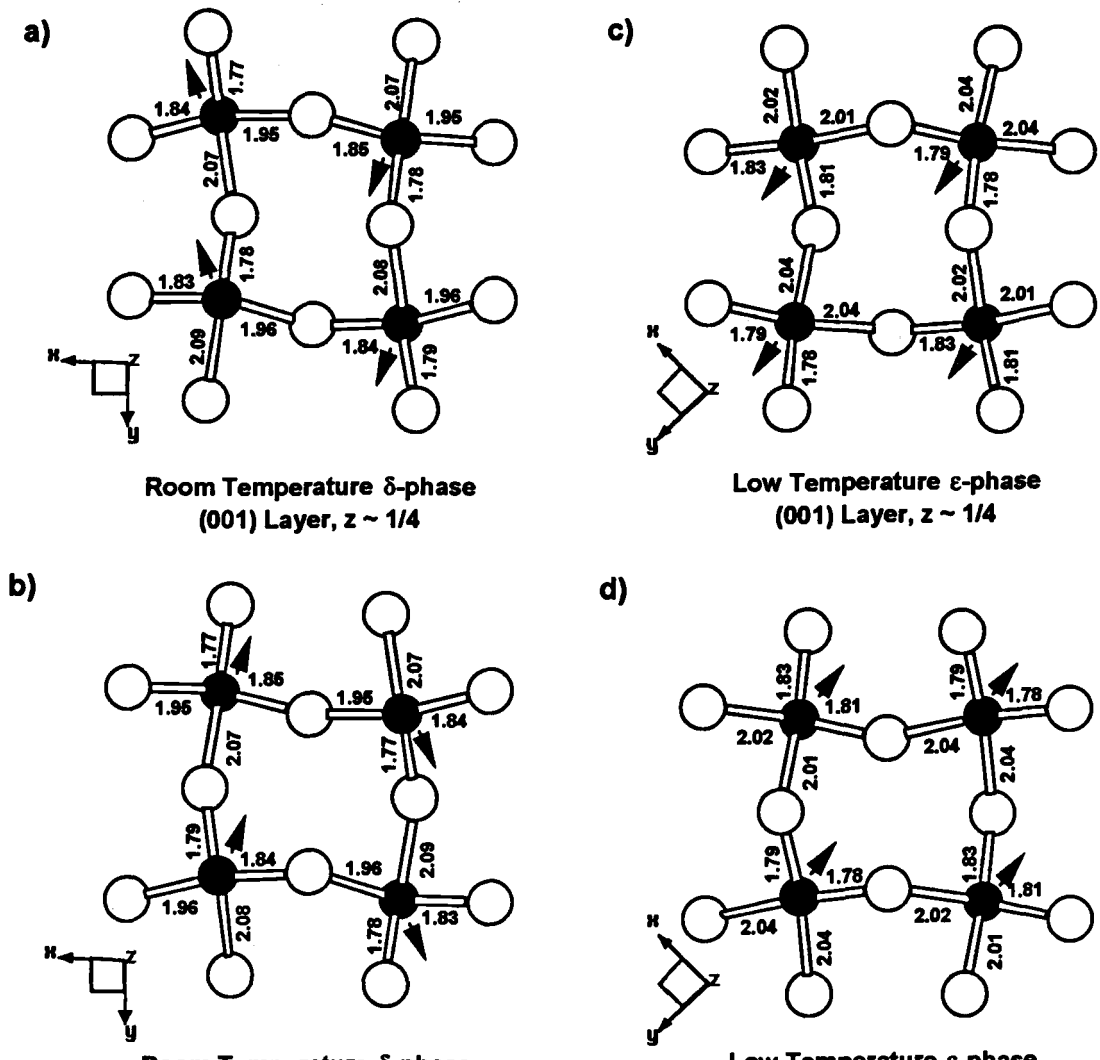

Figure 8.4 : A view of the tungsten oxygen linkages in the (001) layers in δ-WO_3 with a) z≅0.25, b) z≅0.75, and ε-WO_3 with c) z≅0.25, and d) z≅0.75. The dark circles represent tungsten, while the open circles represent oxygen. The arrows indicate the direction of the tungsten shifts, and the bond distances in angstroms are listed next to each bond.

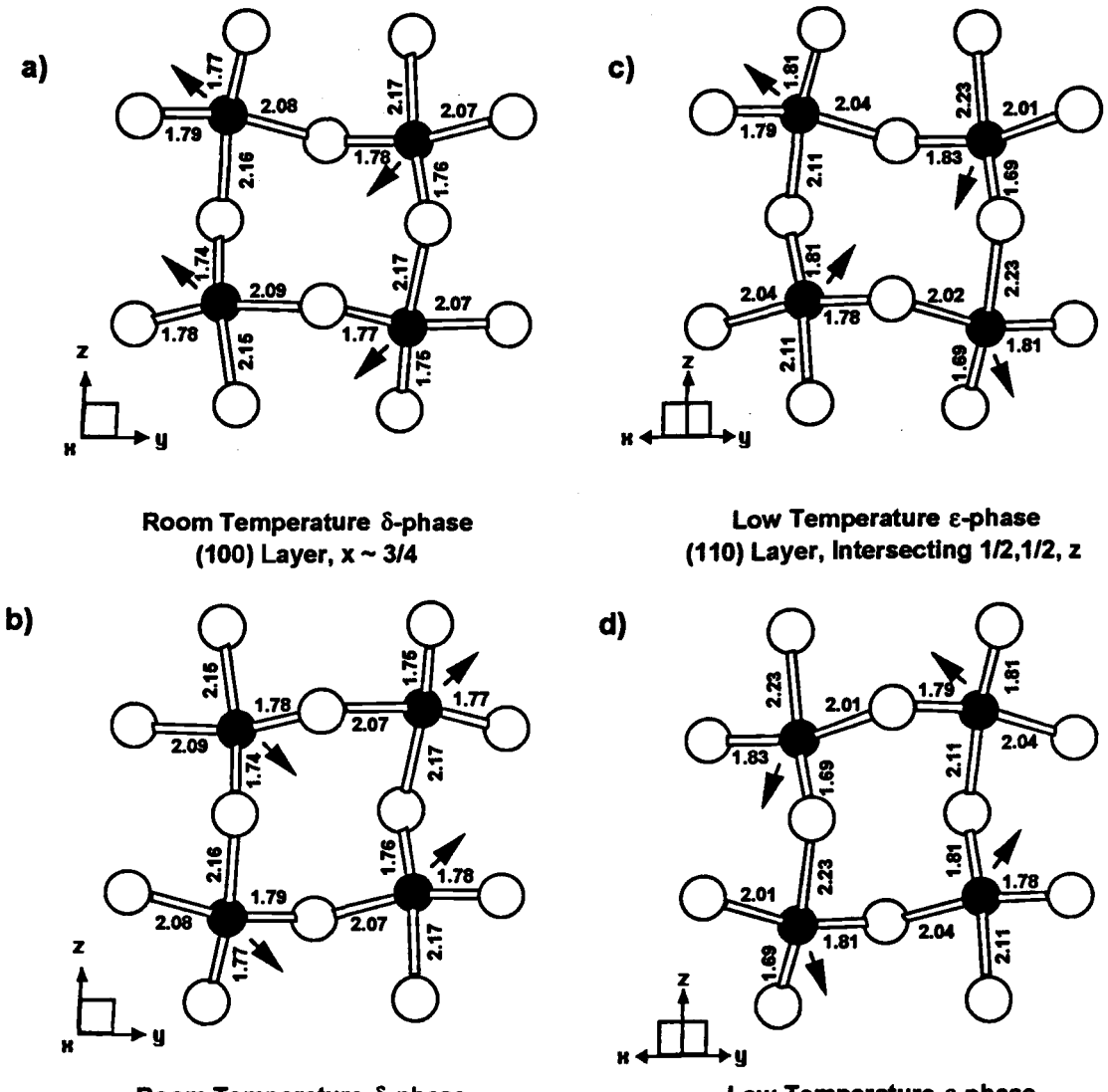

Figure 8.5 : A view of the tungsten oxygen linkages in the (100) layers of δ-WO_3 with a) x≅0.75, b) x≅0.25, and the (110) layers of ε-WO_3 passing through c) 0.5,0.5,z and d) 0,0,z. The dark circles represent tungsten, while the open circles represent oxygen. The arrows indicate the direction of the tungsten shifts, and the bond distances in angstroms are listed next to each bond.

	Delta Phase				Eta Phase				
Octahedron	**x**	**y**	**z**		**x**	**y**	**z**		**Distance**
1	0.000	0.000	0.000		0.000	0.000	0.000		0.000
2	-0.064	3.765	-0.022		-0.078	3.678	0.118		0.165
3	3.665	-0.111	-0.090		3.694	-0.006	-0.045		0.118
4	3.609	3.650	-0.053		3.603	3.687	0.000		0.065
5	-0.005	-0.005	3.837		0.006	0.006	3.832		0.016
6	-0.072	3.755	3.821		-0.069	3.685	3.787		0.078
7	3.660	-0.116	3.746		3.700	0.000	3.787		0.129
8	3.601	3.640	3.788		3.609	3.693	3.832		0.069

Table 8.4 : The Cartesian coordinates (in angstroms) of the volume centers of the eight WO_6 octahedra present in the large cell (Z=8). These values were calculated with the program IVTON (Zunic & Vickovic, 1996) and shifted so that the origin in each structure corresponds to the volume center of the first octahedron.

see that the tungsten positions have changed significantly upon transformation to the ε-phase. To describe the differences between the two structures it is most convenient to decompose the structure into one dimensional W-O chains running roughly parallel to each of the three Cartesian axes. The chains of course intersect at the tungsten ions to give the three dimensional structure. By examining the direction and magnitude of the tungsten shifts in each chain the structures can be qualitatively described.

The most striking differences between the two structures can be found in the xy plane. Beginning with the δ-phase the tungsten ions show an average shift of 0.17Å in the y direction, but only a 0.03Å shift in the x direction. This gives rise to a much more pronounced long-short bond alternation in the y direction, as shown in figure 8.4a. Furthermore, in each xy plane the shifts in the y direction are in opposite directions in neighboring chains. This results in a long-short bond alternation in each chain which is out phase with bond alternation in both neighboring chains. In the x direction the shifts, although much smaller, are in the same direction in neighboring chains, resulting in an in-phase relationship within the xy plane. The shifts in the layer immediately above (and below), shown in figure 8.4b, can be derived from the inversion center which relates the two layers.

Examining now the ε-phase there are two important differences between it and the δ-phase. First of all, the magnitude of the shifts has increased in the x-direction and decreased in the y-direction, so that the two are now comparable. This appears to be responsible for the unit cell contraction of the b lattice constant and the expansion of the a

lattice constant. This enhances the long-short bond alternation in the x-direction and has important consequences on the physical properties. This will be discussed in greater detail later. The second obvious difference between δ and ε phases is the direction of the shifts in the y direction. In the ε-phase all of the y direction shifts within a single xy plane are in the same direction. This gives in phase long-short bond alternation in both x and y directions, as shown in figure 8.4c. However, as shown in figure 8.4d the c glide plane causes the tungsten ions in neighboring xy planes to shift in the exact opposite direction. This results in an overall net shift of zero in both the x and y directions (see table 8.5).

A final point which has not yet been discussed is the volume contraction that occurs upon transformation into the ε-phase. The contraction could occur as a result of compression of the WO_6 octahedra or it could be realized by increased tilting of the octahedra. Table 8.6 contains a summary of the main structural features of the γ, δ, and ε phases. These results indicate that the latter mechanism, increased octahedral tilting, is responsible for the decreased volume of the ε-phase.

	Delta Phase				Eta Phase		
Octahedron	**x**	**y**	**z**		**x**	**y**	**z**
1	0.050	0.136	0.248		0.035	0.081	-0.321
2	0.007	0.148	-0.252		0.088	0.112	0.227
3	0.037	-0.180	-0.230		0.088	0.112	0.227
4	-0.012	-0.201	0.225		0.035	0.081	-0.321
5	-0.037	0.180	0.230		-0.035	-0.081	-0.321
6	0.012	0.201	-0.225		-0.088	-0.112	0.227
7	-0.050	-0.136	-0.248		-0.088	-0.112	0.227
8	-0.007	-0.148	0.252		-0.035	-0.081	-0.321
Net Shift	0	0	0		0	0	-0.376
Average Shift	0.027	0.166	0.239		0.062	0.097	0.274

Table 8.5 : The Cartesian coordinates (in angstroms) of the tungsten shifts (with respect to the octahedral volume centers) for the set of octahedra listed in table 8.4. These values were calculated with the program IVTON (Zunic & Vickovic, 1996).

Comparing the tungsten shifts in the z direction, in figure 8.5, one sees that shift directions are the same for both structures. Each chain that runs in the z-direction has two neighboring chains in the x direction and two neighboring chains in the y-direction. If the tungstens shift in the positive z direction in the central chain, then the tungsten shifts

in all four neighboring chains will be in the opposite direction. This results in an out of phase relationship in the long-short bond alternation between the central chain and all four of the neighboring chains. This relationship is common to both structures. However, if the magnitude of the shifts are carefully examined differences between the two structures are revealed. Whereas, in the δ-phase the magnitude of the shifts in the z-direction are all roughly the same, in the ε-phase the shifts in the negative z direction are larger than those in the positive z direction. Because of the inequality of shifts in the z direction a net spontaneous polarization develops along the c axis of the ε-phase. The presence of an inversion center precludes any such moment arising in the δ-phase. The presence of a net polarization along the polar c axis would explain the observance of hysteresis loops in the dielectric behavior WO_3 at low temperatures (Lefkowitz, Dowell & Shields, 1975; Matthias & Wood, 1951; Bihan & Vacherand, 1970). The fact that the tungsten shifts partially cancel each other may also help to explain why the hysteresis signal is weak and difficult to observe reproducibly. Drawing an analogy with magnetism, the crystal structure of the ε-phase is most appropriately described as ferrielectric rather than ferroelectric.

	γ-Phase	**δ-Phase**	**ε-Phase**
a	7.306 Å	7.309 Å	7.378 Å
b	7.540 Å	7.522 Å	7.378 Å
c	7.692 Å	7.686 Å	7.664 Å
α	90.00°	89.85°	88.73°
β	90.88°	90.91°	91.27°
γ	90.00°	90.94°	91.34°
Volume	423.7 $Å^3$	422.5 $Å^3$	417.0 $Å^3$
Average Octahedral Volume	9.30 $Å^3$	9.30 $Å^3$	9.32 $Å^3$
Tilt System	$a^-b^+c^-$	$a^-b^-c^-$	$a^-b^-c^-$
Average Tilt Angle			
x	156°	156°	154°
y	159°	159°	155°
z	161°	160°	157°
Average W-O Distance			
x	1.86/1.94Å	1.84/1.96Å	1.80/2.03 Å
y	1.76/2.11Å	1.78/2.08Å	1.80/2.03Å
z	1.74/2.18Å	1.75/2.16Å	1.75/2.17Å

Table 8.6 : A summary of the main structural features of the γ, δ, and ε phases of WO_3. The ε-phase has been converted to the large (Z=8) cell for comparison with the other two polymorphs.

8.4.2 Relationship to Physical Properties

The preceding discussion gives the details of the structural changes which accompany the δ to ε phase transition. However, the relationship between these structural changes and the remarkable changes in the electrical and optical properties associated with this phase transition have up to this point been ignored. To understand this relationship a qualitative understanding of the electronic band structure of WO_3 is needed. Both the valence and conduction bands are formed from overlap of the bonding orbitals on tungsten and oxygen. Because oxygen is more electronegative than tungsten it will make a larger contribution to the valence band, while tungsten will make a larger contribution to the conduction band. Nonetheless, due to the electronegativity and large formal charge on tungsten there will be a significant degree of covalency in the bonds. The high electrical conductivity and yellow color of WO_3 are evidence of the covalency in the tungsten-oxygen bonds at room temperature. Consider first an isolated WO_6 octahedron. The bonding overlap between tungsten and oxygen lowers the energy of the bonding orbitals and raises the energy of the antibonding orbitals, with respect to the isolated atomic orbitals. Increasing the overlap will increase the splitting of the bonding and antibonding levels, and decreasing the overlap will have the opposite effect. If the isolated octahedra are now brought together to form crystalline WO_3 the bonding and antibonding orbitals will overlap to some extent and broaden into the valence and conduction bands respectively. The width of these bands will be dependent upon the degree of orbital overlap between neighboring octahedra. In this way the energy separation between the centers of the conduction and valence bands, U, will depend on the orbital overlap within each octahedron, and the width of these bands, W, will depend upon the orbital overlap across the octahedral linkages (W-O-W interactions). The band gap, E_g, will depend upon both of these factors as shown in figure 8.6. These ideas are not new, but are just a simplification of the ideas developed by Mott and Hubbard. An excellent, easy to follow, description of the Hubbard model is given by Cox (1991).

Considering the WO_3 structure this time from a bonding point of view. Each tungsten is shifted off of the center of its octahedron toward one or more oxygen ions. This presumably results in a net increase in bonding within the octahedron. However, the long-short bond alternation that accompanies this distortion is certain to decrease the orbital overlap between neighboring octahedra. According to the above arguments this

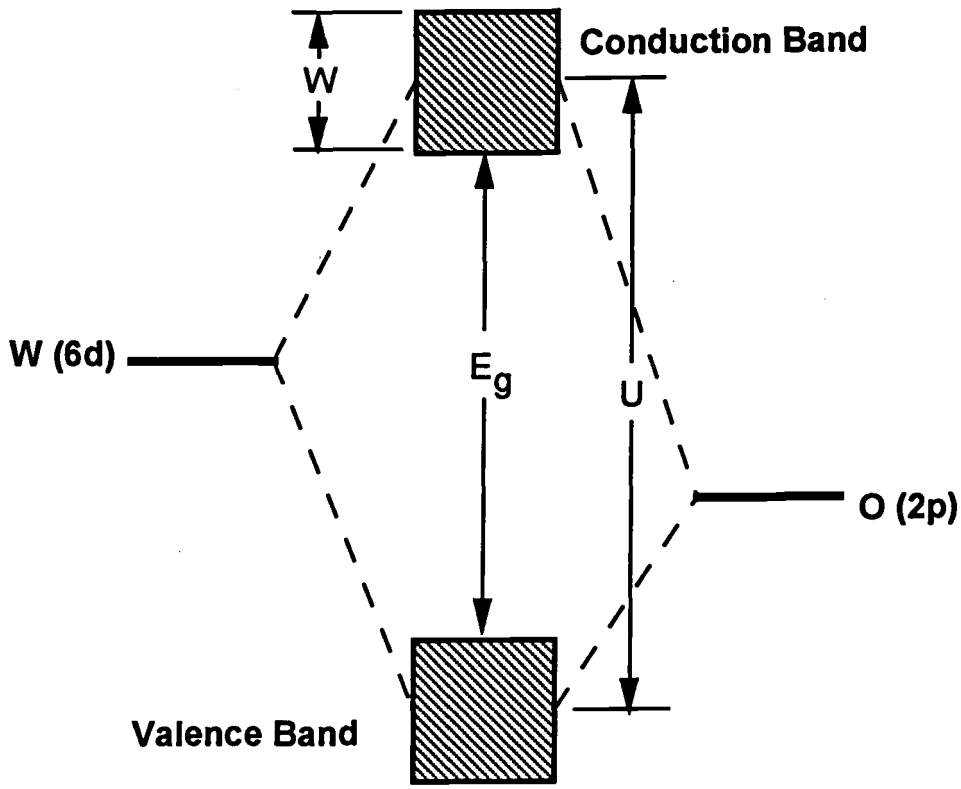

Figure 8.6 : A schematic diagram representing the formation of valence and conduction bands in WO_3. U is the Hubbard U parameter, W the band width, and E_g is the band gap.

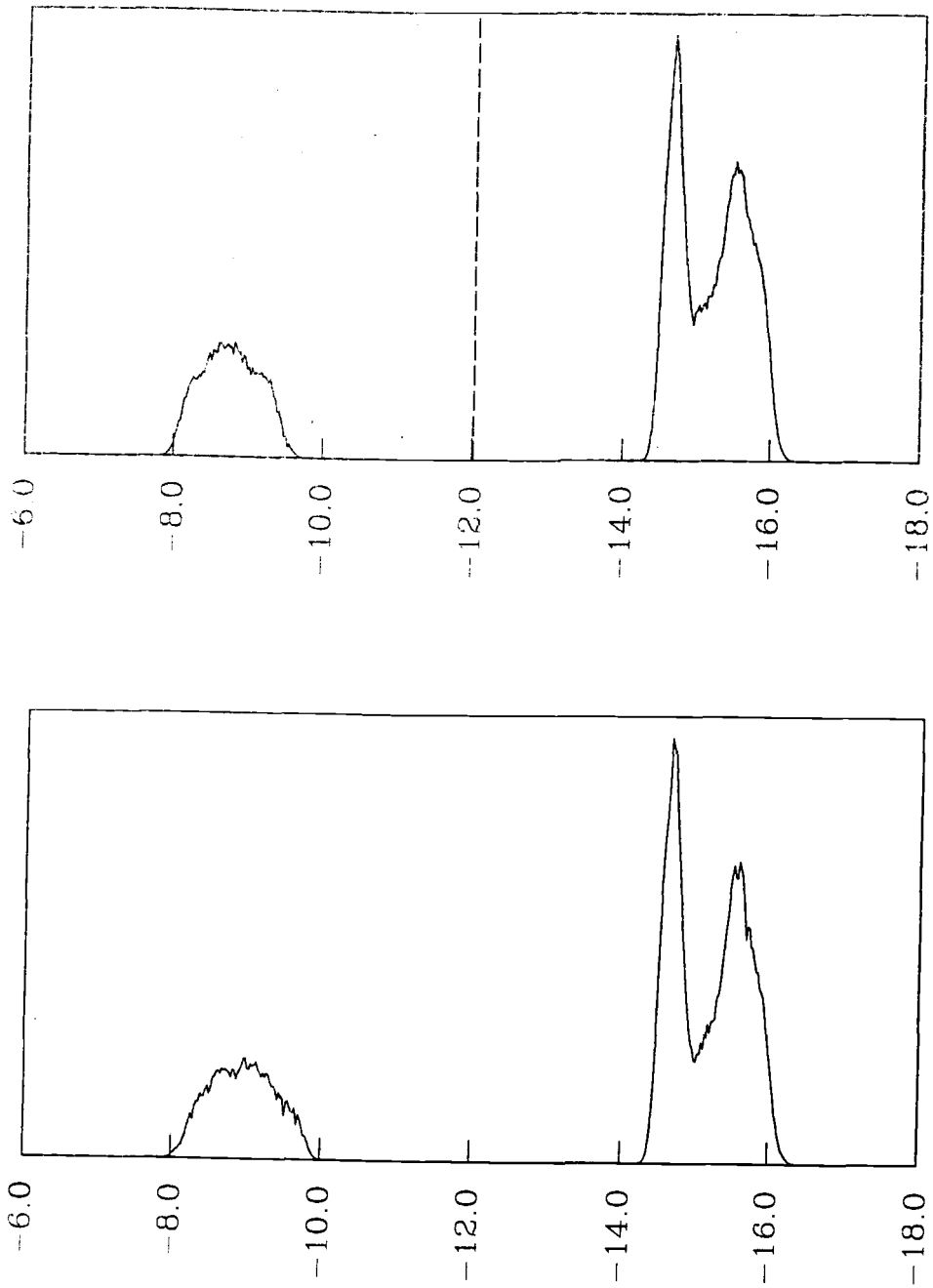

Figure 8.7 : Density of states plots for the valence and conduction bands of a) ε-WO_3 and b) a hypothetical WO_3 structure with oxygen positions identical to ε-WO_3 and tungsten positions in the volume center of the ochahedra. The band structures were calculated using the extended Hückel method. Energy values on the y axis are in units of electron volts.

should result in an increase in U and a decrease in W, both of which should increase the band gap. Now, if we examine the structural details of the δ to ε phase transition and pay special attention to the tungsten-oxygen bonding interactions, the major difference between the two structures is the enhanced long-short bond alternation present in the x direction of the ε-phase. Qualitatively this would appear to be the structural change responsible for the dramatic change in the optical band gap. Table 8.6 compares the structural features of the γ, δ, and ε phases. The increased bond distance alteration in the x direction of the ε-phase is apparent, whereas no such bond distance change is associated with the γ to δ phase transition.

In order to quantify the arguments of the preceding paragraph band structure calculations using the extended Hückel method (Hoffmann, 1963; Whangbo & Hoffmann, 1978; Hoffmann, 1988) were performed on the ε-WO_3 structure and a hypothetical structure identical to ε-WO_3 except that each tungsten was forced to lie at the volume center of its octahedron. This hypothetical structural was chosen rather than the δ-WO_3 structure to exaggerate the effect of distorting the symmetrical tungsten-oxygen bonding interactions by introducing the long-short bond distance alternation. The extended Hückel calculations were performed using the program NEW5, written by Dr. Gordon Miller of Iowa State University (Miller, 1990). The results are shown in figure 8.7. There is little change in the position or the width of the valence band upon shifting the tungstens to the volume centers of the octahedra, but the conduction band is noticeably broadened and shifted to slightly lower energy. The density of states curves indicate that the conduction band has a width of 1.84 eV and is centered at -8.76 eV in ε-WO_3, whereas in the hypothetical structure its width is 2.08 eV and its centroid is located at -8.96 eV. The calculated band gap value for the ε-phase is 4.56 eV, while it is 4.24 eV for the hypothetical structure. These values are much higher than the experimentally determined values, but that is not unusual for band gaps calculated using the extended Hückel method. However, the absolute numbers are not as important as the confirmation that shifting the tungsten off of the center of the octahedron both narrows the conduction band and shifts it to higher energy. This finding is in agreement with the qualitative arguments of the preceding paragraph. Similar effects were seen upon comparison of δ-WO_3 and ε-WO_3 but the magnitude of the differences between calculated band structures were much smaller.

Although WO_3 displays a rather high electrical conductivity above the ε to δ phase transition, a simple band structure argument would predict that it should be an insulator. The valence band is empty and the band gap of 2.6 eV is too large to expect a large

concentration of thermally excited carriers at room temperature. However, if the carrier mobility is high enough then a relatively low concentration of carriers introduced through either impurities or nonstoichiometry could account for the values of conductivity typically observed. Assuming this to be true the drop in conductivity observed upon transition to the ε-phase is a result of a sudden decrease in the electron mobility. The temperature dependence of the conductivity in ε-WO_3 is suggestive of activated hopping of charge carriers (Salje & Viswanathan, 1975). For an electron to hop from one tungsten site to a neighboring tungsten site it must traverse through both a long W-O bond and a short W-O bond. As the anisotropy of the tungsten oxygen bonds increases the orbital overlap of the long W-O bond decreases. This will increase the activation energy required to jump from one tungsten site to a neighboring tungsten site and decreasing the electron mobility. The moderate long-short bond alternation which exists in the x direction of the δ-phase apparently provides a relatively low energy/high mobility path for electronic conduction. However, when this bond alternation is enhanced in the ε-phase no low energy pathway exists for electrons to move between tungsten sites, because transport involves crossing a long tungsten-oxygen bond in all three directions. In a similar vein the fact that conductivity in the z direction is two orders of magnitude smaller that in the xy plane is consistent with the observation that the bond distance anisotropy is greatest in the z direction.

8.4.3 Incomplete Phase Transformation

The presence of hysteresis in the δ to ε phase transition temperature (Salje & Viswanathan, 1975, Tanisaki, 1960) and a sharp endothermic peak in the DTA (Tanisaki, 1960) strongly suggest the phase transition is first order. The structure of the ε-phase is not inconsistent with this conclusion, in that even though the connectivity of the lattice does not change upon transformation, the direction of the strong tungsten-oxygen bonds does change. What is unusual is the observation that seemingly a small amount of the high temperature phase is still present under 200K, below the δ to ε phase transition temperature. A similar effect on powder samples was noted by Salje (1976).

Such behavior is not unique to the δ to ε phase transition. The γ to δ transition is well documented to be sluggish, and near the phase transition it is not at all unusual for both phases to be present simultaneously in either crystals (Salje & Viswanathan, 1975, Tanisaki, 1960) or powders, as seen in chapter seven. However, the temperature range

over which both γ and δ phases have been simultaneously observed is much smaller than the two-phase temperature range observed in this experiment. The effect of particle size, impurities, and nonstoichiometry on the transition of individual crystallites are all possible explanations for the behavior. Through addition of niobium Roth and Waring (1966) were apparently able to stabilize the ε-phase up to 1010K, where it transformed directly to the α-phase. Berak and Sienko (1970) found that the presence of oxygen vacancies decreased both the γ to δ and δ to ε phase transition temperatures. So it is apparent that the transition temperatures can be significantly altered by subtle changes in the composition. As alluded to earlier in the paper the possibility of another phase existing in the intermediate temperature range (150K-220K), may also help explain this behavior. The second phase present in the low temperature diffraction patterns may well be a new phase of WO_3 rather than δ-WO_3, and the transition temperature for transformation from this unknown phase and ε-WO_3 could be much lower than 220K. Another factor to keep in mind, is that there is not much thermal energy available at these low temperatures to overcome activation energy barriers associated with the phase change. Further work is necessary to fully understand this behavior.

8.5 Conclusions

The structure of ε-WO_3 at 15K has been accurately determined for the first time. The structural differences with the room temperature triclinic δ-WO_3 structure are highlighted. The main structural change which drives the transition is a shift of the tungsten atoms. In particular the increased long-short tungsten-oxygen bond alternation in the x-direction appears to be responsible for the observed increase in the band gap and decrease in the electron mobility. A small net moment of spontaneous polarization is present in ε-WO_3, but antiparallel shifts of tungsten ions in the c direction indicate the material is not expected show a strong ferroelectric effect. Increased octahedral tilting angles are responsible for the decreased volume of the ε-phase.

8.6 References

Altomere, A., Burla, M.C., Cascarano, G., Giacovazzo, C., Guagliardi, A., Moliterni A.G.G. & Polidori, G. (1995). *J. Appl. Cryst.* **28**, 842.

Altomere, A., Cascarano, G., Giacovazzo, C., Guagliardi, A., Burla, M.C., Polidori, G. & Camalli, M. (1994). *J. Appl. Cryst.* **27**, 435.

Berak, J.M. & Sienko, M.J. (1970). *J. Solid State Chem.* **2**, 109.

Bihan, R.L. & Vacherand (1970). *J. Phys. Soc. Jpn.* **28**, 159.

Cox, D.E. (1992). *Syncrotron Radiation Crystallography*, ed. P. Coppens, Academic Press, London, pp. 186-254.

Cox, P.A. (1991). *The Electronic Structure and Chemistry of Solids,* Oxford University Press, Oxford.

Diehl, R. Brandt, G. & Salje, E. (1978). *Acta Cryst.* B**34**, 1105.

Gehlig, R. & Salje, E. (1983). *Phil. Mag.* B**47**, 229.

Hamilton, W.C. (1965). *Acta Cryst.* **18**, 502.

Hoffmann, R. (1963). *J. Chem. Phys.* **39**, 1397.

Hoffmann, R. (1988). *Solids and Surfaces: A Chemist's View of Bonding in Extended Structures*, VCH Publishers, New York.

Larson, A.C. & Von Dreele, R.B. (1994). *LANSCE*, Los Alamos National Laboratory, Los Alamos, NM.

LeBail, A., Duroy, H. & Forquet, J.L. (1988). *Math. Res. Bull.* **23**, 447.

Lefkowitz, I., Dowell, & M.B. Shields, M.A. (1975). *J. Solid State Chem.* **15**, 24.

Loopstra, B.O. & Rietveld, H.M. (1969). *Acta Cryst.* B**25**, 1420.

Matthias, B.T. & Wood, E.A. (1951). *Phys. Rev.* **84**, 1255.

Miller, G. (1990). NEW5, Extended Hückel band structure calculation program. Iowa State University.

Rao, C.N.R. & Rao, B.V.S. (1974). *Natl. Stand. Ref. Data Ser. Natl. Bur. Stand.* **49**, 117.

Roth, R.S. & Waring, J.L. (1966). *J. Res. Natl. Bur. Stand. (U.S.)* **70A** (Phys. and Chem.), 281.

Salje, E. & Viswanathan, K. (1975). *Acta Cryst.* A**31**, 356.

Salje, E. (1974). *J. Appl. Cryst.* **7**, 615.

Salje, E. (1976). *Ferroelectrics*, **12**, 215.

Salje, E. (1977). *Acta Cryst.* B**33**, 547.

Salje, E. (1995). *Polarons and Bipolarons in High T_c Superconductors and Related Materials*, ed. E.K.H. Salje, A.S. Alexandrov, L.Y. Liang, Cambridge University Press, Cambridge, pp. 110-132.

Tanisaki, S. (1960). *J. Phys. Soc. Jpn.* **15**, 566.

Whangbo, M.-H. & Hoffmann, R. (1978). *J. Am. Chem. Soc.* **100**, 6093.

Woodward, P.M., Sleight, A.W. & Vogt, T. (1995). *J. Phys. Chem. Solids* **56**, 1305.

Zunic, T.B. & Vickovic, I. (1996). *J. Appl. Cryst.* **29**, 305.

Bibliography

Abrahams, S.C. & Bernstein, J.L. (1967). *J. Phys. Chem. Solids* **28**, 1685.

Ahtee, A., Ahtee, M., Glazer, A.M. & Hewat, A.W. (1976). *Acta Cryst.* B**32**, 3243.

Ahtee, M. & Darlington, C.N.W. (1980). *Acta Cryst.* B**36**, 1007.

Ahtee, M., Glazer, A.M. & Megaw, H. (1972). *Phil. Mag.* **26**, 995.

Albright, T.A., Burdett, J.K. & Whangbo, M.-H. (1985). *Orbital Interactions in Chemistry*, Wiley, New York.

Aleksandrov, K.S. (1976). *Kristallografiya* **21**, 249.

Almaer, S.A., Battle, P.D., Lightfoot, P., Mellen, R.S. & Powell, A.V. (1993). *J. Solid State Chem.*, **102**, 375.

Alter, E. (1974). *Z. Anorg. Allg. Chem.* **408**, 115.

Altermatt, C. & Brown, I.D. (1987). *Acta Cryst.* A**43**, 125.

Altomere, A., Burla, M.C., Cascarano, G., Giacovazzo, C., Guagliardi, A., Moliterni A.G.G. & Polidori, G. (1995). *J. Appl. Cryst.* **28**, 842.

Altomere, A., Cascarano, G., Giacovazzo, C., Guagliardi, A., Burla, M.C., Polidori, G. & Camalli, M. (1994). *J. Appl. Cryst.* **27**, 435.

Alvarez, I., Lopez, M.L., Gonzales, C., Jerez, A., Veiga, M.L. & Pico, C. (1993). *Solid State Ionics* **63**, 609.

Amador, U., Hetherington, C.J.D., Moran, E. & Alario-Franco, M.A. (1992). *J. Solid State Chem.*, **96**, 132.

Anderson, M.T. & Poeppelmeier, K.R. (1991). *Chem. Nat.*, **3**, 476.

Anderson, M.T., Greenwood, K.B., Taylor, G.A. & Poeppelmeier, K.R. (1993). *Prog. Solid State Chem.* **22,** 197.

Attfield, M.P., Battle, P.D., Bollen, S.K., Gibb, T.C. & Whitehead, R.J. (1992b). *J. Solid State Chem.* **100**, 37.

Attfield, M.P., Battle, P.D., Bollen, S.K., Kim, S.H., Powell, A.V. & Workman, M. (1992a). *J. Solid State Chem.* **96**, 344.

Bacher, P., Antoine, P., Marchand, R., L'Haridon, P., Laurent, Y. & Roult, G. (1988). *J. Solid State Chem.* **77**, 67.

Bartram, S.F. & Fryxell, R.E. (1970). *J. Inorg. Nucl. Chem.* **32**, 3701.

Battle, P.D. & Jones, C.W. (1989). *J. Solid State Chem.* **78**, 108.

Battle, P.D. & Macklin, W.J. (1984). *J. Solid State Chem.* **52**, 138.

Battle, P.D. (1981). *Mater. Res. Bull.* **16**, 397.

Battle, P.D., Gibb, T.C. & Lightfoot, P. (1990). *J. Solid State Chem.* **84**, 271.

Battle, P.D., Gibb, T.C., Herod, A.J. & Hodges, J.P. (1995). *J. Mater. Chem.*, **5**(1), 75.

Battle, P.D., Goodenough, J.B. & Price, R. (1983). *J. Solid State Chem.*, **46**, 234.

Battle, P.D., Jones, C.W. & Studer, F. (1991). *J. Solid State Chem.*, **90**, 302.

Bayer, G. (1969). *Fortschr. Miner.* **46**, 42.

Bell, R.O. (1968). *J. Phys. Chem. Solids*, **29**, 1.

Benner, G. & Hoppe, R. (1990). *J. Fluorine Chem.* **46** 283.

Bensch, W., Schmalle, H.W. & Reller, A. (1990). *Solid State Ionics* **43**, 171.

Berak, J.M. & Sienko, M.J. (1970). *J. Solid State Chem.* **2**, 109.

Bernier, J.-C., Chauvel, C. & Kahn, O. (1974). *J. Solid State Chem.* **11**, 265.

Bidaux, R. & Mériel, P. (1968). *J. Phys. Radium* **29**, 220.

Bihan, R.L. & Vacherand (1970). *J. Phys. Soc. Jpn.* **28**, 159.

Biosym (1993). Insight II, ver. 2.3.5. Crystal structure analysis software. San Diego: Biosym Technologies.

Blasse, G. (1964). *J. Inorg. Nucl. Chem.* (1964). **26**, 1191.

Blasse, G. (1965). *J. Inorg. Nucl. Chem.* **27**, 993.

Bochu, B., Deschizeaux, N.N., Joubert, J.C., Collomb, A., Chenevas, J. & Marezio, M. (1979). *J.Solid State Chem.* **29**, 291.

Bouloux, J.-C. & Galy, J. (1976). *J. Solid State Chem.* **16**, 385.

Brandle, C.D. & Fratello, V.J. (1990). *J. Mater. Res.*, **5**, 2160.

Brese, N.E. & O'Keeffe, M. (1991). *Acta Cryst.* B**47**, 192.

Briceño, G., Chang, H., Sun, X., Schultz, P.G. & Xiang, X.-D. (1995). *Science* **270**, 273.

Brixner, L.H. (1960). *J. Inorg. Nucl. Chem.* **14**, 225.

Brochu, R., Padiou, J. & Grandjean, D. (1970). *C.R. Acad. Sci. Ser. C* **271**, 642.

Brown I. D. (1978). *Chem. Soc. Rev.* **7**, 359.

Brown, I.D. (1981). *Structure and Bonding in Crystals,* Vol. 2, edited by M. O'Keeffe & A. Navrotsky, pp. 1-30. New York: Academic Press.

Brynestad, J., Yakel, H.L. & Smith, G.P. (1966). *J. Chem. Phys.* **45**, 4652.

Burbank, R.D. (1970). *J. Appl. Cryst.* **3**, 112.

Burdett, J.K. & Mitchell, J.F. (1993). *Chem. Mater.* **5**, 1465.

Burdett, J.K. (1980). *Molecular Shapes*, Chapter 2. New York: John Wiley & Sons.

Burns, G. & Glazer, A.M. (1990). *Space Groups for Solid State Scientists*, 2nd ed., Appendix A9-6 Boston: Academic Press.

Bush, T.S. Catlow, C.R.A., Chadwick, A.V., Cole, M. Geatches, R.M., Greaves, G.N. Tomlinson, S.M. (1992). *J. Mater. Chem.* **2**, 309.

Bush, T.S., Gale, J.D., Catlow, R.A. & Battle, P.D. (1994). *J. Mater. Chem.* **4**, 831.

Buttner, R.H. & Maslen, E.N. (1988). *Acta Cryst.* C**44**, 1707.

Chenevas, J., Joubert, J.C., Marezio, M. & Bochu, B. (1975). *J. Solid State Chem.* **14**, 25.

Choisnet, J., Rulmont, A. & Tarte, P. (1989). *J. Solid State Chem.* **82**, 272.

Choy, J.-H., Park, J.-H., Hong, S.-T., Kim, D.K. (1994). *J. Solid State Chem.*, **111**, 370.

Christoph, C.G., Larson, A.C., Eller, P.G., Purson, J.D., Zahrt, J.D., Penneman, R.A. & Rinehart, G.H. (1988). *Acta Cryst.* B**44**, 575.

Clearfield, A. (1963). *Acta Cryst.* **16**, 135.

Collomb, A., Samaras, D., Buevoz, J.L., Levy, J.P. & Joubert, J.C. (1983). *J. Magn. Magn. Mater.* **40**, 75.

Cox, D.E. & Sleight, A.W. (1979). *Acta Cryst.*, **B35**, 1.

Cox, D.E. (1992). *Syncrotron Radiation Crystallography*, ed. P. Coppens, Academic Press, London, pp. 186.

Cox, D.E., Shirane, G. & Frazer, B.C. (1967). *J. Appl. Phys.* **38**, 1459.

Cox, P.A. (1991). *The Electronic Structure and Chemistry of Solids,* Oxford University Press, Oxford.

Currie, R.C., Vente, J.F., Frikkee, E. & IJdo, D.J.W. (1995). *J. Solid State Chem.*, **116**, 199.

Daleveld, E.W., Bruntich, D.J., Dotman, J.P. & Blasse, G. (1973). *J. Inorg. Nucl. Chem.*, **35**, 3928.

Dann, S.E., Currie, D.B., Weller, M.T., Thomas, M.F. & Al Rawwas, A.D. (1994). *J. Solid State Chem.* **109**, 134.

Darlington, C.N.W. (1971). Thesis, Univ. of Cambridge.

Darriet, J., Bontchev, R., Dussarrat, C., Weill, F. & Darriet, B. (1993). *Eur. J. Solid State Chem.* **30**, 273.

Deblieck, R. (1986). *Acta Cryst.* A**42**, 318.

Deblieck, R., Van Tendeloo, G., Van Landyt, J. & Amelinckx, S. (1985). *Acta Cryst.* B**41**, 319.

Demazeau, G., Parent, C., Pouchard, M. & Hagenmueller, P. (1972). *Mater. Res. Bull.* **7**, 913.

deRango, C., Tsoucaris, G. & Zelwer, C. (1966). *Acta Cryst.* **20**, 590.

Derighetti, B., Drumheller, J.E., Laves, F., Müller, K.A. & Waldner, F. (1965). *Acta Cryst.* **18**, 557.

Deschizeaux, M.N., Joubert, J.C., Vegas, A., Collomb, A., Chenevas, J. & Marezio, M. (1976). *J. Solid State Chem.* **19**, 45.

Dickens, P.G. & Powell, A.V. (1991). *J. Mater. Chem.* **1**, 137.

Diehl, R. & Brandt, G. (1975). *Mater. Res. Bull.* **10**, 85.

Diehl, R. Brandt, G. & Salje, E. (1978). *Acta Cryst.* B**34**, 1105.

Elemans, J.B.A., van Laar, B, van der Veen, K.R. & Loopstra, B.O. (1971). *J. Solid State Chem.* **3**, 238.

Ferretti, A., Rogers, D.B. & Goodenough, J.B. (1965). *J. Phys. Chem. Solids* **26**, 2007.

Fesenko, E.G., Filip'ev, V.S. & Kupriyanov, M.F. (1964). *Izv. Akad. Nauk SSSR, Ser. Fiz.*, **28**, 669.

Fesenko, E.G., Razumovskaya, O.N., Shuvaeva, V.A., Gridneva, G.G. & Bunina, O.A. (1991). *Isv. Akad. Nauk SSSR, Neorg. Mater.* **27**, 1991.

Filip'ev, V.S. & Fesenko, E.G. (1965). *Sov. Phys. Crystallogr.*, **10**(3), 243.

Filip'ev, V.S. & Fesenko, E.G. (1966). *Sov. Phys. Crystallogr.*, **10**(5), 532.

Filip'ev, V.S., Shatalova, G.E. & Fesenko, E.G. (1974). *Kristalographiya* **19**, 236.

Flocken, J.W., Guenther, R.A., Hardy, J.R. & Boyer, L.L. (1986). *Phys. Rev. Lett.* **56**, 1738.

Flocken, J.W., Guenther, R.A., Hardy, J.R. & Boyer, L.L. (1986). *Phys. Rev. B Cond. Matter* **56**, 1738.

Fontcuberta, J., Martinez, B., Seffar, A., Piñol, S., Garcia-Munoz, J.L. & Obradors, X. (1996). *Phys. Rev. Lett.* **76**, 1122.

Forquet, J.E., Renou, M.F., De Pape, R., Theveneau, H., Man, P.P., Lucas, O. & Pannetier, J. (1983). *Solid State Ionics* **9**, 1011.

Galasso, F. & Darby, W. (1962). *J. Phys. Chem.* **66**, 131.

Galasso, F.S. (1969). *"Structure, Properties, and Preparation of Perovskite Type Compounds"*, Pergammon Press, Oxford.

Galasso, F.S., Layden, G.K. & Flinchbaugh, D.E. (1966). *J. Chem. Phys.*, **44**(7), 2703.

Gale, J.D. (1992-1994). GULP. General Utility Lattice Program. Royal Institution and Imperial College, London.

Geguzina, G.A., Fesenko, E.G. & Devlikanova, R.U. (1976). *Sov. Phys. Crystallogr.* **20**(4), 518.

Gehlig, R. & Salje, E. (1983). *Phil. Mag.* B**47**, 229.

Geller, S. & Wood, E.A. (1956). *Acta Cryst.* **9**, 563.

Glazer, A. M. (1972). *Acta Cryst.* B**28**, 3385.

Glazer, A.M. & Megaw, H. (1972). *Phil. Mag.* **25**, 1119.

Goldschmidt, V.M. (1926). *Naturwissenschaften* **14**, 477.

Goodenough, J.B. & Kafalas, J.A. (1972). *J. Solid State Chem.* **6**, 493.

Goodenough, J.B. & Longo, J.M. (1970). *Landolt-Börnstein* **4**, 126.

Goodenough, J.B. (1963). *"Magnetism and the Chemical Bond,"* New York, Interscience and Wiley.

Goodenough, J.B. (1967). *Phys. Rev.* **164**, 785.

Goodenough, J.B. (1971) *Prog. Solid State Chem.* **5**, 145.

Greedan, J.E., Willmer, K.L. & Gibbs, H.F. (1992). *Eur. J. Solid State Chem.* **29**, 505.

Groen, W.A., & IJdo, D.J.W. (1987). *Acta Cryst.* C**43**, 1033.

Groen, W.A., van Berkel, F.P.F. & IJdo, D.J.W. (1986). *Acta Cryst.* C**42**, 1472.

Hägg, G. (1935). *Z. Phys. Chem.* B**29**, 192.

Hahn, T. Ed. (1983). *International Tables for Crystallography, Vol. A*, Reidel Pub. Co., Boston.

Hamilton, W.C. (1965). *Acta Cryst.* **18**, 502.

Harrison, W.T.A., Reis, K.P., Jacobson, A.J., Schneemeyer, L.F. & Waszczak, J.V. (1995). *Chem. Mater.* **7**, 2161.

Hemley, R.J., Cohen, R.E., Yeganeh-Haeri, A., Mao, H.K., Weidner, D.J. & Ito, E. (1989). *Geophysical Monographs, Vol. 45 (Perovskite - A Structure of Great Interest to Geophysics and Materials Science)*, ed. by A. Navrotsky & D. Weidner, pp. 35-44. Washington D.C.:American Geophysical Union.

Hepworth, M.A., Jack, K.H., Peacock, R.D. & Westland, G.J. (1957). *Acta Cryst.* **10**, 63.

Hoffmann, R. (1963). *J. Chem. Phys.* **39**, 1397.

Hoffmann, R. (1988). *Solids and Surfaces: A Chemist's View of Bonding in Extended Structures*, VCH Publishers, New York.

Hohnstedt, C. & Meyer, G. (1993). *A. Anorg. Allg. Chem.* **619**, 1374.

Hong, S.-T. (1994). Ph.D. Thesis, Seoul National Univ.

Hönle, W. & Simon, A. (1986). *Z. Naturf. B. Anorg. Chem. Organ. Chem.* **41**, 1391.

Hönle, W., Miller, G. & Simon, A. (1988). *J. Solid State Chem.* **75**, 147.

Horowitz, A., Amit, M., Makovsky, Ben Dor, L. & Kalman, Z.H. (1982). *J. Solid State Chem.* **43**, 107.

Huang, T.C. Parrish, W., Toraya, H., Lacorre, P. & Torrance, J.B. (1990). *Mater. Res. Bull.* **25**, 1091.

Hwang, H.Y., Cheong, S-W., Radaelli, P.G., Marezio, M. & Batlogg, B. (1995). *Phys. Rev. Lett.* **75**, 914.

Hwang, H.Y., Palstra, T.T.M., Cheong, S.-W. & Batlogg, B. (1995b). *Phys. Rev.* **52**, 15046.

Hyde, B.G. & Andersson, S. (1988). *Inorganic Crystal Structures*, Chapter XI. New York: Wiley Interscience.

Ibers, J.A. & Hamilton, W.C. (1974). *International Tables for Crystallography, Vol. IV*, Kynoch Press, Birmingham, U.K.

Izumi, F. (1989). *Rigaku J.*, **6**, 10.

Izumi, F. (1993). *The Rietveld Method*, ed. R.A. Young, Oxford University Press, Oxford, Ch. 13.

Jacobson, A.J., Tofield, B.C. & Fender, B.E.F. (1972). *Acta Cryst.* B**28**, 956.

Jin, S., McCormack, M., Tiefel, T.H. & Ramesh, R. (1994). *J. Appl. Phys.* **76**, 6929.

Jirak, Z., Pollert, E., Andersen, A.F., Grenier, J.-C. & Hagenmuller, P. (1990). *Eur. J. Solid State Inorg. Chem.* **27**, 421.

Johnson, C.K. (1976). *ORTEP-II.* Report ORNL-5138, Oak Ridge National Laboratory, TN.

Jones, C.W., Battle, P.D., Lightfoot, P. & Harrison, W.T.A. (1989). *Acta Cryst.* C**45**, 365.

Jung, D.-Y. & Demazeau, G. (1995). *J. Solid State Chem.*, **115**, 447.

Kamata, K., Nakamura, T. & Sata, T. (1975). *Chem. Lett.* **1**, 81.

Kawashima, S., Nishida, M., Ueda, I. & Ouchi, H. (1983). *J. Am. Ceram. Soc.*, **66**(6), 421.

Kehl W. L, Hay R G. and Wahl D. (1952). *J. Appl. Phys.* **23**, 212.

Keller, H.L., Meier, K.H., Müller-Buschbaum, H. (1975). *Z. Naturf.* **30**, 277-278.

Khattak, C.P. & Cox, D.E. (1977). *Mater. Res. Bull.* **12**, 463-472.

Khattak, C.P., Cox, D.E. & Wang, F.F.Y. (1975). *J. Solid State Chem.* **13**, 77-83 (1975).

Kijima, N., Tanaka, K. & Marumo, F. (1981). *Acta Cryst.* B**37**, 545.

Kijima, N., Tanaka, K. & Marumo, F. (1983). *Acta Cryst.* B**39**, 557.

Kim, S.H. & Battle, P.D. (1995). *J. Solid State Chem.*, **114**, 174.

King, G., Goo, E., Yamamoto, T. & Okazaki, K. (1988). *J. Amer. Cer. Soc.*, **71**(6), 454.

Knochenmuss, F., Reber, C., Rajasekharan, M.V. & Güdel, H.U. (1986). *J. Chem. Phys.* **85**, 4280.

Koehl, P., Schultze-Rhonhof & Reinen, D. (1970). *Z. Anorg. Allg. Chem.* **378**, 129.

Köhl, V.P. (1973). *Z. Anorg. Allg. Chemie,* **401**, 121.

Kohn, K., Inoue, K., Horie, O. & Akimoto, S.-I. (1976). *J. Solid State Chem.* **18**, 27.

Koopmanns, H.J.A., van de Velde, G.M.H., & Gellings, P.J. (1983). *Acta Cryst.* C**39**, 1323.

Kupriyanov, M.F. & Filip'ev, V.S. (1963). *Sov. Phys. Crystallogr.*, **8**(3), 278.

Kuwata, J., Fujita, Y., Matsuoka, T., Tohda, T., Nishikawa, M. & Abe, A. (1984). *Proc. of the SID*, **25**(3), 177.

Labeau, M., Bochu, B., Joubert, J.C. & Chenevas, J. (1980). *J. Solid State Chem.* **33**, 257.

Lacorre, P., Torrance, J.B., Pannetier, J. Nazzal, A.I., Wang, P.W. & Huang, T.C. (1991). *J. Solid State Chem.* **91**, 225.

Larson, A.C. & Von Dreele, R.B. (1994). *LANSCE*, Los Alamos National Laboratory, Los Alamos, NM.

LeBail, A., Duroy, H. & Forquet, J.L. (1988). *Math. Res. Bull.* **23**, 447.

Lefkowitz, I., Dowell, & M.B. Shields, M.A. (1975). *J. Solid State Chem.* **15**, 24.

Leinenweber, K. & Parise, J. (1995). *J. Solid State Chem.* **114**, 277.

Leinenweber, K. (1996). *Personal Communication.*

Lenz, A., Mueller-Buschbaum, H. (1990). *J. Less Common Metals*, **161**, 141.

Liu, G., Zhao, X. & Eick, H.A. (1992). *J. Alloys Comp.* **187**, 145.

Loopstra, B.O. & Rietveld, H.M. (1969). *Acta Cryst.* B**25**, 1420.

Lopez, M.L., Alvarez, I., Gaitan, M., Jerez, A., Pico, C. & Veiga, M.L. (1993b). *Solid State Ionics* **63**, 599.

Lopez, M.L., Jerez, A., Pico, C., Saez-Puche, R. & Veiga, M.L. (1993a). *J. Solid State Chem.* **105**, 19.

Lopez, M.L., Veiga, M.L., Rodriguez-Carvajal, J., Fernandez, F., Jerez, A. & Pico, C. (1992). *Mater. Res. Bull.* **27**, 647.

Luetgert, B. & Babel, D. (1992). *Z. Anorg. Allg. Chemie* **616,** 133.

Mackrodt, W.C. (1984). *Solid State Ionics* **12**, 175.

MacLean, D.A., Ng, H.-K. & Greedan, J.E. (1979). *J. Solid State Chem.* **30**, 35.

Marezio, M., Dernier, P.D. & Remeika J.P. (1972). *J. Solid State Chem.* **4**, 11.

Marezio, M., Dernier, P.D., Chenevas, J. & Joubert, J.C. (1973). *J. Solid State Chem.* **6**, 16.

Marezio, M., Remeika, J.P. & Dernier, P.D. (1970). *Acta Cryst.* B**26**, 2008.

Marx, D.T., Radaelli, P.G., Jorgensen, J.D., Hitterman, R.L., Hinks, D.G., Pei, S. & Dabrowski, B. (1992). *Phys. Rev. B Cond. Matter* **46**, 1144.

Matthias, B.T. & Wood, E.A. (1951). *Phys. Rev.* **84**, 1255.

Megaw, H.D. & Darlington, C.N.W. (1975). *Acta Cryst.* A**31**, 161.

Megaw, H.D. (1968). *Acta Cryst.* A**24**, 583.

Menyuk N., Dwight, K. & Raccah, P.M. (1967). *J. Phys. Chem. Solids* **28**, 549.

Messer, C.E., Eastman, J.C., Mers, R.G. & Maeland, J.A. (1964) *Inorg. Chem.* **3**, 776.

Michel, C., Moreau, J.-M., Achenbach, G., Gerson, R. & James, W.J. (1969). *Solid State Commun.* **7**, 701.

Miller, G. (1990). NEW5. Extended Hückel band structure calculation program. Iowa State University.

Minkiewicz, V.J., Fujii, Y. & Yamada, Y. (1970). *J. Phys. Soc. Japan* **28**, 443.

Miyata, N., Tanaka, K. & Marumo, F. (1983). *Acta Cryst.* B**39**, 561.

Morin, F.J. (1961). *J. Appl. Phys.* **32**, 2195.

Müller, J., Haouzi, A., Laviron, C., Labeau, M. & Joubert, J.C. (1986). *Mater, Res. Bull.* **21**, 1131.

Nakagawa, T. & Nomura, S. (1966). *Japan J.Appl. Phys.*, **5**(7), 578.

Nakamura, T. & Sata, T. (1971). *J. Phys. Soc. Japan*, **30**, 1501.

Navrotsky, A. & Weidner, D.J. (1989). *"Perovskite: A Structure of Great Interest to Geophysics and Materials Science"*, Am. Geopysical Union (Geopysical Monograph #45), Wahington D.C., pp. xi.

Navrotsky, A. (1989). *Geophysical Monographs, Vol. 45 (Perovskite - A Structure of Great Interest to Geophysics and Materials Science)*, edited by A. Navrotsky & D. Weidner, pp. 67-69. Washington D.C.:American Geophysical Union.

Newnham, R.E. (1989). *"Perovskite: A Structure of Great Interest to Geophysics and Materials Science"*, Am. Geopysical Union (Geopysical Monograph #45), Wahington D.C., pp. 91.

Noël, H., Padiou, J. & Prigent (1975). *C.R. Acad.Sci. Ser. C* **280**, 123.

Nomura, S. & Nakagawa, T. (1971). *J. Phys. Soc. Japan*, **30**(2), 491.

Nowotny, H. & Ettmayer, P. (1969). *J. Inst. Met.* **97**, 180.

Odenthal, R.H. & Hoppe, R. (1971). *Monatsh. Chem.* **102**, 1340.

Okazaki, A. & Suemune, Y. (1961). *J. Phys. Soc. Jpn.* **16**, 176.

O'Keeffe, M. (1989). *Struct. Bonding (Berlin)*, **71**, 162.

O'Keeffe, M. (1992). Eutax. Program for calculating bond valences. EMLab Software, Phoenix, Arizona.

O'Keeffe, M. & Hyde, B.G. (1977). *Acta Cryst.* B**33**, 3802.

Ozaki, Y., Ghedira, M., Chenevas, J., Joubert, J.C. & Marezio, M. (1977) *Acta Cryst.* B**33**, 3615.

Parise, J.B., McCarron III, E.U. & Sleight, A.W. (1987). *Mater. Res. Bull.* **22**, 803.

Patrat, G., Brunel, M. & deBergevin, F. (1976). *J. Phys. Chem. Solids* **37**, 285.

Pauling, L. (1929). *J. Am. Chem. Soc.* **51**, 1010.

Perri J. A., Banks E. and Post B. (1957). *J. Appl. Phys.* **28**, 1272.

Poeppelmeier, K.R., Leonowicz, M.E., Scanlon, J.C., Longo, J.M. & Yelon, W.B. (1982). *J. Solid State Chem.* **45**, 71.

Powell, A.V., Gore, J.G. & Battle, P.D. (1993). *J. Alloys Comp.*, **201**, 73.

Quezel-Ambrunaz, S. (1968). *Bull. Soc. Franc. Minér. Crist.* **91**, 339.

Randall, C.A., Bhalla, A.S., Shrout, T.R. & Cross, L.E. (1990). *J. Mater. Res.*, **5**(4), 829.

Rao, C.N.R. & Rao, B.V.S. (1974). *Natl. Stand. Ref. Data Ser. Natl. Bur. Stand.* **49**, 117.

Reinen, C. & Weitzel, H. (1976). *Z. Anorg. Allg. Chem.* **424**, 31.

Reis, K.P. Jacobson, A.J. & Kulik, J. (1993). *Chem. Mater.*, **5**, 1070.

Reis, K.P., Jacobson, A.J. & Nicol, J.M. (1993). *J. Solid State Chem.* **107**, 428.

Rey, M.J., Dehaudt, P.H., Joubert, J.C., Lambert-Andron, B., Cyrot, M. & Cyrot-Lackmann, F. (1990). *J. Solid State Chem.* **86**, 101.

Rietveld, H.M. (1966). *Acta Cryst.* **22**, 151.

Ritter, H., Ihringer, J., Maichle, J.K., Prandl, W., Hoser, A. & Hewat, A.W. (1989). *Z. Physik* **B75**, 297.

Rodier, N. & Laruelle, P. (1970). *C.R. Acad. Sci.* **270**, 2127.

Rodier, N., Julien, R. & Tien, V. (1983). *Acta Cryst.* C**39**, 670.

Rosen, C., Banks, E. & Post, B. (1957). *Acta Cryst.* **9**, 475.

Roth, R.S. & Waring, J.L. (1966). *J. Res. Natl. Bur. Stand. (U.S.)* **70A** (Phys. and Chem.), 281.

Roth, R.S. (1957). *J. Research N.B.S.* **58**, 75.

Saiki, A., Seto, Y., Seki, H., Ishizawa, N., Kato, M. & Mizutani, N. (1991). *J. Chem. Soc. Japan* (1), 25.

Sakuma, H. Hashizume, H. & Yamanaka, A. (1990). *Acta Cryst.* B**46**, 693.

Salje, E. & Viswanathan, K. (1975). *Acta Cryst.* A**31**, 356.

Salje, E. (1974). *J. Appl. Cryst.* **7**, 615.

Salje, E. (1976). *Ferroelectrics*, **12**, 215.

Salje, E. (1977). *Acta Cryst.* B**33**, 547.

Salje, E. (1995). *Polarons and Bipolarons in High T_c Superconductors and Related Materials*, ed. E.K.H. Salje, A.S. Alexandrov, L.Y. Liang, Cambridge University Press, Cambridge, pp. 110.

Sasaki, S. Prewitt, C.T. & Liebermann, R.C. (1983). *Am. Miner.* **68**, 1189.

Sasaki, S., Prewitt, C.T., Bass, J.D. & Schulze, W.A. (1987). *Acta Cryst.* C**43**, 1668.

Sato, M., Jin, T., Hama, Y. & Uematsu, K. (1993). *J. Mater. Chem.* **3**, 325.

Sawada, S. (1956). *J. Phys. Soc. Jpn.* **11**, 1237.

Scott, H.G. (1983). *J. Appl. Cryst.* **16**, 159.

Seinen, P.A., van Berkel, F.P.F., Groen, W.A. & IJdo, D.J.W. (1987). *Mater. Res. Bull.* **22**, 535.

Setter, N. & Cross, L.E. (1980). *J. Appl. Phys.*, **51**(8), 4356.

Shannon, R.D. (1976). *Acta Cryst.* A**32**, 751.

Shimizu, Y., Syono, Y. & Akimoto, S. (1970). *High Temp. High Press.* **2**, 113.

Shirane, G., Danner, H. & Pepinski, R. (1957). *Phys. Rev.,* **105**(3), 856.

Shuvaeva, E.T. & Fesenko, E.G. (1970). *Sov. Phys. Crystallography*, **14**(6), 926.

Sleight, A.W. & Prewitt, C.T. (1973). *J. Solid State Chem.* **6**, 509.

Sleight, A.W. (1964). Thesis--*Disertation Abstracts,* **24**, 64-3565, U. Connecticut--1963.

Sleight, A.W. Gillson, J.L. & Bierstedt, P.E. (1975). *Solid State Commun.*, **17**, 27.

Sleight, A.W., Ward, R. (1962). *Inorg. Chem*, **1**(4), 790.

Smith, A.J. & Welch, A.J.E. (1960). *Acta Cryst.* **13**, 653.

Smolenski, G.A. (1970). *J. Phys. Soc. Jpn. (Suppl.)*, **28**, 26.

Subramanian, M.A., Toby, B.H., Ramirez, A.P., Marshall, W.J., Sleight, A.W. & Kwei, G.H. (1996). *Science* **273**, 81.

Subramanian, M.A., Ganguli, A.K., Willmer, K.L. & Greedan, J.E. (1991). *J. Solid State Chem.* **95**, 447.

Svensson, C. & Stahl, K. (1988). *J. Solid State Chem.* **77**, 112.

Svensson, G. & Werner, P.-E. (1990). *Mater. Res. Bull.* **25**, 9.

Takano, M. Nasu, S., Abe, T., Yamamoto, K. Endo, S. Takeda, Y. & Goodenough, J.B. (1991) *Phys. Rev. Lett.* **67**, 3267.

Takano, M., Okita, T., Nakayama, N. Bando, Y., Takeda, Y., Yamamoto, O. & Goodenough, J.B. (1988). *J. Solid State Chem.* **73**, 140.

Tanisaki S. (1960). *J. Phys. Soc. Jpn.* **15**, 573.

Thomas, N.W. & Beitollahi, A. (1994). *Acta Cryst.* B**50**, 549.

Thomas, N.W. (1989). *Acta Cryst.* B**45**, 337.

Thomas, N.W. (1996). *Acta Cryst.* B**52**, 16.

Thompson R, Cox D. E. and Hastings J. B. (1987). *J. Appl. Crystallogr.* **20**, 79.

Thornton, G. & Jacobson, A.J. (1976). *Mater. Res. Bull.* **11**, 837.

Thornton, G. & Jacobson, A.J. (1978). *Acta Cryst.*, **B34**, 351.

Thornton, G., Tofield, B.C. & Hewat, A.W. (1986). *J. Solid State Chem.* **61**, 301.

Tornero, J.D., Cano, F.H., Fayos, J. & Martinez-Ripoll, M. (1978). *Ferroelectrics* **19**, 123.

Trunov, V.K., Sirotinkin, V.P. & Evdokimov, A.A. (1983). *Russ. J. Inorg. Chem.*, **28**(3), 349.

Unoki, J. & Sakudo, T. (1967). *J. Phys. Soc. Japan* **23**, 546.

Vallet-Regi, M., Garcia, E. & Gonzales-Calbet, J.M. (1988). *J. Chem. Soc. Dalton Trans.*, **3**, 775.

van Duivenboden, J.C. & IJdo, D.J.W. (1986). *Acta Cryst.*, **C42**, 523.

Vegas, A., Vallet-Regi, M., Gonzales-Calbet, J.M. & Alario-Franco, M.A. (1986). *Acta Cryst.* B**42**, 167.

Wang, Q., Gu, B. & Zhang, S. (1990). *J. Phys.:Condens. Matter*, **2**, 9815.

Wang, Y., Lu, X., Gao, G.D., Lieberman, R.C. & Dudley, M. (1991). *Mater. Sci. Eng.* A**132**, 13.

Whangbo, M.-H. & Hoffmann, R. (1978). *J. Am. Chem. Soc.* **100**, 6093.

Whangbo, M-H., Evain, M., Canadell, E. & Ganne, M. (1989). *Inorg. Chem.* **28**, 267.

Wiseman, P.J. & Dickens, P. (1973). *J. Solid State Chem.* **3**, 374.

Wittman, V.U., Rauser, G. & Kemmler-Sack, S. (1981). *A. Anorg. Allg. Chem.* **482**, 143.

Woodward, P.M. (1996). Masters Thesis, Oregon State University.

Woodward, P.M., Hoffmann, R.-D. & Sleight, A.W. (1994). *J. Mater. Res.* **8**, 2118.

Woodward, P.M., Sleight, A.W. & Vogt, T. (1995). *J. Phys. Chem. Solids* **56**, 1305.

Yamada, K., Funabiki, S., Horimoto, H., Matsui, T., Okuda, T. & Ichiba, S. (1991). *Chem. Lett.* 801.

Young, R.A. (Ed.) (1993). *The Rietveld Method*, IUCr Monographs on Crystallography, **5**, Oxford University Press, Oxford, pp. 1-38.

Young, R.A., Prince, E. & Sparks, R. (1982). *J. Appl. Cryst.* **15**, 430.

Yvon, K., Jeitschko, W. & Parthe, E. (1977). LAZY PULVERIX: A computer program for calculating X-ray and neutron diffraction powder patterns. *J. Appl. Cryst.* **10**, 73.

Zhao, C., Feng, S. Zhicheng, C., Shi, C. Xu, R. & Ni, J. (1996). *Chem. Commun.* 1641.

Zubkov, V.G., Berger, I.F., Pesina, Z.M., Bazuev, G.V. & Shveikin, G.P. (1986). *Sov. Phys. Dokl.* **31**, 459.

Zunger, A. (1980). *Phys. Rev. B* **23**, 5839.

Zunic, T.B. & Vickovic, I. (1996). *J. Appl. Cryst.* **29**, 305.

APPENDICES

Appendix 1

Crystallographic Descriptions of the Perovskite Structure in All 23 Glazer Tilt Systems

A practical difficulty of working with distorted perovskites is the widespread use of nonstandard cell settings. These types of descriptions are useful when comparing two different structures, but can be confusing when many different compounds and space groups are examined. Transforming to a standard setting, which is necessary when using many software packages, can sometimes be confusing, time consuming and lead to possible errors. Adding to the confusion is the fact that among the space groups corresponding to the different tilt systems there are several different choices of origin and unit cell size. In the course of this analysis, using POTATO, the standard space group description of each tilt system was determined. These descriptions are given in table A1.1 for simple perovskites and in table A1.2 for ordered perovskites. One note of caution: both the $a^0b^-c^-$ (#19) tilt system among simple perovskites and the $a^0b^-b^-$ (#20) tilt system for ordered perovskites belong to the I2/m space group, but the atomic positions are different for the two tilt systems. Hopefully, this information will be of practical assistance to others working with distorted perovskite structures.

Table A1.1 : Atomic positions and unit cell descriptions for all of the space groups generated by simple tilting of the MO_6 octahedra. The number immediately below the space group name is the space group number in volume A of the *International Tables for Crystallography* (Hahn, 1983). All of the space group descriptions are standard settings. The other number in the first column signifies the tilt systems corresponding to each space group.

Table A1.2 : Atomic positions and unit cell descriptions for all of the space groups generated by tilting of the octahedra in combination with 1:1 cation ordering. The number immediately below the space group name is the space group number in volume A of the *International Tables for Crystallography* (Hahn, 1983). All of the space group descriptions are standard settings. The other number in the first column signifies the tilt systems corresponding to each space group. Note that the ordered tilt system #20 and simple tilt system #19 both are assigned to space group I2/m, but the choice of origin and atomic positions are different for the two structures.

Space Group	Unit Cell Size	Cation Positions	Anion Positions	Comments
Immm *(A-71)* Tilt Systems 1,2 & 15	$a \cong 2a_p$ $b \cong 2a_p$ $c \cong 2a_p$	*A Cation* (2a) 0,0,0 (2b) 0,½,½ (2c) ½,½,0 (2d) ½,0,½ *M Cation* (8k) ¼,¼,¼	(8l) 0,y,z y≅¼,z≅¼ (8m) x,0,z x≅¼,z≅¼ (8n) x,y,0 x≅¼,y≅¼	Origin Choice 2 Shift by ¼,¼,¼
$Im\bar{3}$ *(A-204)* Tilt System 3	$a \cong 2a_p$ $b \cong 2a_p$ $c \cong 2a_p$	*A Cation* (2a) 0,0,0 (6b) 0,½,½ *M Cation* (8c) ¼,¼,¼	(24g) 0,y,z y≅¼,z≅¼	Origin Choice 2 Shift by ¼,¼,¼
Pmmn *(A-59-2)* Tilt Systems 4 & 6	$a \cong 2a_p$ $b \cong 2a_p$ $c \cong 2a_p$	*A Cation* (2a) ¼,¼,z z≅¼ (2a) ¼,¼,z z≅¾ (2b) ¼,¾,z z≅¼ (2b) ¼,¾,z z≅¾ *M Cation* (4c) 0,0,0 (4d) ½,½,½	(4e) ¼,y,z y≅0,z≅0 (4e) ¼,y,z y≅0,z≅½ (4f) x,¼,z y≅0,z≅0 (4f) x,¼,z y≅0,z≅½ (8g) x,y,z x≅0,y≅0,z≅¼	Origin Choice 1 No origin shift Out of phase tilting about the c axis.
$P4_2/nmc$ *(A-137-2)* Tilt Systems 5 & 7	$a \cong 2a_p$ $b \cong 2a_p$ $c \cong 2a_p$	*A Cation* (2a) ¾,¼,¾ (2b) ¾,¼,¼ (4d) ¼,¼,z z≅¼ *M Cation* (8e) 0,0,0	(8g) ¼,y,z y≅0,z≅0 (8g) ¼,y,z y≅½,z≅½ (8f) x,-x,¼ x≅½	Origin Choice 1 No origin shift Out of phase tilting about the c axis.
$P2_1/m$ *(A-11-1)* Tilt Systems 8 & 9	$a \cong \sqrt{2}a_p$ $b \cong 2a_p$ $c \cong \sqrt{2}a_p$ $\beta \neq 90°$	A Cation (2e) x,¼,z x≅0,z≅0 (2e) x,¼,z x≅½,z≅½ M Cation (2b) ½,0,0 (2c) 0,0,½	(2e) x,¼,z x≅0,z≅½ (2e) x,¼,z x≅½,z≅0 (4f) x,y,z x≅¼,y≅0,z≅¼ (4f) x,y,z x≅¼,y≅0,z≅¾	Origin Choice B In phase tilting about the b axis
Pnma *(A-62)* Tilt Systems 10 & 11	$a \cong \sqrt{2}a_p$ $b \cong 2a_p$ $c \cong \sqrt{2}a_p$ $\beta \neq 90°$	A Cation (4c) x,¼,z x≅0,z≅0 M Cation (4b) ½,0,0	(4c) x,¼,z x≅0,z≅½ (8d) x,y,z x≅¼,y≅0,z≅¼	Origin Choice B In phase tilting about the b axis
$F\bar{1}$ *(A-2)* Tilt System 12	$a \cong 2ap$ $b \cong 2ap$ $c \cong 2a_p$ $\alpha \neq \beta \neq \gamma \neq 90°$	*A Cation* (8i) x,y,z x≅¼,y≅¼,z≅¼ *M Cation* (4a) 0,0,0 (4b) 0,0,½	(8i) x,y,z x≅¼,y≅0,z≅0 (8i) x,y,z x≅0,y≅¼,z≅0 (8i) x,y,z x≅0,y≅0,z≅¼	Origin Choice 1 The standard setting is $P\bar{1}$, add face centered generators for $F\bar{1}$
I2/a *(A-15-3)* Tilt System 13	$a \cong 2a_p$ $b \cong \sqrt{2}a_p$ $c \cong \sqrt{2}a_p$ $\beta \neq 90°$	*A Cation* (4e) ¼,y,0 y≅0 *M Cation* (4b) 0,½,0	(4e) ¼,y,0 y≅½ (8f) x,y,z x≅0,y≅¼,z≅¼	Origin Choice B

Table A1.1

$R\bar{3}c$ *(A-167-2)* Tilt System 14	$a\cong\sqrt{2}a_p$ $b\cong\sqrt{2}a_p$ $c\cong\sqrt{2}a_p$ $\alpha\neq\beta\neq\gamma\cong60°$	*A Cation* (2a) ¼,¼,¼ *M Cation* (2b) 0,0,0	(6e) x,½-x,¼ x≅¾	Rhombohedral Cell
I4/mmm *(A-139)* Tilt System 16	$a\cong2a_p$ $b\cong2a_p$ $c\cong2a_p$	*A Cation* (2a) 0,0,0 (2b) 0,0,½ (4c) ½,0,0 *M Cation* (8f) ¼,¼,¼	(8h) x,x,0 x≅¼ (16n) 0,y,z y≅¼,z≅¼	Origin Choice 2 Shift by -¼,¼,¼ No tilting about the c axis
Cmcm *(A-63)* Tilt Systems 17 & 18	$a\cong2a_p$ $b\cong2a_p$ $c\cong2a_p$	*A Cation* (4c) 0,y,¼ y≅0 (4c) 0,y,¼ y≅½ *M Cation* (8d) ¼,¼,0	(8e) x,0,0 x≅¼ (8f) 0,y,z y≅¼,z≅0 (8g) x,y,¼ x≅¼,y≅¼	Origin Choice 3 Shift by ¼,-¼,0 In phase tilting about the c axis
I2/m *(A-12-3)* Tilt System 19	$a\cong\sqrt{2}a_p$ $b\cong2a_p$ $c\cong\sqrt{2}a_p$ $\beta\neq90°$	*A Cation* (4i) x,0,z x≅¼,z≅¾ *M Cation* (4e) ¼,¼,¼	(4i) x,0,z x≅¼,z≅¼ (4g) 0,y,0 y≅¼ (4h) ½,y,0 y≅¼	Origin Choice C Shift by ¼,¼,¼ No tilting about the b axis
Imma *(A-74)* Tilt System 20	$a\cong2a_p$ $b\cong\sqrt{2}a_p$ $c\cong\sqrt{2}a_p$	*A Cation* (4e) 0,¼,z z≅¾ *M Cation* (4c) ¼,¼,¼	(4e) 0,¼,z z≅¼ (8f) x,0,0 x≅¼	Origin C Shift by ¼,¼,¼ No tilting about the a axis
P4/mbm *(A-127)* Tilt System 21	$a\cong\sqrt{2}a_p$ $b\cong\sqrt{2}a_p$ $c\cong a_p$	*A Cation* (2c) 0,½,½ *M Cation* (2a) 0,0,0	(2b) 0,0,½ (4g) x,x+½,0 x≅¼	Origin Choice A No origin shift In phase tilting about the c axis
I4/mcm *(A-140)* Tilt System 22	$a\cong\sqrt{2}a_p$ $b\cong\sqrt{2}a_p$ $c\cong2a_p$	*A Cation* (4b) 0,½,¼ *M Cation* (4c) 0,0,0	(2b) 0,0,¼ (4g) x,x+½,0 x≅¼	Origin Choice A No origin shift In phase tilting about the c axis
Pm3m *(A-221)* Tilt System 23	$a=b=c=a_p$	*A Cation* (1b) ½,½,½ *M Cation* (1a) 0,0,0	(3d) ½,0,0	Origin Choice 1 No origin shift

Table A1.1 (Continued)

Space Group	Unit Cell Size	Cation Positions	Anion Positions	Comments
Pnnn *(A-48-1)* Tilt Systems 1,2, & 15	a≅2a$_p$ b≅2a$_p$ c≅2a$_p$	*A Cation* (2a) 0,0,0 (2b) 0,½,½ (2c) ½,½,0 (2d) ½,0,½ *M & M' Cations* (4e) ¼,¼,¼ (M) (4f) ¾,¾,¾ (M')	(8m) x,y,z x≅0,y≅¼,z≅¼ (8m) x,y,z x≅¼,y≅0,z≅¼ (8m) x,y,z x≅¼,y≅¼,z≅0	Origin Choice 2 Shift by ¼,¼,¼
Pn$\bar{3}$ *(A-201-1)* Tilt System 3	a≅2a$_p$ b≅2a$_p$ c≅2a$_p$	*A Cation* (2a) 0,0,0 (6d) 0,½,½ *M & M' Cations* (4b) ¼,¼,¼ (M) (4c) ¾,¾,¾ (M')	(24h) x,y,z x≅0,y≅¼,z≅¼	Origin Choice 2 Shift by ¼,¼,¼
P2/c *(A-13-5)* Tilt Systems 4 & 6	a≅2a$_p$ b≅2a$_p$ c≅2a$_p$	*A Cation* (2e) ¼,¼,z z≅¼ (2e) ¼,¼,z z≅¾ (2f) ¼,¾,z z≅¼ (2f) ¼,¾,z z≅¾ *M & M' Cations* (2a) 0,0,0 (M) (2b) ½,0,½ (M) (2c) 0,0,½ (M') (2d) ½,0,0 (M')	*6x*(4g) x,y,z x≅¼,y≅0,z≅0 x≅0,y≅¼,z≅0 x≅0,y≅0,z≅¼ x≅0,y≅¼,z≅½ x≅½,y≅0,z≅¼ x≅¼,y≅0,z≅½	Origin Choice 1 No origin shift Out of phase tilting about the c axis.
P4$_2$/n *(A-86)* Tilt Systems 5 & 7	a≅2a$_p$ b≅2a$_p$ c≅2a$_p$	*A Cation* (2a) ¼,¼,¼ (2b) ¼,¼,¾ (4e) ¾,¼,z z≅¼ *M & M' Cation* (4c) 0,0,0 (M) (4d) ½,½,½ (M')	(8g) x,y,z x≅¼,y≅0,z≅0 (8g) x,y,z x≅¼,y≅0,z≅½ (8g) x,y,z x≅0,y≅0,z≅¼	Origin Choice 1 No origin shift Out of phase tilting about the c axis.
P2$_1$/n *(A-14-2)* Tilt Systems 10 & 11	a≅√2ap b≅√2ap c≅2ap β≠90°	A Cation (4e) x,y,z x≅0,y≅0,z≅¼ *M & M' Cations* (4c) 0,½,0 (M) (4d) ½,0,0 (M')	(4e) x,y,z x≅¼,y≅¼,z≅0 (4e) x,y,z x≅¼,y≅¼,z≅½ (4e) x,y,z x≅½,y≅0,z≅¼	Origin Choice B In phase tilting about the b axis
P$\bar{1}$ *(A-2)* Tilt Systems 8 & 9 F$\bar{1}$ *(A-2)* Tilt Systems 12 & 13 I$\bar{1}$ *(A-2)* Tilt System 19	a≅2ap b≅2ap c≅2a$_p$ α≠β≠γ≠90°	*A Cation* (2i) x,y,z x≅¼,y≅¼,z≅¼ (2i) x,y,z x≅¾,y≅¼,z≅¼ (2i) x,y,z x≅¼,y≅¾,z≅¼ (2i) x,y,z x≅¼,y≅¼,z≅¾ *M Cation* (1a)+(1e)+(1f)+(1g) *M' Cation* (1b)+(1c)+(1d)+(1h)	*12x*(2i) x,y,z x≅¼,y≅0,z≅0 x≅0,y≅¼,z≅0 x≅0,y≅0,z≅¼ x≅¼,y≅½,z≅0 x≅¼,y≅0,z≅½ x≅0,y≅¼,z≅½ x≅½,y≅¼,z≅0 x≅0,y≅½,z≅¼ x≅½,y≅0,z≅¼ x≅¼,y≅½,z≅½ x≅½,y≅¼,z≅½ x≅½,y≅½,z≅¼	Origin Choice 1 No origin shift The standard setting is P$\bar{1}$ For F$\bar{1}$ use face cent. generators in addition For I$\bar{1}$ use body cent. generators in addition

Table A1.2

$R\bar{3}$ *(A-148-2)* Tilt System 14	$a \cong \sqrt{2}a_p$ $b \cong \sqrt{2}a_p$ $c \cong \sqrt{2}a_p$ $\alpha \cong \beta \neq \gamma \cong 60°$	*A Cation* (2c) x,x,x x≅¼ *M & M' Cations* (1a) 0,0,0 (M) (1b) ½,½,½ (M')	(6f) x,y,z x≅¾,y≅¾,z≅¼	Rhombohedral Cell
$P4_2/nnm$ *(A-134-1)* Tilt System 16	$a \cong 2a_p$ $b \cong 2a_p$ $c \cong 2a_p$	*A Cation* (2a) 0,0,0 (2b) 0,0,½ (4c) ½,0,0 *M & M' Cations* (4e) ¼,¼,¼ (M) (4f) ¾,¾,¾ (M')	(8m) x,x,z x≅¼,z≅0 (16n) x,y,z x≅¼,y≅½,z≅¾	Origin choice 2 Shift by -¼,¼,¼ No tilting about the c axis
C2/c *(A-15-1)* Tilt Systems 17 & 18	$a \cong 2a_p$ $b \cong 2a_p$ $c \cong 2a_p$	*A Cation* (4e) 0,y,¼ y≅0 (4e) 0,y,¼ y≅½ *M & M' Cations* (4c) ¼,¼,0 (M) (4d) ¼,¼,½ (M')	(8f) x,y,z x≅¼,y≅0,z≅0 (8f) x,y,z x≅0,y≅¼,z≅0 (8f) x,y,z x≅¼,y≅¼,z≅¼	Origin Choice 3 Shift by ¼,-¼,0 In phase tilting about the c axis
I2/m *(A-12-3)* Tilt System 20	$a \cong \sqrt{2}a_p$ $b \cong \sqrt{2}a_p$ $c \cong 2a_p$ $\beta \neq 90°$	*A Cation* (4i) x,0,z x≅½,z≅¼ *M & M' Cations* (2a) 0,0,0 (M) (2d) ½,½,0 (M')	(4i) x,0,z x≅0,z≅¼ (8j) x,y,z x≅¼,y≅¼,z≅0	Origin Choice A No tilting about the b axis
P4/mnc *(A-128)* Tilt System 21	$a \cong \sqrt{2}a_p$ $b \cong \sqrt{2}a_p$ $c \cong 2a_p$	*A Cation* (2c) 0,½,¼ *M & M' Cations* (2a) 0,0,0 (M) (2b) 0,0,½ (M')	(4e) 0,0,z z≅¼ (8h) x,y,0 x≅¼,y≅¼	Origin Choice A In phase tilting about the c axis
I4/m *(A-87)* Tilt System 22	$a \cong \sqrt{2}a_p$ $b \cong \sqrt{2}a_p$ $c \cong 2a_p$	*A Cation* (4b) 0,½,¼ *M & M' Cations* (2a) 0,0,0 (M) (2b) 0,0,½ (M')	(4e) 0,0,z z≅¼ (8h) x,y,0 x≅¼,y≅¼	Origin Choice A Out of phase tilting about the c axis
Fm3m *(A-225)* Tilt System 23	$a=b=c=2a_p$	*A Cation* (8c) ¼,¼,¼ *M & M' Cations* (4a) 0,0,0 (M) (4b) ½,½,½ (M')	(24e) x,0,0 x≅¼	Origin Choice 1 No origin shift

Table A1.2 (Continued)

Appendix 2

Vector Proof of Distorted Octahedra in ++- and 0+- Tilt Systems

In Glazer's original paper he points out that a mirror plane exists perpendicular to any axis about which there is either no tilting or in phase tilting (Glazer, 1972). These mirror planes are located halfway between the octahedra they separate (for example at x=¼ and x=¾ in the doubled unit cell). With this in mind consider any of the ++- or 0+- tilt systems mentioned above. All of these tilt systems have mirror planes located perpendicular to the x and y axes. As a consequence of having two mutually perpendicular mirror planes these tilt systems must have orthogonal axes. Now consider the octahedron centered at the origin and the octahedron located directly above it along the c axis. The orientation of each octahedron can be uniquely described by three metal-oxygen vectors pointing approximately down the x, y, and z axes. For the octahedron at the origin these vectors will be denoted by:

$$\mathbf{V}_{1x} = A1\mathbf{x} + B1\mathbf{y} + C1\mathbf{z},$$

$$\mathbf{V}_{1y} = A2\mathbf{x} + B2\mathbf{y} + C2\mathbf{z},$$

$$\mathbf{V}_{1z} = A3\mathbf{x} + B3\mathbf{y} + C3\mathbf{z}.$$

While for the second octahedron under consideration the metal-oxygen vectors describing the tilting of this octahedra can be defined as:

$$\mathbf{V}_{2x} = a1\mathbf{x} + b1\mathbf{y} + c1\mathbf{z},$$

$$\mathbf{V}_{2y} = a2\mathbf{x} + b2\mathbf{y} + c2\mathbf{z},$$

$$\mathbf{V}_{2z} = a3\mathbf{x} + b3\mathbf{y} + c3\mathbf{z}.$$

The relationship between these six vectors is shown in figure A2.1. The other three M-O vectors associated with each octahedron can be generated using the inversion center at the origin of the octahedron and provide no additional information about the orientation of the octahedra.

The inversion center that must be present at the origin of each octahedron restricts the M cation positions to lie on the unit cell axes. The metal centers of these two octahedra will be located at (0,0,0) and (0,0,½). Couple this with the fact that the axes are orthogonal and it is

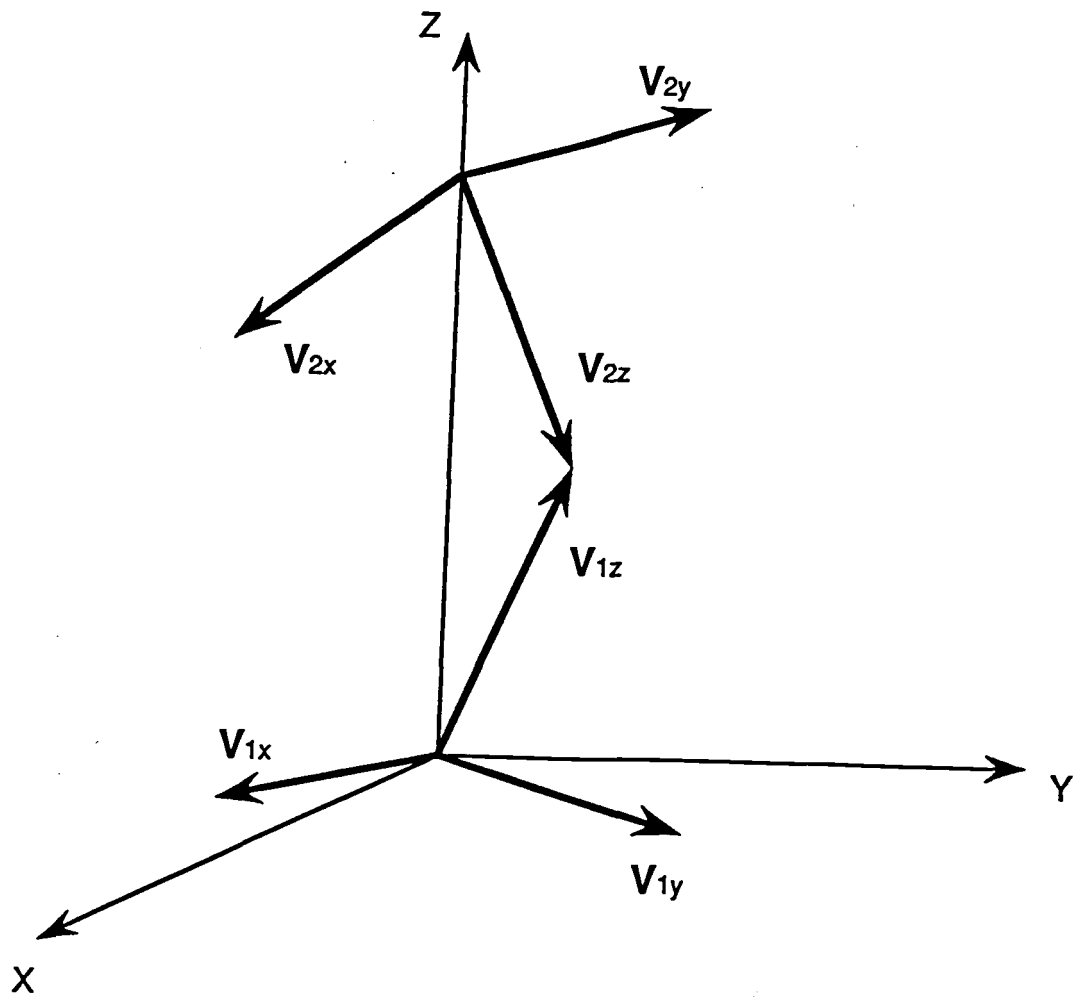

Figure A2.1 : The metal oxygen vectors discussed in the text for two octahedra linked along the z axis of an $a^+a^+a^-$ tilted perovskite.

clear that in order for the two octahedra to be linked together and the second metal cation to be located directly above the first metal cation on the z axis the following relations must hold:

$$a3 = A3,$$

$$b3 = B3,$$

and in order to keep all of the M-O vectors the same length (necessary to maintain perfect octahedra) the third component of vector $\mathbf{V}_{2z}$ is also uniquely determined:

$$c3 = -C3.$$

Therefore, in any of the ++- or 0+- tilt systems an arbitrary tilt of the octahedron at the origin fixes the vector $\mathbf{V}_{2z}$.

The vectors $\mathbf{V}_{2x}$ and $\mathbf{V}_{2y}$ are also subject to several constraints. To begin with, the oxygen ions at the end of both of these vectors must lie on the mirror planes discussed previously. This requirement also holds true for the octahedron at the origin so that:

$$a1 = A1 = \tfrac{1}{2}\mathbf{a},$$

$$b2 = B2 = \tfrac{1}{2}\mathbf{b}.$$

where **a** and **b** are the lattice constants along the x and y axes respectively. Now the only unknown components remaining are b1, c1, a2, and c2. In other words once the tilting of the first octahedron has been specified, five of the nine coefficients describing the orientation of the second octahedron are determined. However, in order to keep the second octahedron perfectly rigid the following equations must be satisfied:

$$D^2 = a1^2 + b1^2 + c1^2, \qquad (1)$$

$$D^2 = a2^2 + b2^2 + c2^2, \qquad (2)$$

$$0 = (a1)(a2) + (b1)(b2) + (c1)(c2), \qquad (3)$$

$$0 = (a1)(a3) + (b1)(b3) + (c1)(c3), \qquad (4)$$

$$0 = (a2)(a3) + (b2)(b3) + (c2)(c3). \qquad (5)$$

The first two equations must be satisfied in order to keep all of the M-O distances constant (where D is the M-O bond distance), and the last three equations must be satisfied to keep all of the O-M-O bond angles 90°. This leaves only four unknowns available to satisfy five linearly independent equations. In general this will not be possible and one of the equations above will not be satisfied. The physical consequence of this is that either one of the bond angles or bond distances must distort from its ideal value in a perfect octahedron. To test this assertion calculations were done to ensure that for an arbitrary tilt of the first octahedron, it was not possible to simultaneously satisfy equations (1) through (5) for the second octahedron. The calculation of $\mathbf{V}_{2x}$, $\mathbf{V}_{2y}$, and $\mathbf{V}_{2z}$ for tilt system $a^+a^+a^-$ is given in Appendix 3, as an example.

Appendix 3

Calculation of the Octahedral Vectors in the $a^+a^+a^-$ Tilt System

Consider the $a^+a^+a^-$ tilt system with three 10° clockwise tilts and a metal-oxygen distance of 2.00Å. Performing 10° tilts about each of the three Cartesian axes results in the origin octahedron having an orientation described by the following vectors:

$$\mathbf{V_{1x}} = 1.9397\mathbf{x} - 0.3132\mathbf{y} + 0.3736\mathbf{z},$$

$$\mathbf{V_{1y}} = 0.3736\mathbf{x} + 1.9397\mathbf{y} - 0.3132\mathbf{z},$$

$$\mathbf{V_{1z}} = -0.3133\mathbf{x} + 0.3736\mathbf{y} + 1.9397\mathbf{z},$$

where the coefficients represent distances in angstroms between the metal ion at the origin and the three oxygen ions defining the octahedral orientation. Imposing the restrictions placed on the second octahedron by the mirror planes and the orthogonal axes gives the following values for the M-O vectors of the second octahedron:

$$\mathbf{V_{2x}} = 1.9397\mathbf{x} + b1\mathbf{y} + c1\mathbf{z},$$

$$\mathbf{V_{2y}} = a2\mathbf{x} + 1.9397\mathbf{y} - c2\mathbf{z},$$

$$\mathbf{V_{2z}} = -0.3133\mathbf{x} + 0.3736\mathbf{y} - 1.9397\mathbf{z}.$$

By combining equations 2 and 4 above the vector $\mathbf{V_{2x}}$ can be found so that it is perpendicular to $\mathbf{V_{2z}}$ and of length 2.00Å. When this calculation is carried out a quadratic equation in c2 is obtained. Because the equation is a quadratic there are two solutions:

$$\mathbf{V_{2x}} = 1.9397\mathbf{x} + 0.4299\mathbf{y} - 0.2305\mathbf{z},$$

$$\mathbf{V_{2x}} = 1.9397\mathbf{x} - 0.3131\mathbf{y} - 0.3736\mathbf{z}.$$

Both of these vectors are 2.00Å long and perpendicular to $\mathbf{V_{2z}}$ but the second vector corresponds to in phase tilting about the z axis, while the first vector is correct for out of phase tilting about the z axis. All of the tilt systems considered here have out of phase tilting

about the z axis, so the first of the two vectors above will be taken as $\mathbf{V}_{2x}$ and the second vector discarded. The final vector $\mathbf{V}_{2y}$ must be perpendicular to both $\mathbf{V}_{2x}$ and $\mathbf{V}_{2z}$. A vector mutually perpendicular to these two vectors can be generated by taking the cross product $\mathbf{V}_{2x} \times \mathbf{V}_{2z}$. The magnitude of this vector is now scaled so that its y component is 1.9397 giving the vector:

$$\mathbf{V}_{2y} = -0.3783\mathbf{x} + 1.9397\mathbf{y} + 0.4347\mathbf{z}.$$

Combining the above calculations the orientation of the second octahedron can be described by the following set of three vectors:

$$\mathbf{V}_{2x} = 1.9397\mathbf{x} + 0.4299\mathbf{y} - 0.2305\mathbf{z},$$

$$\mathbf{V}_{2y} = -0.3783\mathbf{x} + 1.9397\mathbf{y} + 0.4347\mathbf{z}.$$

$$\mathbf{V}_{2z} = -0.3133\mathbf{x} + 0.3736\mathbf{y} - 1.9397\mathbf{z}.$$

The way in which these vectors were calculated guarantees they will satisfy equations 1,3,4, and 5, but no constraint has been placed on the length of vector $\mathbf{V}_{2y}$. Calculating the length of $\mathbf{V}_{2y}$ gives a value of 2.024Å, slightly longer than all of the other M-O vectors. This result can be extended to all of the ++- and 0+- tilt systems. Therefore, we see that it is mathematically impossible to achieve linked octahedra in these tilt systems without distortions of the octahedra. The magnitude of these distortions will depend on the size of the tilt angles and the length of the M-O bonds.

Note that when calculating the $\mathbf{V}_{2x}$ vector two solutions were found, the second vector was discarded because it corresponded to in phase tilting about all three axes. However, if the calculations are carried through with this vector the final orientation of the second octahedra satisfies all five equations. This is in agreement with the fact that POTATO is able to generate structures possessing perfectly rigid octahedra in the +++ and 0++ tilt classes.

Appendix 4

POTATO : a program for generating perovskite structures distorted by tilting of rigid octahedra

A4.1 The Crystallographic Problem

The framework of the perovskite structure is a three dimensional network of corner sharing octahedra. Both simple, AMO_3, and double, $A_2MM'O_6$, perovskite compounds are commonly distorted from the ideal cubic structure by tilting of the octahedra. Often times there is very little distortion of the octahedral unit. In these cases the structure can be almost completely described by specifying the magnitude of the tilts and the sense in which the octahedra tilt with respect to each other. For simple tilting distortions there are 23 possible tilting combinations which can occur. The space group predictions for all 23 tilt systems both with and without 1:1 cation ordering are given in chapter 2. Although the space group predictions are useful, it is often times very desirable to know the exact lattice constants and atomic positions. This is particularly useful for comparing actual structures with the idealized structures, and for generating starting models to use in Rietveld refinements.

A4.2 Method of Solution

Given the Glazer tilt system, tilt angles, M-O bond distance (M-O and M'-O bond distances for ordered perovskites), and the identity of the ions as input, POTATO generates a complete crystallographic description of the unit cell as output. Two output files are created. One file contains a description of the unit cell in space group $P\bar{1}$ (Z=8), and the second file contains a unit cell description where the underlying symmetry of the structure has been properly taken into account. Both files are in *.xtl format. To obtain this solution first the individual octahedra are tilted independently, according to the tilt system and tilt angles entered as input. The are then linked together at the corner to form a three dimensional network. Finally, the program calculates the unit cell constants and coverts from Cartesian to fractional coordinates. The coordination of the A cation is not

optimized, but rather the A cation is simply paced in the center of its eight nearest neighbor M ions (M and M' for ordered perovskites). Note that because the separate tilt operations about each of the three Cartesian axes do not belong to an Abelian group, the final crystallographic description will depend upon the order in which the tilt operations are carried out (Glazer, 1972). This complication has been circumvented by tilting in 0.01° increments about each of the Cartesian axes in the order x, y, z, x, y, z, x, ... until the final tilting angles are achieved.

A4.3 Software and Hardware Specifications

The program was written in standard FORTRAN 77 and has been compiled for both PC and UNIX systems. The program contains 5379 lines of FORTRAN 77 code, including comment lines. The executable file occupies 118 kilobytes of memory, and the source code 145 kilobytes of memory. Typical running tiles on a 486/66 MHz PC are 1-10 seconds. The PC version was compiled using a Microsoft FORTRAN compiler. The PC compiled program runs on X86 IBM PC computers and clones with a mathematical coprocessor. The UNIX compiled program has been implemented on a Silicon Graphics Indigo workstation, but should also work on other UNIX based machines.

Appendix 5

Extended Hückel Parameters

The atomic parameters used in the extended Hückel calculations were provided by the software package used in the calculations (Miller, 1990). They are given below in table A5.1.

	H_{ii} (eV)			orbital exponent, ζ		
Atom	**d**	**s**	**p**	**d***	**s**	**p**
O		-32.30	-14.80		2.28	2.28
Al		-12.30	-6.50		1.37	1.36
Sr		-6.62	-3.92		1.21	1.21
Y	-8.32	-8.13	-5.14	1.56 (0.8316) 3.55 (0.3041)	1.74	1.70
Mo	-11.06	-8.77	-5.60	4.54 (0.5899) 1.90 (0.5899)	1.96	1.90
Ru	-14.62	-10.79	-5.74	5.38 (0.5573) 2.30 (0.6642)	2.08	2.04
Sn		-16.16	-8.32		2.12	1.82

Table A5.1 : Extended Hückel parameters used in this work. *The d orbitals are modeled using a double ζ expansion. For a desciption of the use of these parameters in the extended Hückel method see Burdett (Burdett, 1980).